EXPLORING THE AERODYNAMIC CHARACTERISTICS OF A BLOWN ANNULAR-WING FOR V/STOL AIRCRAFT

A thesis submitted for the degree of Doctor of Philosophy

by

Burhan Saeed

School of Engineering & Design

Brunel University

Project Supervisor(s): Dr Guy Gratton & Dr Cristinel Mares

September 2010

ABSTRACT

This research programme explores, theoretically and experimentally, a new lift-system for Vertical/Short Take-off and Landing (V/STOL) Aircraft. It is based upon an annular wing wrapped around a centrifugal flow generator, potentially creating a vehicle with no external moving parts, reduced vehicle aerodynamic losses compared to previous V/STOL technologies and substantially eliminating induced drag. It is shown that such a wing works best with a thick aerofoil section, and appears to offer greatest potential at a micro-aerial vehicle scale with regard to fundamental performance parameter “lift to weight ratio”. Certain efficiency losses are encountered mainly occurring from annular flow expansion and problems with achieving acceptable blower slot heights. Experimental methods are described along with results, and a comparison shows that the experimental values remain below theoretical values, partly due to flow asymmetry but possibly also other factors. Symmetrical blowing, as initially hypothesised, was found to be impracticable; this suggested use of pure upper surface blowing with Coanda effect. The modified approach was further explored and proved viable.

The ultimate goal of this work was to develop an understanding and the facility to integrate the annular-wing into a vehicle to achieve controlled powered flight. To serve the purpose, issues encountered on current and past V/STOL aircraft are being investigated to set a path for further research/development and to validate/justify the design of future V/STOL aircraft. Also, presented is a feasibility study where different physical scales and propulsion systems are considered, and a turbofan has shown to achieve the best performance in terms of Range and Endurance. This privilege allows one to accurately study the V/STOL technologies around.

Acknowledgements

"In the name of Allah the most beneficent and merciful"

First of all I would like to express gratitude to my supervisor Dr Guy Gratton, who continuously monitored progress of this project and channelised my efforts in the best possible way. He has always been enthusiastic, encouraging and friendly making my PhD studies enjoyable and stimulating at intellectual plane. I strongly feel, beside formal duties, his aim was to assist me to acquire the skills of a professional scientist who could perform well in a competitive environment. I would also like to thank Dr Cristinel Mares for his guidance, support and highly intellectual discussions during the research.

Special thanks to Dr Reza Mokhtarzadeh, Dr T P Chong and Dr Chris Toomer (UWE) for reviewing the thesis rigorously which helped me improve the legibility of this technical document.

I would like to thank Professor Alan Champneys and Dr Mark Lowenberg of University of Bristol for enhancing my skills and passion for engineering discipline during my MSc studies. The experience gained was invaluable and later proved to be the prerequisite for this demanding PhD research studies.

I wish to convey my sincere thanks to Mr Kevin Robinson (Lab Technician) who helped me with building the experimental rig and most importantly helped me meet deadlines.

I would like to acknowledge that this project has been funded by the EPSRC CASE programme, along with the financial and intellectual input of Mr Peter Frost-Gaskin who also holds international patents for this form of wing.

Keywords

Annular wing; Blown wing; Coanda Effect; Upper surface blowing; V/STOL

List of publications resulted from this research

Journal Papers

1. Saeed, B. and Gratton, G. *An evaluation of the historical issues associated with achieving non-helicopter V/STOL capability and the search for the flying car*. Aero J Vol. 114 No 1152, pp91-102, February 2010.
2. Saeed, B. and Gratton, G. *Exploring the Aerodynamic Characteristics of a Blown-Annular-Wing for V/STOL Applications*. Submitted to IMechE Journal of Aerospace Engineering {Accepted}.
3. Saeed, B. and Gratton, G. *An Approach to Evaluate Lift Generated by an Annular-Coanda-Wing with USB for V/STOL*. Developed, to be submitted to AIAA Journal of Aircraft.
4. Saeed, B, Gratton, G and Mares, C. *A Feasibility Study into V/STOL Capable Annular-Wing Aircraft*. Under Development, to be submitted to AeroJ.

Conference Papers

1. Saeed, B. and Gratton, G. *Numerical evaluation of the aerodynamic characteristics of annular wingform for V/STOL applications*. RAeS International Conference: The Aerodynamics of Novel Configurations capabilities and Future Requirements, October 2008.
2. Saeed, B. *Flying Cars – The Next Generation*. SED International Research Conference Brunel University, June 2008.

Contents

List of Figures

Nomenclature

A_C	Compressor or blower outlet cross-sectional area (m^2)
$A_{C.S}$	cross-sectional area facing the flow (m^2)
A_r	Cross-sectional area facing the flow at a distance r from blower central axis (m^2)
A_O	compressor outlet cross-sectional area (m^2)
A_{ref}	Wing surface area (m^2)
a	Lift curve slope $\partial C_L / \partial \alpha$
C_P	pressure coefficient
C_{Po}	Power coefficient
C_D	Drag coefficient
C_L	Lift coefficient
C_{Lmax}	maximum lift coefficient
C_M	Pitching moment coefficient
CTOL	Conventional take-off and landing
C.P.	Centre of Pressure
CSFF	Cross-sectional area facing the flow

CG	centre of gravity
C	Wing chord length (m)
C_μ	Jet moment coefficient
D	Drag Force (N)
d	Fan diameter (m)
g	Gravitational acceleration (m/s^2)
E_e	Electrical energy (J)
E_m	Mechanical enegy (J)
F_A	Horizontal or axial force component (N)
F_N	Normal or vertical force component (N)
f_a	Annular reduction factor
k_s	Suckdown factor
L	Lift (N)
L/D	lift to drag ratio
L/W	lift to weight ratio
LID	lift improvement device
L_{OGE}	Lift generated in out of ground effect (N)

L_f	Jet fountain lift (*N*)
L_s	Suckdown lift (*N*)
L_h	effective lift from the annular wing in hover (*N*)
M	Structural mass (*kg*)
$\dot{m}$	Mass flow rate (*kg/s*)
NTSB	National Transport Safety Board
P	Compressor input power (*Watt*)
P_{atm}	Atmospheric pressure (*Pa*)
P_s	Body surface pressure (*Pa*)
R_e	Reynolds number
R_0	outer radius of annulus (*m*)
r	Radial distance away from blower central axis (*m*)
r_s	Surface radius (*m*)
r_t	wing trailing edge radius (*m*)
r_o	Blower outer or annulus inner radius (*m*)
r'	Non dimensional distance away from blower central axis r/r_o

$r_{c/4}$	Radius at quarter chord (m)
S	wing surface area (m^2)
S_d	Propeller disk area (m^2)
S_0	Take-off ground roll (m)
s	Surface path (m)
s_i	Surface panel length (m)
STOL	short take-off and landing
T	Horizontal thrust generated by the blower (N)
T_R	Reversed engine thrust (N)
T_{atm}	Atmospheric temperature (^{0}C)
T_{req}	Thrust required for VTOL (N)
T_{dp}	Thrust generated by a ducted propeller (N)
t	Longitudinal thickness {control volume} (m)
$t_{c/4}$	Longitudinal thickness at quarter chord {control volume} (m)
$t_{\max}$	Maximum aerofoil thickness (m)
t_t	Wall-jet flow depth at trailing edge (m)

t_x	Aerofoil thickness at a distance *x* from the leading edge (*m*)
UAV	unmanned aerial vehicle
U	translational velocity (*m/s*)
U_C	compressor outlet flow velocity (*m/s*)
$U_{c/4}$	Local airspeed at quarter chord (*m/s*)
U_{eff}	Effective flow velocity (*m/s*)
U_{max}	Maximum flow velocity at outlet (*m/s*)
U_r	flow velocity at a distance r (*m/s*)
U_{ref}	Flow velocity at quarter chord (*m/s*)
U_x	translational velocity (*m/s*)
u	Local flow velocity (*m/s*)
u_m	Maximum wall-jet velocity (*m/s*)
$u_{m/2}$	$u_m/2$ (*m/s*)
VTO	vertical take-off
VTOL	vertical take-off and landing
V/STOL	vertical/short take-off and landing

V_{ref}	approach speed (*m/s*)
v_c	Rate of climb or climb velocity (*m/s*)
v	local flow velocity (*m/s*)
W	Weight (*N*)
W_0	gross weight (*N*)
y_{m}	Radial distance from surface to the point where $u = u_{\mathrm{m}}$ (*m*)
$y_{\mathrm{m/2}}$	Radial distance from surface to the point where $u = u_{\mathrm{m/2}}$ (*m*)
ϕ	Area ratio between fan and duct exhaust
μ	dry friction coefficient
η_p	Propulsive efficiency
α	Angle of attack (deg)
δ_f	Flow turn angle (deg)
η_L	Lifting efficiency
η_t	Turning efficiency
ψ	Azimuth angle (radians)
ρ	air density at sea level $(=1.225\ kg/m^3)$

Chapter 1. Introduction

1.1 General Introduction

Since the invention of aircraft extensive research has been conducted in the area of Vertical/Short Take-Off and Landing (V/STOL) technologies. Aircraft with V/STOL capability are highly demanded by “blue light” (military and emergency services) operators. This is self-evident: it cuts the need for long runways and reduces the time to achieve horizontal flight. The most successful aircraft of this kind is the helicopter. However, implementation of the capability in a fixed-wing aircraft has been a challenge and rarely been achieved. The BAe Harrier, Bell-Boeing Osprey V-22 and Joint Strike Fighter F-35 are the most successful fixed-wing aircraft to have achieved V/STOL.

It is clearly the net vertical force during take-off and landing that distinguishes a V/STOL aircraft from a conventional aeroplane. To that perspective a new and relatively untried strategy is proposed to achieve V/STOL with the wing fixed; the approach being is to generate lift from a static-blown-wing whereas in a conventional aircraft the wing is propelled through air to produce lift. Figure 1 presents a schematic layout of the novel static-blown-wing. This static wing comprises a ring portion 2 having an aerofoil shaped cross-section. Positioned above the centre aperture of the ring portion 2 is a diffuser plate 3, the diffuser plate is

optionally arranged to be moveable vertically (as shown by the arrow on the figure) between a closed operational position and an open operational position. At the outer circumference of the ring portion 2 there are provided a plurality of elevators 4 which are moveable. The wing may be connected with a propulsion system by means of a mechanical coupling 5. Counter-rotating fans 6a, 6b may be driven by a jet engine 7 to induce air to flow from an intake 8 to the underside of the diffuser plate 3, which in its open position directs the air over the upper surface of the ring portion 2 to generate lift {from [1]}.

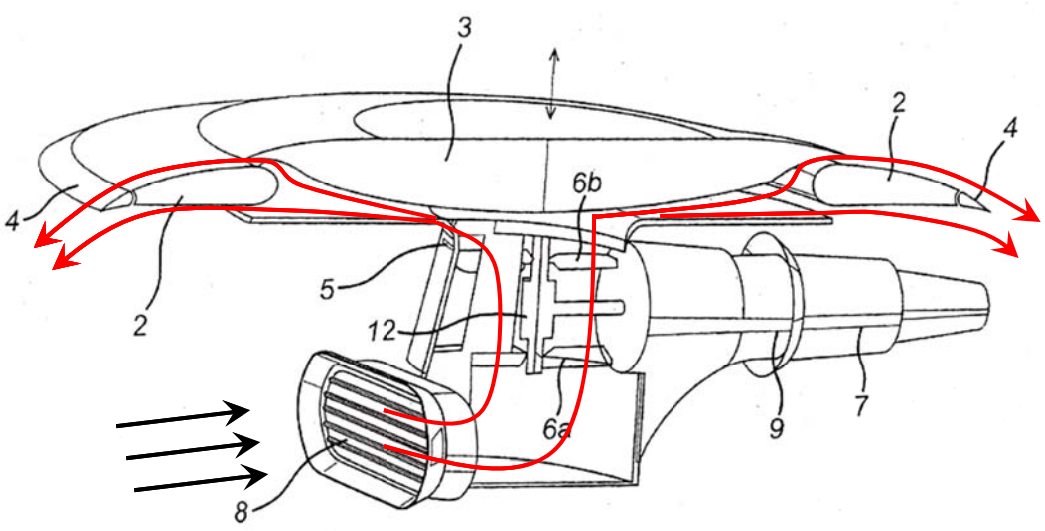

Figure 1: Proposed powered-lift system for a V/STOL aircraft {derived from [1]}.

This research focuses on the ring portion (or the annular wingform) of the lift system. The ring portion is extracted from the system, simplified and further conceptualised as depicted in Figure 2. The hypothesis being that a centrifugal fan or compressor (blowing away from the centre) blows air over the wing, set at an angle to the flow, which will then produce lift. The supposition on the flow generated by the centrifugal compressor is that the flow streamlines are parallel to the chord line i.e. a source like flow. The annular wing would produce lift/thrust to hover with sufficient fan power; however, its efficiency needs to be evaluated quantitatively: specifically *lift to drag* and *lift to weight* ratios. This efficiency evaluation must consider the case of the hover, and also where the wing is in forward flight and the flow over/around the annulus becomes asymmetric.

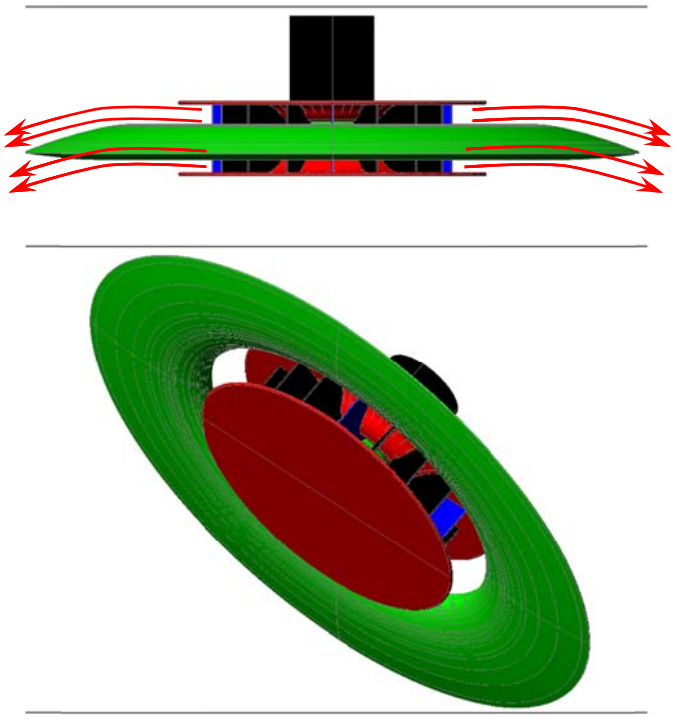

Figure 2: A 3-D depiction of ring wing and blower

1.2 Motivation

At first sight, some potential advantages of this wingform may be seen:

- It will achieve vertical take-off by net lift generated by the annular wing rather than propulsive thrust thus minimising ground effect upon propulsion
- It should experience no induced drag in hovering flight since it has no free ends. So long as translational velocity is substantially less than compressor outlet velocity, then translational induced drag should also be minimal whilst annular flow and lift effects dominate.
- It should be relieved from the typical aerodynamic losses experienced by most previous V/STOL aerial vehicles including suckdown, recirculation, hot-gas ingestion, thrust vectoring and reaction control system resulting in excessive fuel consumption {these phenomena are described in detail in [2]}.
- Balance and thrust matching problems encountered with Jet-V/STOL aircraft should be at-least alleviated.
- It should have no external moving parts unlike the helicopter or tilt rotor aircraft.

1.3 Objectives

- Generate theoretical models for the wing in hover and translational flight modes
- Perform analysis of the wing based on the models generated and define its aerodynamic characteristics
- Evaluate geometry of the annular wing e.g. inner and outer radii of the annulus
- Design and conduct an experiment to validate and/or improve the theories generated
- Generate and develop ideas to improve aerodynamic efficiency of the wing
- Carry out an analytical review of past V/STOL capabilities to understand specific design criteria for this particular class of aircraft
- Perform feasibility studies to integrate the annular wing into a useable aircraft and establish design rules

1.4 Novel Research Approach

Initially, this research task was split into theoretical analysis and experimental tests of the wing, and hoping that each validates and helps refine the other. The longer term aim has then been to modify the basic wing shape in order to improve its aerodynamic efficiency and to develop design rules so that the wing design may be utilised in a flyable vehicle. Specifically, the author has set out to follow the road map displayed in Figure 3.

The quest was motivated and complemented by relevant literature survey and has run in parallel to other tasks. The novel aerodynamic/mathematical model of the wing is initially based on fundamental aerodynamic laws and further developed as necessary. The theoretical predictions are made visual by numerical simulations using software package MatLab. An experimental setup is designed to support/validate the theories generated and, in particular, to investigate the crucial parameters. Once the correlation between the theoretical and the experimental results is achieved, the main performance parameters (as listed in the road map) and their relationships are

established. Then optimisation of the performance parameters is sought with literature backing up. It will ultimately lead to a prototype model to fully demonstrate the technology.

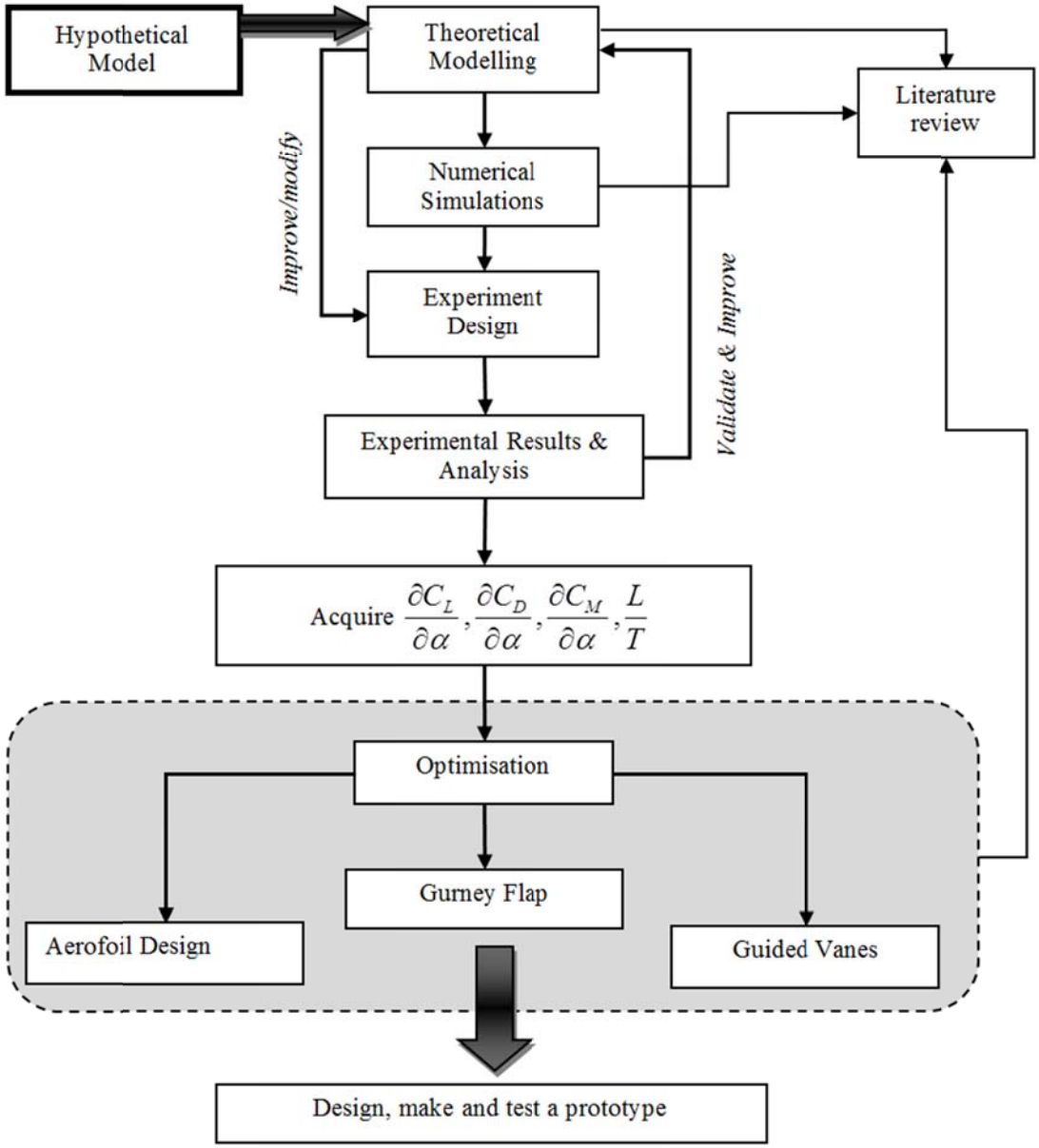

Figure 3: Research road map.

1.5 Summary of Contributions

This research work provides an insight into aerodynamic challenges encountered with the unconventional wingform. The most critical finding has been the rectification of initial hypothetical model. Consequently, certain contributions have

been made across a broad range of aircraft design that will assist the technical community with on-going research and development of V/STOL technologies.

- Evaluation of the historical issues associated with achieving non-helicopter V/STOL capability and the search for the flying car.
- First quantitative exploration of annular-blown-wing.
- Experimentally demonstrated the Coanda effect and flow attachment on circular blown wings
- Designed, manufactured and tested several different blower and wing geometries.

1.6 Thesis Chapter Summary

- Chapter 2: The chapter collects the background information on blown wings that must be understood to a certain extent before embarking on the task of evaluating aerodynamic forces acting on the wing. The subsections provide with sufficient mathematical tools to solve related problems.
- Chapter 3: A thorough illustration of the experimental strategy is presented.
- Chapter 4: A hypothetical flow model for the annular wing is rendered. Forces generated are evaluated theoretically and experimentally. Analysis is performed and a modification in the initial hypothetical model is proposed.
- Chapter 5: The proposed upper surface blowing with Coanda effect is explored by means of theoretical analysis and experimental testing
- Chapter 6: Lift enhancement proposals are explored, including the Gurney flap and guided vanes.
- Chapter 7: Historical issues concerned with V/STOL aircraft are explored. In light of historical experience the performance of future V/STOL flying cars is evaluated and analysed.
- Chapter 8: Develops the understanding and the facility to achieve controlled powered flight at different physical scales. Moving further towards that end, several aircraft of varying physical size and capability have been conceptualised.
- Chapter 9: Summarises the crucial findings and concludes the quest.

Chapter 2. Literature Survey and Case Study

2.1 Blown Wings

The literature on blown wings is large but scattered and there exists no standard definition of a blown wing. Most often, it has been referred to as a wing with partial blowing over the upper surface of a multi element (flaps, slats and tabs) aerofoil. However, herein, the blown wing scenario is different: the whole surface area of the annular wing is wetted into the blown air. So, what could be learned from previous blown wings and how is it relevant to the annular wing under consideration? The most common characteristic of blown wings is the ability to divert the flow by large angles (~ 90^{o}).

The science behind blown wings also relates to the Coanda effect [3], which is the tendency of a fluid jet to stay attached to an adjacent curved surface that is very well shaped. It is this effect which achieves 90 degree thrust deflection. Typically, a Coanda wing/flap can divert horizontal engine thrust into vertical lift/thrust at the cost of 20 to 30% thrust loss [4] but with substantial increases in lift.

It is anticipated that any successful annular wing will use the Coanda effect at least at the upper surface.

Vertical/short take-off and landing requires much higher $C_{L_{\max}}$ values than conventional take-off and landing, typically $5 < C_{L_{\max}} < 10$ (from [5]). These high values are achieved by external/internal blowing over the flaps or by blowing over the upper surface of the wing. Typically, the blowing source is the compressed bypass air collected from the outer core of a gas turbine engine as shown in Figure 4. Such lift enhancement has been referred to as powered lift, although this term is also used in some other contexts – such as helicopters or jetborne aeroplanes.

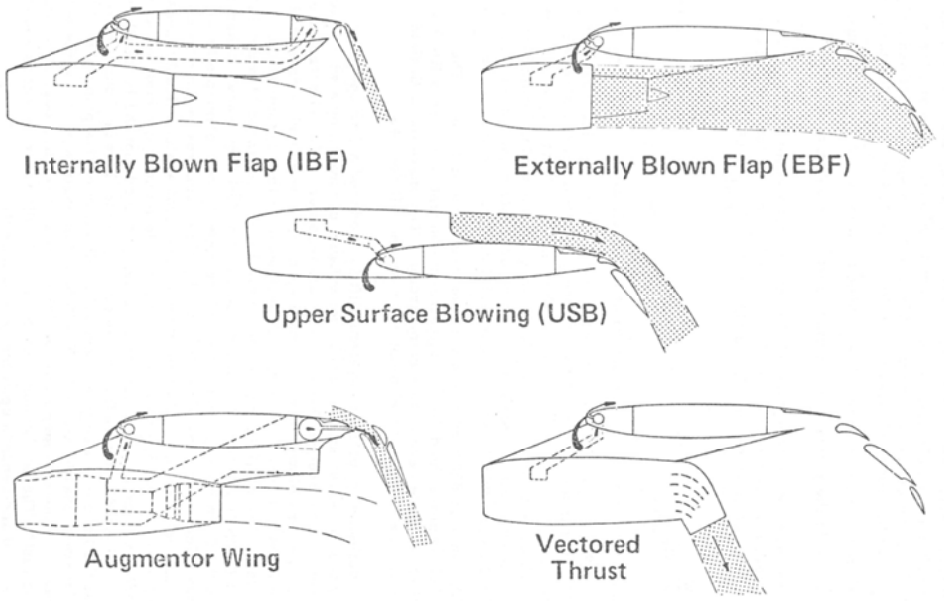

Figure 4: Typical powered lift concepts {from [5]}.

From the above arrangements the internally blown flap, also known as jet flap, is the most efficient with highest lift to drag ratios [6]. The jet flap is an arrangement for obtaining high lift on an aerofoil by ejecting a thin sheet of high velocity air with a downward inclination from a slot near the trailing edge. It supplies lift both 1) by the reaction to the vertical momentum of the jet, which appears as pressure on the internal ducting, and 2) by the vertical component of the pressure on the outer surface of the aerofoil, which arise from asymmetry induced in the main stream by the presence of the jet. Similarly, thrust is obtained from the corresponding horizontal components [7].

2.2 Coanda Effect Circulation Control

The Coanda effect is the tendency of a fluid jet to stay attached to an adjacent curved surface that is very well shaped. The phenomenon was discovered by Henri Coanda, a Romanian aerodynamicist, also arguably responsible for building the world's first powered jet aircraft [8]. Coanda had originally used this device for a totally different purpose: as a means to deflect the exhaust of a radial piston engine away from a wooden aircraft fuselage. During its first flight, these shielding plates actually entrained the hot exhaust flow inward, igniting and destroying the aircraft. Figure 5 shows the basic Coanda device as later formulated by him (after the described exhaust accident) and its application to a fixed wing aircraft. Note that in these (and in all other Coanda cases found), Coanda aligns acute-angle steps downstream of one side of a jet-nozzle to deflect the jet to that side and entrain large masses of fluid from the opposite side. The distinctive steps and angles were intended to generate a vortex flow at each corner, and thus enhance mixing there. The concept was subsequently applied by Coanda and others to many other devices, including car engine exhaust scavengers, wind-tunnel turning vanes, thrust augmentors, water propulsion units, injection wind tunnels, deflection surfaces, and rotary pumps. However, efficiency questions arose because of added friction along all the steps and separated flow at each corner.

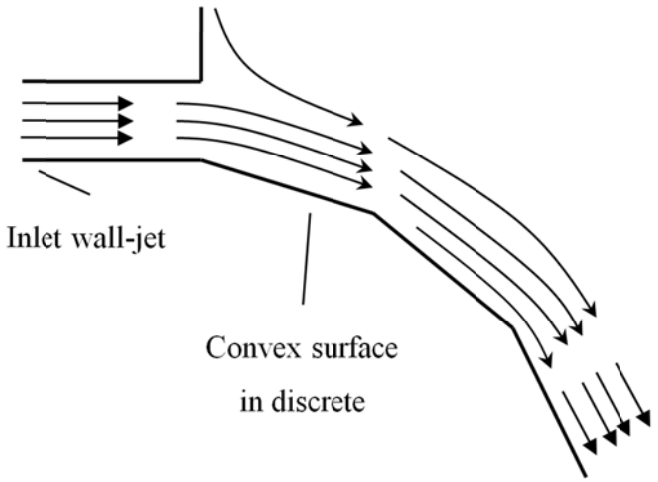

Figure 5: Original Coanda device {derived from Ref. [9]}.

A wall jet is a thin jet of fluid blown tangentially along a wall, where the surrounding fluid may be either at rest or co-flowing. The wall jet resembles half of a free jet with a wall boundary layer imposed, and in most practical applications the wall jet will be fully turbulent. Wall jets are thin relative to other dimensions in the flow, and they have a greater stream wise velocity than the surrounding fluid [10]. The adjacent wall may be either straight or have streamwise curvature. One of the most interesting and useful features of the wall jet is the Coanda effect, whereby the jet remains strongly attached to a convex surface. As opposed to a curved boundary layer flow, the wall jet can resist the adverse pressure gradient associated with convex curvature long enough to remain attached for turning angles of greater than 200 degrees [11]. In addition to strong attachment, curved wall jets display an increase in their mixing with the surrounding fluid compared with straight wall jets. These two properties, wall attachment and increased mixing, enable the wall jet to delay separation of an external stream from a curved surface.

Henri Coanda went on producing multiple patents [12,13] utilizing the effect he observed and studied to generate propulsion for aircraft. Later, an experiment by Von Glahn found that placing curved and flat plates near a nozzle would result in a ratio of lift to undeflected thrust of about 0.8-0.9, depending on the total deflection angle [14]. Thus a Coanda nozzle could achieve a 90° deflection of the jet-stream and result in a vertical lifting force in the order of 0.8 of the undeflected thrust. This shows that Coanda nozzles can produce lift as well as maintain thrust.

Lift is created on the curved surface of a nozzle where the lower pressure regions form. Coanda attempted to use this idea with jet engines to generate flow over outer curved surfaces of crafts he designed. His patent for a lenticular craft gave an insight into the uses of the Coanda effect in the area of aircraft propulsion [15]. The generation of this lift principle can also be seen in the upcoming flying-disc/saucer hovercraft shown in Figure 6 and Figure 7. These flying vehicles use high speed airflow, from a centrifugal fan, over the upper surface of the disc which creates a relatively lower pressure region at that surface. This low pressure region creates lift and causes the craft to hover. The high speed flow is able to create the low pressure region by remaining attached to the craft as it flows around it.

Figure 6: Flying-Disc hovercraft prototype demonstrating USB {from [16]}.

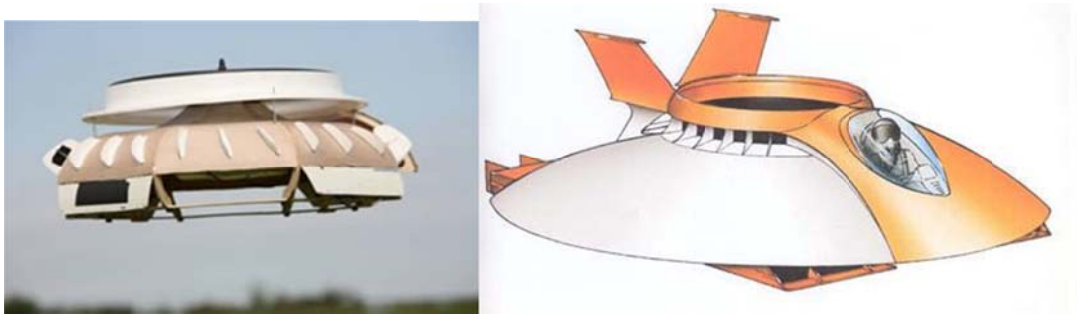

Figure 7: MIRA Flying Saucer prototype and conceptual design [17].

The aerodynamic concept now known as Circulation Control (CC), Figure 8, is a logical follow-on to these devices, with one very important difference which has made a significant performance improvement. The tangential jet sheet exits over the curved trailing edge of the surface replacing the flap, and this curvature can turn through a full 180° or more. The jet remains attached to that curved surface because of a balance between the sub-ambient pressure in the jet sheet and the centrifugal force in the jet going around the curvature [18].

The most important parameter of circulation control science, as observed in the literature, is the blowing momentum coefficient $C\mu$ which is defined as

$$C_{\mu} = (\text{mass flow rate} \times \text{jet velocity}) \ / \ (\text{dynamic pressure} \times \text{wing planform area})$$

$$C_{\mu} = \frac{\dot{m} U_C}{qS}$$

Circulation Control by Coanda blowing over a rounded trailing edge has proven to be the most power efficient method for high lift generation. Only two circulation-control aircraft have ever been build and flight-tested in the past 30 years. “Why”

was one of the questions posed at the end of the 2004 ONR-NASA circulation control workshop? Other high lift systems, such as the jet flap, upper surface blowing, augmenter wing and flap type thrust deflectors have found many applications on STOL aircraft. The two Circulation Control aircraft were the WVUCC Technology Demonstrator STOL flight-tested in 1974 and the Grumman A-6Aflight-tested in 1979 [19].

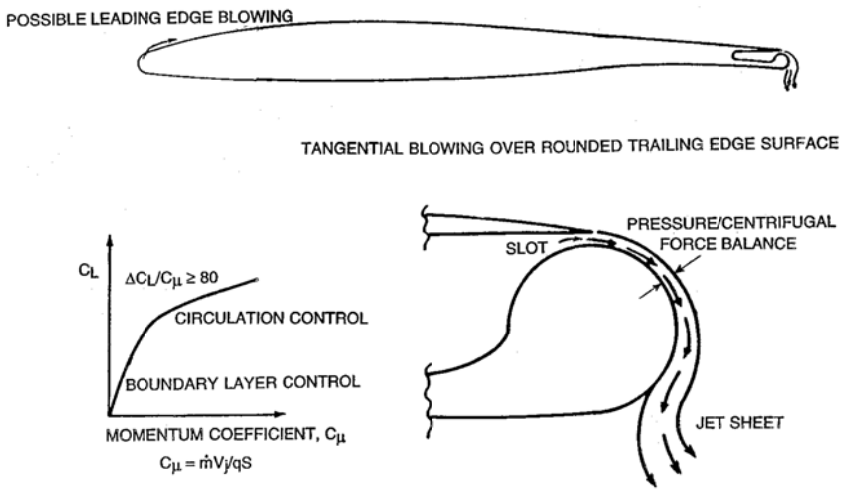

Figure 8 Basics of circulation control aerodynamics {from [18]}

Several flight-tests were performed on WVUCC aircraft which concluded that flying level at slow speed and high C_L, required the entire available power (134 kW), which means flying on the backside of the power curve. This leaves no power to spare to assist in wing stall recovery. Stall produces rapid roll and around 170 metres of altitude is needed for recovery. Other high lift systems, using blowing air, do not have such a severe problem as much of their lift is provided by deflected engine thrust. This may explain why only two such aeroplanes have been built in the past 30 years [19].

Figure 9 presents a typical experimental aerofoil to test circulation control; the figure also presents the pressure distribution over its surface. The pressure over the rounded trailing edge increases significantly with $C\mu$ and which enhances the overall lift generated by the wing.

Figure 10 highlights the difference between the net lift generated by single slot blowing at upper surface and with the 2nd slot blowing. At relatively low C_μ there

exists no difference with blowing from both slots whereas at higher C_μ values only 5% of total blowing at the lower slot the lift increases by 150%. The reason to this is that, by Coanda turning, the jet generates high suction force on the rounded upper surface and separates at the lower surface stagnation point where the flow from lower surface meets, generates the required circulation and enhances the lift [20].

Circulation control theory has been extensively investigated both theoretically and experimentally. The technology has been used in several applications including V/STOL aircraft, wind turbine blades and centrifugal fans (Figure 11). The key features of circulation control are listed below.

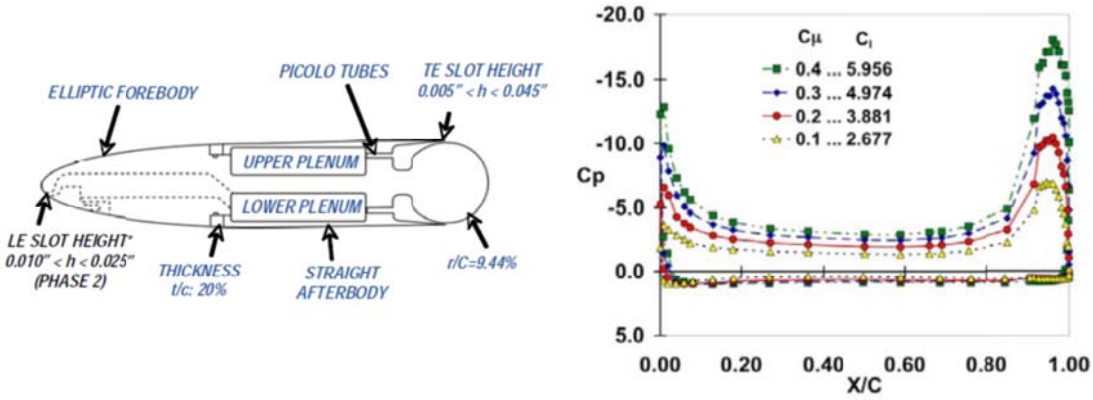

Figure 9: CC-E0020EJ aerofoil, experimental pressure distributions and corresponding lift for different jet momentum coefficient {from [21]}

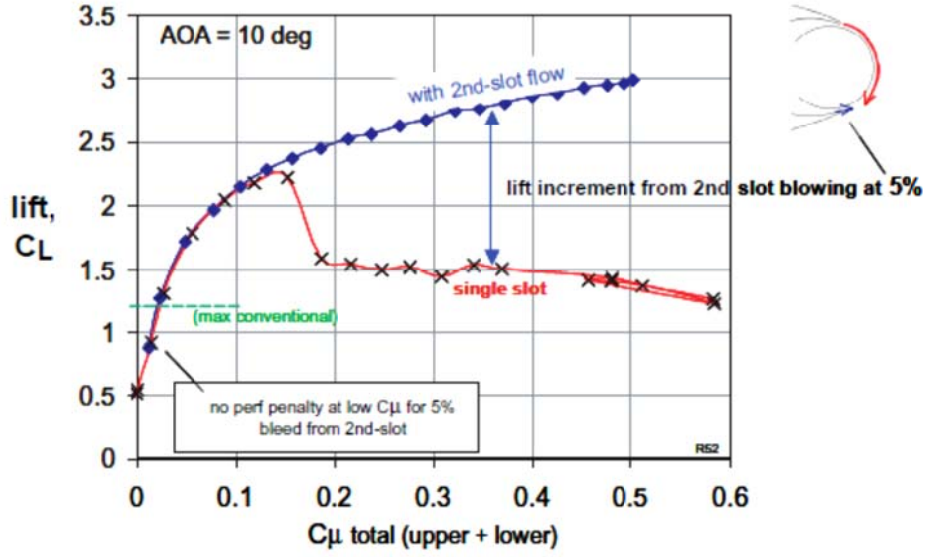

Figure 10: Lift benefit of dual slot activation {from [21]}

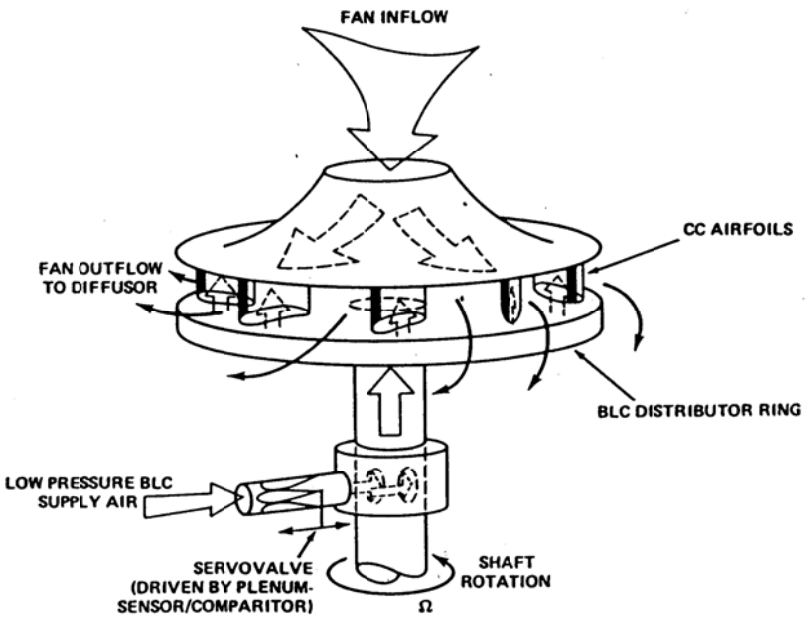

Figure 11: CC implemented on a centrifugal fan {from [26]}

2.3 Upper Surface Blowing

One of the most efficient powered-lift concepts, implemented for vertical/short take-off and landing V/STOL applications is Upper Surface Blowing (USB). Conventionally, it is achieved by placing the engines above the wing and the engine exhaust jet becomes attached to the upper surface for example see Figure 12. The jet thrust can then be vectored by use of the trailing edge curvature since the jet flow tends to remain attached by the Coanda effect. Many wind tunnel and flight-testing have shown USB aircraft to be capable of producing maximum lift coefficients near 7 [22]. The upper-surface blown flap concept has been found to be generally quieter than the other concepts because the wing tends to act as a noise shield producing more noise above the wing but much less noise below the wing [23] and hence the sound waves propagate upwards away from ground. The technology has been successfully demonstrated in the past on experimental and research aircraft including Boeing Yc-14, NAL ASKA and NASA Quiet short haul research aircraft QSRA [22].

Given the potential gains from USB aircraft, one would expect that conceptual design methods exist for their development. This is not the case, whilst relatively

complex solutions are available; there is currently no adequate low-fidelity methodology for the conceptual and preliminary design of USB or USB/distributed propulsion aircraft.

Figure 12: Proposed USB Navy STOL aircraft {from [18]}.

2.4 Circular Wing

One of the most unusual V/STOL aircraft programmes was the Avrocar VZ-9 (see Figure 13). The Avrocar had the same basic shape as a Frisbee, with the upper surface of the disk curved, and the lower rather flattened. The disk was 5.5 metres in diameter and 1.1 metres thick. The main structural truss was a large equilateral triangle, to which the various components were attached. A 124-blade turborotor sat in the centre of the triangle, with most of the rotor's thrust directed straight down through an opening in the lower surface, but some was bled off to power the control system running along the outer rim of the disk [24]

A similar shaped wing to the Avrocar was built and tested by Rogers and Imber [25]. Figure 14 presents the cross-sectional view of the circular wing with rounded trailing edge, also known as Coanda disc or CC-disk. The wing possesses the capability of full perimeter circulation control. The proposal was to investigate the efficiency of circulation control on relatively low aspect ratio wings and to explore the viability of a CC enhanced omnidirectional type of control surface or vehicle.

Figure 15 presents the aerodynamic characteristics of the circular wing acquired experimentally in [26]. Lift is presented as a function of the region of blowing. It

starts with unblown and then increasing the perimeter region blown until full 360-degree blowing. The lift is enhanced by increasing the jet momentum coefficient C_μ at any region of the perimeter blowing; the optimum value for the lift is achieved at 225-degree perimeter blowing. An interesting point to be noted here is that full perimeter blowing does not achieve the maximum lift, this is because the region facing the oncoming external translational flow reduces the effect of resultant flow in that region. Furthermore, with the optimum azimuthal blowing angle, 225-degree, an increase in angle of attack increases lift linearly.

The most severe issue encountered with the circular wing is the pitching moment generated due to the asymmetric blowing around the perimeter as mentioned above. The pitching moment is reduced by increasing the jet momentum coefficient C_μ.as increasing the jet momentum increases the blown flow and reduces the effect of external flow.

Figure 13: A photograph of Avrocar VZ-9 [27]

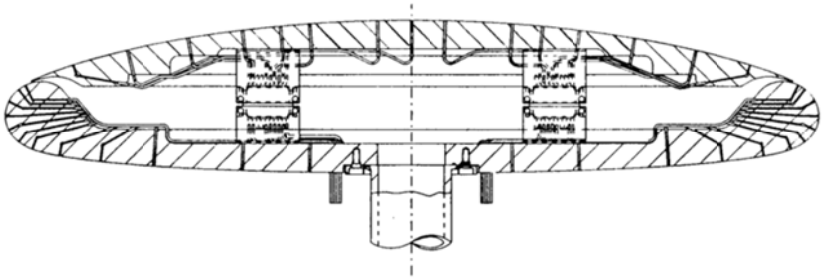

Figure 14: Cross-sectional view of circular blown wing {from [26]}

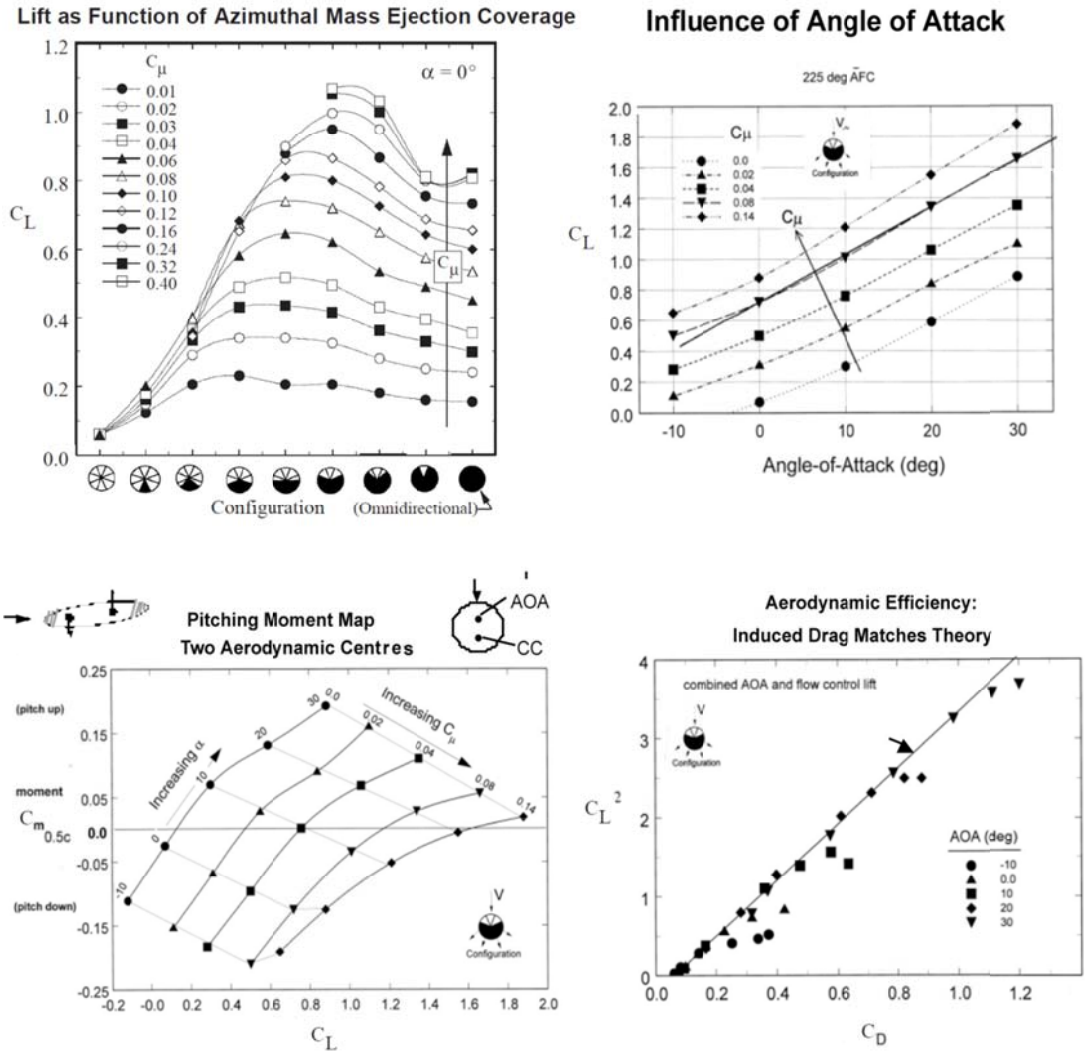

Figure 15: Aerodynamic characteristics of circular wing – lift, drag and pitching moment coefficients variation with jet momentum coefficient and azimuthal blowing {derived from [26]}.

2.5 Prediction Methods for Blown Wing Aerodynamics

From an engineering perspective, the obvious parameter value required is the aerodynamic efficiency of Coanda flow which typically is defined as the ratio of lift/normal force to the horizontal undeflected thrust. Earliest predictions are largely based on empirical formulae [28, 29, 30] and a best fit of previous experimental data [31] defines the lifting efficiency, η_L, in terms of flow deflection angle, δ_f, as $\eta_L = e^{-0.0022\delta_f}$. Where the flow deflection angle δ_f depends on the ratio of radius of curvature, r_f, to nozzle height, t_C, as $\delta_f \sim \left(r_f / t_C\right)^{-0.104}$ (see Section 5.2 for further

description). This indicates that the primary parameters defining any two-dimensional incompressible Coanda flow are the nozzle slot height and radius of curvature. Another crucial characteristic of blown wings is the angle of separation which is defined in [32] as $\theta_{sep.} = 245 - 391\left(\frac{t_C/r_f}{1+9t_C/8r_f}\right)$. However, this is most valid for flows with high Reynolds number (10^6) requiring turning beyond 90 degree for reverse thrust. Herein, the aim is to generate maximum lift from the annular wing with probably 90 degree flow deflection and hence the parameter, $\theta_{sep.}$, will be disregarded in the analysis. Reynolds number and pressure differential across the flow field are also governing parameters. However, with static surrounding conditions (i.e. zero external flow), the value of Reynolds number is not effective at large Reynolds numbers [33, 34].

The current state-of-the-art predictions are numerical (CFD) methods based on the Navier-Stokes equations with the aid of a potential flow panel method [7, 35]. However, this is a complicated, high-fidelity model and cannot reasonably be implemented at the preliminary conceptual design phase. Low-fidelity models have merely changed from those established in [28, 29, 30].

2.6 Theory of Aerofoil Wing-Sections

At the start of twentieth century the science of aeronautics took a step forward when Ludwig Prandtl showed that the aerodynamic consideration of wings could be split into two parts: firstly the study of the section of a wing or aerofoil and secondly the modification of such aerofoil properties to account for the complete finite wing. As stated by Theodorsen “without the knowledge of the theory of the airflow around aerofoils it is well-nigh impossible to judge or interpret the results of experimental work intelligently or to make other than random improvements at the expense of much useless testing” [36]. Thus in this section the physics of flow around a wing section will be explored in order to highlight the relationship between the aerodynamic forces and the geometrical properties of standard aerofoil sections e.g. thickness distribution, negative/positive camber and mean line. The main objective of aerofoil theory is to study and to predict the aerodynamic forces, lift and drag, experienced by an aerofoil immersed in fluid flow.

An aerofoil is a device that provides reactive force when in motion relative to the surrounding airflow and can lift (force vector perpendicular to the flow) or control an aircraft in flight. An aerofoil is a superposition of chord line, camber line drawn with respect to the chord line and thickness that is measures perpendicular to the chord line as can be seen from Figure 16. Typically, an aerofoil is used in lift/thrust generating devices such as wings, propellers, turbofans, helicopter rotors, compressors, turbines, hydrofoils or windmills.

Figure 17 shows the upper and lower surface pressure distribution for a typical aerofoil at moderate angle of attack. The maximum positive pressure occurs at the leading edge also known as the stagnation point and the minimum negative occurs at the upper surface typically around 25% of chord. The pressure recovery region is where the pressure gradient becomes negative which is associated to the boundary layer transition. The lower surface sometimes carries a positive pressure, but at many design conditions is actually pulling the wing downward. In this case, some suction (negative C_p→ downward force on lower surface) is present near the mid-chord. The pressure at the trailing edge is related to the aerofoil thickness and shape near the trailing edge. For thick aerofoil the pressure here is slightly positive (the velocity is a bit less than the free-stream velocity). For infinitely thin sections $C_p = 0$ at the trailing edge. Large positive values of C_p at the trailing edge imply more severe adverse pressure gradients [37]. A more comprehensive illustration of the flow pressure, acceleration and velocity is depicted in Figure 18. One of the most important points to be noted here is that the flow diverts before the leading edge and decelerates till a maximum pressure is reached at the leading edge.

The performance of an aerofoil is directly related to its geometrical shape. The leading edge curvature sets the positive pressure gradient and a reasonable selection can give a good region for laminar boundary layer which subsequently gives lower drag. Maximum aerofoil thickness sets the location of minimum C_p which determines maximum local flow velocity and hence indicates shock formation. An adverse pressure gradient near the trailing edge leads to flow separation and determines the extent of friction drag. There exist several aerofoil families designed to serve specific tasks and the most commonly used one is the NACA 4-Digit series

which possess good stall characteristics, small centre of pressure movement across large speed range and serves both subsonic and supersonic aircraft.

There are several methods to design and analyse the flow over an arbitrary shaped aerofoil e.g. conformal mapping, thin aerofoil theory, surface panel methods and inverse design methods described in [37, 38]. Herein, for the annular-wing, symmetrical aerofoils, NACA-0012 and NACA-0024 are exclusively used. This is because the symmetrical aerofoils, particularly the NACA 0012, are the oldest and certainly the most tested of all aerofoils: and these have been studied in dozens of separate wind tunnels over a period of more than 50 years. However, a study on the different available sets of data from experimenters shows that there is considerable difference in the data and no single experiment provides a complete set of reliable data [39], see Figure 19. Herein, the 2-dimensional aerofoil data is acquired from the software package XFoil which shows a good match with the data acquired from different sources at moderate range of angle of attack [40].

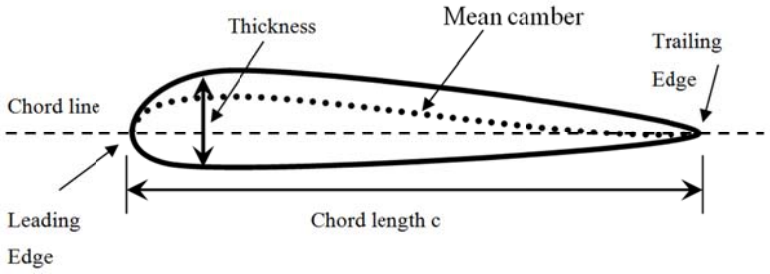

Figure 16: Standard aerofoil nomenclature.

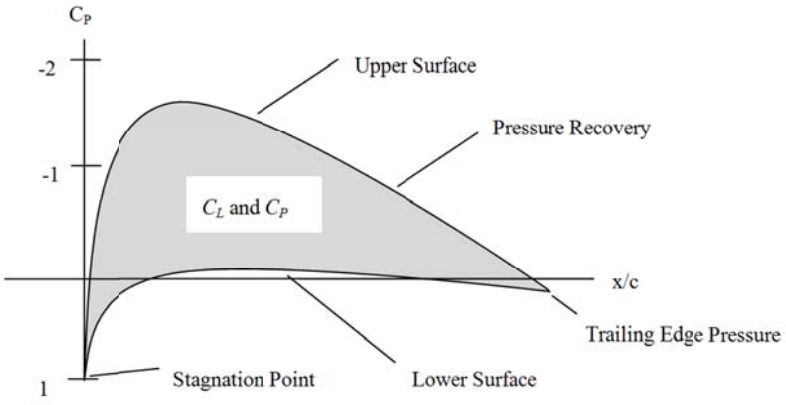

Figure 17 Pressure distribution of a typical aerofoil.

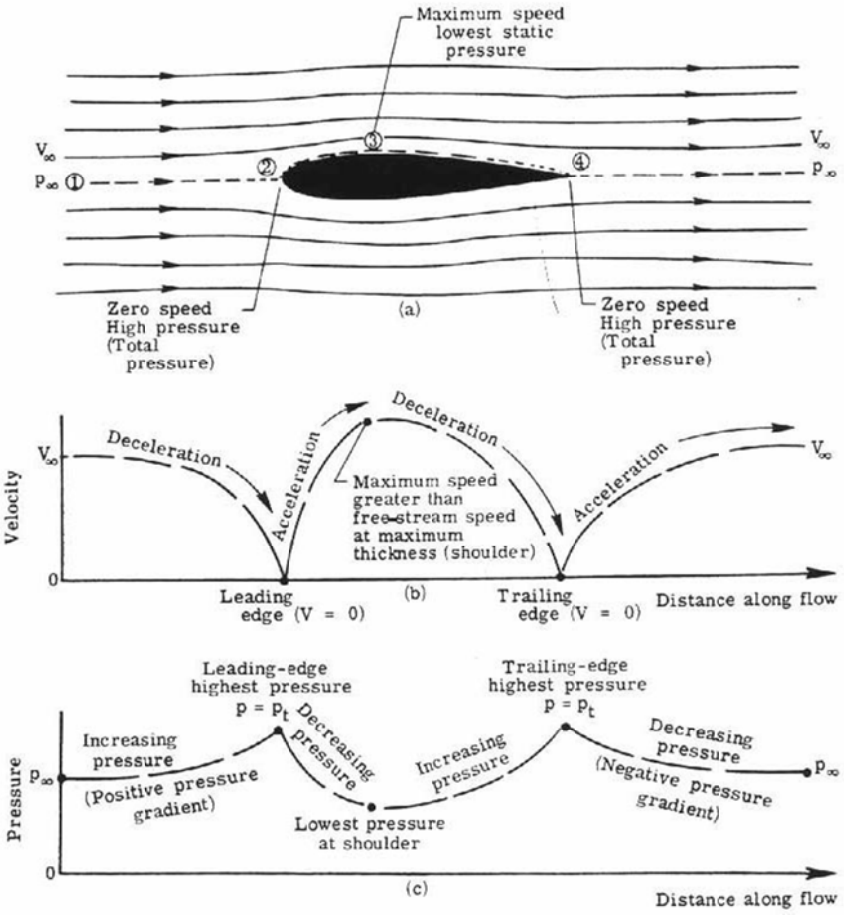

Figure 18: Aerodynamic characteristics of a typical aerofoil {from [41]}.

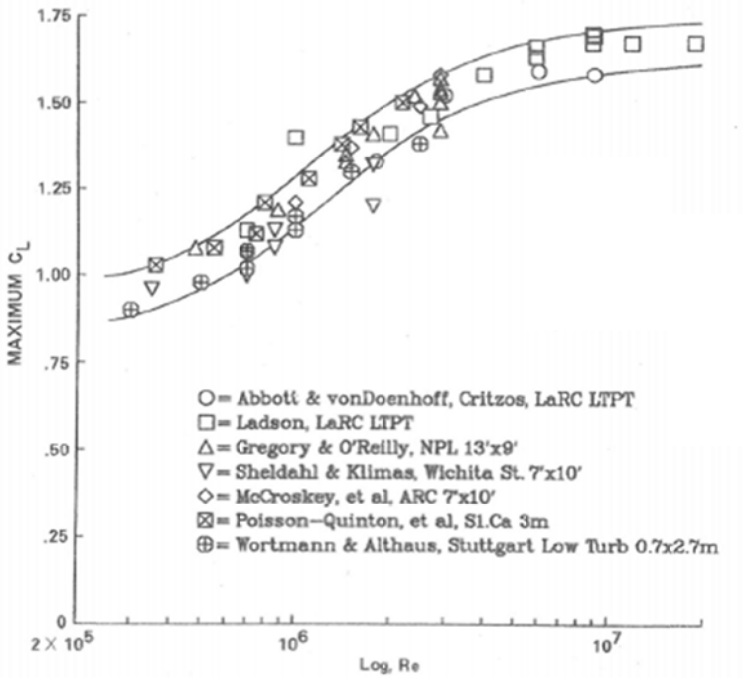

Figure 19: Available data on NACA-0012 from different wind tunnel tests {from [39]}.

2.7 Summary

Circular/annular blown-wings are coming into existence to revolve V/STOL capabilities e.g. MIRA flying disc and flying saucer. However, a literature review of blown wings has revealed that no documented method to predict/evaluate Coanda lift is available at the present time. Also, most of the previous work, numerical and experimental, on blown wings is particularly concerned with high flow speeds and Reynolds number (10^5-10^7). Therefore, aerodynamic characteristics of annular wing, initially considered with relatively low Reynolds number (10^3-10^4), are anticipated to be not easily tractable to analytical treatment or solved by current computational aerodynamic techniques. For the immediate future any prediction method development must be based on experimental data, and hence will lead to, largely, empirical methods. Therefore, for a preliminary prediction a method is to be derived based on basic/standard aerodynamic principles and complemented by experimental testing. The fundamental theory will be based on the aerofoil theory, as illustrated in Section 2.6, dealing with flow acceleration and pressure differentials.

A critical point to be noted here is that much of the work on circulation control, upper surface blowing or Coanda effect is primarily based on two-dimensional flow scenario. Whereas the fundamental difference between the annular wing and any past wing is the three-dimensional effect, the annular flow expansion, as described in Section 4.3. Also, the literature is largely concerned with dual flow case, internal (jet flow) and external (free stream) whereas the annular-wing initially is concerned with singular jet-flow. Therefore, the literature predominately aids in understanding the qualitative behaviour of blown wings and hence in the analyses of annular wing (Chapter 4) no direct comparisons between the Author's results and previous results are attempted.

Chapter 3. Experimental Methods and Apparatus

3.1 Introduction

It is well known within the technical community of aerodynamic sciences that the evaluation of aerodynamic forces on a solid body, particularly with a relatively new geometry, is ultimately achieved by wind tunnel experiments. In order to achieve this objective an experimental strategy is sought to evaluate the aerodynamic forces experienced by the annular wing. The main objective of this experiment is to validate, modify and improve the theories generated. The investigation required designing and building two experimental rigs for examining different aerodynamic phenomena.

The rig 1 is mainly composed of three parts including a radial-flow generator, annular wing and a compact digital-load-cell as shown in Figure 20. The wing sits on the load cell with the aid of support arms such that it transmits axial load only, see Figure 21. The wing, blower and support arms are held rigid to the load-cell so that any movement caused by the aerodynamic loads will not misalign the flow from the blower. The load cell measures the aerodynamic loads directly in real time. The flow

is measured by hot-wire anemometer[a] which is mounted on a wooden stand. The hot-wire anemometer allows 2-dimensional, translational and longitudinal, movement by means of a manual rack equipped with digital scales.

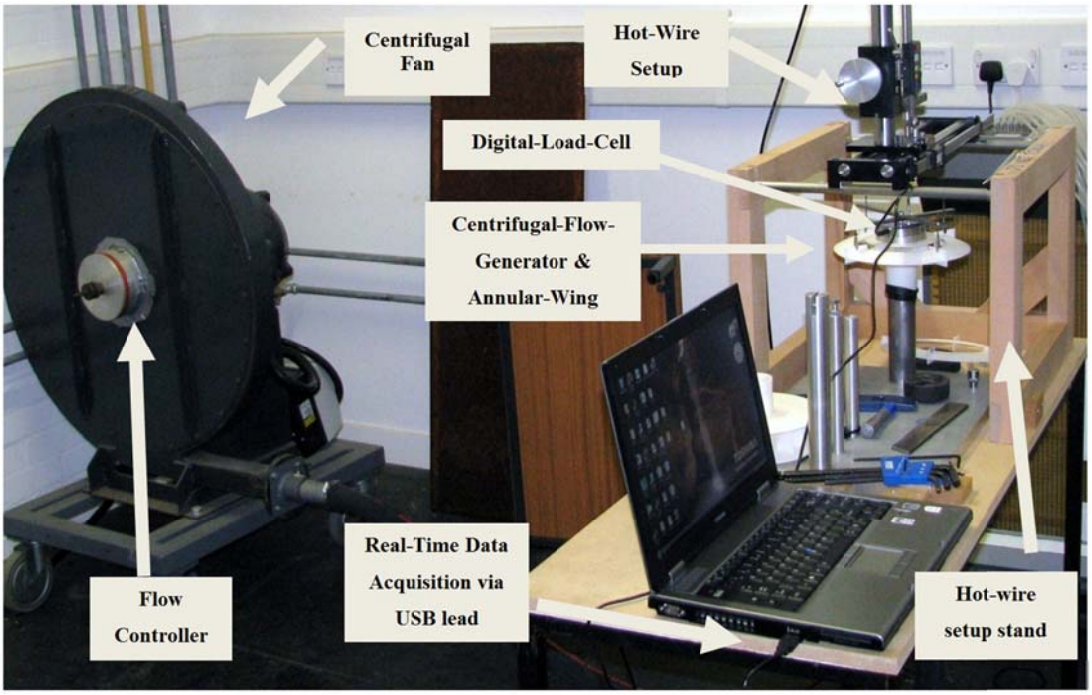

Figure 20: Experimental Setup, Rig 1 annular blowing.

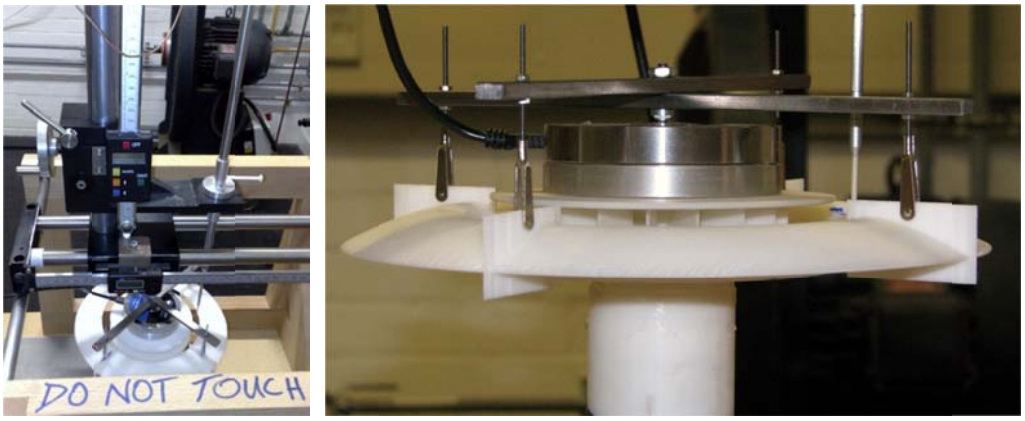

Figure 21: Different views of annular-wing, load-cell and radial-flow-generator configuration.

[a] Note: To measure pressure distribution a singular hot-wire was chosen instead of a conventional/simple pressure tap because it proved impractical to embed pressure taps into the annular wing surface with the available manufacturing facility. However, pressure taps were used later when testing the arc-wing.

There are several methods available to measure lift and drag experienced by a wing. In this experiment two methods were used to obtain aerodynamic forces: 1) by integrating the measured pressure distribution over the surface of the wing section and 2) by direct measurement through a mechanical arrangement of a load cell where local pressure distribution cannot be measured.

The lift force can be calculated by integrating, numerically, the pressure around the surface of the aerofoil as

$$L = \int_s (P_i - P_\infty)\sin(\theta_i)ds \tag{3.1}$$

Where L is the lift force, force perpendicular to the flow direction, p_i is the total pressure at location i on the aerofoil surface, P_∞ is the free-stream static pressure, and θ_i is the angle of surface normal to the free-stream flow at each of the traverse point as shown in Figure 30.

Similarly the drag force was calculated as

$$D = \int_s (P_i - P_\infty)\cos(\theta_i)ds. \tag{3.2}$$

3.2 Data Acquisition and Apparatus

Figure 22 displays the schematic layout of data acquisition plan. The local flow velocity over the surface of the model wing is measured by the hot-wire anemometer. The local dynamic pressure is deduced with the aid of a pitot tube which is connected to a pressure scanner in conjunction with a micro manometer (Furness FCO510) with data logging capability. The differential pressure is measured between the stagnation pressure and the local pressure. The analogue signals are input to an analogue to digital converter which can then display the measurements in Lab-view based software.

The digital USB load cell is self-sufficient and connects directly to the PC which displays the data in MatLab (version 7.01) or HyperTerminal in millponds.

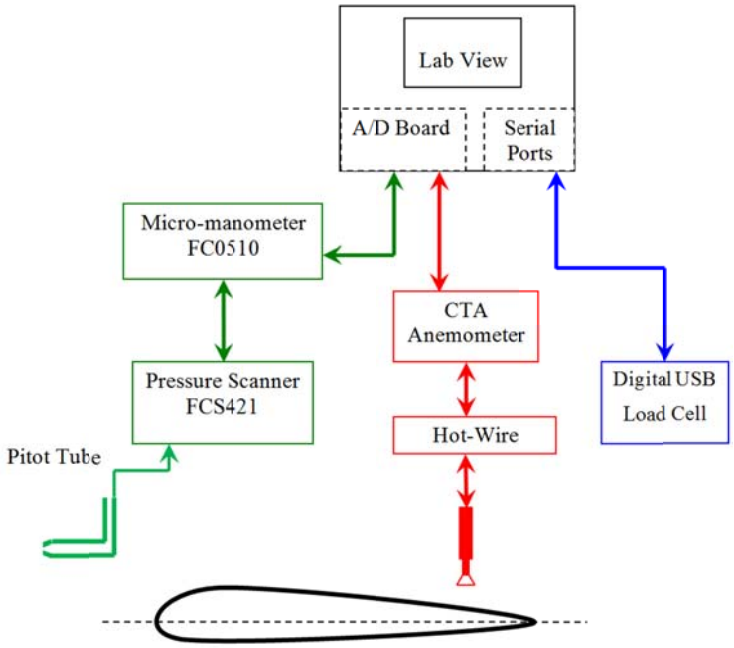

Figure 22: Data acquisition plan.

3.2.1 Load Cell

A load cell/sensor is an electrical device or transducer (energy converter) that converts a force into an electrical voltage. The conversion is done by a built in strain gauge, which deforms proportionally with the applied force. There are a variety of load sensors with multi strain gauges to measure the forces in three-dimensions. However, for this experiment a 1-D digital load cell (Figure 23) was chosen which works with a relatively new technology. It uses a variable capacitor rather than a strain gauge and the main advantage of this approach is that it improves sensitivity by generating much larger voltage signals (0-5volts) whereas a strain gauge only produces up to 20 millivolts [42].

Figure 23: Digital USB Load Sensor [42].

3.2.2 Hot-Wire Anemometer

A hot-wire anemometer measures flow velocities by sensing the change in voltage to keep a constant temperature across the wire. The hot-wire anemometer comes with its own data acquisition system. A CTA anemometer is used to keep a constant temperature across the wire that uses a Wheatstone bridge which works like a feedback circuit. The signals are amplified and fed into an A/D converter which connects to a pc and special software is used to analyse and display the measurements. Figure 24 summarises the data acquisition strategy for a hot-wire anemometer. Furthermore, a singular L-shaped hot-wire was used in this experiment, see Figure 25.

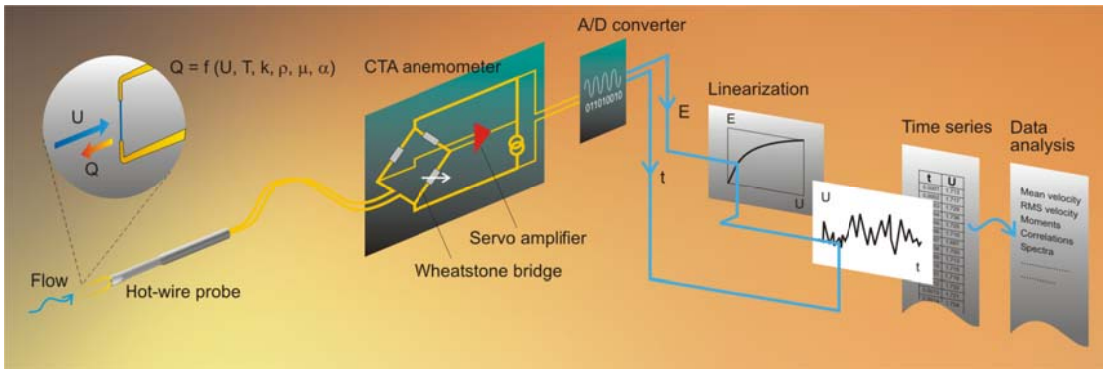

Figure 24: Schematic layout of data acquisition plan for a hot-wire anemometer [43].

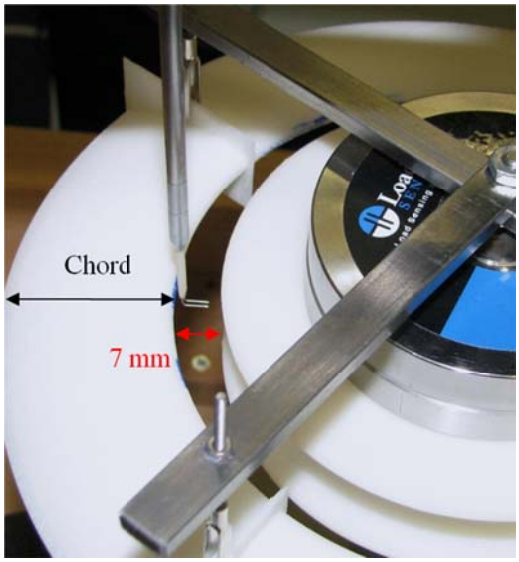

Figure 25: Hot-wire location

3.2.3 Pressure Scanner and Manometer

A 20-channel pressure scanner (FCS421) with digital display was used to receive pressure signals from multiple sources or taps. The output from the scanner was fed into a digital micro-manometer (FC0510) which can read differential pressures in mmH2O. The differential pressure is the difference between the pressures from the source, e.g. tap, to the atmospheric where the atmospheric pressure was input.

Figure 26: A photograph of pressure scanner and micro-manometer used in the experiments.

3.3 Experimental Procedure for Rig 1

Following procedure was a routine to ensure accurate results.

1. The load-cell was placed in the intended location of use for twelve hours so that the sensor was soaked in that environment and has reached steady state (as stated in product manual).
2. Before operating the sensor, it was allowed to warm up by connecting it to the main power for at least half an hour. This allows the signal conditioning electronics to stabilise and perform more accurately (from guidelines in the product manual).
3. Laboratory atmospheric temperature and pressure were recorded using the compact digital barometer and fed into micro-manometer for precise differential pressure values.

4. Hot-wire-probe was powered prior to testing for at least 40 minutes for the temperature to stabilise across the wire.
5. The annular wing was held on to the load cell via support arms and levelled manually.

The hot-wire probe was calibrated by a special apparatus provided by the manufacturer. The calibration data is presented in Figure 27 that shows the difference between the users commanded values (or the input values) and the actual measured values. A maximum error recorded was ~2%. The outlet velocity of the blower was examined using the hot-wire anemometer at 1 mm longitudinal increments. The data recorded by the anemometer is presented in Table 18.The hot-wire takes measurement at 1000 frames/samples per second (fps) with a low-pass filter set at 500 Hz. Figure 28 shows velocity signals recorded by the hot-wire at different locations across the vertical axis of the blower. It can be seen that the velocity signal fluctuates significantly across its mean value and that the magnitude of the fluctuation varies with the location. This indicates that the system produces flow that may be high in the turbulence intensity.

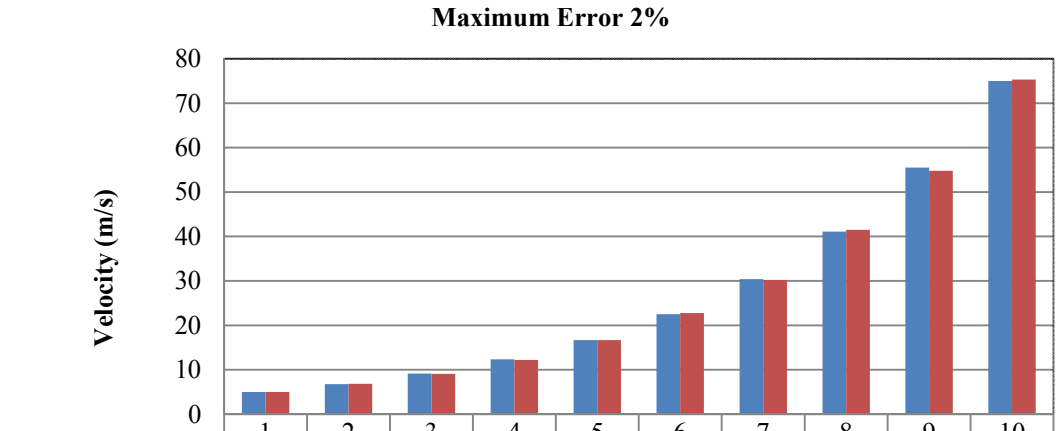

	1	2	3	4	5	6	7	8	9	10
Input Values	5.00	6.76	9.13	12.33	16.66	22.51	30.41	41.09	55.51	75.00
Measured Values	4.99	6.84	9.06	12.21	16.67	22.77	30.23	41.51	54.78	75.32

Figure 27: Calibration data and chart for hot-wire probe.

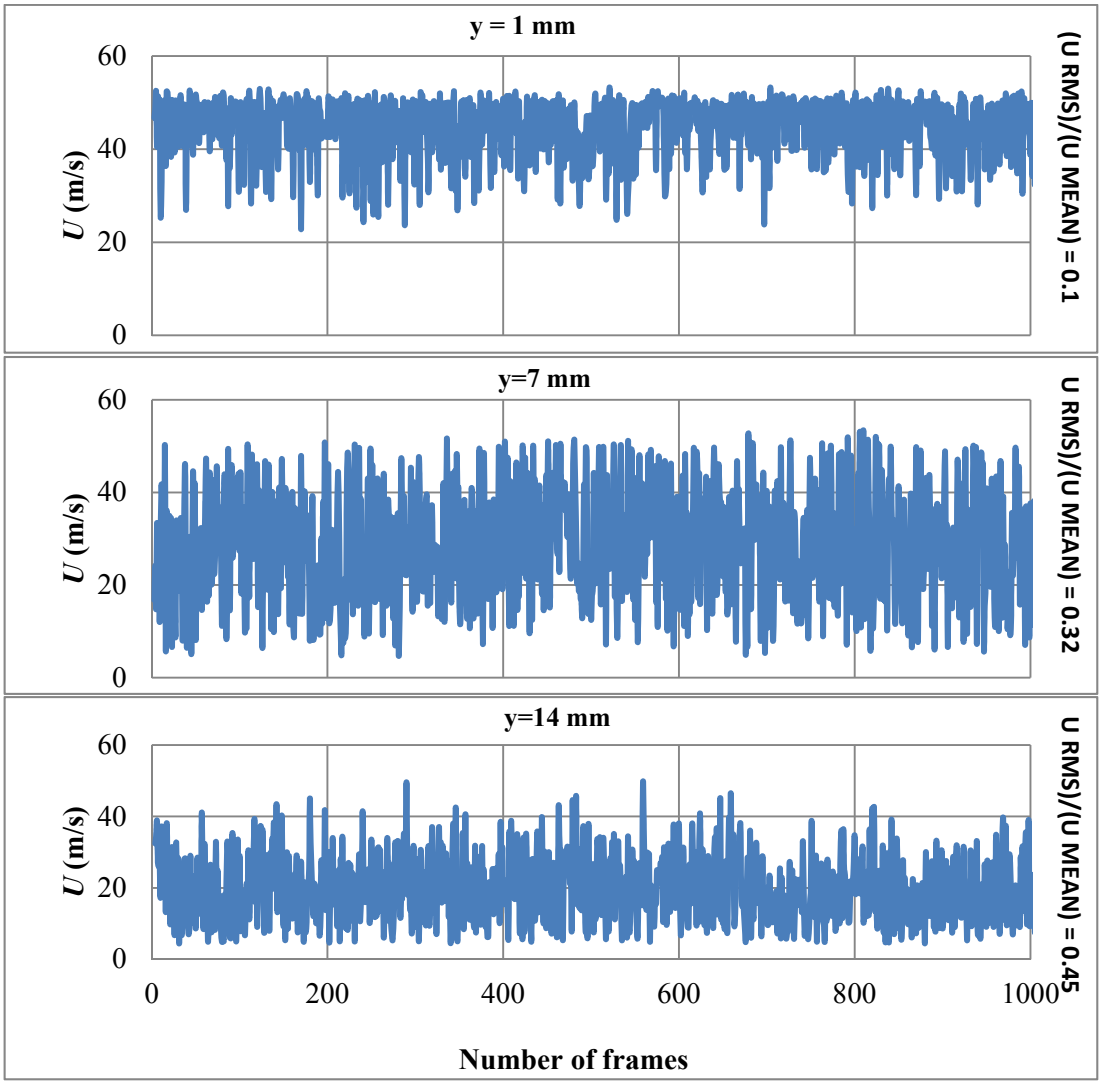

Figure 28: Velocity signal obtained by hot-wire anemometer at 1000 frames per second.

3.4 Lift Measurement via Load Cell

Lift is measured by the load cell directly for different angles of attack and wing-sections. The load-cell is set to measure prior to any flow through the system fan, as the fan is turned on an impulse load is observed and the lift generated by the wing is given by the mean amplitude of the impulse sensed. A crucial point to be noted here is that the load cell measures at 5 Hz whereas the hot-wire anemometer records at 1000 Hz. Nevertheless, the load cell at 5 fps should detect any changes in the loads transmitted due to variation in outlet velocity.

Figure 29 shows the signals recorded by the load cell for the NACA-0024 at 12deg and it can be seen that the fluctuation amplitude in the signal has reduced

significantly as compared to the NACA-0012 at 12deg wing (Figure 147). This is because the thicker wing section allows the outlet flow less cross-sectional area to fluctuate. This may have increased the frequency of vibration present during the tests. However, this effect is irrelevant when calculating the mean aerodynamic lift force.

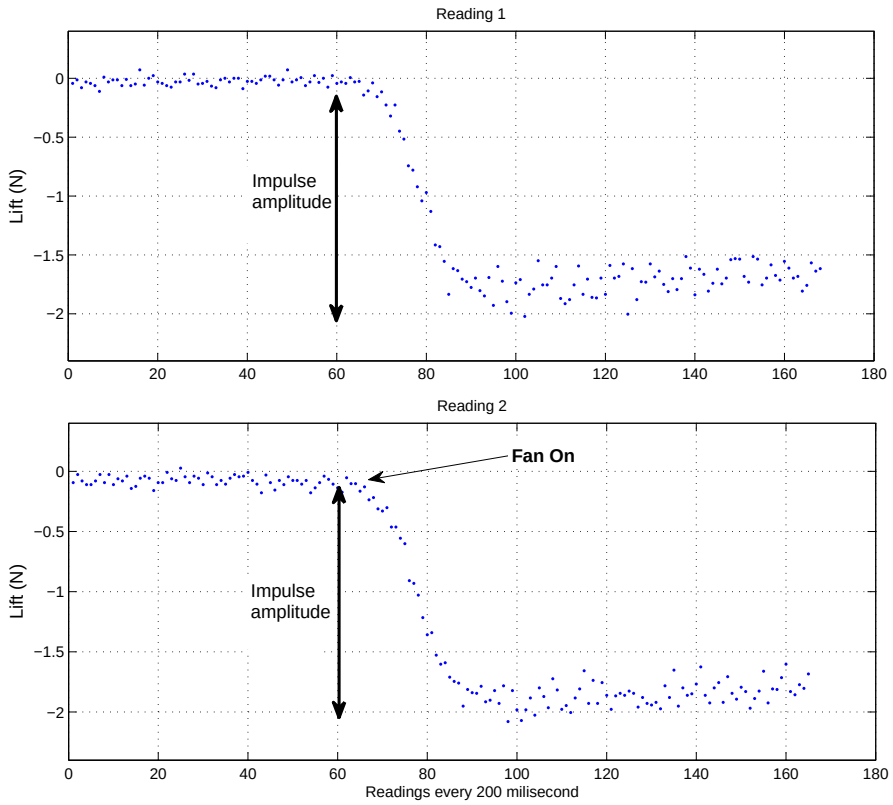

Figure 29: load cell data {Parameters: $\alpha = 12^o$, $U_{eff} = 20$ m/s, $T_{atm} = 22.3^o C$, $P_{atm} = 102.3$ kPa }.

Figure 146 depicts the signals recorded by the load cell for different angles of attack for the wing-section NACA-0012. From the figures it can be seen that the variation in the signal is amplified as the fan is turned on, this is due to the fact that the outlet velocity is varying as described above in Figure 28. In order to extrapolate the actual lift values the maxima and minima points are labelled and defined as the maximum and minimum lift values respectively. The extracted lift values are given in Table 22. A similar approach was taken for all the other test cases as shown in Figure 145 to Figure 148.

3.5 Local Flow Measurement

In order to investigate the local flow over the annular wing the asymmetry of flow across the outlet thickness needs to be incorporated. This may be achieved by locating the wing within the upper half of the outlet where the flow is dominated and linearly varying. The local flow velocity was measured at traverse points defining the most crucial points over the surface of the aerofoil, see Figure 30. Several different wing configurations were tested to validate the theories generated in Chapter 4 including NACA-0012, NACA-0024 and NACA-4412 at a range of angle of attack.

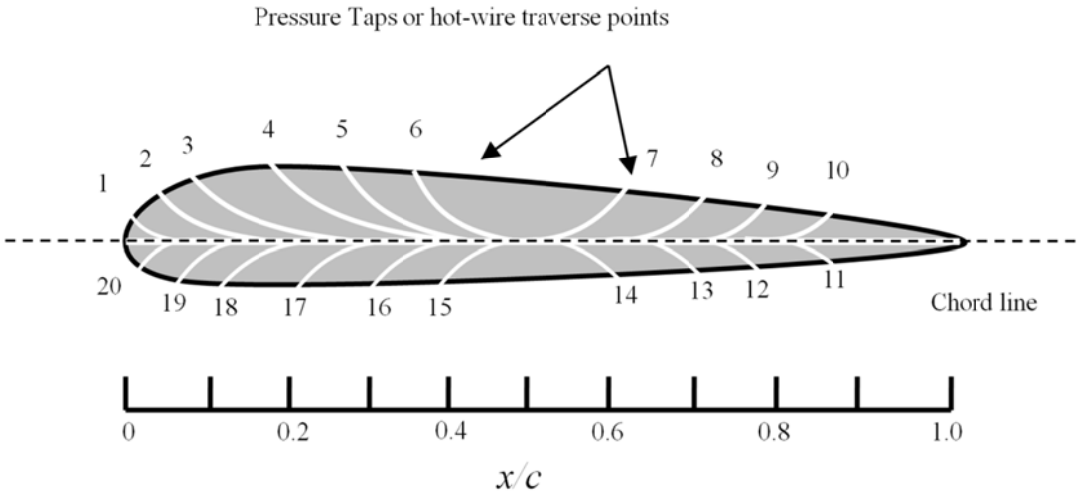

Figure 30: Traverse points layout.

3.6 Experiment 2: Longitudinal Symmetrical Blowing

In order to fully establish how the annular wing performs with uniform wall-jet another experimental rig was constructed. This rig is intended to eliminate the fluctuation in the outlet along the longitudinal axis unlike the radial flow generator described above. The rig was designed to allow testing the wing with laminar flow at low Reynolds number (~10^3). Figure 31 shows the rig that may well achieve the goal. The rig is designed primarily for achieving the standard aerodynamic testing capabilities. The rig comprises of a diffuser, an arc wing (Figure 32) with pressure taps (Figure 33), wake rake and a pressure scanner. In order to avoid radial flow expansion the flow is kept axial via a diffuser and only one quarter of the annular

wing is blown. The wing is kept static and the angle of incidence is changed by rotating the diffuser at its pivotal point and elevating the wing accordingly. The flow is provided by a centrifugal pump. Further illustration of the apparatus is given in Figure 149 and Figure 152.

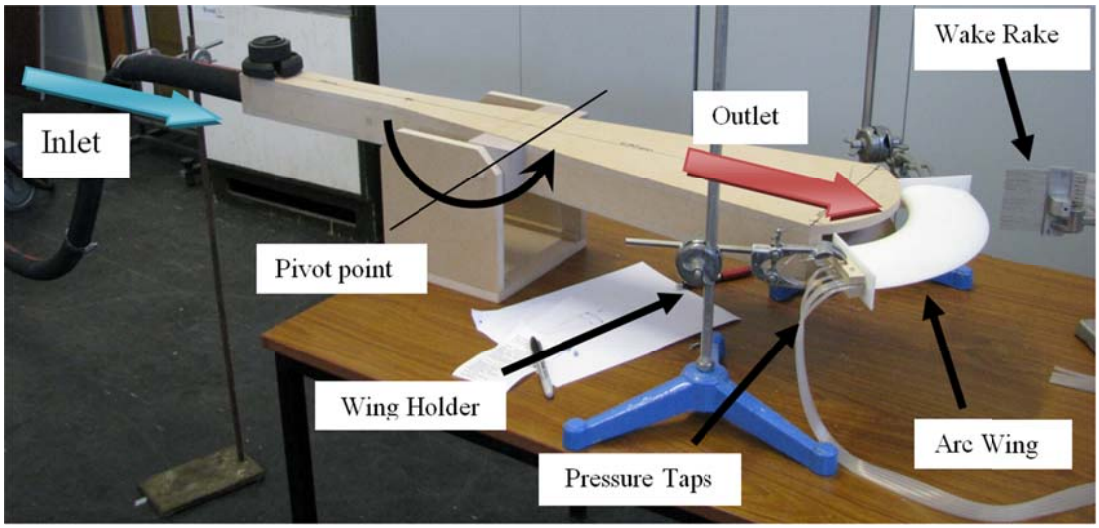

Figure 31: Rig2 Blown Annular-Arc-Wing

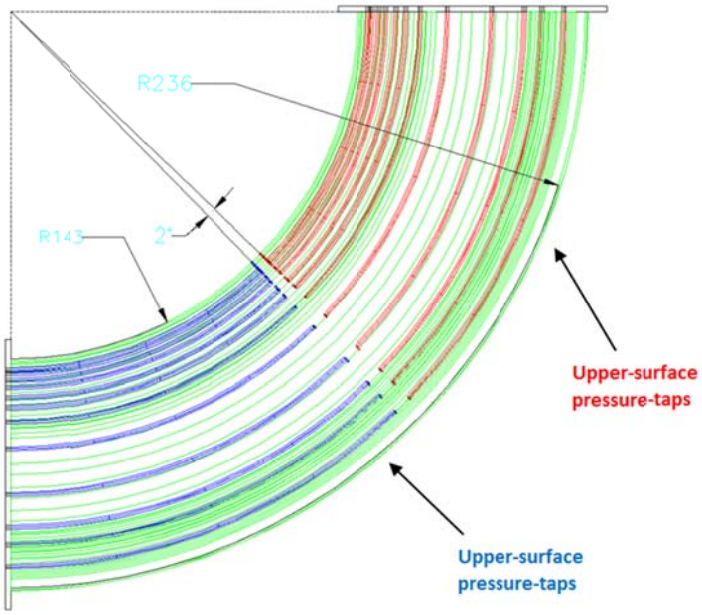

Figure 32: Arc-wing with pressure taps (the red lines show the pathway of pressure taps){all units in mm}

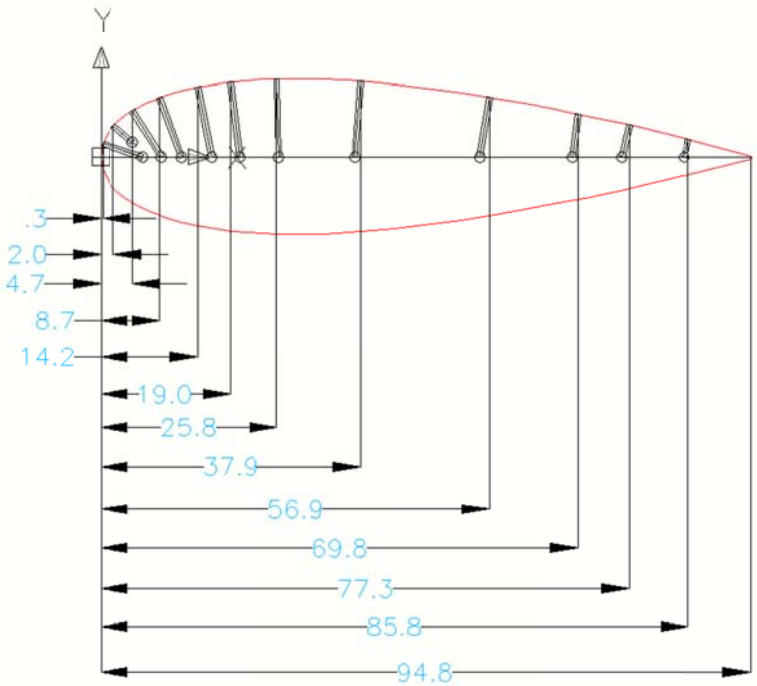

Figure 33: Pressure taps location points {all units in mm}

A flow diffuser is designed to lead the flow to the wing's leading edge without causing much disturbance to the flow. Generally, a diffuser converts kinetic energy to pressure and hence exerts adverse pressure gradient. The most important parameter to define a diffuser is the expansion angle. In order to avoid separation and unsteadiness at the walls of the diffuser, an ideal diffuser angle is around 6 degrees [44] that allows no separation at the walls but it requires relatively large diffuser lengths so this sets the first constraint for the diffuser design. For the diffuser under consideration here the diffuser angle is chosen to be 16 degrees based upon the width of the wing's inlet. This diffuser angle falls into the 3D-transitory separation flow regime and large scale separated flows are expected at the diffusing walls. Further stability was achieved by implementing multiple guided vanes within the diffuser. Also, another solution to this may be attained by allowing the turbulent flow at walls to exit outboard of the arc-wing from both sides as shown in Figure 34.

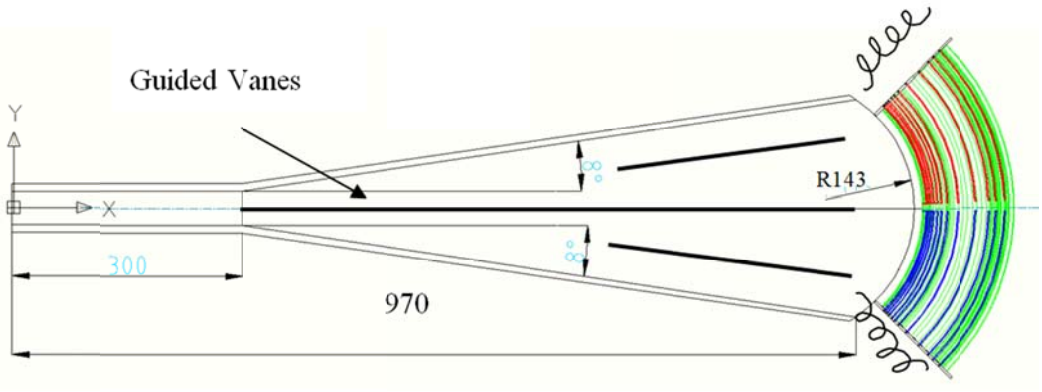

Figure 34: Flow diffuser layout (all units in mm)

3.7 Manufacturing

The complex geometries of the annular wing and the centrifugal blower were constructed with Stereolithography which is a specific technology of rapid prototyping that uses photopolymer as the base material. This manufacturing technique takes virtual designs from computer aided design (CAD) or animation modelling software and transforms into a solid object via a 3-D printer. Stereolithography is an additive manufacturing process that uses a vat of liquid UV-curable photopolymer "resin" and a UV laser to build parts of a layer at a time. On each layer, the laser beam traces a part cross-section pattern on the surface of the liquid resin. Exposure to the UV laser light cures, or, solidifies the pattern traced on the resin and adheres it to the layer below [45].

3.8 Experimental Error Sources and Evaluation

The centrifugal fan undergoes several aerodynamic losses due to temperature rise (partially transmitted from the motor that drives the fan) and apparently never reaches an equilibrium state. Hence, it becomes responsible for one of the major sources of error for this experiment, which is the reduction in flow rate with time. Several tests showed a continuous reduction in the outlet flow velocity with time. Figure 35 shows the velocity measured (non-dimensionalised with respect to the initial flow velocity U_{in}) at 30 seconds intervals for two different atmospheric conditions. The figure shows that the flow rate decays in a logarithmic manner and

the ambient conditions impose significant difference in the recorded values. For a typical test the time required was 300 to 400 seconds that subsequently leads to a flow rate reduction of approximately 2.5%. This reduction was incorporated in to all the calculations presented in the relevant sections. Certain error was present in all the measuring equipment: Figure 36 presents a block diagram of the possible experimental error sources.

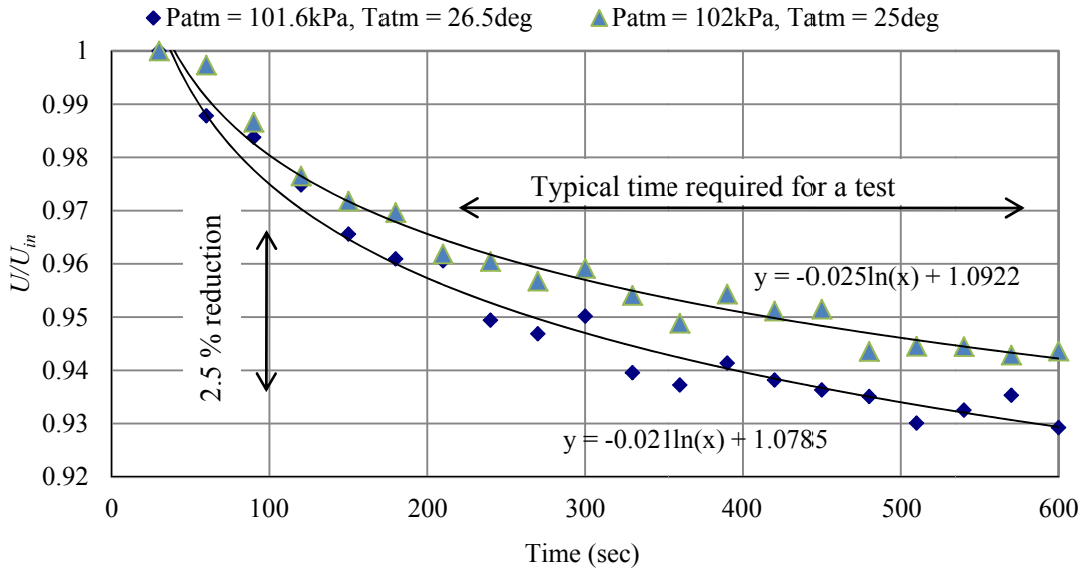

Figure 35: Reduction in flow-rate with time.

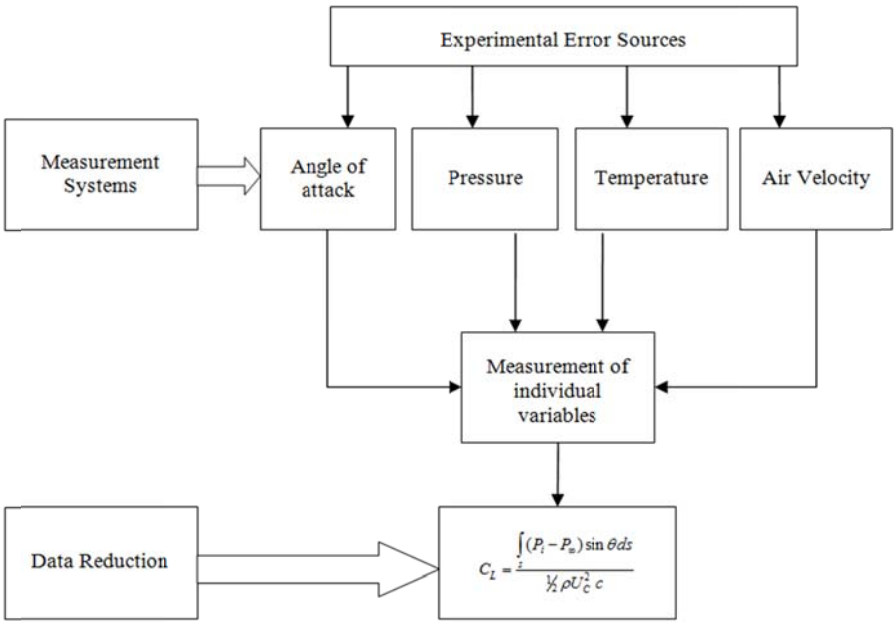

Figure 36: Block diagram specifying route for determining lift coefficient.

The uncertainty analyses, herein, are based on the most reliable and commonly used method presented in [46]

The pressure coefficient C_P is a function of

$$C_P = f\left(P_i - P_\infty, \rho(P_{atm}, T_{atm}), U_\infty\right) \tag{3.3}$$

However, here, bias and precision limits for differential pressure $\left(P_i - P_\infty\right)$ will only be used for data reduction. The total uncertainty for each pressure tap is defined as {from [46]}

$$U_{C_P}^2 = B_{C_P}^2 + P_{C_P}^2 \tag{3.4}$$

where the capital letters *U*, *B* and *P* denote total uncertainty, bias limit and precision limit respectively.

The bias limit for the surface pressure taps is given by

$$B_{C_P}^2 = \theta_{(P_i - P_\infty)}^2 B_{(P_i - P_\infty)}^2 \tag{3.5}$$

where $\theta_{(P_i - P_\infty)}$ is the sensitivity coefficient defined by averaging the individual variables as

$$\theta_{(P_i - P_\infty)} = \frac{\partial C_P}{\partial X_i} = \frac{\partial C_P}{\partial (P_i - P_\infty)} = \frac{2}{\rho U_\infty^2} \tag{3.6}$$

The precision limit for each pressure tap $P_{C_P,i}$ is given by

$$P_{C_P,i} = \frac{tS_i}{\sqrt{N}} \tag{3.7}$$

where $t = 2$ for the number of samples $N = 10$ and S_{C_P} is the standard deviation given by

$$S_i = \sqrt{\sum_{k=1}^{N} \frac{\left(X_k - \overline{X_i}\right)^2}{N-1}} \tag{3.8}$$

The data reduction equation for the lift coefficient C_L is given by

$$C_L = f(P_i - P_\infty, U_\infty, \rho, \theta) \tag{3.9}$$

Considering only the bias limits for differential pressure $\left(P_i - P_\infty\right)$ from the taps, the total uncertainty is given by

$$U_{C_L}^2 = B_{C_L}^2 + P_{C_L}^2 \tag{3.10}$$

similarly

$$B_{C_L}^2 = \theta_{(P_i - P_\infty)}^2 B_{(P_i - P_\infty)}^2 \tag{3.11}$$

$$B_{C_L}^2 = B_{(P_i - P_\infty)}^2 \sum_{i=1}^{k} \left[\frac{\partial C_L}{\partial \left(P_i - P_\infty\right)} \right]^2 = B_{(P_i - P_\infty)}^2 \left[\frac{2}{\rho U_\infty^2 c} \right]^2 \sum_{i=1}^{k} \left[\sin\theta_i ds_i \right]^2 \tag{3.12}$$

After running several tests, before recording any measurements, precision limits were set for all the variables involved in calculating the coefficients, e.g. C_L, C_D, C_M

Typical Precision limits:

Angle of attack in degrees $\alpha \rightarrow \pm 1$

Non-dimensional Differential Pressure $\frac{\Delta P}{P} = \frac{(P_i - P_\infty)}{P} \rightarrow \pm 0.05$

Non-dimensional air velocity $U_\infty / U_m \rightarrow \pm 0.03$

The precision limits impose a maximum error of approximately ±5% on all the coefficients calculated in the following Chapters.

3.9 Summary

The experimental setup has been designed from scratch to test the unconventional wingform. The most critical component was the blower which was designed and tested several times to improve the flow quality. Ideally a laminar flow was desired but never achieved; it was always turbulent due to annular flow expansion, as discussed in the following Chapter. The challenge was to achieve symmetrical flow across the vertical axis of the blowers; this often led to adding guided vanes and the designs were improved by testing vanes with different geometries. Another encounter was the continuously varying lift force detected by the load-cell which was due to the highly unstable flow; this was incorporated by extrapolating the mean force generated for the corresponding mean flow velocity.

Chapter 4. Aerodynamic Characteristics of Simple Annular Wing

4.1 Introduction

The blown annular wing comprises of two interrelated lift/thrust producing devices as shown in Figure 37. These are: a centrifugal compressor/blower and the annular/circular wing. The centrifugal compressor also produces axial thrust due to a change in linear momentum [47] as the flow is diverted at 90 degrees. Axial thrust can be estimated by applying simple momentum theory across the control volume channels AB and CD. Centrifugal compressors undergo several energy losses including aerodynamic losses, disk friction loss and leakage loss. These losses leave a typical centrifugal compressor 80% efficient at optimum flow rate [48]. Therefore, the losses must be accounted for when evaluating the overall efficiency of the static-blown-wing. The axial thrust generated by a centrifugal compressor depends on the net flow rate and it can be defined as

$$T = \frac{d(mu)}{dt} = \rho A_0 U_0^{\,2} \tag{4.1}$$

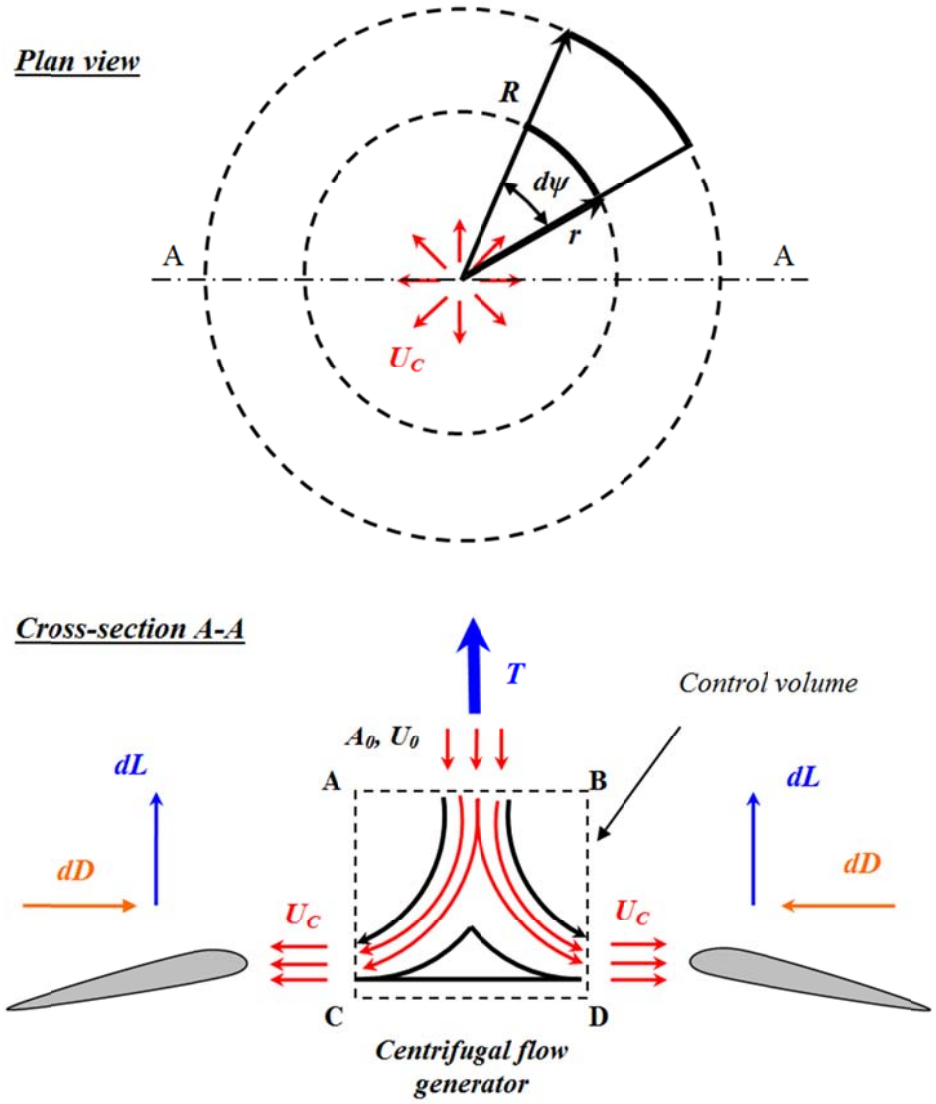

Figure 37: Hypothetical layout of blown annular-wing with symmetrical blowing.

4.2 Effect of Blower-Slot Height and Jet Momentum Coefficient

Jet momentum coefficient C_μ is a non-dimensional quantity specifying thrust force or change in flow momentum from a source with reference to a fixed dynamic pressure and area In this case U_{ref} is taken to be the flow velocity at quarter chord length and A_{ref} is the wing surface area.

$$C_\mu = \frac{\dot{m} U_C}{\frac{1}{2}\rho_\infty U_{ref}^2 A_{ref}} = \frac{2\pi r t_C \rho U_C^2}{\frac{1}{2}\rho_\infty U_{C/4}^2 S} \tag{4.2}$$

From this, it is clear that the jet momentum coefficient C_μ is the driving parameter for blown wings. Normally, high velocities generated at the jet-slot-exit require specification of certain boundary conditions including the total pressure and total temperature of the jet. However, for the current analysis: adiabatic, isentropic, inviscid and incompressible flow conditions will be assumed.

Jet/blower slot height jet t_C is the main parameter in the powered-lift system under consideration. This is because the outlet velocity is proportional to the slot height and that the net mass flow rate is also a function of this parameter. This implicitly sets out the power coefficient C_{Po} required for certain flow rate at the jet-slot exit.

$$C_{P_0} = \frac{2\pi r t_C \rho U_C^3}{\frac{1}{2}\rho_\infty U_{C/4}^3 S} \tag{4.3}$$

Figure 38 shows how the lift coefficients vary with the slot height at different angle of attack. This result is derived from previous experimental work on blown wings. This shows that as the slot height increases lift also increases. The net mass flow rate will increase provided that the input power is also increased. The stall angle also significantly increases as the slot height reduces. This is because the Coanda effect gives a thinner jet-sheet which has greater flow attachment. Flow attachment to the surface also depends upon the depth of the airflow (or slot height) and the camber angle; the thinner the depth of the flow the greater the camber angle, although at the expense of some lift force due to lesser amount of airflow blown onto the aerofoil [49, 50]. In wind tunnel testing, in order to mimic a wing being propelled through static air, (that is slot height $\rightarrow\infty$), more than 2 chord lengths of working section is normally satisfactory [51], otherwise lift will always be less than a standard propelled wing. Lift generated by a blown wing is also a function of standard parameters, angle of attack α and Reynolds number, R_e, as well as the blower slot height, t_c.

$$\Rightarrow C_L = f(t_C, \alpha, R_e) \tag{4.4}$$

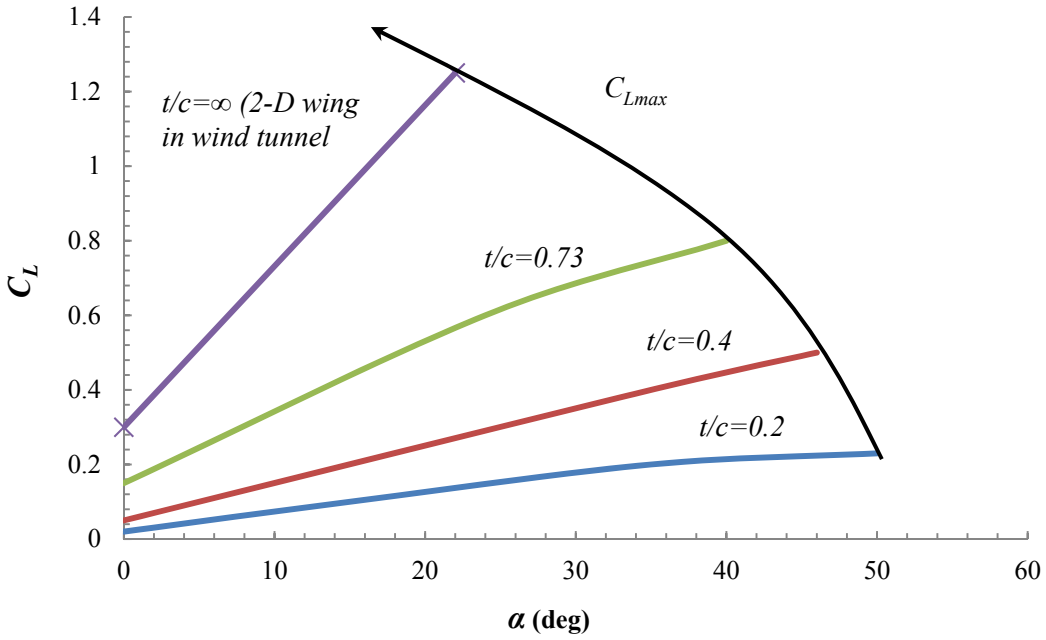

Figure 38: C_L-alpha plots of a basic wing section for different blowing slot heights [52].

4.3 Static Annular-Wing Pressure Distribution Profile

The annular wing in static-state or hovering flight mode was first set to be under symmetrical blowing which implies that the leading edge is aligned to the centre line of the blower outlet. Take an arc-strip of the annulus and draw a control volume around it as illustrated in Figure 39. Applying the law of conservation of mass (continuity) between the compressor outlet flow and at any arbitrary point along the radius gives

$$\rho_C A_C U_C = \rho_r A_r U_r \tag{4.5}$$

For the incompressible flow, $\rho_C = \rho_r$

$$\Rightarrow U_r = \frac{A_C U_C}{A_r} \tag{4.6}$$

and simplifying further gives

$$U_r = \frac{A_C U_C}{2\pi r t_C} = \frac{2\pi r_0 t_C U_C}{2\pi r t_C}, \quad \Rightarrow \frac{U_r}{U_C} = \frac{r_0}{r} = \frac{1}{r'} \tag{4.7}$$

So, continuity law shows that the radial flow velocity U_r is inversely proportional to the radius r and reduces as the radius increases. Thus, dynamic pressure [defined as $\frac{1}{2}\rho U_r^2$] decreases along the radius as the area increases. The flow rate reduction factor r_0/r is referred to as annular reduction factor f_a.

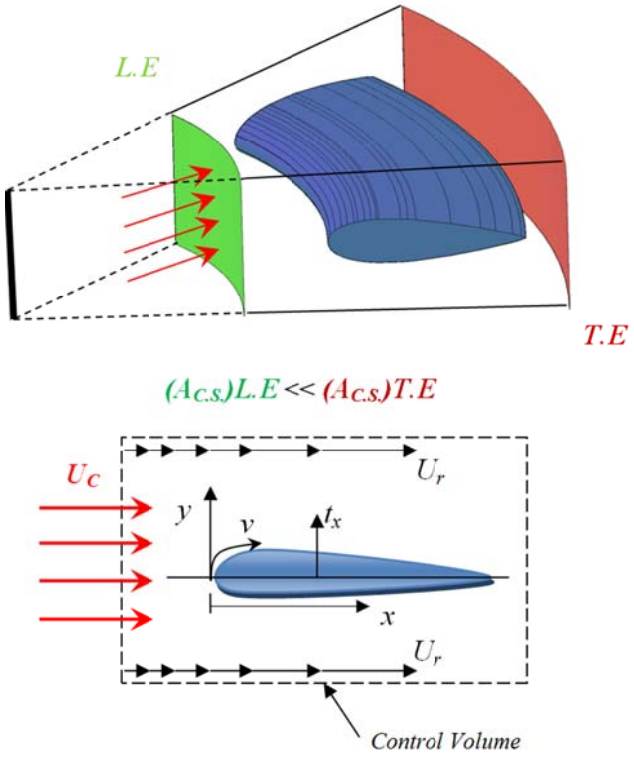

Figure 39: Control volume diagram of an annular strip with symmetrical flow at the inlet.

Now, examining the local flow over the annular wing by immersing a strip of the annular wing into the control volume as defined above and applying continuity to a strip of the annulus:

$$v = \frac{A_c U_c}{2\pi r(t_c - t_x)} = \frac{2\pi r_0 t_c U_c}{2\pi r(t_c - t_x)} = \frac{r_0 t_c U_c}{r(t_c - t_x)} \tag{4.8}$$

Where v is the local flow velocity over the surface of the wing at a distance along the radius $r + r_o$, U_c is the blower outlet velocity, t_c the blower slot height. The aerofoil thickness distribution t_x, for a symmetrical aerofoil, along the chord line at distance x from the leading edge is given by the 4th order polynomial as {taken from [93]}.

$$\pm t_x = \frac{t_{\max}}{0.2}\left(0.2969\sqrt{x} - 0.1260x - 0.3516x^2 + 0.2843x^3 - 0.1015x^4\right) \tag{4.9}$$

The change in angle of attack α was incorporated by transforming the fixed aerofoil coordinates, x and y, (origin being the leading edge) into a new set of coordinates, x' and y' (see Figure 40), and these are defined as the following.

$$\left.\begin{aligned} x' &= 1 - \sqrt{(1-x)^2 + y^2}\cos\left(\tan^{-1}\left(\frac{y}{1-x}\right) + \alpha\right) \\ y' &= \sqrt{(1-x)^2 + y^2}\sin\left(\tan^{-1}\left(\frac{y}{1-x}\right) + \alpha\right) \end{aligned}\right\} \tag{4.10}$$

Figure 40 below illustrates the coordinate transformation methodology.

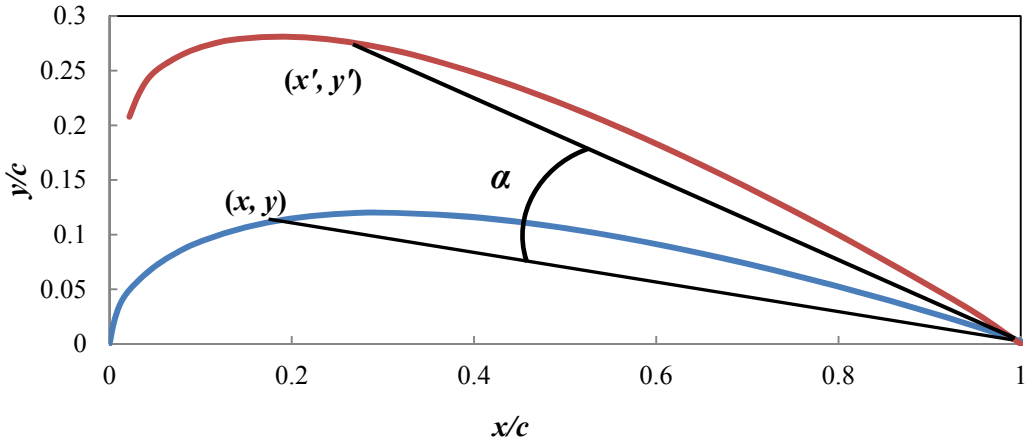

Figure 40: Coordinate transformation methodology.

From the local flow velocity distribution the pressure coefficient can be calculated using Bernoulli's equation and, implicitly, the lift on the wing.

$$C_P = 1 - \frac{v^2}{U_C{}^2} \tag{4.11}$$

Initially, a symmetrical aerofoil, the NACA-0012/0024, was chosen to allow consideration of the local flow around the wing surface. The data for the aerofoil is extracted from standard sources e.g. [53] and [54].

Figure 41 shows that the local pressure at any point over the surface of the annular wingform is lower compared to the rectangular wing. This is because the compressor

outlet velocity U_C reduces away from the source. A crucial point to be noted here is that the minimum pressure shifts about 10 % of chord length closer to the leading edge for the annular wing compared to the rectangular wing. This indicates that the centre of pressure will also move forward.

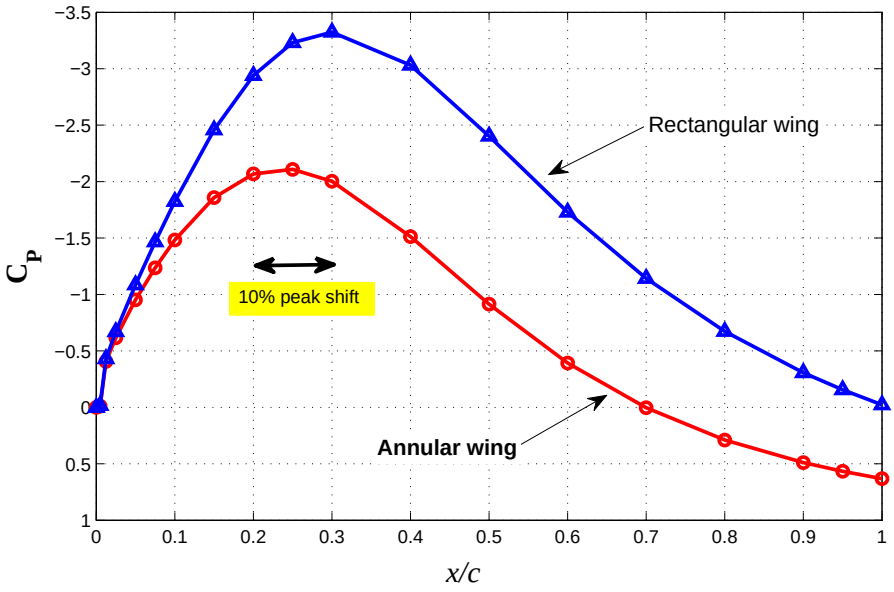

Figure 41: A theoretical comparison of local pressure for rectangular and annular wingforms.

Figure 42 presents a comparison of different thickness distribution and it shows that the loss of dynamic pressure will be significantly lower for a thicker aerofoil section such as the NACA-0024. NACA-0012, with annular configuration, loses around 45 percent of the dynamic pressure and NACA-0024 loses around 30 percent with reference to the rectangular wingform.

This shows that the annular wing lifting efficiency depends upon positioning the centre of pressure as close as possible to the leading edge; this can be achieved by pushing the maximum aerofoil thickness closer to the leading edge such as by using a NACA-0024 section. Furthermore, the non-linearity in the dynamic pressure along the radius indicates that the section lift would also be less for the annular wing when compared to the rectangular wing i.e. the total lift generated for a certain surface area would not be the same for the two wings.

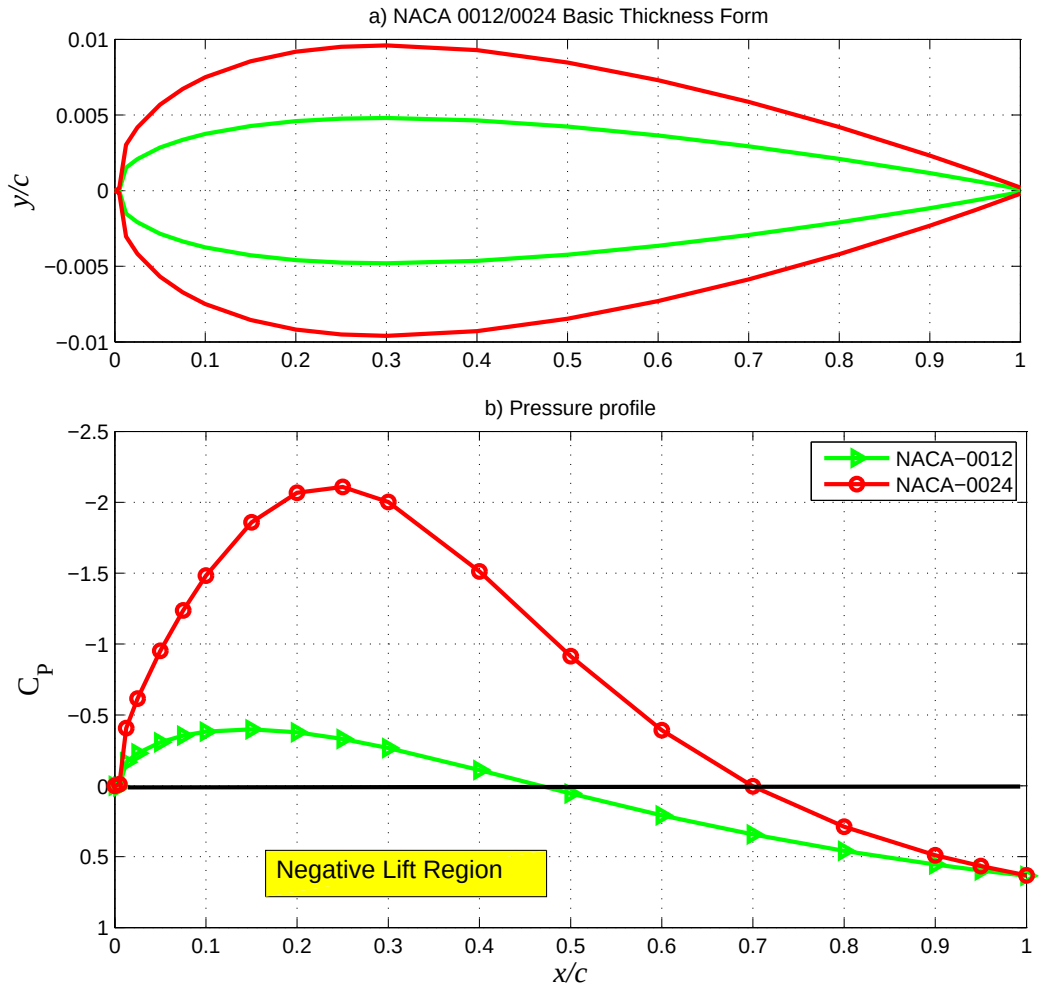

Figure 42: Local pressure comparison for different aerofoil thickness.

4.4 Preliminary Wing Size Evaluation

The size of the annular wing is deduced by considering the desired lift force generated and the structural mass of the wing. Hence, lift to mass ratio, *L/M*, is the proposed design factor to be optimised. Firstly, the lift generated by the annular wing needs to be defined and in order to achieve this, lift is assumed to be generated at quarter chord based upon flow at that station: $U_{\frac{c}{4}} = \frac{\dot{m}}{2\pi\rho r_{\frac{c}{4}} t_{\frac{c}{4}}}$

where $\dot{m}$ is the mass flow rate and $U_{\frac{c}{4}}$ is the flow velocity at quarter chord. Hence, the total effective lift from the annular wing in hover flight is given by

$$L_h = \frac{1}{2}\rho\left(\frac{\dot{m}}{2\pi\rho r_{\frac{c}{4}} t_{\frac{c}{4}}}\right)^2 \pi\left(R_0{}^2 - r_0{}^2\right)a\alpha \tag{4.12}$$

Substituting $r_{\frac{c}{4}} = r_0 + \frac{R_0 - r_0}{4} = \frac{R_0 + 3r_0}{4}$ into the above equation and simplifying gives

$$L_h = \frac{2\rho \dot{m}^2}{t_{\frac{c}{4}}{}^2 \rho\pi} \frac{\left(R_0{}^2 - r_0{}^2\right)}{\left(R_0 + 3r_0\right)^2} a\alpha. \tag{4.13}$$

Subsequently the following relationships may be defined:

$$\Rightarrow \begin{cases} L_h \propto \dot{m}^2 \\ L_h \propto \dfrac{1}{t_{\frac{c}{4}}{}^2} \\ L_h \propto \dfrac{R_0{}^2 - r_0{}^2}{\left(R_0 + 3r_0\right)^2} \end{cases} \tag{4.14}$$

The first two relationships clearly indicate that the total lift is proportional to the mass flow rate square at the quarter chord and that decreasing the thickness would increase the total lift. Maximising $\dot{m}$ is a function of the design, but it is noted that typically for a centrifugal compressor the relationship between the mass flow rate and the input power is defined as $\dot{m} \propto P$. This subsequently allows derivation of the relationship between the total lift and the input power as $L_h \approx P^2$ which implies that higher the power, the more efficient the lift system becomes.

The third relationship is a function of wing size and to understand this further the function is plotted for a range of inner and outer radii. Figure 43 shows that lift is maximised by decreasing the inner radius and increasing the outer radius, which simply means that a greater wing surface area produces more lift. This implies that design constraints need to be added into the model, including the dominant one which is the structural mass.

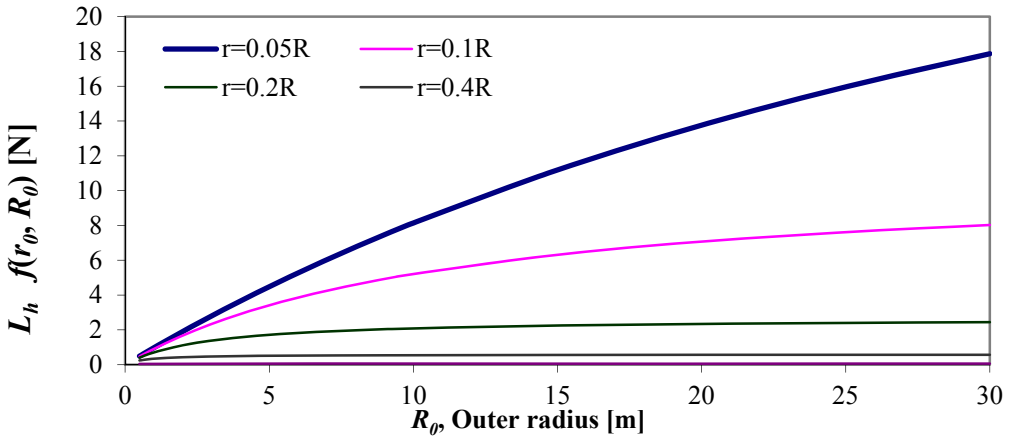

Figure 43: Theoretical lift versus outer radius for different inner radius values.

It will be assumed that the structural mass of the wing is proportional to the cross-sectional area at the quarter chord facing the flow times the circumference at the quarter chord.

$$\Rightarrow m_a \propto t_{\max} 2\pi \left(r_0 + \frac{R_0 - r_0}{4} \right) \left(R_0 - r_0 \right) \tag{4.15}$$

Also, assume that thickness to chord ratio around the annulus is constant and the mean chord length is defined as $\bar{c} = R_0 - r_0$.

$$\Rightarrow m_a \propto \left(R_0 - r_0 \right)^2 \left(R_0 + 3r_0 \right) \tag{4.16}$$

Thus the design factor comes out to be

$$\Rightarrow \frac{L_h}{m_a} \propto \frac{\left(R_0^2 - r_0^2 \right)}{\left(R_0 - r_0 \right)^2 \left(R_0 + 3r_0 \right)^3} \tag{4.17}$$

Maximising this design factor will then achieve maximum lift for minimum structural mass. Figure 44 shows a plot of the design factor L_h / m versus the inner and outer radii and it can be seen that the relationship between them is exponential, indicates that the smaller the wing, the higher the L_h / m factor. This is a simplified model since it ignores Reynolds number effects at extremes of scale, and also the different efficiencies of different sizes of powerplant, but nonetheless gives a good first indication of scale effects.

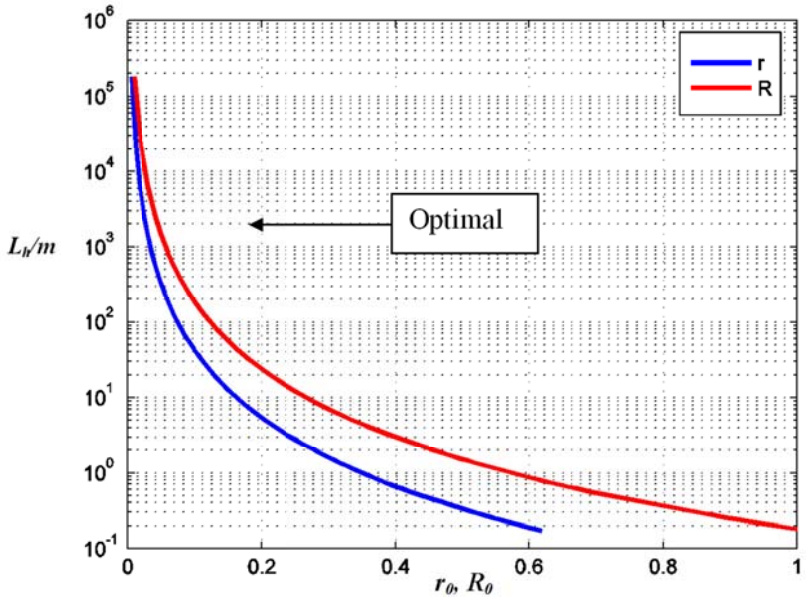

Figure 44: Searching for the optimum of the design factor L_h/m.

To quantify wing the size let us now define a relationship between the radii for optimum design factor that is obtained by differentiating the design factor function with respect to r_0 as following.

$$\frac{d}{dr_0}\left(\frac{L_h}{m_t}\right)=\frac{9r_0^{\,2}+6R_0r_0-7R_0^{\,2}}{\left(r_0-R_0\right)^2\left(R_0+3r_0\right)^4}=0 \tag{4.18}$$

$$\Rightarrow 9r_0^{\,2}+6R_0r_0-7R_0^{\,2}=0,\quad r_0=\frac{R_0}{18}\left[-6\pm\sqrt{288}\right]=0.6R_0 \tag{4.19}$$

This suggests that the optimal chord length of the wing is 40% of the outer radius. Hence, if the dimensions of the centrifugal compressor are known, a preliminary design surface area for the wing can be calculated.

4.5 Results and Analysis

An initial slot height was chosen to be $t_C/c=0.5$ based upon the source (centrifugal fan used in the experiment) capacity and to be in the common $C_L-\alpha$ range (0-16^0) given in Figure 38 above.

4.5.1 Radial Flow Examination

Measurements have shown that the outlet velocity of the blower varies significantly across its vertical axis or thickness as shown in Figure 45; the maximum occurs near the diffuser-plate and the minimum occurs near the bottom-plate. In Figure 46 the normalised root mean square (RMS) values of the signals at different traverse positions across the outlet are plotted. The RMS value of a signal simply defines the average magnitude of the fluctuating velocity or the turbulence intensity. The turbulence profile indicates that the overall flow is highly turbulent. Furthermore, at the lower half ($0.45 < y / t_C < 1$) the flow is separated as the plots become unsmooth.

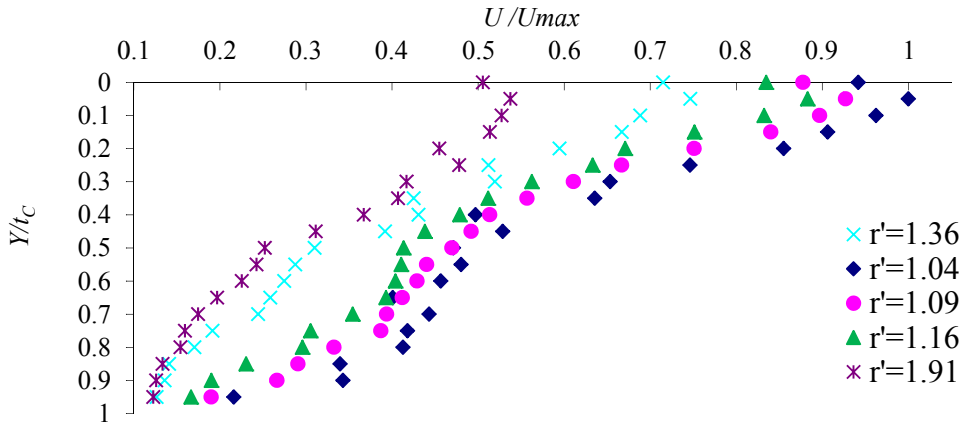

Figure 45: Flow variation across outlet longitudinal axis {Parameters: $U_{\max} = 45\text{m/s}$, $t_C = 20\text{mm}$, $P_{atm} = 101.2kPa$, $T_{atm} = 21.5^{o}C$}.

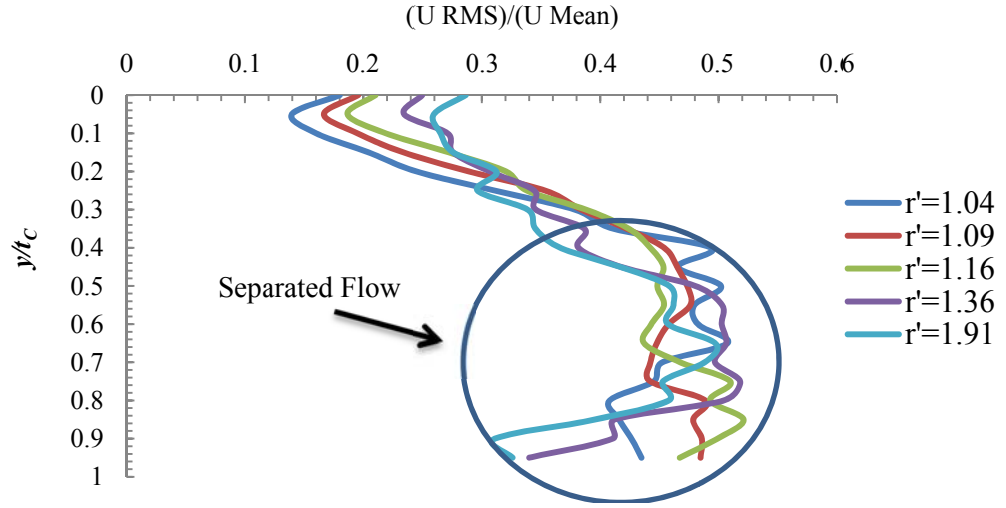

Figure 46: Turbulence intensity across horizontal and vertical axis of blower.

This outlet-flow asymmetry was initiated by unavoidable inlet flow distortion. The flow velocity is reduced at the inlet-walls due to shear stress and skin friction that forces the flow through the centre line of the inlet (Figure 47). The vertical inertial momentum of the flow also contributes, because the flow naturally sticks to the diffuser plates. These variations in the outlet flow also imply that the high turbulence may subsequently affect the results. Nevertheless, this fluctuation could be, and was, reduced by implementing longer flow straightening fins and working at lower flow speeds.

Figure 48 presents the relationship of mean outlet velocity and the distance away from the outlet. This is deduced by taking the average of each plot in Figure 45. The plot shows that the average-mean velocity is inversely proportional to the distance r' away from the source outlet as discussed in Section 4.3. The best fit of experimental data is derived as

$$\frac{U_r}{U_C} = 0.9875\left(\frac{r}{r_0}\right)^{-0.996} \approx \frac{1}{r'} \tag{4.20}$$

A small deficit, compared to theoretical values, occurred: probably because of some combination of turbulence and stream expansion.

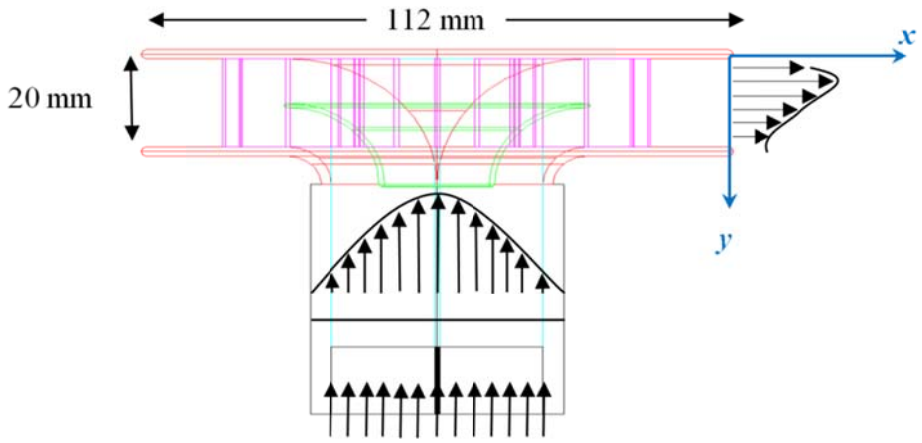

Figure 47: Illustration of flow structure at inlet and outlet of blower, $^{t_C}/_{C} = 0.5$.

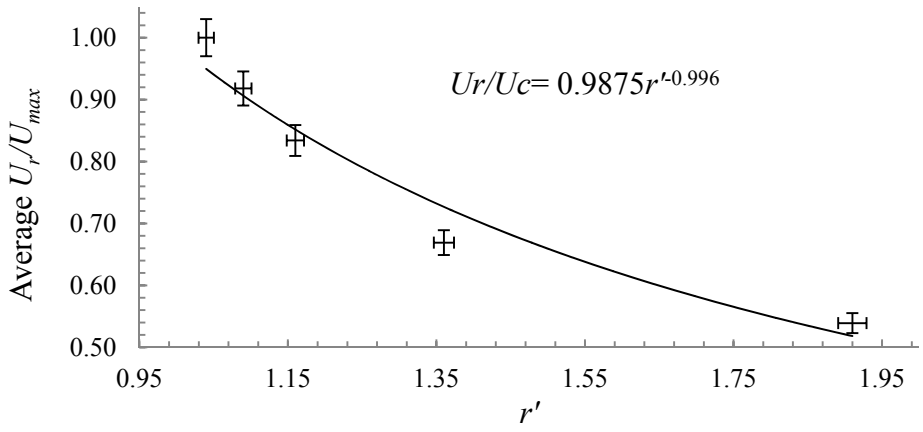

Figure 48: Reduction in average radial flow velocity away from blower outlet.

4.5.2 Local Flow Profile of Annular Wing-Section

Figure 49 shows the local upper surface velocity distribution over the wing surface along the chord length for data acquired experimentally and predicted theoretically (Equation 4.8). From the figure it can be seen that the local flow velocity decreases after reaching its maximum at 10% of chord length. In comparison to the theoretical plot, the experimental values show lower velocities at any point along the chord length. This is because in the theory ideal flow conditions, i.e. inviscid, incompressible, were assumed and hence residues are expected. For the relatively thicker aerofoil, NACA-0024, the local distribution resembles the theoretical curve until the maximum as shown in Figure 50. After the maximum the experimental plot deviates the theoretical values and re-joins at 50mm chord length. The unexpected decrease in flow velocity may be due to turbulence in the outlet flow.

The investigation of the local flow distribution has shown that the dynamic pressure loss over the surface of annular wingform is of significance and hence validating the theory. The lift generated by the annular wing is approximately equal to 70% of that generated by a conventional rectangular wing.

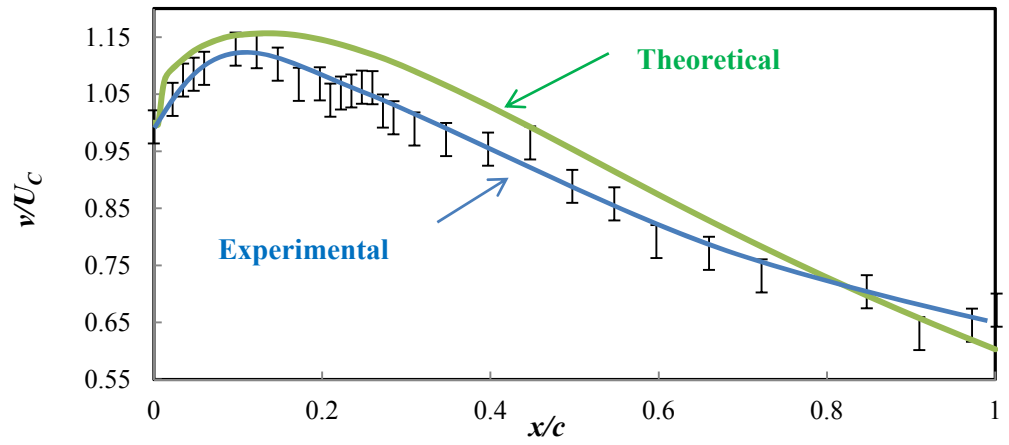

Figure 49: Local flow distribution for NACA-0012{Parameters: $\overline{U}_{L.E} = 10.46$ m/s , $\alpha = 0$, $r_0 = 0.12m$, $R_0 = 0.20m$ }.

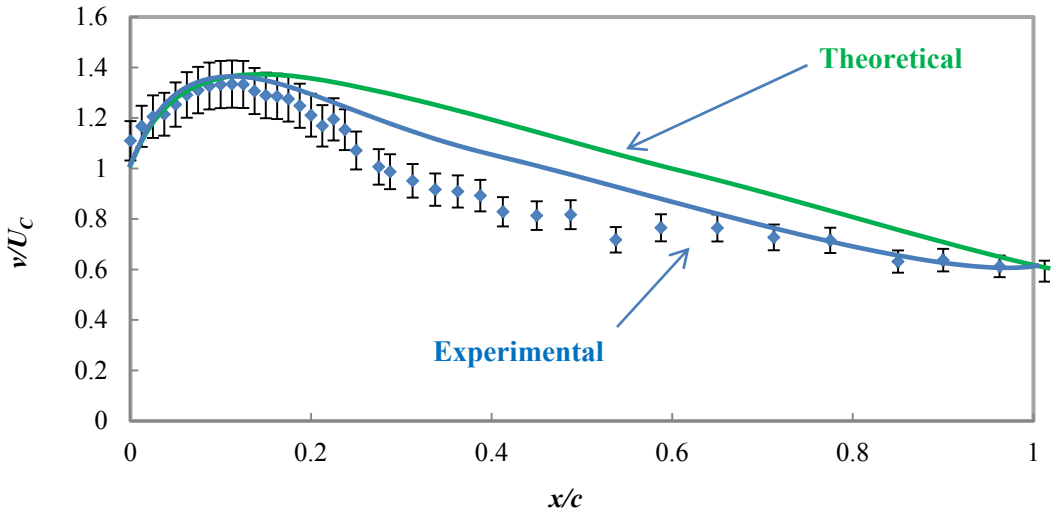

Figure 50: Local flow distribution for NACA-0024{Parameters: mean $U_C = 23$ m/s , $\alpha = 0$, $r_o = 0.12m$, $R_o = 0.20m$ }.

4.5.3 C_L-Alpha Plots

The lift generated by the annular wing with two different aerofoils, measured experimentally, is shown in Figure 51 where the mean line corresponds to the mean flow velocity and other data points correspond to minimum and maximum flow velocities (further explained in Section 3.4). The figure also compares the experimental plot to the approximate theoretical plot which is deduced by taking 70% percent of the lift generated by a rectangular wing-section with all the other

parameters remaining the same[b]. An important point to be noted here is that the theoretical curve only includes the loss of lift due to annulus flow expansion whereas for a blown wing the blowing slot height becomes crucial.

There is approximately a 16% difference between experimental and theoretical C_{Lmax} values. This suggests strongly that the stall-angle is significantly higher for the annular wingform compared to the rectangular wingform. Possible sources of error are that the theoretical calculations did not take into account the loss of lift due to blowing slot thickness being much smaller, i.e. h/c << 2 chord lengths. Furthermore, the wing with section NACA-0024 at 12° achieves much higher lift compared to NACA-0012 at 12° which indicates that the flow attachment is greater. The thicker aerofoil receiving the same airflow tends to perform better as the jet stream diverted at the leading edge follows a relatively narrow path, so the airflow depth is thinner and the Coanda effect is enhanced. This suggests a strong relationship between the optimal maximum aerofoil thickness and the optimal blowing slot height.

Note: Herein, the angle of attack is defined as the angle between the chord line and the horizontal, also known as the geometrical angle. This may raise a critical question – what is the effective angle of attack? Recalling that the effective angle of attack is measured from the orientation where the wing has zero lift [55]. Since the source flow from the blower is turbulent/disturbed, it is anticipated the effective angle of attack values are somewhat different. Also, the presence of the aerofoil in the finite-size blower outlet causes flow curvature and downwash deflection of the incident flow. This ultimately effects the lift distribution, hence the "effective" angle of attack. However, the particular experimental setup did not allow measuring any flow deflection at the inlet; thus the geometrical angle has been assumed to be the effective angle of attack for initial comparison. This difference should not matter as the critical angle of attack, the stall angle, is not the scope of discussions here. Therefore, the linear trendlines drawn at the experimental data, in Figure 51, are set to cross the axis at zero.

---

[b] The rectangular wing-section data was acquired by Xfoil-6.94 (Software Package) using the corresponding input data i.e. Reynolds number, Mach number, viscosity etc.

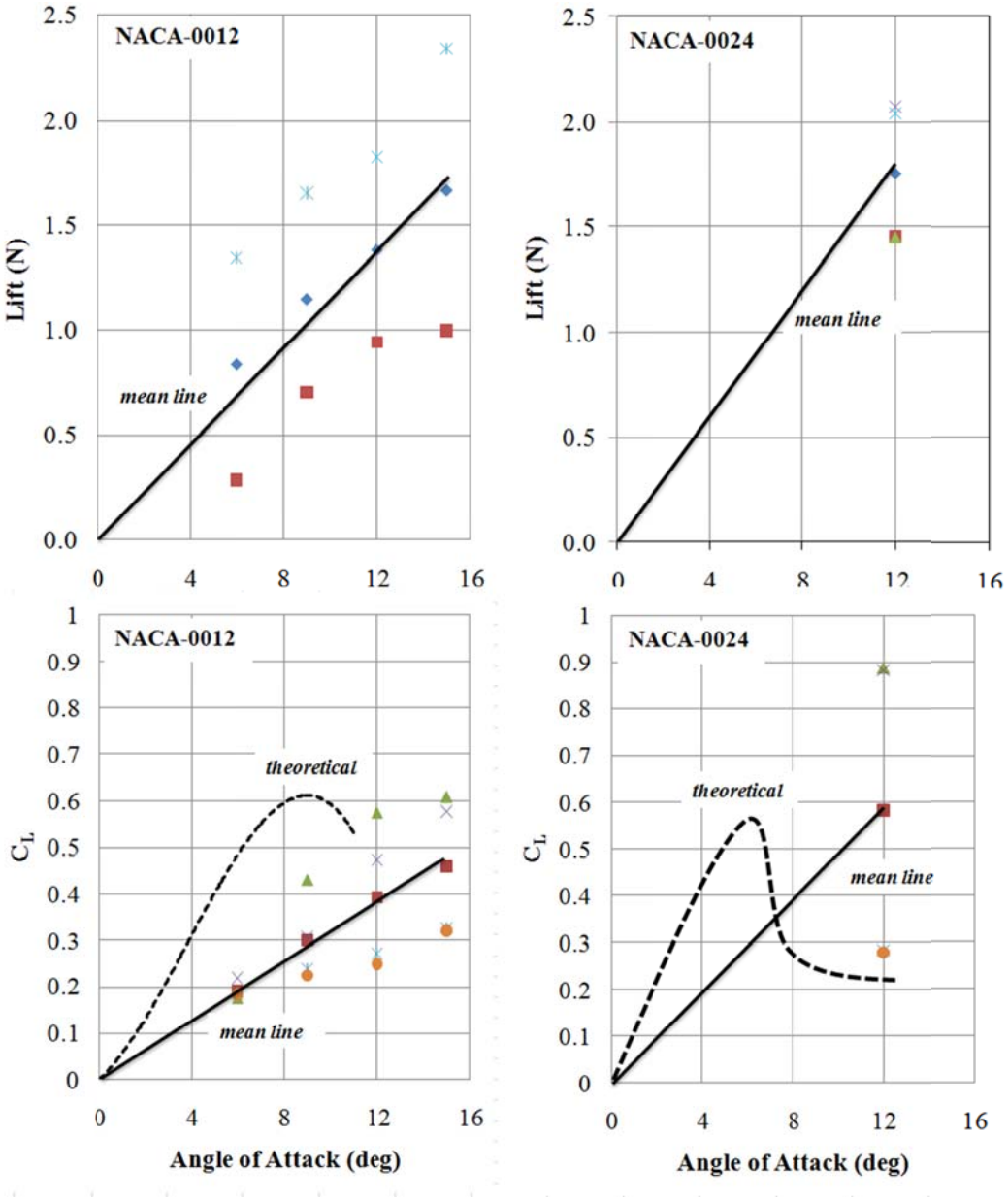

Figure 51: Lift-alpha and C_L-alpha plot for NACA-0012/0024 (forces measured with load-cell) {Parameters: $U_{eff} = 20$ m/s, $r_0 = 55$ mm, $R_0 = 95$ mm }.

4.5.4 Change in Lift with Flow Velocity

The forces measured by the load cell at different flow velocities for three different wing-sections at 12 degrees of angle of attack are presented in Table 20 and Table 21. Figure 52 shows lift versus effective flow velocity at quarter chord for three wing sections: NACA 0012, 0024 and 4412. In general, the lift force varies with the leading edge flow velocity square $L \propto U^2$, so all the different wing configurations follow conventional aerodynamic behaviour. Furthermore, maximum lift is achieved

by the thicker wing-section NACA-0024 which once again indicates that a relatively thicker aerofoil is best utilised for annular wingform. Subsequent discussion will therefore concentrate upon use of the best aerofoil section, NACA-0024, with some comparison discussion of the NACA-0012, but intermediate NACA-4412 section disregarded.

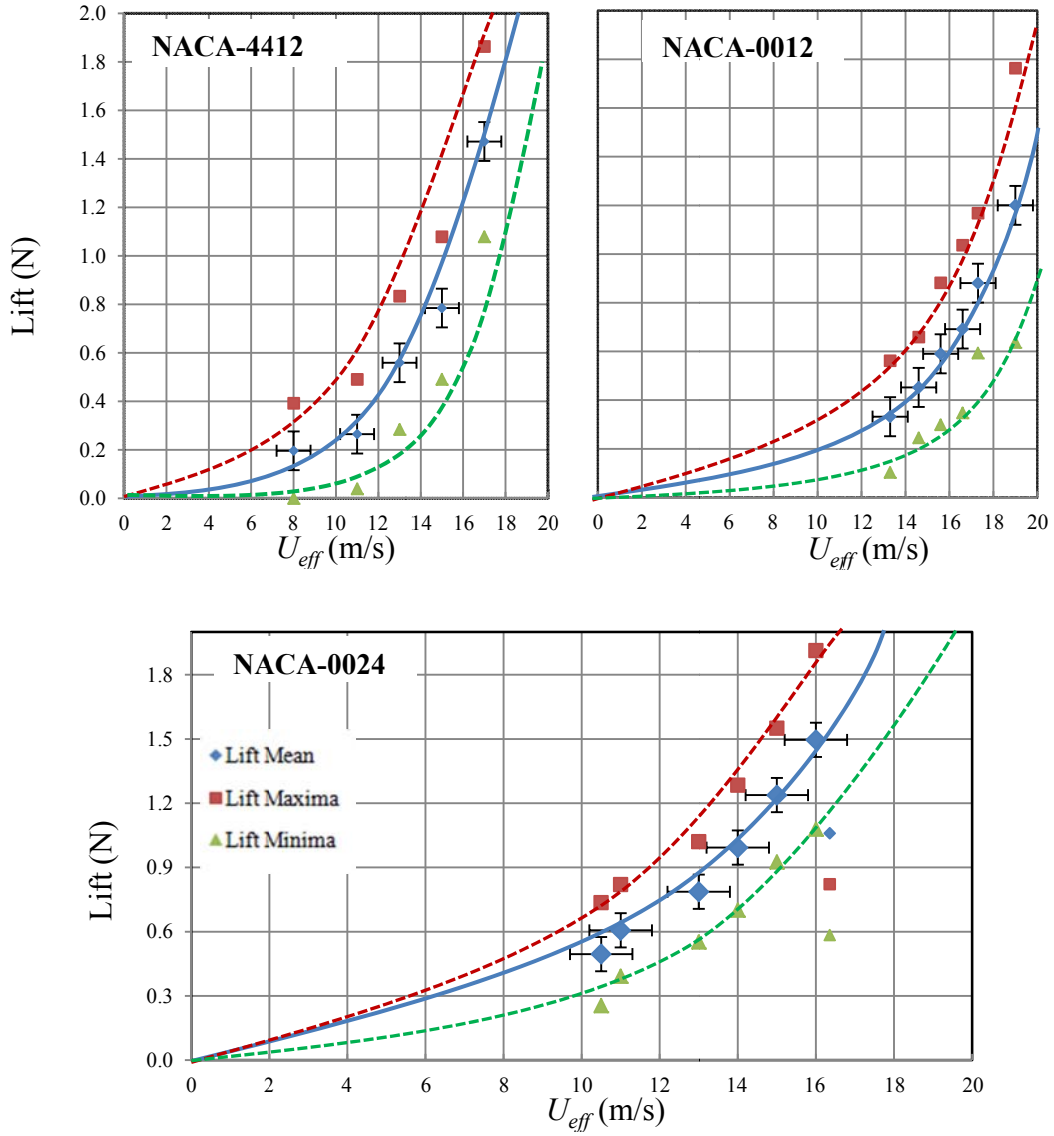

Figure 52: Lift force variation with effective flow velocity for different wing-sections (forces measured with load-cell) {Parameters: $\alpha = 12^o$, $r_o = 55$ mm, $R_o = 95$ mm }.

4.5.5 Examination of Flow in the Wake of Annular Wing

Two different horizontal locations were chosen for the measurements; fore of the leading edge $r / r_0 = 1.04$, and aft of trailing edge $r / r_0 = 1.91$. Figure 53 examines the

jet flow profile with and without the wing for NACA-0012 wing-section at different angles of attack. From this figure it can be seen that lesser flow leaves at the lower surface compared to the upper surface this is due to the asymmetry at the inlet as shown in Figure 45. Examination of the wake at $r/r_0 = 1.91$ shows that for all these different wing configurations the maximum flow velocity shifts from $y/t_C \approx 0.1$ to just near the surface. From this the flow attachment is apparent and that the Coanda effect is present.

To further investigate the flow attachment the thicker aerofoil, NACA-0024 at 12°, was immersed in the flow. The leading edge was aligned at $y/t_C \approx 0.4$. The flow profile at the upper surface, from $y/t_C = 0$ to approximately $0.075t_C$ (~1.5 mm) away from the surface[c], was measured at different locations, using the hot-wire probe. The velocity profiles are plotted in Figure 54 and from this it can be seen that the flow immediately after the leading edge tends to follow the aerofoil curvature and the maximum flow velocity shifts towards the surface. After reaching a maximum the flow velocity starts to decrease, suggesting viscosity is present in the flow layers. Furthermore, beyond $r/r_0 = 1.5$ the flow profile settles and this particular profile is generic for wall-jets as described in Section 5.2.

Now, the next question arises; what happens to a uniform outlet flow unlike the flow profile discussed above? In order to conduct an investigation another experimental rig is sought as described in Section 3.6 and the analysis follow.

[c] A precautionary distance of 1.5 mm from the surface was kept to avoid any damage to the extremely thin hot wire.

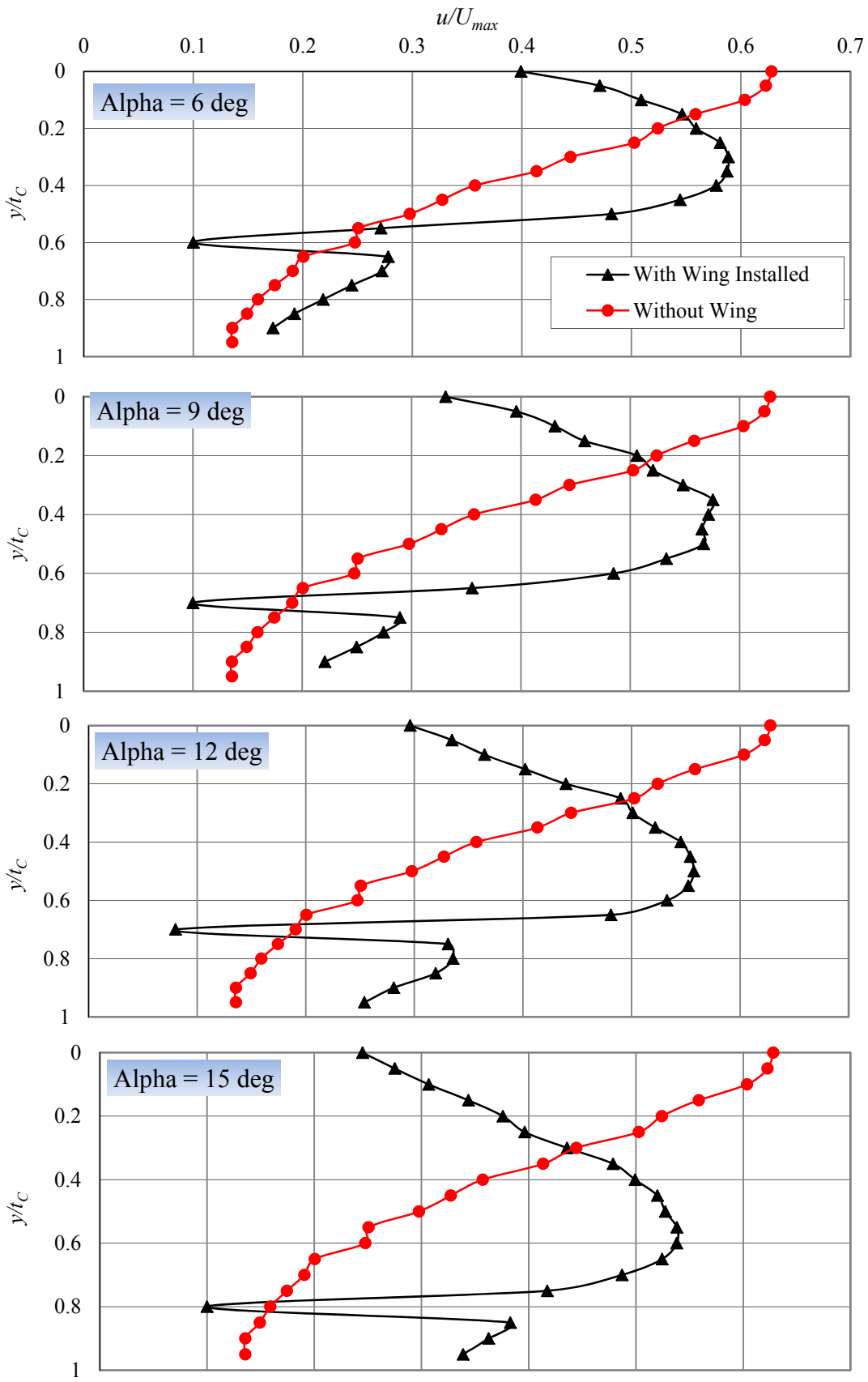

Figure 53: NACA-0012 Wake profile at $r / r_0 = 1.91$ measured with hot-wire.

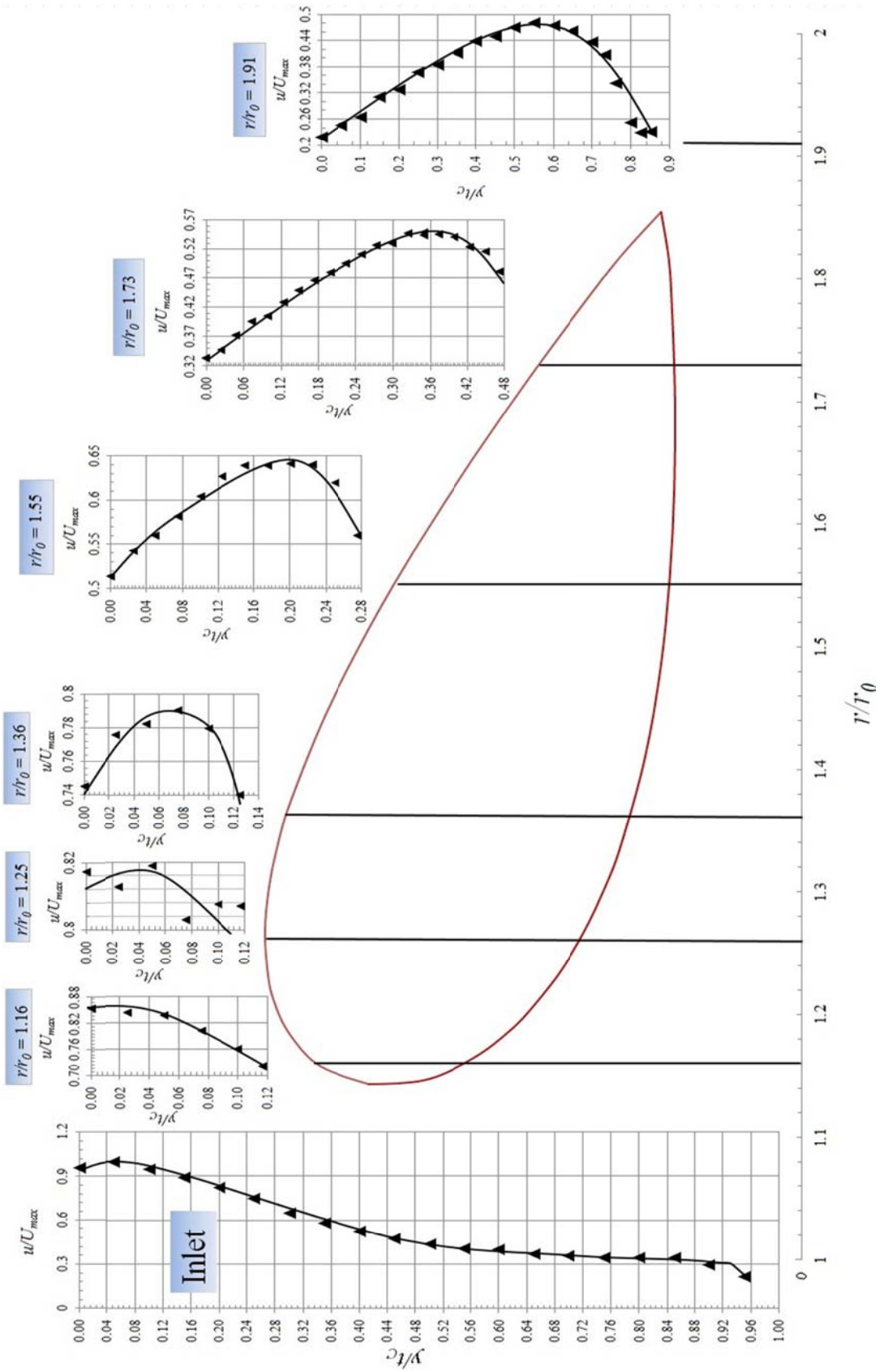

Figure 54: Flow attachment profile at the upper surface of NACA-0024@12deg, measured with hot-wire {Parameters: $U_{\max} = 43\text{m/s}$, $t_c = 20\text{mm}$, $P_{atm} = 101.1kPa$, $T_{atm} = 21^{O}\mathbf{C}$}.

4.6 Static Annular-Wing's Aerodynamic Characteristics with Symmetrical Blowing

Figure 55 shows the slot exit flow profile for the blower at different azimuthal angles and distances away from the exit. This shows that this blower has generated a good symmetrical flow across its longitudinal axis with a higher degree of uniformity than achieved with the annular blower. There is asymmetry in the azimuthal/lateral axis of the outlet due to flow attachment at the blower walls; however, this asymmetry should have minimal effect on the 2-D aerodynamic characteristics. There is also turbulence in the flow; however, again this has significantly reduced as shown in Figure 56. Furthermore, the outlet-flow profile is visibly of parabolic form which is a typical for free jets issuing from a nozzle.

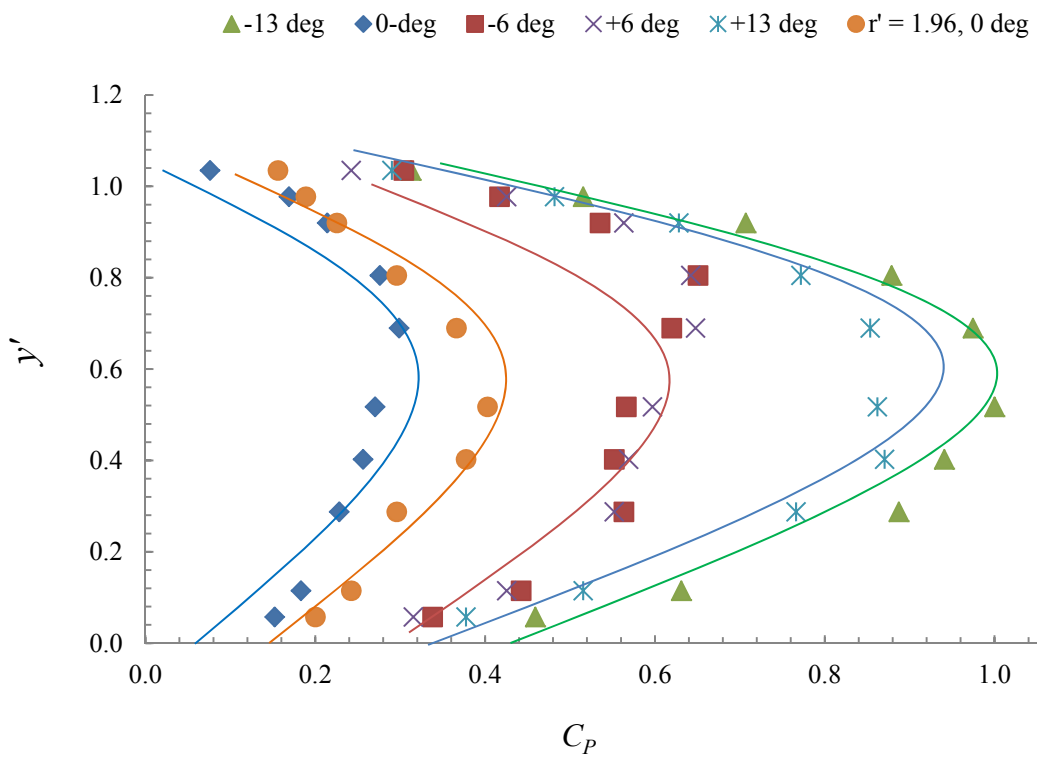

Figure 55: Outlet flow profile with parabolic best fits from Rig2 setup {Parameters: $U_{\max} = 20\text{m/s}$, $t_C = 44\text{mm}$, $r_0 = 143\text{ mm}, R_0 = 240\text{ mm}$ $P_{atm} = 101.2kPa$, $T_{atm} = 20^o C$ }..

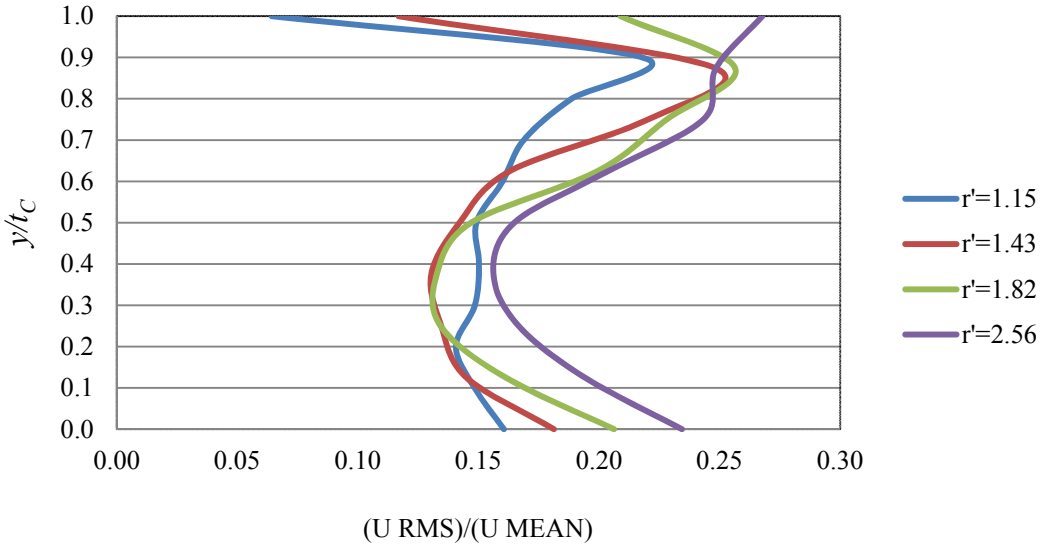

Figure 56: Turbulence intensity profile from blower of Rig 2.

An arc-wing (NACA-0024) embedded with pressure taps around the surface was immersed into the potential flow to examine the pressure distribution around the aerofoil. The measured pressure distribution at different angles of attack is presented in Table 1 and plotted in Figure 57. The pressure distribution profile is of standard form based on thickness distribution; however, the magnitude of local pressure is lower than the normal rectangular wingform.

The pressure around the surface is integrated to obtain the 2-D aerodynamic characteristics given in Figure 58.

$$\left.\begin{aligned} C_L &= -0.002\alpha^2 + 0.064\alpha \\ C_D &= 0.0007\alpha^2 + 0.0044\alpha - 0.0602 \\ C_M &= -0.0102\alpha \end{aligned}\right\} \qquad (4.21)$$

The figure shows, conventionally, that as the angle of attack is increased the lift, drag and pitching moment coefficients increase. At zero angle of attack a small negative drag force is experienced possibly due to a negative ‘effective’ angle of attack as described in Section 4.5.3. Lift increases linearly with drag for the range $0 \leq \alpha \leq 14°$ then the drag rise becomes much steeper. This suggests that an optimum value for lift to drag ratio lies within this angle of attack range.

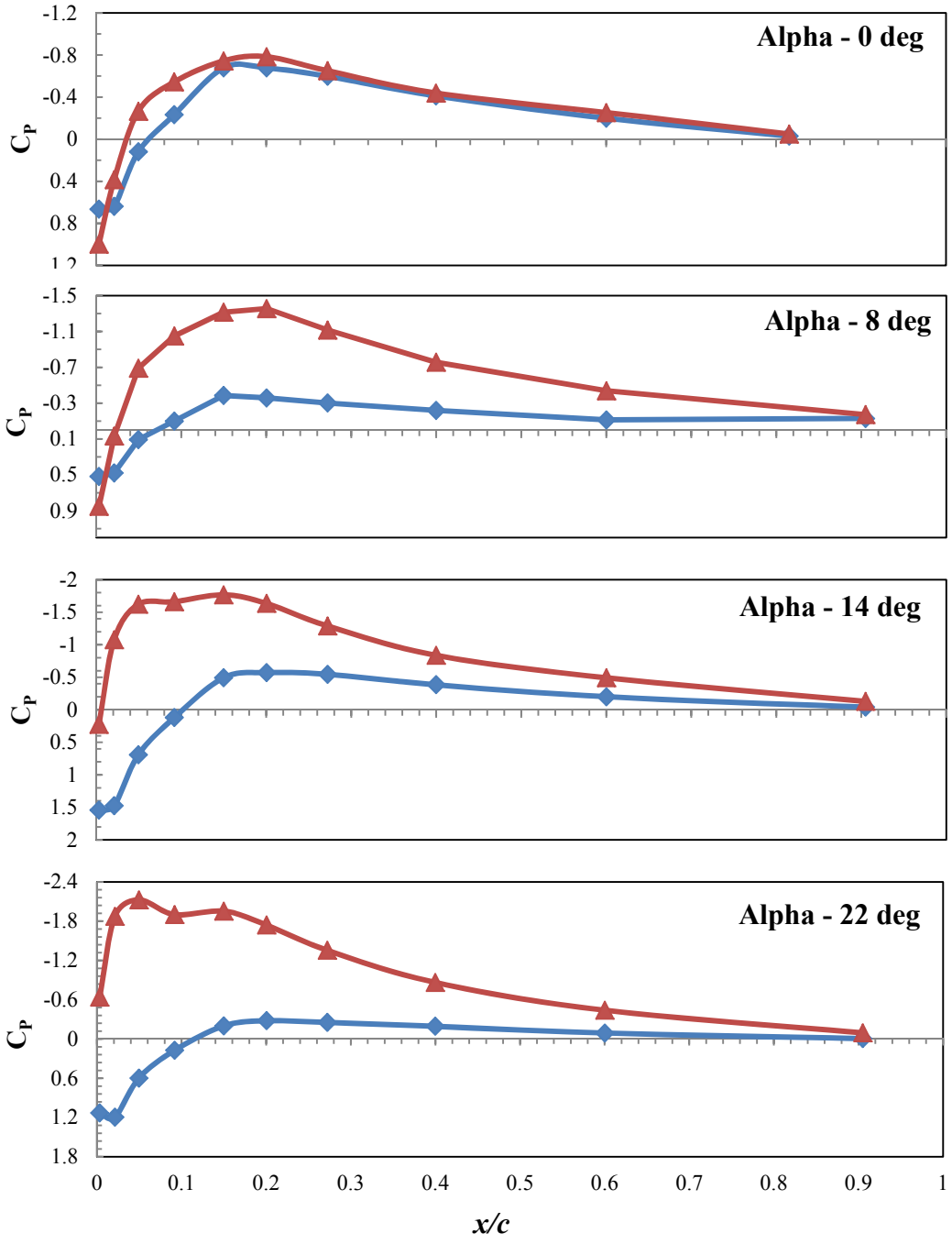

Figure 57: Pressure distribution over the surface of arc-wing measured experimentally.

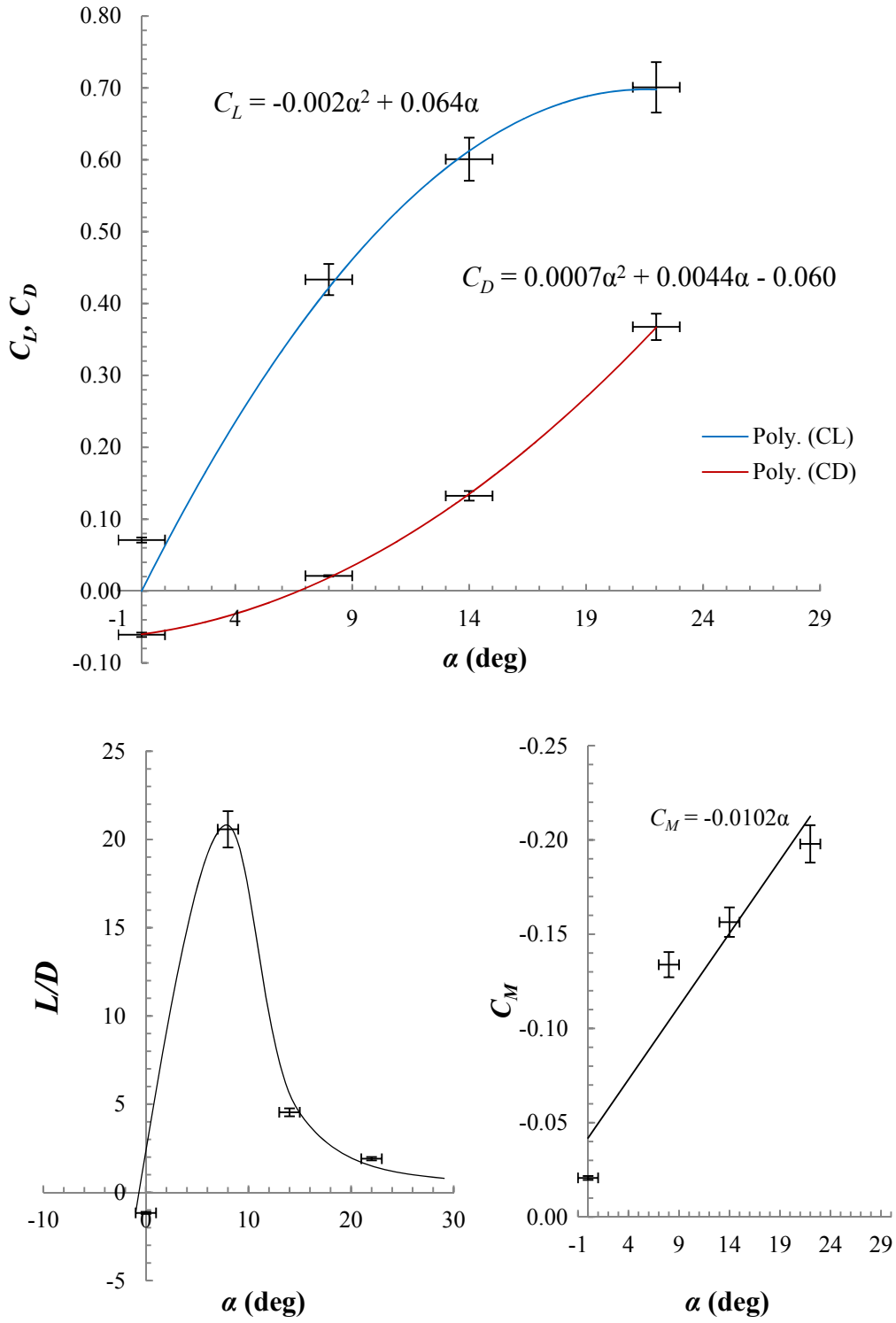

Figure 58: 2-D aerodynamic characteristics of annular wing established experimentally.

			α	**0**	**8**	**14**	**22**
y/c	x/c	s/c	beta	Cp	Cp	Cp	Cp
-0.0211	0.003	0.030	162	0.664	0.518	1.541	1.129
-0.04852	0.021	0.038	139	0.6377	0.478	1.474	1.195
-0.07068	0.050	0.044	122	0.1195	0.106	0.690	0.597
-0.09072	0.092	0.057	110	-0.232	-0.0996	0.119	0.172
-0.10654	0.150	0.055	101	-0.677	-0.385	-0.491	-0.199
-0.11498	0.200	0.062	97	-0.677	-0.358	-0.571	-0.279
-0.1192	0.272	0.084	91	-0.597	-0.301	-0.544	-0.252
-0.11603	0.400	0.154	86	-0.411	-0.219	-0.385	-0.193
-0.09177	0.600	0.203	81	-0.199	-0.112	-0.199	-0.090
-0.04958	0.815	0.184	77	-0.029	-0.128	-0.0398	-0.0066
-0.02743	0.905	0.147	76	0.9965	0.8503	0.225	-0.637
0.021097	0.003	0.030	198	0.3853	0.0664	-1.076	-1.873
0.048523	0.021	0.038	221	-0.265	-0.690	-1.621	-2.125
0.070675	0.050	0.044	238	-0.544	-1.0496	-1.660	-1.900
0.090717	0.092	0.057	250	-0.7440	-1.315	-1.767	-1.953
0.10654	0.150	0.055	259	-0.783	-1.355	-1.634	-1.740
0.114979	0.200	0.062	263	-0.6510	-1.116	-1.288	-1.355
0.119198	0.272	0.084	269	-0.438	-0.757	-0.8371	-0.863
0.116034	0.400	0.154	274	-0.2524	-0.438	-0.491	-0.438
0.091772	0.600	0.203	279	-0.0491	-0.172	-0.128	-0.093
0.049578	0.815	0.184	283	-3.752	0.5182	1.5413	1.129
0.027426	0.905	0.147	284	0.6643	0.4783	1.474	1.195
			C_L	0.071	0.433	0.601	0.701
			C_D	-0.061	0.021	0.132	0.368
			C_M	-0.021	-0.134	-0.156	-0.198

Table 1: Experimental data and calculations for arc-wing

4.7 The Annular-Wing in Translational Flight Mode with Symmetrical Blowing

Figure 59 shows the annular wing in translational flight, the azimuth angle ψ is measured from the datum in the direction of forward flight. In translational flight the wing divides into two halves: one is where the translational velocity is added to the compressed flow velocity $(\pi/2 < \psi < 3\pi/2)$ and second half $(3\pi/2 < \psi < \pi/2)$ experiences reverse flow where the forward velocity is subtracted from the compressed flow velocity. The two halves can also be described as advancing side and retreating side.

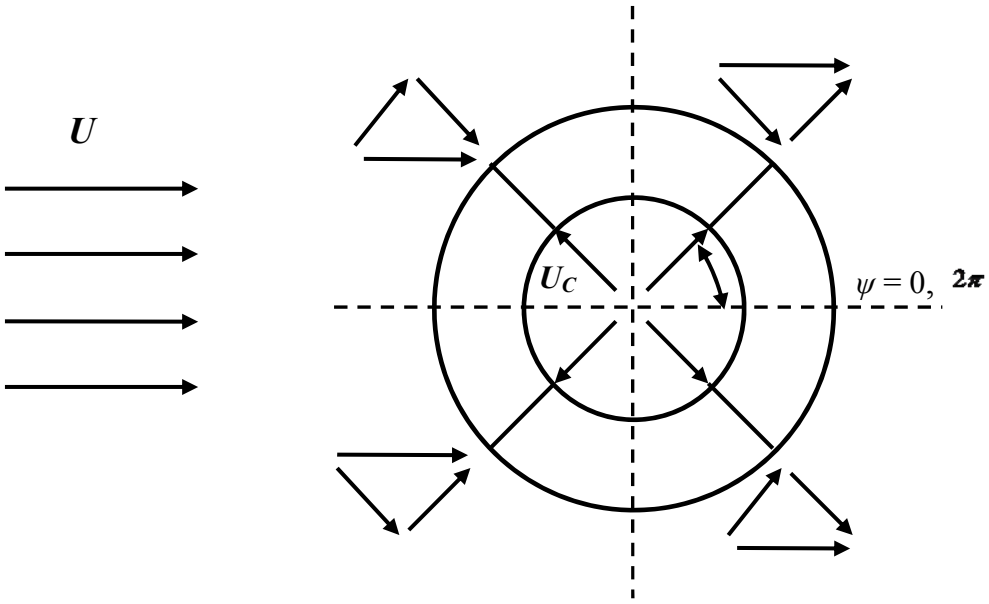

Figure 59: Plan form view of the annular wing in translational flight.

The effective flow around the annulus is defined by

$$U_{eff} = U_C + U\cos\psi \tag{4.22}$$

where U is the translational velocity.

The function of wing section lift can be defined in terms of the azimuth angle as

$$dL_F = \frac{1}{2}\rho\left[U_C + U\cos\psi\right]^2\left[\frac{1}{2}\left(R^2 - r^2\right)d\psi\right]a\alpha \tag{4.23}$$

$$L_F = \frac{1}{4}\rho a\alpha(R_0^2 - r_0^2)\int_0^{2\pi}\left[U_C^2 + 2U_C U\cos\psi + U^2\cos^2\psi\right]d\psi \tag{4.24}$$

and integrating the function gives the total lift generated by the annulus.

$$L_F = \frac{\pi}{4}\rho a\alpha\left(R^2 - r^2\right)\left[2U_C{}^2 + U^2\right] \tag{4.25}$$

The wing will inevitably experience during translational flight a net pitching moment due to asymmetric flow across the annulus. Taking moments about a lateral axis through the centre of the annulus and the moment arm δ may be defined as

$$\delta = \left(\frac{R_0 - r_0}{4} + r\right)\cos\psi = \left(\frac{R_0 + 3r_0}{4}\right)\cos\psi \tag{4.26}$$

Upon integrating the section lift and taking moments about the center defines total pitching moment generated by the annulus as

$$dM = dL_F\delta = \frac{1}{2}\rho\left[U_C + U\cos\psi\right]^2\left[\frac{1}{2}\left(R^2 - r^2\right)d\psi\right]\left(\frac{R_0 + 3r_0}{4}\right)\cos\psi C_L \tag{4.27}$$

$$\begin{aligned} M = {} & \frac{1}{16}\rho C_L\left[\left(R_0^2 - r_0{}^2\right)\left(R_0 + 3r_0\right)\right]... \\ & ...\int_0^{2\pi}\left[U_C^2\cos\psi + 2U_C U\cos\psi + U_C^2\cos^3\psi\right]d\psi \end{aligned} \tag{4.28}$$

$$\Rightarrow M = \frac{\pi}{8}\rho a\alpha\left(R_0{}^2 - r_0{}^2\right)\left(R_0 + 3r_0\right)\left[U_C U\right] \tag{4.29}$$

Figure 60 shows the section lift distribution around the annulus and it can be seen that the maximum section lift occurs at azimuth angles 0 or 2π and the minimum occurs at π where the wing would experience the maximum reverse flow. Section lift varies in a cosine wave manner and the total lift is given by the area under the plot. The magnitude of lift increases with both the blown-flow velocity and forward velocity. The blown-flow dominates even for the translational flight case as it is distributed around the annulus uniformly whereas the forward flow loses effectiveness at ±π/2. However, the limiting factor in any real vehicle will most likely be the pitching moment which is a product of the two velocities.

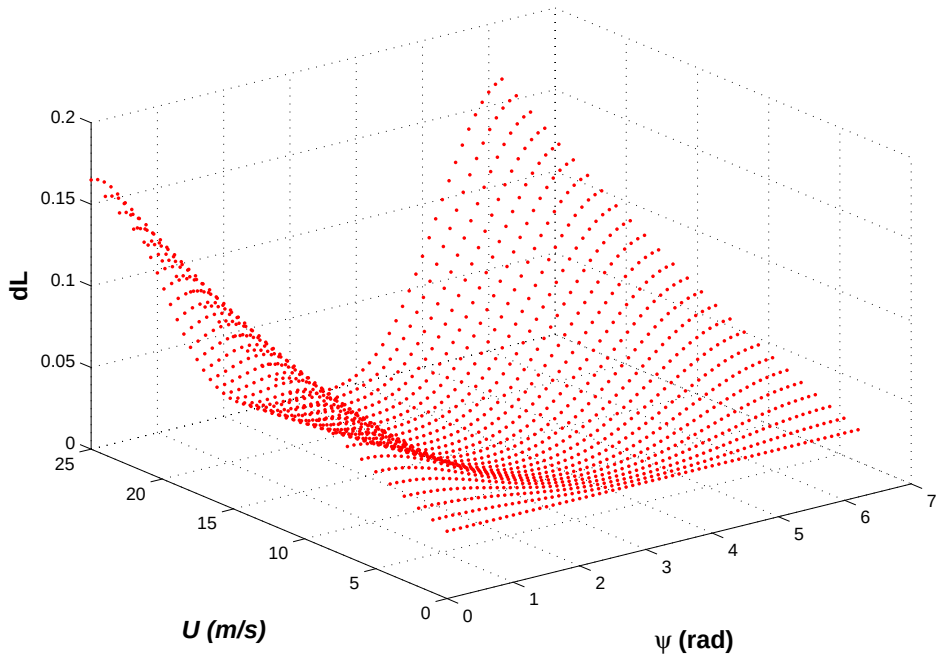

Figure 60: Section lift variation around the annulus at different translational velocities {Parameters: $U_C = 25m/s, C_L = 0.84, \quad \alpha = 6^0$, NACA-0024}.

A case study presented in Section 2.4 has shown that in translational flight mode circular blowing around the perimeter must be constrained to an azimuth angle of $\psi = 5/4\,\pi$ for optimum performance. Thus, herein, $\psi = 5/4\,\pi$ of perimeter blowing is assumed. This leaves the portion of annular wing with $5/8\,\pi \le \psi \le 11/8\,\pi$ in the reverse flow regime where the maximum reverse flow will be experienced at $\psi = \pi$. The reverse flow scenario is illustrated in Figure 61.

Investigating the reverse flow case where the annular wing is immersed into the flow with trailing edge facing the flow as shown in Figure 62. The pressure profiles for different angles of attack are given in Figure 63. From the figure it can be seen that the maximum suction pressure, at x/c=0.2, is approximately the same for lower and upper surfaces and a change in the angle of attack has minimal effect at this location. The maximum pressure difference is experienced at the trailing edge facing the flow and 50% of the chord length downstream remains unaffected.

Figure 64 shows the lift, drag and pitching moment experienced by the arc wing in reverse flow. Approximate linear relationships from the experimental data can be derived as:

$$\left.\begin{aligned} C_{L\leftarrow} &= 0.0046\alpha \\ C_{D\leftarrow} &= -0.001\alpha + 0.0793 \\ C_{M\leftarrow} &= 0.0085\alpha \end{aligned}\right\} \tag{4.30}$$

The wing generates minimal negative lift and relatively higher pitching moment. This will imply a nose down resultant moment.

$$\begin{aligned} M = \frac{1}{16}\rho\left[\left(R_0^2 - r_0^2\right)\left(R_0 + 3r_0\right)\right]... \\ ...\left\{2\times\int_0^{\frac{5}{8}\pi}\left[U_C^2\cos\psi + 2U_C U\cos\psi + U_C^2\cos^3\psi\right]C_L d\psi\right\} \end{aligned} \tag{4.31}$$

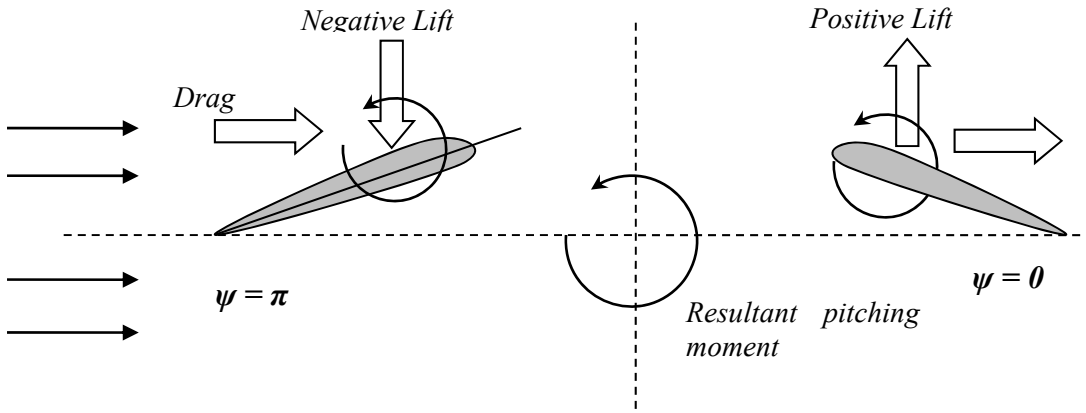

Figure 61: Reverse flow scenario at $\psi = \pi$.

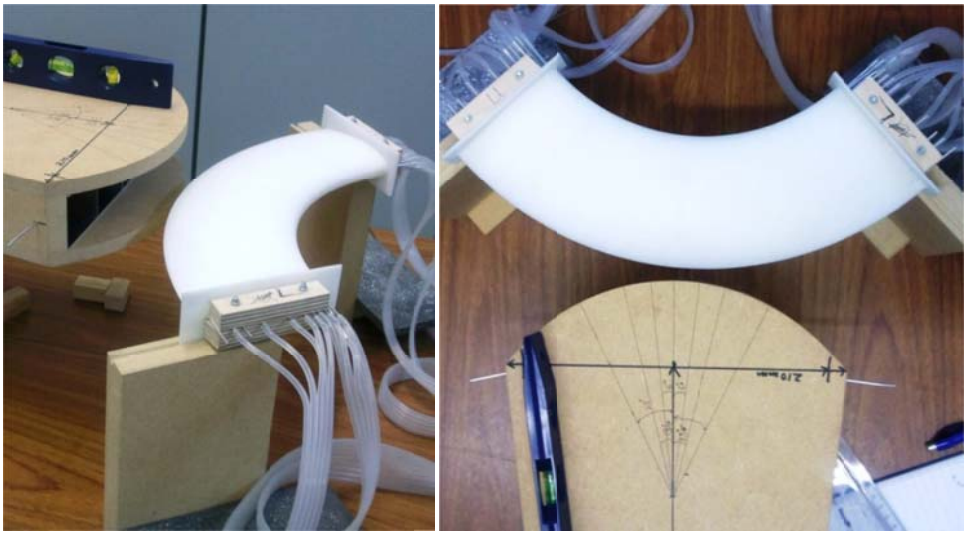

Figure 62: Depiction of experimental setup for the reverse flow testing.

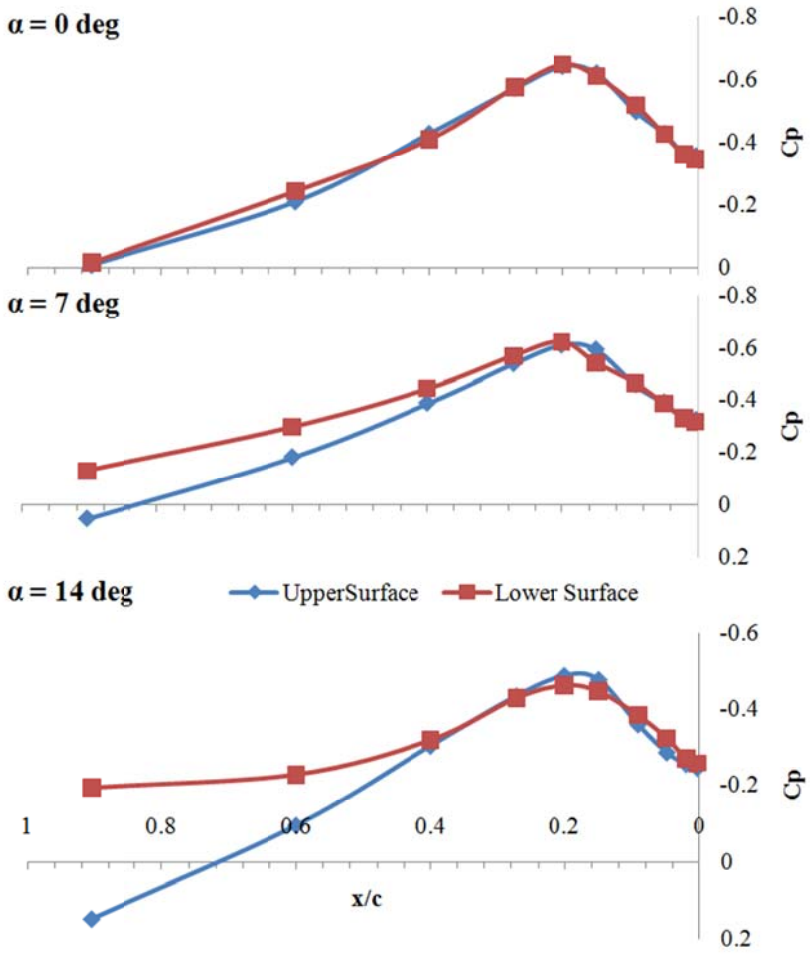

Figure 63: Pressure distribution around the aerofoil surface in reverse flow at $\psi = \pi$.

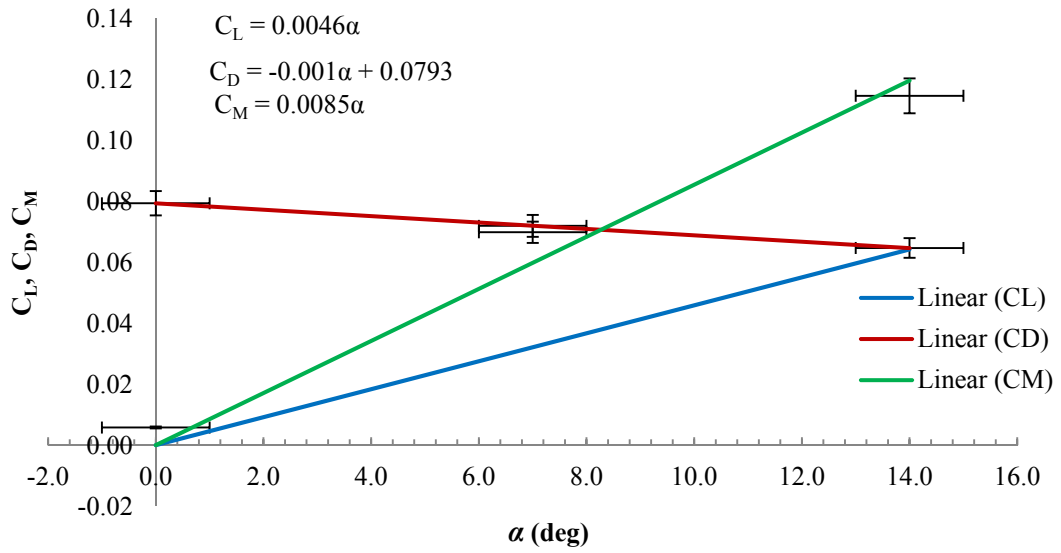

Figure 64: 2-D aerodynamic characteristics of arc-wing in reverse flow at $\psi = \pi$.

y/c	x/c	s/c	beta	Cp	Cp	Cp
-0.0211	0.003	0.030	162	-0.35876	-0.32687	-0.24581
-0.04852	0.021	0.038	139	-0.36407	-0.33484	-0.25777
-0.07068	0.050	0.044	122	-0.42918	-0.3933	-0.28833
-0.09072	0.092	0.057	110	-0.4996	-0.46107	-0.36141
-0.10654	0.150	0.055	101	-0.62184	-0.5966	-0.47834
-0.11498	0.200	0.062	97	-0.64443	-0.61387	-0.48897
-0.1192	0.272	0.084	91	-0.57401	-0.54212	-0.43582
-0.11603	0.400	0.154	86	-0.42918	-0.39065	-0.30561
-0.09177	0.600	0.203	81	-0.21127	-0.18336	-0.097
-0.04958	0.815	0.184	77	-0.0093	0.052883	0.147489
-0.02743	0.905	0.147	76	-0.34813	-0.31757	-0.25777
0.021097	0.003	0.030	198	-0.36274	-0.33218	-0.27239
0.048523	0.021	0.038	221	-0.42652	-0.38799	-0.32554
0.090717	0.092	0.057	250	-0.61254	-0.54478	-0.44778
0.10654	0.150	0.055	259	-0.64975	-0.6245	-0.46373
0.114979	0.200	0.062	263	-0.578	-0.57135	-0.43051
0.119198	0.272	0.084	269	-0.41058	-0.44512	-0.32022
0.116034	0.400	0.154	274	-0.24581	-0.29896	-0.22987
0.091772	0.600	0.203	279	-0.0186	-0.13022	-0.19532
0.049578	0.815	0.184	283	-0.35876	-0.32687	-0.24581
0.027426	0.905	0.147	284	-0.36407	-0.33484	-0.25777
			C_L	-0.008	0.040	0.060
			C_D	0.079	0.072	0.065
			C_M	0.006	0.070	0.115
			α	0	7	14

Table 2: Experimental data for arc-wing in reverse flow.

4.8 Practicality Test

The annular expansion causes significant turbulence and flow separation due to increasing cross-sectional area of the radial-flow generator. The outlet annular cross-sectional area should be less than or equal to the inlet to avoid a fluctuation across the longitudinal axis of the blower. This is because in a typical centrifugal compressor the inlet to outlet ratio is in the range of 0.7 to 3.8 [56], leaving a minimal blower-slot-height and question - whether a wing-section can be fully immersed in the flow with a centrifugal compressor? As shown in Section 4.2 that for optimal aerodynamic performance of a blown-wing the slot height should be around 60% of chord length. And the performance is also optimised by maximising the ratio of wing lift and the jet power.

To establish whether a centrifugal compressor within the annular-wingform could give optimal results, a micro-compressor as in Figure 65 is considered. Setting the slot height of the compressor to 60% chord length, (0.6c=2.4), gives 4mm of chord length. These values contradict those calculated by evaluating the optimum annular-wing performance which states that the chord length should be 67% of the inner radius of the annulus. If diffuser outlet diameter is taken to be the inner diameter, then the chord length is 20mm. Thus the compressor-annular-wing lift system may not be the optimal solution as yet. However, better performance may be achieved by utilising complete upper surface blowing and the Coanda effect.

From engineering perspective, ultimately, the annular wing will achieve maximum lift/thrust by diverting the entire flow, generated by the radial blower, vertically downwards for hover flight mode - behaving more like a thrust deflector. Such a system, with upper surface blowing only, is likely to suffer large losses from skin friction which, nevertheless, is approximately halved compared to a fully wetted wing. A modification to the annular wing is proposed and described in Figure 66: depicting the annular-wing with flaps attached to the trailing edge that may achieve 90^{o} flow deflection. The diversion duct coordinates may be adapted from [57] that are used for standardised centrifugal compressors thus promoting uniform and symmetric outlet flow. To further ensure smooth flow outlet cross-section area has been kept the same as the inlet.

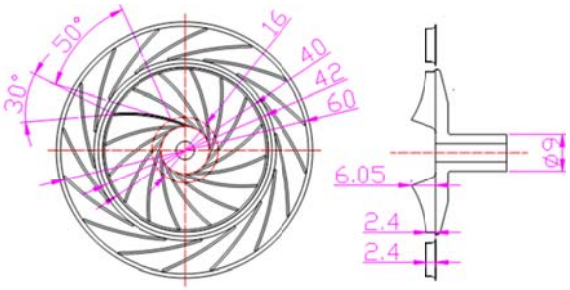

Impeller	Inlet diameter [mm]	20
	Outlet meter [mm]	40
	Number of blades	16
	Blade thickness [mm]	0.5
	Inlet blade height [mm]	6.05
	Outlet blade height [mm]	2.4
	Inlet blade angle [deg]	50
	Outlet blade angle [deg]	30
	Outlet flow angle [deg]	76
Diffuser	Inlet diameter [mm]	42
	Outlet diameter [mm]	60
	Number of blades	16
	Blade thickness [mm]	0.5
	Blade height [mm]	2.4

Figure 65: Typical micro centrifugal compressor drawings and data sheet [58].

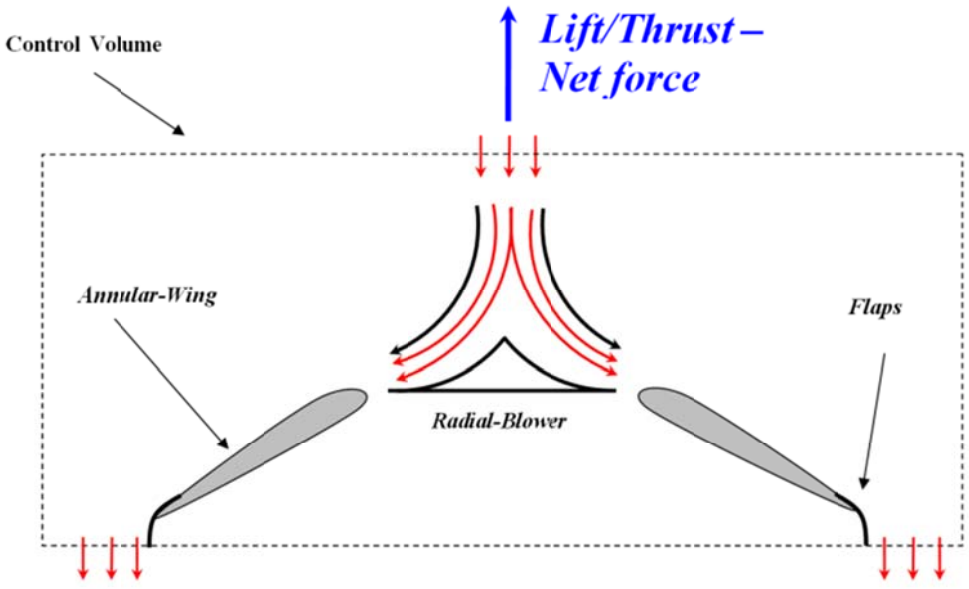

Figure 66: Proposed modification – annular-wing with flaps and pure upper surface blowing (drawing not to scale)

Chapter 5. Lift Generated by Annular-Wing with Upper Surface Blowing

It is an observed fact that when a stream or sheet of fluid issues through a suitable orifice, into another fluid, it will carry along with it a portion of the surrounding fluid, if its velocity is sufficient.

{*Henri Coanda*, [59]}

5.1 Introduction

Initially, the wing under consideration was of circular/annular form and the radial flow, from a centrifugal flow generator, was assumed to be symmetrical over the upper and lower surfaces of the wing. However, it has been shown that symmetrical blowing for optimal wing size is nearly impossible with the current centrifugal compressors available. This suggested a shift/modification in the blowing layout for realistic size and compatibility: that is to have pure upper surface blowing with Coanda effect, for at least hover flight case. This Section takes the quest further and evaluates the efficiency of the proposed annular-Coanda-Wing approach. A

preliminary prediction method has been derived based on standard aerodynamic principles and complemented by experimental testing.

5.2 Characteristics of a Coanda Wing

This section aims at producing a concise guide to predict/evaluate velocity profile, flow decay/spread rate and pressure distribution for a Coanda surface/wing. The following sub-sections provide a summary of the available information, both theoretical and experimental, on the aerodynamic properties pertinent to a Coanda Wing.

Typically, for 2-D USB the wall-jet is considered to comprise two parts: an inner flow adjacent to the wall having a highly non-linear velocity profile characteristics of a turbulent wall flow (boundary layer), and an outer flow having a velocity profile more typical of a free turbulent plane jet [60, 61]. The dividing line between the layers is at the point of maximum flow velocity. This theory has been validated by limited experimental work [62, 63] for engineering purposes but there are limitations to this theory imposed by the range of Reynolds number covered by the experiments. Furthermore, it has been shown [63] that the multilayer model is not theoretically justified, because the shear stress is non-trivial at the point of maximum velocity.

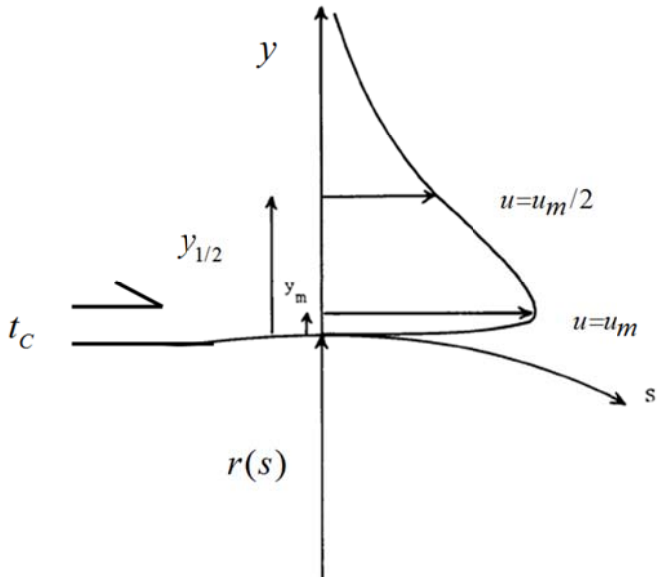

Figure 67: Schematic structure of a typical wall jet flow with static ambient conditions.

The primary parameters that describe the flow are shown in Figure 67. The jet emerges from a point source into a fluid at rest and spreads, increasing its width and decreasing its velocity due to turbulent diffusion in the jet and friction at the wall. At a distance *s* downstream of the jet exit the longitudinal velocity profile *u* can be expressed as

$$u = u_m(s) f(y/t) \tag{5.1}$$

$$\frac{u}{u_m} = \sec h^2 \left[\frac{k(y - y_m)}{y_{m/2} - y_m} \right], y > y_m \tag{5.2}$$

$$\frac{u}{u_m} = \left[2\left(\frac{y}{y_m} \right)^{\frac{1}{n}} - \left(\frac{y}{y_m} \right)^{\frac{2}{n}} \right], y < y_m \tag{5.3}$$

where u_m is the maximum velocity, occurring at $y = y_m$, and $y_{m/2}$ is the half width of the jet and *k* is a constant and is defined as $k = \tanh^{-1}\left(\frac{1}{\sqrt{2}} \right) = 0.8814$.

The evaluation of y/y_m experimentally and numerically yield a band of values $0.14 < y/y_m < 0.16$ corresponding to $7 > n > 6$ [60] for a Reynolds number in the range of $10^4 < R_e < 10^5$.

Flow decay rate over a circular cylinder is a function of surface length $r_s\delta_f$ and the turning angle. A best fit of previous experimental data [10] provides:

$$\frac{u_m}{U_{\max}} = \left[(12.7 - 2.28\delta_f) \frac{t_C}{r_s \delta_f} \right]^{1/2} \tag{5.4}$$

Similarly jet expansion is:

$$\frac{y_{m/2}}{r_s} = \frac{0.11\delta_f}{1 - 0.165\delta_f} \tag{5.5}$$

For $0.5 < \delta_f < 3$ where δ_f is in radians. This shows that the surface velocity profile is proportional to surface length and flow deflection. The wall-jet deflection is a function of surface deflection with flow turning angle [64] which in terms of the forces generated can be defined as

$$\delta_f = \tan^{-1}\left(\frac{F_N}{-F_A}\right) \tag{5.6}$$

Where F_A and F_N are the axial and normal forces acting on the convex surface. Subsequently, the turning efficiency η_t is defined by

$$\eta_t = \frac{\sqrt{F_N{}^2 + F_A{}^2}}{T} \tag{5.7}$$

Where T is horizontal thrust from the source and η_t is 1 for perfect (theoretical) efficiency and 0 for complete blockage. A best fit of previous experimental data [64] defines the flow turning efficiency as

$$\eta_t = e^{-0.0022\delta_f} \tag{5.8}$$

It has been established that the 2-D longitudinal velocity profile of a plane wall-jet is similar to a fully attached and developed jet flowing round a circular cylinder [65], however, the corresponding decay and jet width spread rate may differ.

Figure 68 depicts the 3-D flow profile of diffusing wall jet along an adjacent surface; the figure enables to understand the qualitative behaviour of wall-jet. From the colour contoured figure it can be seen that the flow spreads like arrays of light; the red straight line being the jet half width z/t where the maximum flow lies.

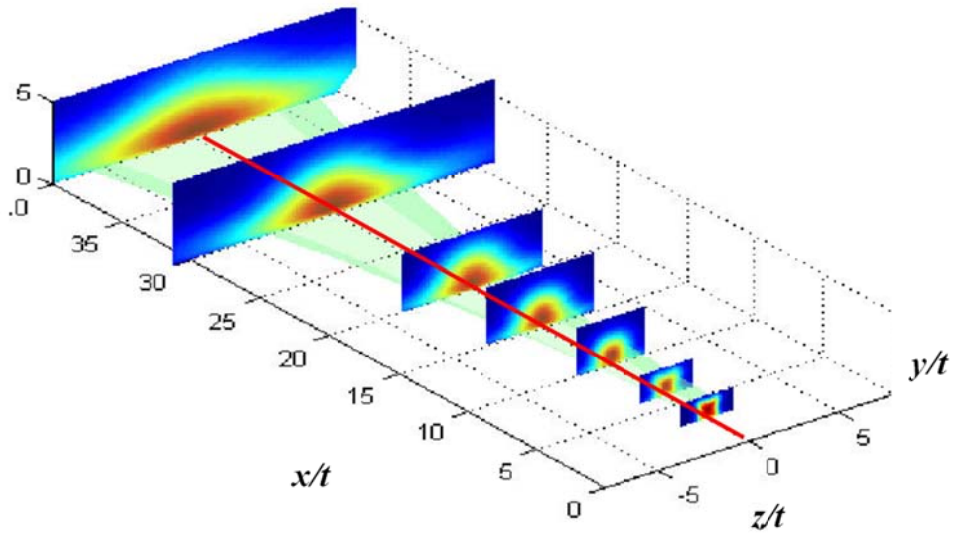

Figure 68: Typical 3-D wall jet diffusion structure: with colour contours increasing intensity from blue to red inwards at each local point (the colours are local to each plane and therefore are for qualitative purposes only) [66].

In Figure 69 data from past V/STOL aircraft using upper surface blowing is plotted and it shows that lift or normal force is maximised by turning the flow 90 degrees. However, best thrust efficiency is obtained by minimum possible turning angle.

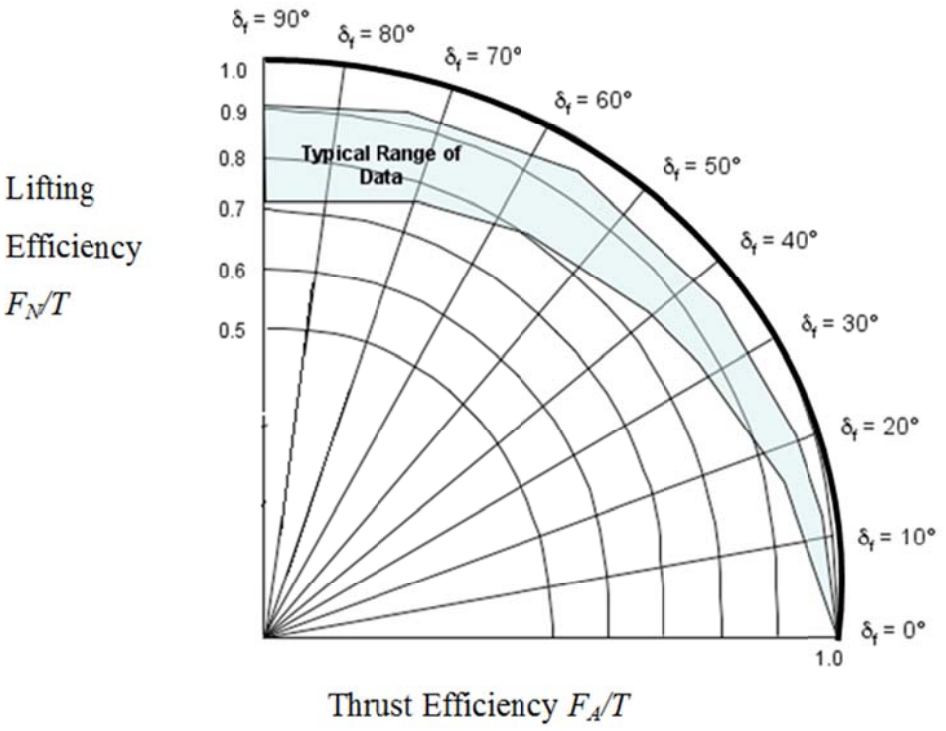

Figure 69: Ideal and empirical static flow turning characteristics {derived from [67]}

5.3 Lift Generated by Annular-Wing

In order to derive a low fidelity mathematical model to predict the forces acting on the annular-wing the following assumptions are made.

- Flow is inviscid and incompressible
- Shear stress distribution over the body surface is negligible and that the forces generated are purely due to pressure difference across the flow depth (flow attached to the surface)
- The flow from the source does not disperse into the atmosphere and hence it is a closed system within which the continuity holds
- The entrainment flow [68] at the assumed zero flow line is negligible[d]

Now, take a free-jet issuing from an annular blower meeting an adjacent convex surface (the annular wing) and following the surface path s with 2-D longitudinal flow profile as described in Figure 67 and defined by Equations 5.1 and 5.2. The jet bounded by the surface is referred to as wall-jet. If the free-jet has a parabolic velocity profile with maximum velocity U_{max} at the centreline $t_C/2$ and upon meeting the convex surface it will follow the same line along s, e.g. at a distance $t_C/2$ from the surface anywhere along s, as shown in Figure 70.

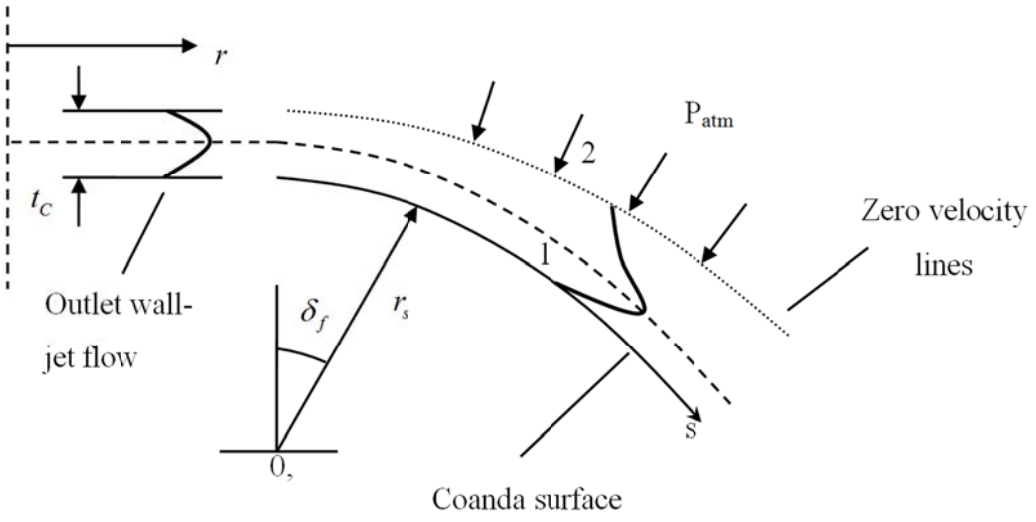

Figure 70: 2-D schematic layout of assumed flow characteristics along a convex surface.

[d] The entrainment flow occurs due to shear stress across the layers of fluid flow; this phenomenon is described in detail in Ref. [75].

As this flow follows the path s it starts to turn at an angle δ_f, and experiences nonuniform circular motion. Therefore, the flow velocity may be defined in terms of the turn rate $d\delta_f/dt$ as

$$U_s = \frac{d\delta_f}{dt} r_s. \tag{5.9}$$

Applying Bernoulli's principle at locations 1, inside the wall-jet, and 2, outside the zero velocity line, as shown gives:

$$P_1 + \frac{1}{2}\rho U_s^2 = P_{atm} \tag{5.10}$$

This can be re-arranged to give the pressure difference ΔP_s at the surface

$$\Delta P_s = P_1 - P_{atm} = -\frac{1}{2}\rho u^2 \tag{5.11}$$

Substituting the turn rate and differentiating with respect to r_s, the change in pressure at a distance away from the surface is:

$$\Rightarrow \frac{dP_s}{dr_s} = -\rho\left(\frac{d\delta_f}{dt}\right)^2 r_s \tag{5.12}$$

Total local pressure may be evaluated by integrating across the wall-jet depth as

$$\Delta P_s = -\rho\left(\frac{d\delta_f}{dt}\right)^2 \int_{r_s}^{r_s+1.75y_{m/2}} r_s dr_s \tag{5.13}$$

where the wall-jet depth at a location is taken to be $1.75y_{m/2}$ and $y_{m/2}$ is defined by Equation 5.5.

$$\Rightarrow \Delta P_s = -\frac{1}{2}\rho\left(\frac{d\delta_f}{dt}\right)^2 \left\{\left[r_s + 1.75y_{m/2}\right]^2 - r_s^2\right\} \tag{5.14}$$

Substituting the annular reduction factor (as defined in Section 4.3) into local flow velocity expression:

$$u = \frac{d\delta_f}{dt} r_s = \frac{r_0}{r} U_C \tag{5.15}$$

$$\Rightarrow \frac{d\delta_f}{dt} = \frac{r_0}{r.r_s} U_C \tag{5.16}$$

and subsequently the pressure difference expression may be written as

$$\Delta P_s = -\frac{1}{2}\rho\left(\frac{r_0}{r.r_s}U_C\right)^2 \left\{\left[r_s + 1.75 y_{m/2}\right]^2 - r_s^2\right\} \tag{5.17}$$

$$\Delta P_s = -\frac{1}{2}\rho U_C^2 \left(\frac{r_0}{r}\right)^2 \left\{\left[1 + 1.75\frac{y_{m/2}}{r_s}\right]^2 - 1\right\} \tag{5.18}$$

Further simplifying into a non-dimensional quantity C_P as

$$C_P = \frac{\Delta P_s}{\frac{1}{2}\rho U_C^2} = -\left(\frac{r_0}{r}\right)^2 \left\{\left[1 + 1.75\frac{y_{m/2}}{r_s}\right]^2 - 1\right\} \tag{5.19}$$

This relationship shows that the local pressure at the upper surface of the annular wing depends on the dynamic pressure, convex surface radius and radial distance from the blower centreline. A larger curvature radius means larger surface length and hence higher flow rate, implicitly giving higher local pressures. Furthermore, dynamic pressure loss away from the blower is inevitable due to the increasing cross-sectional area.

5.3.1 Methodology and Solution

In order to solve Equation 5.23 it is required to evaluate r_s and $y_{m/2}$ respectively. Let the convex surface path s be the aerofoil (or wing-section) thickness distribution along the chord line at distance *x* from the leading edge, defined by Equation 4.9 and 4.10.

Now let r_s be the distance from a location (x', y') on the surface to the origin defined as $x' = 0.25,\ y' = 0$ where $x' \geq 0.25$

$$\Rightarrow r_s = \sqrt{|x' - 0.25|^2 + y'^2} \tag{5.20}$$

$$\Rightarrow \delta_f = \tan^{-1}\left(\frac{|x' - 0.25|}{y'}\right) \tag{5.21}$$

Substituting the above into Equation 5.5, the wall-jet depth can be evaluated. Finally, the radial distance away from the blower is given by

$$r = r_o + x' \tag{5.22}$$

To calculate the forces acting on the annular wing, the blown surface was divided into discrete panels, as shown in Figure 71. The Pressure forces were resolved to obtain lift and drag, given by:

$$L = F_N = \sum_{i=1}^{i=n} \left(s_i P_i \cos\theta_i\right) \text{ \{per unit span\}} \tag{5.23}$$

$$D = F_A = \sum_{i=1}^{i=n} \left(s_i P_i \sin\theta_i\right) \text{ \{per unit span\}} \tag{5.24}$$

where θ_i is the angle between the ith panel and the horizontal and s_i is the surface panel length.

Thrust generated by the radial-flow generator, is then:

$$T = 2\pi r_0 \rho t_C U_C{}^2 \tag{5.25}$$

where U_C is the free-jet velocity profile.

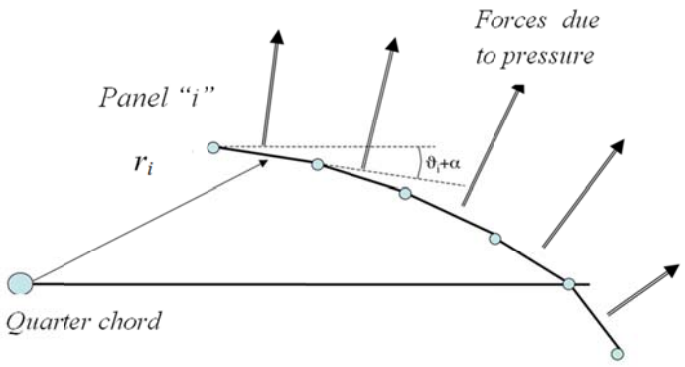

Figure 71: Discretised surface panels to calculate forces

5.4 Experimental Setup

The experimental setup was similar to those discussed in Chapter 3, however, a new blower was incorporated in to the rig to facilitate upper surface blowing. The geometry of this blower is shown in Figure 72; this particular geometry was designed to generate symmetrical flow at the outlet. In order to avoid flow expansion and reduce turbulence inlet-to-outlet cross-section area ratio was set to ~1, leaving the outlet slot height to only 4 mm.

NACA-0024 aerofoil section was chosen, for which the surface-panel geometry is defined in Figure 73. The local dynamic pressure at the panels were measured via hot-wire anemometer and integrated to calculate the forces (see Table 3).

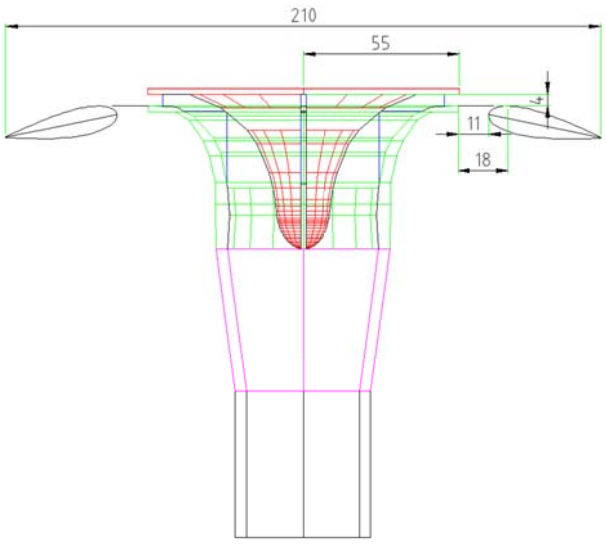

Figure 72: Geometry of blower and annular wing {all units in mm}.

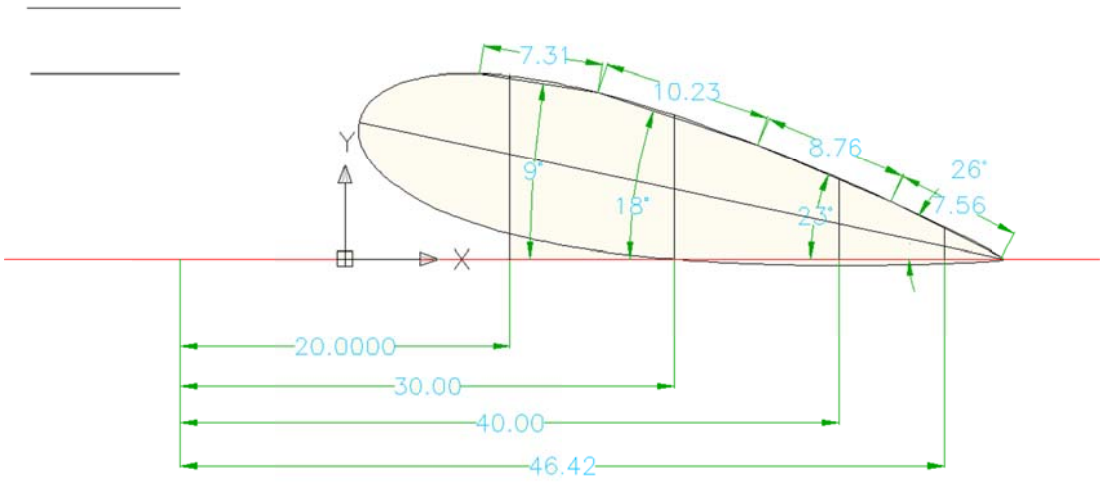

Figure 73: Surface-panel geometry of the wing section NACA-0024 { α=12^0 , $t_{max} = 9.6,$ all units in mm}.

5.5 Results & Analysis

The flow profile of the free-jet (without the wing attached) along the radial axis is shown in Figure 74. The free-jet settles away from the blower and at $r' = 1.16 / 1.45$ forms a parabolic shape which is generic for an axisymmetric free-jet. The turbulence intensity is a mirror image of velocity plots as displayed in Figure 75; the maximum occurs near the walls and minimum slightly above the central axis at $y / t_C = 0.4$.

Figure 76 shows the developed velocity profile at the upper surface of the wing (downstream at $r' = 1.6$). The figure establishes that the flow developed at the upper surface is purely a Coanda wall-jet and matches the theoretical model defined by Equations 5.2 and 5.3. Figure 77 shows the flow development over the surface of NACA-0024 wing-section - the jet broadens and decelerates along the surface due to jet turbulent diffusion and wall friction. The wall-jet velocity profiles at all location at the surface mimic the shape of the theoretical non-dimensional profile. Furthermore, the spread of jet is underestimated, theoretically, as compared to the experimentally measured (see Figure 78). This is believed to be primarily due to the theory not taking into account the shear stress present within the flow layers.

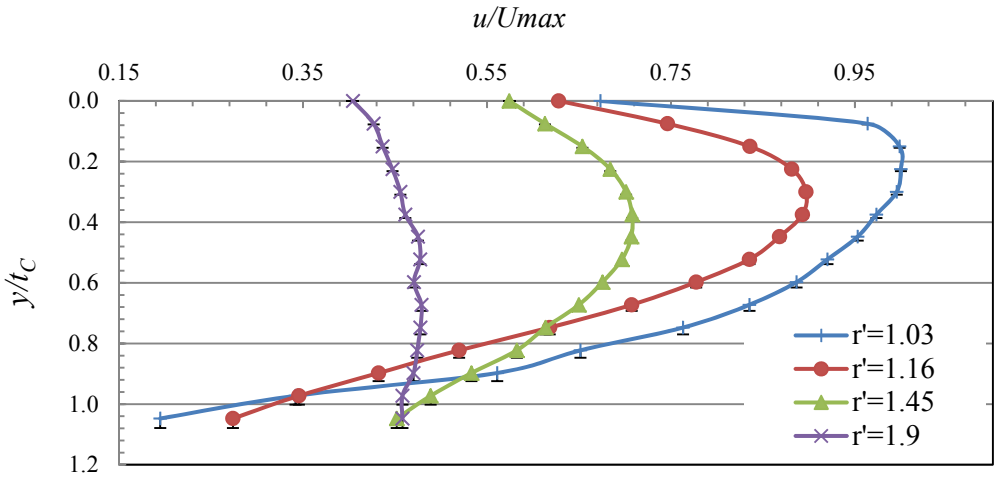

Figure 74: Free-jet velocity profile at distances away from the outlet determined experimentally using hot-wire anemometer {Parameters: $U_{\max}$ = 48m/s , t_C=4mm , P_{atm}=102.6kPa , T_{atm}=25.6^{o}C }.

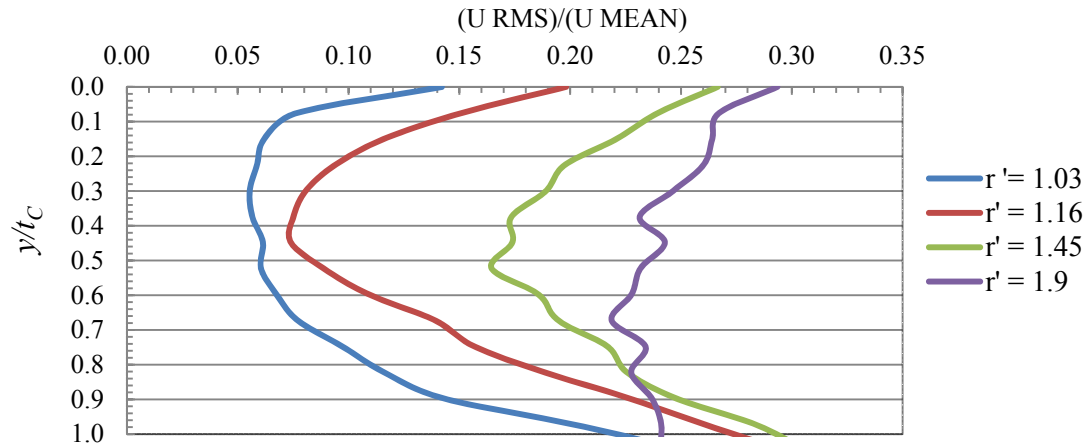

Figure 75: Turbulence intensity from blower.

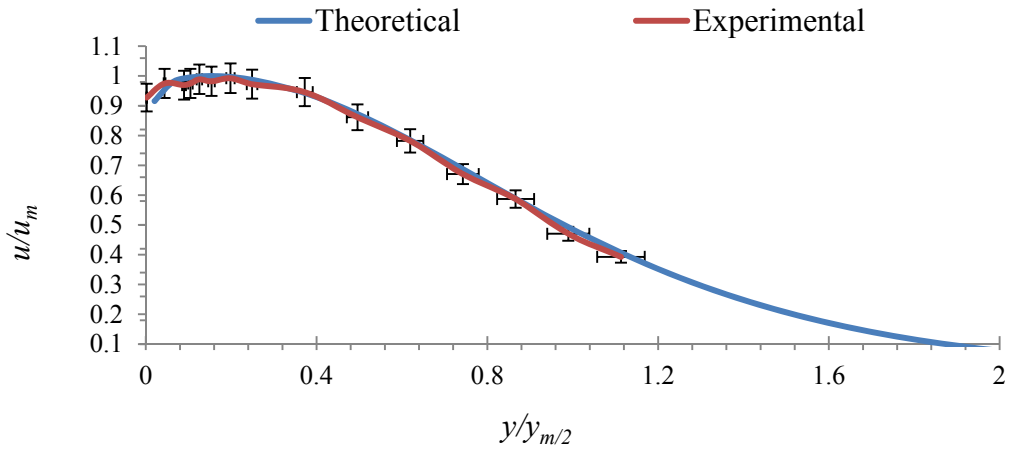

Figure 76: Non-dimensional wall-jet velocity profile {Parameters: u_m = 28m/s , r' = 1.6 }

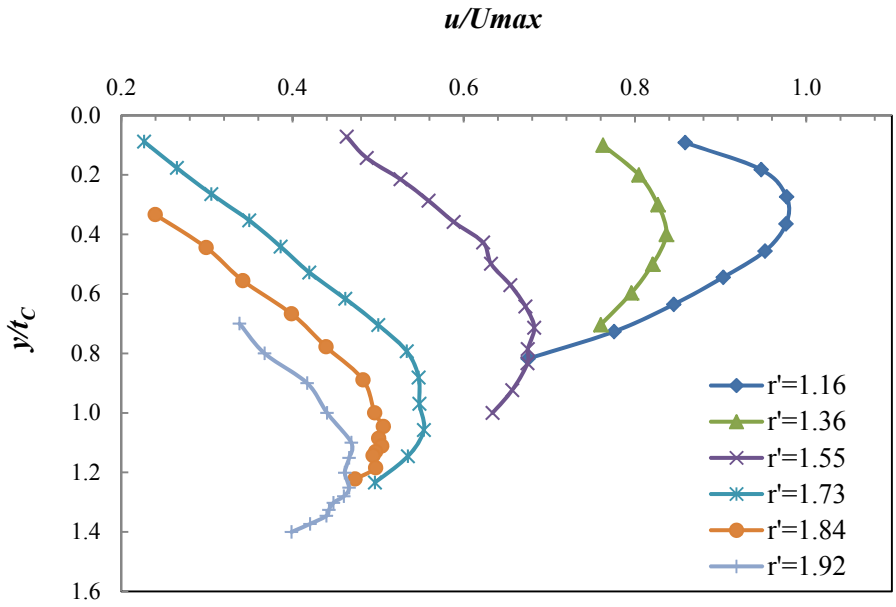

Figure 77: Flow profile of wall-jet at different locations along the wing upper surface, determined experimentally {Parameters: $U_{\max} = 48\text{m/s}$, $t_c = 4\text{mm}$, $P_{atm}=102.6kPa$, $T_{atm}=25.6^{o}C$ }.

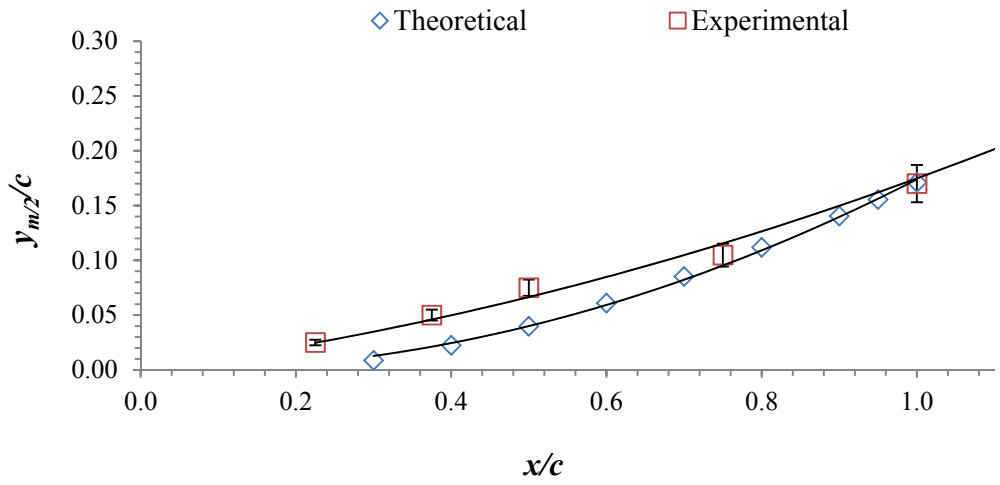

Figure 78: Spread of maximum velocity, jet-width versus chord length.

The experimental data and theoretical calculations for the pressure coefficient and lift force are presented in Table 3 and Table 4. The local pressure coefficient along the surface of the wing obtained theoretically and experimentally is plotted in Figure 79. An important point to be noted here is that the theoretical plot from the leading edge up to the quarter chord ($0.25c$) is positive for the pressure coefficient distribution. This is because the theoretical model defined the surface radius r_s with

origin at quarter chord and the flow turning angle $\delta_f = 0$ with the vertical. Hence, from the leading edge to the quarter chord inputs a negative angle into the set of equations; therefore the theoretical model becomes valid only beyond quarter chord. Furthermore, beyond quarter chord the theoretical pressure values are always higher than the experimental values. This is probably caused by the assumption made in the model that the flow is conserved within the assumed control volume defined in Figure 70.

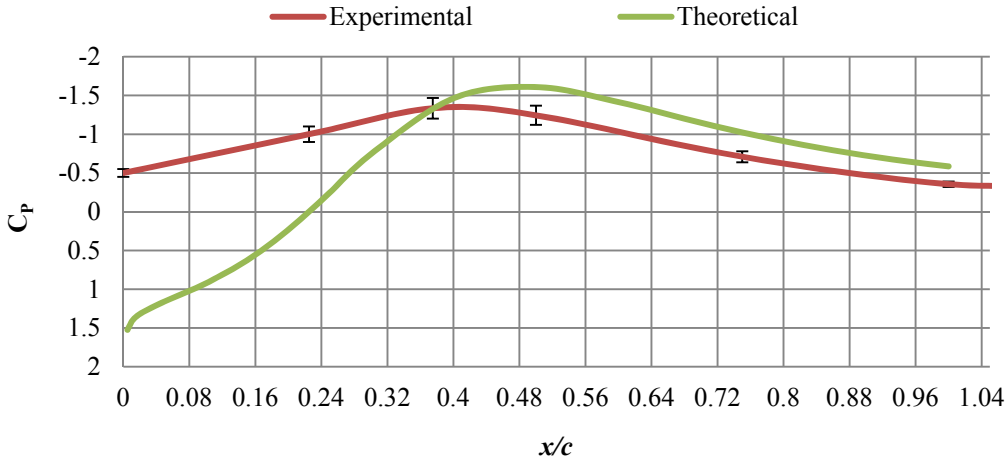

Figure 79: Pressure coefficient versus chord length acquired experimentally and theoretically using panel code method.

From the pressure plots the lift force is evaluated. The lift to thrust ratio, or lifting efficiency, is theoretically $\eta_L = 0.45$ and experimentally $\eta_L = 0.36$. The relatively values suggest that the flow needs further turning to increase the lifting efficiency. This is also suggested by Figure 77 where the wall-jet flow at trailing edge is deflected at 26 degrees and yet travelling at $\sim 0.48U_{\max}$ (Figure 77). In other words, the flow deflected just by 26 degrees still possesses significant energy and if turned by 90 degrees would substantially enhance lifting efficiency. Furthermore, the deflection of 26 degrees at the trailing suggests $\sim \eta_L = 0.42$ by referring to Figure 69. Further losses in lifting efficiency are anticipated to be due to annular flow expansion.

The flow needs further turning for better lifting efficiency, becomes clearer from Figure 80: comparing the flow decay rate along the radial axis for free-jet (without the wing attached) and wall-jet. For the wall-jet case, maximum flow velocity

increases at the leading edge $(r' = 1.2)$. This difference is maintained until the final panel $(r' = 1.55)$. Flow velocity reduces upto the trailing edge, and it eventually coincides with the free-jet. Thus, maximum flow velocity at the upper surface must always be higher than the free-jet for higher efficiency.

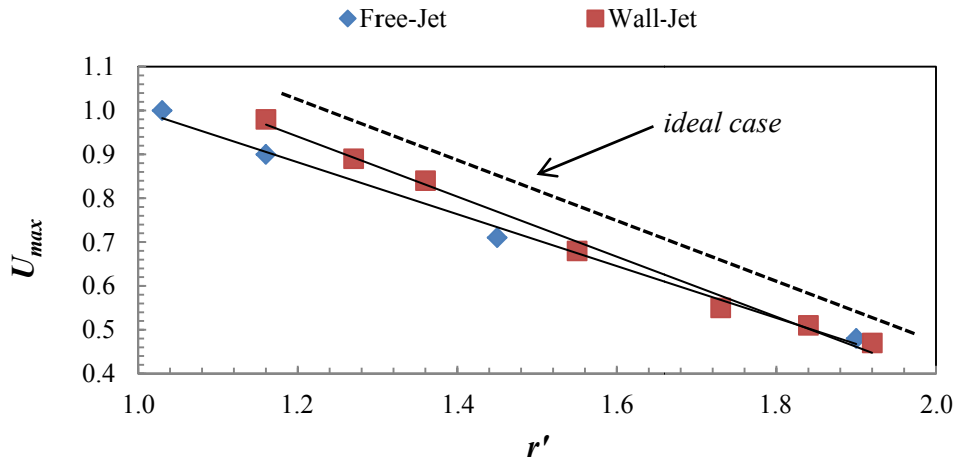

Figure 80: Decay rate comparison for free-jet and wall-jet along the wing surface.

5.6 Lift/Thrust generated with 90 degree flow deflection

To fully deflect the flow, a curved flap was attached to the trailing edge of the wing (Figure 81); flap size was set so that $t_C << r_f$. A multi-pitot-rake was used to measure the flow velocity profile at the trailing edge as shown in Figure 82.

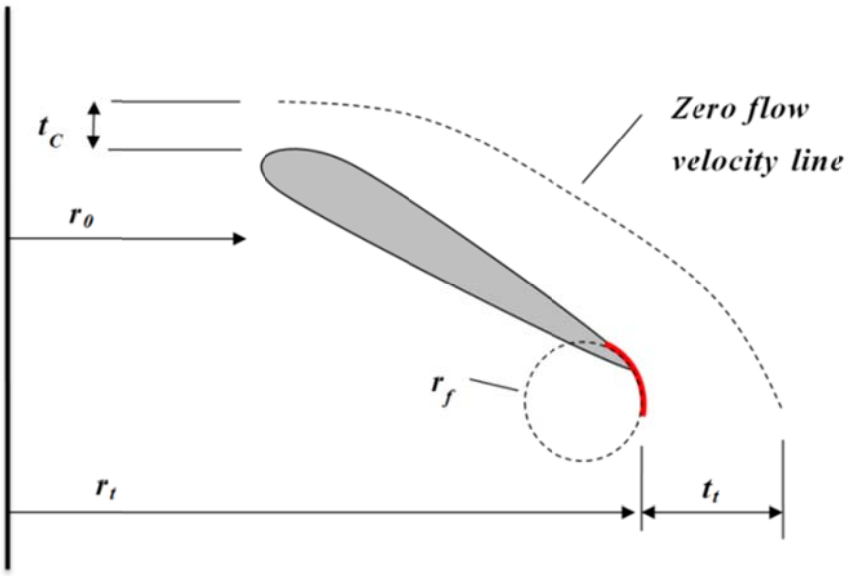

Figure 81: Schematic layout of annular-wing with a flap to achieve 90 degree flow deflection.

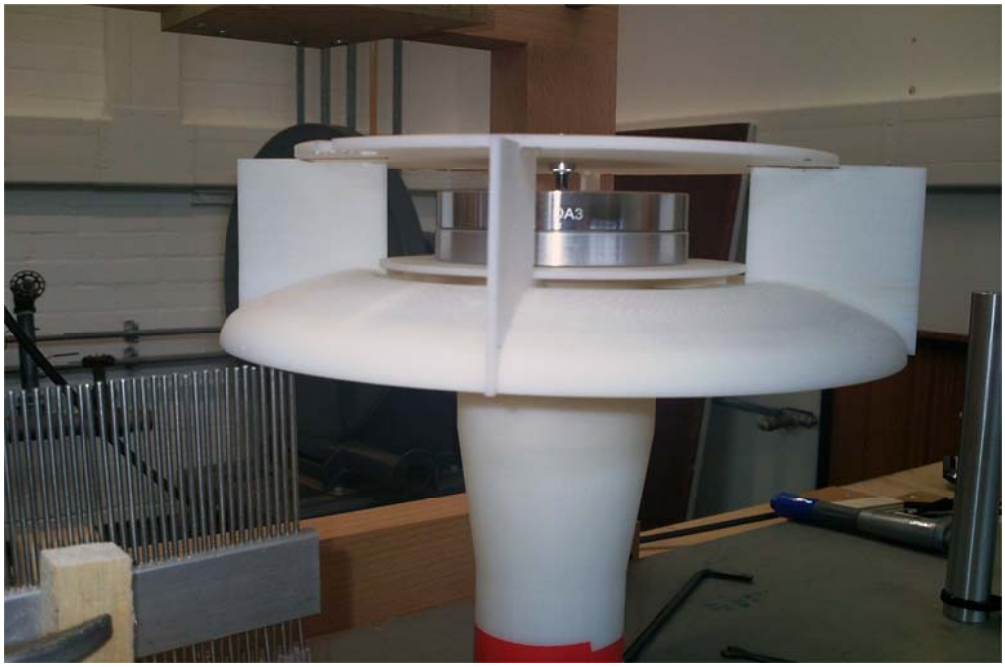

Figure 82: A close-up of Annular-wing with flap, load-cell, pitot-rake and radial-flow-generator configuration.

Assume that the flow is fully deflected at trailing edge just before leaving the wing. Apply conservation of momentum across the inlet (leading edge) and outlet (trailing edge), $F = \frac{d(mu)}{dt}$, to drive the undeflected thrust T and normal force F_N:

$$T = \rho(2\pi r_0)\int_0^{t_C} u^2 dy \tag{5.26}$$

$$\Rightarrow T = \rho(2\pi r_0)t_C U_C^2 \tag{5.27}$$

$$F_N = \rho 2\pi \int_{r_t}^{(r_t+t_t)} u^2 r dr \tag{5.28}$$

$$\Rightarrow F_N = \rho\pi\left[(r_t+t_t)^2 - r_t^2\right]u^2 \tag{5.29}$$

where t_t is the depth of flow at the trailing edge just before leaving the wing. The flow depth at trailing edge is estimated by Eqn. 5.5, with the assumption $t_t = 1.75.y_{m/2}$ as

$$\frac{t_t}{r_s} = 1.75\left(\frac{y_{m/2}}{r_s}\right) = \frac{1.75\times 0.11\left(\delta_f = \pi/2\right)}{1-0.165\left(\delta_f = \pi/2\right)} \tag{5.30}$$

$$\Rightarrow t_t = 0.466 r_s \tag{5.31}$$

Now, apply continuity to determine the annular reduction factor f_a as

$$f_a = \frac{u}{U_C} = \frac{2r_0 t_C}{\left((r_t + t_t)^2 - r_t^2\right)} \tag{5.32}$$

$$\Rightarrow F_N = \rho\pi\left[(r_t + t_t)^2 - r_t^2\right]\left[f_a U_C\right]^2 \tag{5.33}$$

For the given parameters in Figure 83 the lift is evaluated via three different means including

Theoretical: $\frac{F_N}{T} = 0.69$

Experimental:

Load Cell $\frac{F_N}{T} = 0.62 \pm 0.01$

By impulse measurement using the pitot rake: $\frac{F_N}{T} = 0.61 \pm 0.05$

Figure 83 shows that the addition of the flap turned the flow vertically downwards. Mass flux was conserved, the flow velocity was reduced and jet was expanded. In comparison to the flow profile recorded for the wing without the flap (Figure 77) the maximum flow velocity has reduced from 0.48 to 0.32, and the flow depth increased to 4 from 3.4.

This shows that a flap can enhance wing lifting efficiency. However, efficiency of the annular-Coanda-wing is still less than a conventional rectangular blown wing, with lifting efficiency in the range of $0.7 < \eta_t < 0.9$, mainly because of annular flow reduction. This can be minimised by reducing the overall wing size or by reducing the geometrical parameters r_0 and r_t.

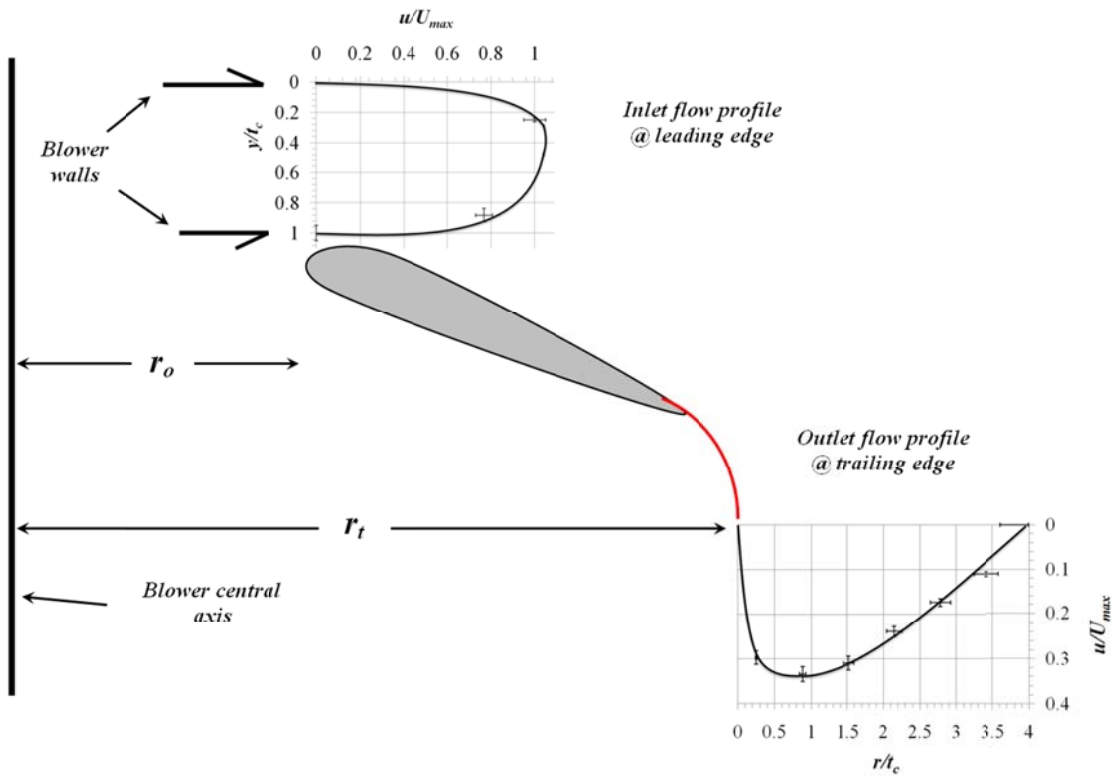

Figure 83: Measured inlet and outlet flow profiles imported onto the annular wing diagram at an enlarged scale {Parameters: $U_{\max}$=57m/s , $r_o = 55\text{mm}$, $r_t = 101\text{mm}$, $t_C = 4\text{mm}$, $T = 4.27N$, $P_{atm} = 102.3$ kPa , $T_{atm} = 25.4^{o}C$ }

5.7 Summary

- The proposal, pure upper surface blowing with Coanda effect, has been investigated theoretically and experimentally.
- A simple mathematical model to evaluate lift generated by the annular-Coanda-wing has been developed. There exists a difference between the theoretical and experimental results; this suggests that including the effect of non-ideal flow conditions in the model may be essential.
- Experimentation showed that 90 degree flow deflection can be achieved by an addition of a curved flap.
- The annular-Coanda-wing with flap achieves a lifting efficiency of approximately 61%, it can potentially be further enhanced by reducing the outer diameter of the blower.

r' = 1.16		r' = 1.36		r' = 1.55		r' = 1.73		r' = 1.84		r' = 1.92	
y	***u/u_m***	***y***	***u/u_m***	***y***	***u/u_m***	***y***	***u/u_m***	***y***	***u/u_m***	***y***	***u/u_m***
0.00	0.75	0.00	0.76	0.00	0.73	0.00	0.43	0.00	0.21	2.00	0.21
0.30	0.88	0.30	0.84	0.30	0.78	0.30	0.47	0.60	0.23	3.00	0.25
0.60	0.97	0.50	0.88	0.60	0.82	0.60	0.50	1.20	0.27	4.00	0.31
0.90	1.00	0.72	0.90	0.90	0.85	0.90	0.54	1.80	0.31	5.00	0.35
1.20	1.00	0.85	0.91	1.20	0.86	1.20	0.57	2.40	0.36	6.00	0.41
1.50	0.97	1.00	0.91	1.50	0.84	1.50	0.60	3.00	0.40	7.00	0.45
1.79	0.92	1.15	0.91	1.79	0.81	1.79	0.64	3.59	0.43	8.00	0.49
2.09	0.87	1.30	0.90	2.11	0.78	2.09	0.65	4.19	0.47	9.00	0.51
2.39	0.79	1.56	0.88			2.39	0.67	4.79	0.51	9.41	0.52
2.69	0.69	1.80	0.83			2.69	0.69	5.39	0.55	9.77	0.51
2.99	0.60	2.00	0.79			2.99	0.70	5.99	0.56	10.00	0.52
3.29	0.49	2.15	0.74			3.29	0.69	6.59	0.56	10.17	0.51
3.59	0.39	2.50	0.66			3.49	0.69	7.19	0.57	10.29	0.51
3.89	0.31					3.87	0.67	7.79	0.55	10.66	0.51
4.19	0.24					4.19	0.65	8.39	0.51	11.00	0.48
Average	0.79		0.84		0.81		0.61		0.42		0.39
C_P	-1		-1.335		-1.245		-0.709		-0.355		-0.35915
Lift Experimental	1.328 N										

Table 3: Experimental Data for upper surface blowing over NACA-0024 at 12 degrees angle of attack $\{T = 3.69N$, T_{atm}=26.5^{o}c , P_{atm}=101.4$kPa\}$

x/c	y/c	x''	y'	δ_f	$y_{m/2}/r_s$	$y_{m/2}$	r_s	$u_m/U_{\max}$	C_P
0.000	0.000	0.022	0.208	-0.866	-0.083	-0.027	0.321		1.699
0.005	0.020	0.031	0.226	-0.805	-0.078	-0.026	0.327		1.525
0.013	0.038	0.042	0.242	-0.747	-0.073	-0.024	0.330		1.384
0.025	0.052	0.057	0.254	-0.690	-0.068	-0.022	0.329		1.288
0.050	0.071	0.086	0.267	-0.596	-0.060	-0.019	0.322		1.158
0.075	0.084	0.113	0.274	-0.511	-0.052	-0.016	0.315		1.044
0.100	0.094	0.139	0.279	-0.429	-0.044	-0.013	0.306		0.924
0.150	0.107	0.191	0.281	-0.263	-0.028	-0.008	0.291		0.627
0.200	0.115	0.241	0.278	-0.090	-0.010	-0.003	0.280		0.232
0.250	**0.119**	**0.291**	**0.272**	**0.090**	**0.010**	**0.003**	**0.273**	**7.111**	**-0.245**
0.300	0.120	0.340	0.263	0.274	0.032	0.009	0.273	4.019	-0.743
0.400	0.116	0.437	0.238	0.622	0.076	0.022	0.293	2.487	-1.463
0.500	0.106	0.533	0.207	0.909	0.118	0.040	0.338	1.860	-1.609
0.600	0.091	0.628	0.172	1.126	0.152	0.061	0.400	1.500	-1.415
0.700	0.073	0.722	0.134	1.285	0.179	0.085	0.475	1.266	-1.147
0.800	0.052	0.815	0.093	1.403	0.201	0.112	0.557	1.103	-0.910
0.900	0.029	0.908	0.049	1.494	0.218	0.140	0.644	0.983	-0.724
0.950	0.016	0.954	0.026	1.533	0.226	0.155	0.689	0.934	-0.649
1.000	0.003	1.000	0.000	1.571	0.233	0.171	0.734	0.890	-0.585

Table 4: Theoretical calculations data for the model given in Equation 1.22 {Lift Theoretical $F_N = 1.662N$, $T = 3.69N$ }.

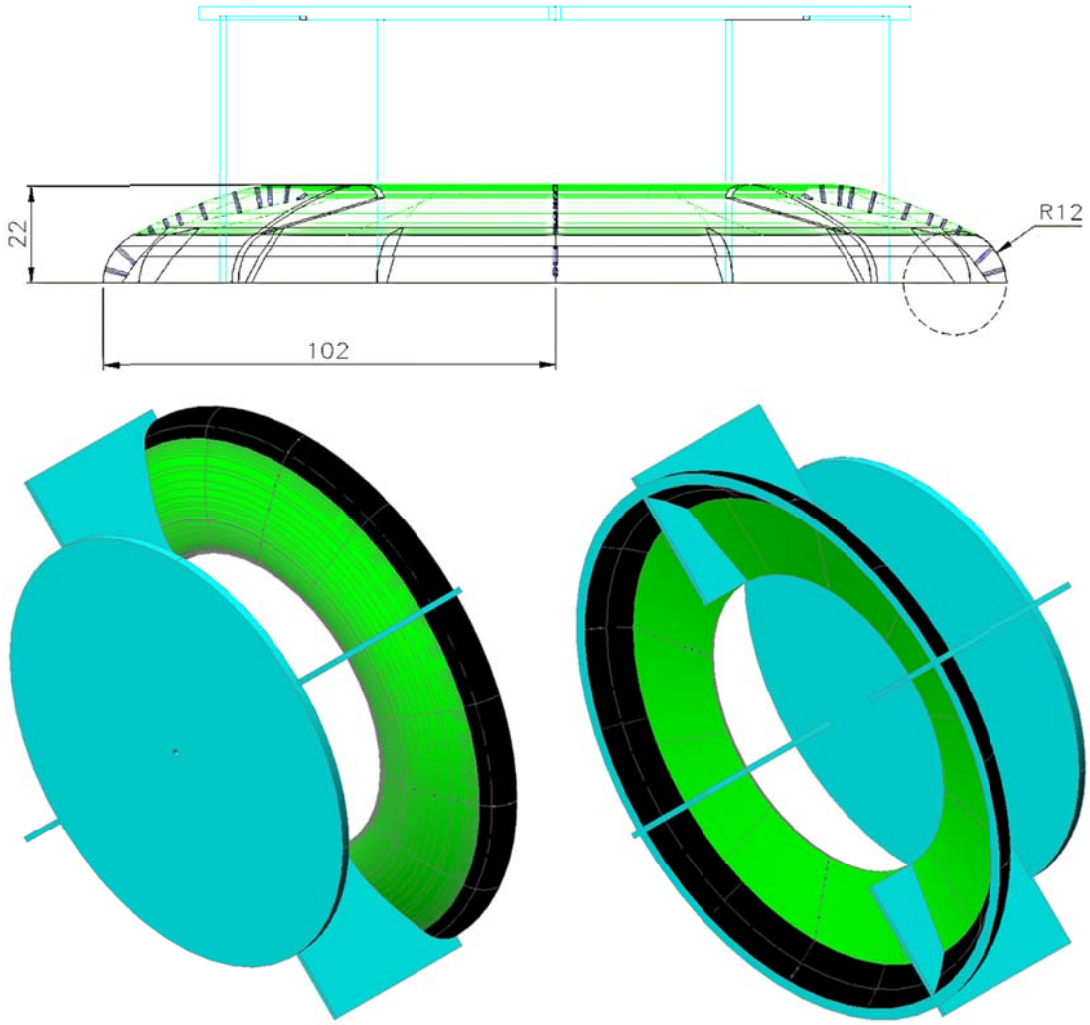

Figure 84: 3-D geometry of annular wing prototype

Chapter 6. Single-Element Aerofoil Lift Enhancement

6.1 Introduction

A single-element aerofoil section has a fixed geometry with reference to the body axes, while a multi-element aerofoil can change its geometrical profile with the aid of active flaps, slats and tabs. In general, frequently used single-element aerofoil sections, e.g. NACA-0012, NACA-0024 or NACA-2412, generate 2-D C_L values in excess of unity at moderate angles of attack. In contrast, the annular wing under investigation achieves C_L values significantly less than unity for reasons discussed previously. Therefore, herein, single-element aerofoil lift enhancement strategy appropriate for the annular wing is sought. Further enhancement may be achieved, if desired, by adopting standard multi-element aerofoil sections, e.g. flaps, tabs and slats.

6.2 Gurney Flap

The most conventional way to increase lift is to increase the pitch (or the angle of attack) while applying more power. This exerts more force on the lower surface and so increases the strength of the vorticity around the wing. To that perspective another technique of increasing 2-D lift coefficient of aerofoil is the use of a passive device known as Gurney flap. The Gurney flap was first introduced by Lieback in 1970 [69]. The Gurney flap, also known as mini-split-flap or trailing-edge wedge, is a small tab attached perpendicular to the lower surface of the aerofoil in the vicinity of the trailing edge, e.g. see Figure 85. Typically, a Gurney flap height can vary from 1% to 5% of the aerofoil chord [70]. The original Gurney flap was installed at the trailing edge of a rectangular race car wing facing upwards. Dan Gurney's race car demonstrated an improved down force and lower drag with the flap [71].

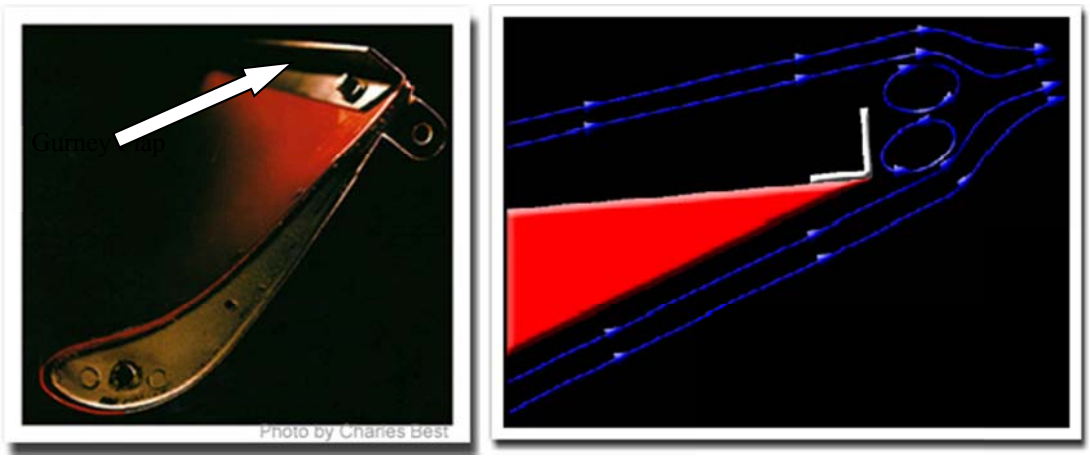

Figure 85: Photographs showing a classic Gurney Flap connected to trailing edge of a cambered aerofoil [72].

Lieback's results showed a significant increment in lift compared to the baseline aerofoil. In general, the drag of the aerofoil increases with the addition of the Gurney flap, but often the percentage increase in lift is much greater, resulting in an increased lift-to-drag ratio and therefore a better efficiency and performance. Lieback suggested that the optimal Gurney flap height should be on the order of 1-2 percent of the aerofoil chord.

Gurney flaps have been thoroughly investigated [73, 74, 75, 76] and used in many applications, e.g. alleviation of aerofoil static and dynamic stall [77, 78, 79], flutter

control, and rotor blade load control [80, 81, 82]. The investigations have led to an establishment of certain aerodynamic characteristics of the Gurney flap: increases the lift coefficient (C_L), decreases the angle of attack for zero lift (α_0), and increases the nose down pitching moment coefficient (C_M), which is consistent with an increase in camber of the aerofoil. Nevertheless, considering the flow structure around a Gurney flap the increase in lift comes from the effective increase in camber on the lower surface having minimum adverse effect on the upper surface flow. The flow structure around a Gurney flap is hypothesised in Figure 86. The figure indicates that the flow turns over the back of the flap and two vortices of opposite signs are formed in the wake of the flap. The significant turning of the upper-surface trailing-edge flow enhances lift and reduces drag due to a relatively larger region of attached flow near the trailing edge. Later other experimental and computational analysis [83, 84] have validated this hypothesis.

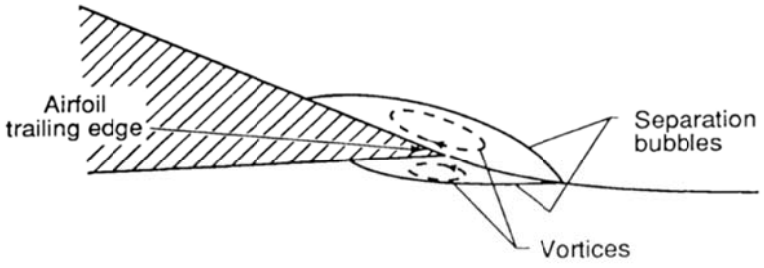

(a) Conventional airfoil at moderate C_L

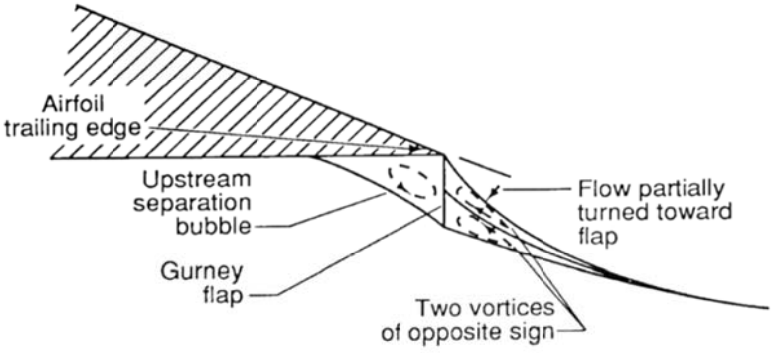

(b) Hypothesized flow near Gurney flap

Figure 86: Gurney flap flow field illustration {from [85]}

A brief review of the Gurney flap presented above indicates that the device can enhance lift generation with varying drag penalty depending on the aerofoils used, flow conditions, and the Gurney flap configurations. The quantitative aerodynamic characteristics of a classic Gurney flap attached to a rectangular wing are summarised in Figure 87: the figure clearly highlights the aerodynamic benefits discussed above.

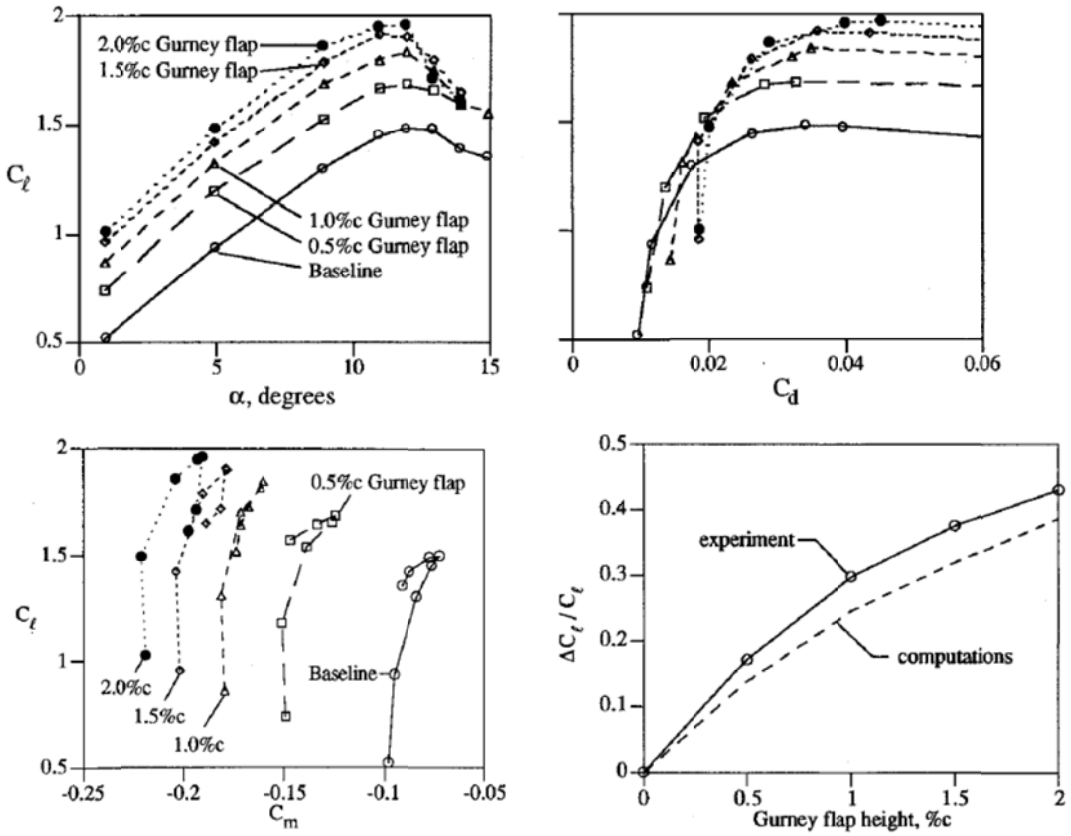

Figure 87: 2-D aerodynamic characteristics of a classic Gurney flap attached to a rectangular wing {from [74]}.

6.2.1 Gurney Flap on Annular Arc-Wing

Figure 88 shows the arc wing with Gurney flap (~4% chord length) attached to the lower surface of the wing. The wing is blown symmetrically by aligning the leading edge to the centre line of the blower. The local static pressure around the surface of the wing is recorded for different angles of attack. The acquired experimental data and calculated coefficients are presented in Table 5.

Figure 89 plots local pressure around the aerofoil surface for different angles of attack. From the plots, the effect of Gurney flap is visible: the pressure difference at the trailing edge has significantly increased compared to the baseline case where the pressure at the trailing approximately equals to zero. Adverse effects are observed with reduction in pressure at the suction side around quarter chord. This is expected due to a larger effective camber caused by the flap. In addition, around 20% of the chord from the trailing edge has become under the influence of the Gurney flap.

Figure 90 presents the lift, drag and pitching moment coefficients calculated by integrating the pressure forces around the surface. The Gurney flap has enhanced the baseline lift coefficient from 34% at zero angle of attack, to 9% at 22 degree. The reduction in incremental lift, with Gurney flap, with increasing angle of attack, is caused by the increasing boundary layer thickness which reduces the effect of the flap, e.g. see Figure 91, also visible from the pressure distribution plot. The increase in lift at lower angles attack, $0 \leq \alpha \leq 14$, has not caused a significant rise in drag. The nose down pitching moment has been increased by 25% on average. A crucial point to be noted here is that at lower angles of attack the drag has found to be lower than the baseline drag which is an expected fact for relatively thicker aerofoils [86].

Lift enhancement with minimal drag penalty and an increase in nose down pitching moment make Gurney flap a favourable modification/addition to the annular wing. Also, a Gurney flap possesses a simple geometry that is easy to construct and add to any existing wing geometry.

Figure 88: Depiction of arc-wing (NACA-0024) with Gurney flap attached to the lower surface.

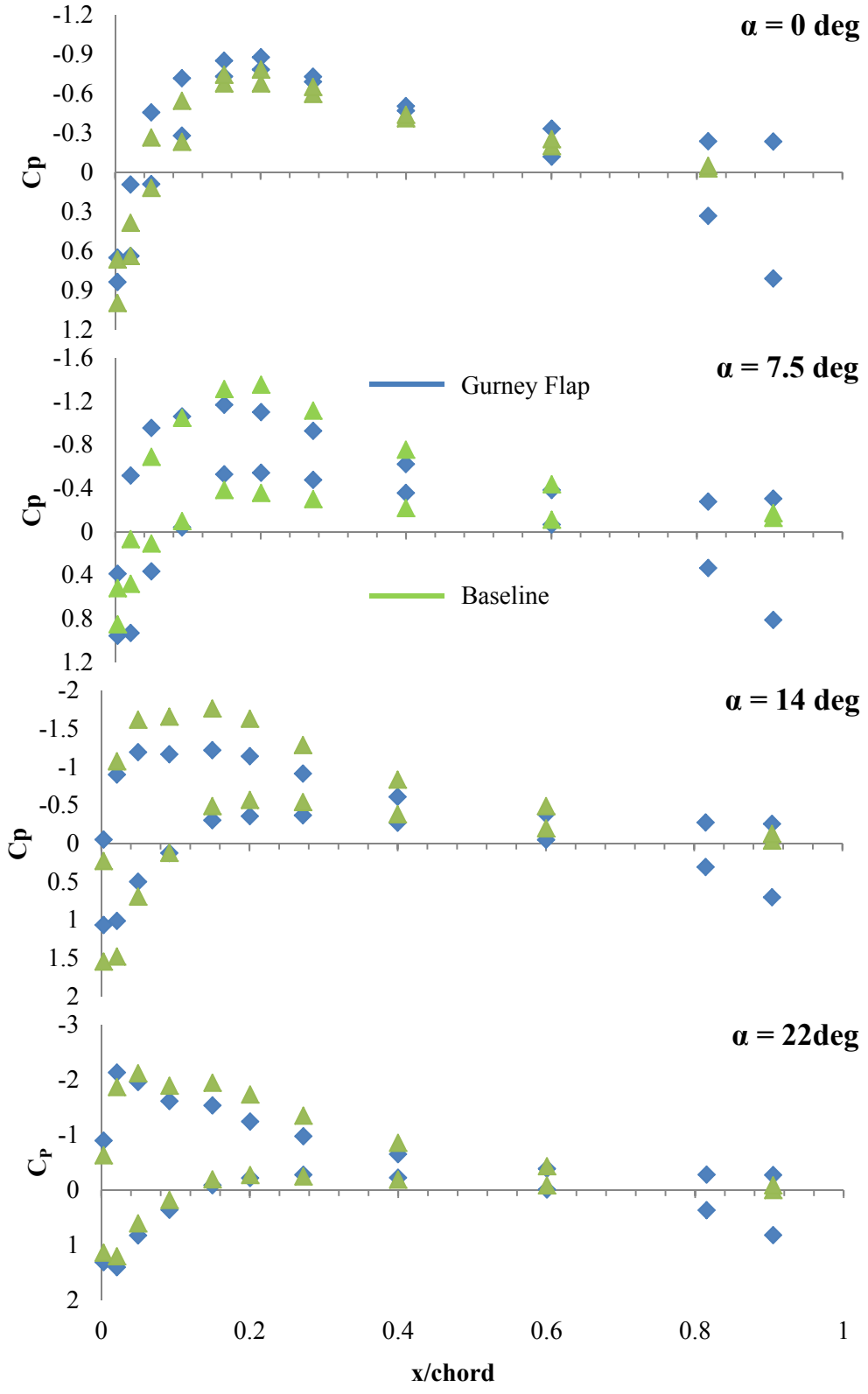

Figure 89: Measured pressure distribution over the surface of arc-wing with and without Gurney flap attached at the lower trailing edge.

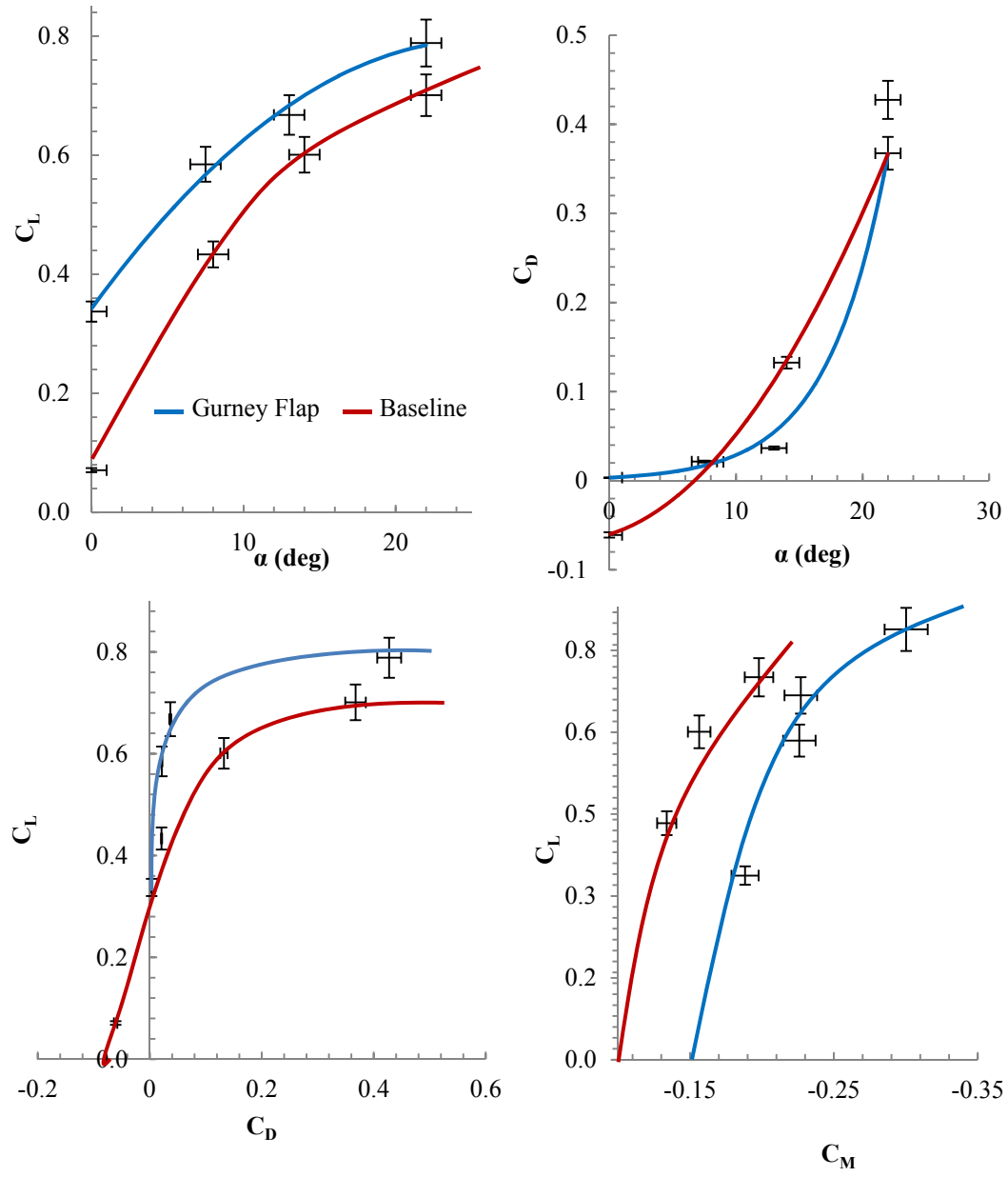

Figure 90: 2-D aerodynamic characteristics of arc-wing with and without Gurney flap acquired experimentally.

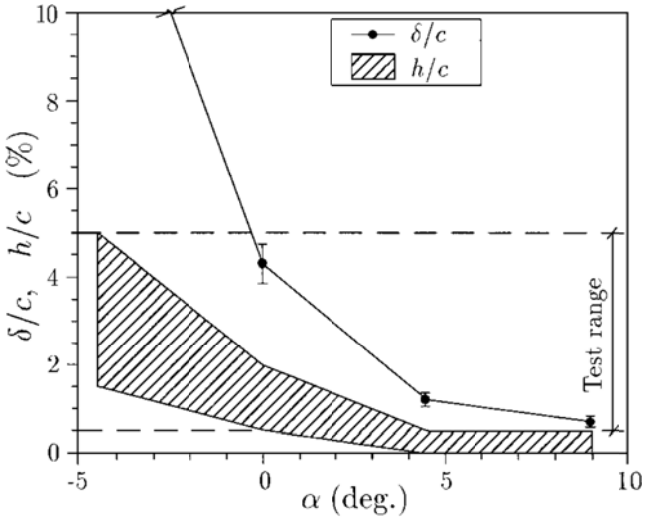

Figure 91: Measured boundary-layer thickness δ / c and range of beneficial Gurney flap height h / c for the LA203A aerofoil as a function of angle of attack {from [87]}.

y/c	x/c	s/c	beta	Cp	Cp	Cp	Cp
-0.0211	0.003	0.030	162	0.651	0.957	1.063	1.302
-0.04852	0.021	0.038	139	0.638	0.930	1.010	1.393
-0.07068	0.050	0.044	122	0.090	0.363	0.498	0.817
-0.09072	0.092	0.057	110	-0.279	-0.041	0.122	0.352
-0.10654	0.150	0.055	101	-0.731	-0.530	-0.306	-0.094
-0.11498	0.200	0.062	97	-0.784	-0.545	-0.359	-0.226
-0.1192	0.272	0.084	91	-0.691	-0.478	-0.371	-0.284
-0.11603	0.400	0.154	86	-0.469	-0.359	-0.274	-0.231
-0.09177	0.600	0.203	81	-0.120	-0.068	-0.049	-0.016
-0.04958	0.815	0.184	77	0.332	0.332	0.306	0.360
-0.02743	0.905	0.147	76	0.811	0.811	0.700	0.811
0.021097	0.003	0.030	198	0.837	0.385	-0.053	-0.904
0.048523	0.021	0.038	221	0.093	-0.518	-0.904	-2.139
0.070675	0.050	0.044	238	-0.457	-0.957	-1.196	-1.967
0.090717	0.092	0.057	250	-0.718	-1.063	-1.169	-1.621
0.10654	0.150	0.055	259	-0.850	-1.169	-1.222	-1.541
0.114979	0.200	0.062	263	-0.877	-1.103	-1.143	-1.249
0.119198	0.272	0.084	269	-0.729	-0.930	-0.917	-0.983
0.116034	0.400	0.154	274	-0.505	-0.625	-0.611	-0.658
0.091772	0.600	0.203	279	-0.332	-0.385	-0.385	-0.393
0.049578	0.815	0.184	283	-0.237	-0.279	-0.276	-0.286
0.027426	0.905	0.147	284	-0.234	-0.306	-0.258	-0.279
			C_L	0.337	0.585	0.668	0.788
			C_D	0.003	0.022	0.037	0.428
			C_M	-0.188	-0.226	-0.227	-0.300
			α	0	7.5	13	22

Table 5: Experimental data for arc-wing with Gurney flap.

6.3 Design of Lift Improvement Device (LID)

The analyses above have shown that the dynamic pressure along the radial axes over the wing surface is significantly lower than a conventional wing. As the result it could make the annular wing relatively inefficient. However, this loss could be alleviated by designing a Lift Improvement Device (LID). The proposal is to implement guided vanes over the surface of the wing as shown in Figure 92. The hypothesis is that the guided vanes are curved in such a way that the leading edge circumference $\overline{C}_{L.E}$ is equal to the trailing edge circumference $\overline{C}_{T.E}$ and hence equalising the outlet area to the inlet area. This makes the total effective surface area of the annular wing equals to a rectangular wing; the lift generated by the annular wing with the guided vanes should equal to a conventional rectangular wing. Furthermore, the difference in the local velocity distribution over the surface, for annular and rectangular wingforms should be markedly reduced.

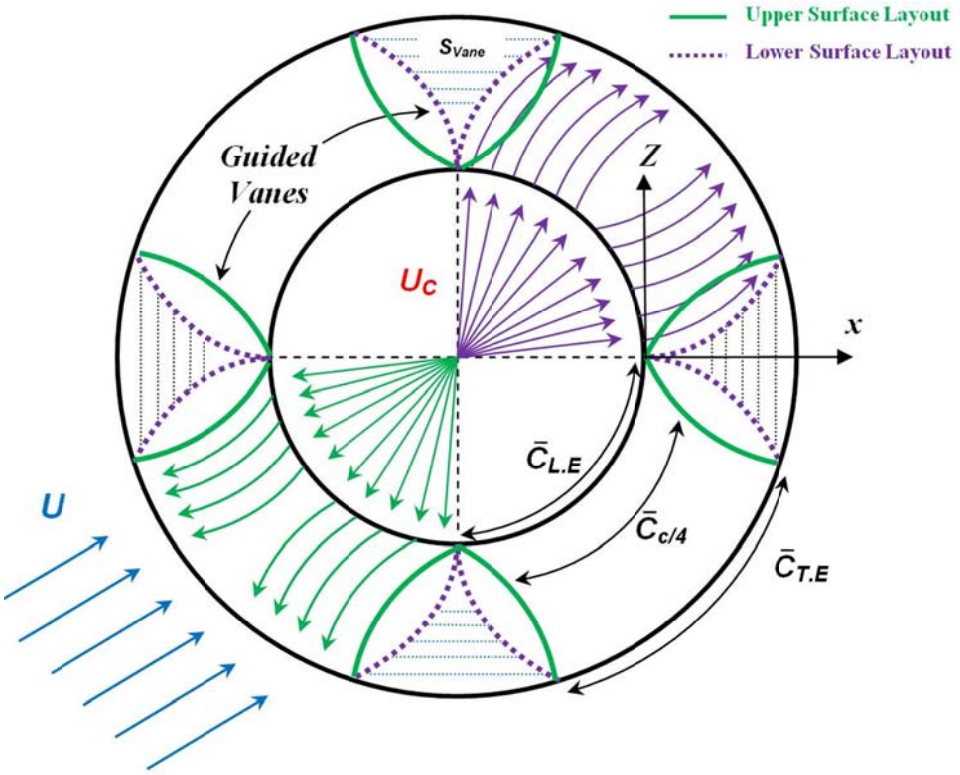

Figure 92: Annular wing with guided vanes a conceptual approach.

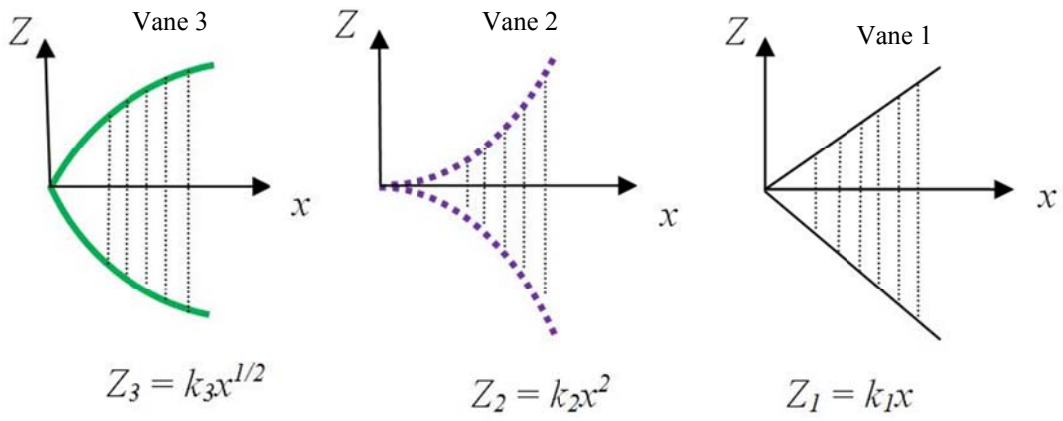

Figure 93: Guided vanes conceptual design.

Figure 93 presents three different proposed vane designs to compensate the dynamic pressure loss due to the annular configuration. First, it is necessary to define what needs to be eliminated from the annulus and if we equate the leading edge circumference to the trailing edge the remaining circumference may well be calculated as

$$\overline{C}_{rem.} = \overline{C}_{T.E} - \overline{C}_{L.E} = 2\pi(R_0 - r_0) \tag{6.1}$$

where r_0 and R_0 are inner and outer radii of the annulus respectively.

The remaining circumference needs to be divided by the number of vanes, i.e. 8. Each circumference has the length given by:

$$\Rightarrow \overline{C}_{rem.} = \frac{\pi}{4}(R_0 - r_0) \tag{6.2}$$

and the azimuth angle ψ of the circumference is given by

$$R_0\psi = \frac{\pi}{4}(R_0 - r_0) \Rightarrow \psi = \frac{\pi}{4}\left(1 - \frac{r_0}{R_0}\right) \tag{6.3}$$

The vanes depicted in Figure 93 may be modelled as $Z_1 = k_1 x$, $Z_2 = k_2 x^2$ and $Z_3 = k_3\sqrt{x}$ respectively and their corresponding constants are defined as

$$k_1 = \frac{\pm R_0 \sin(\psi)}{R_0 \cos(\psi) - r_0}, \quad k_2 = \frac{\pm R_0 \sin(\psi)}{\left(R_0 \cos(\psi) - r_0\right)^2}, \quad k_3 = \frac{\pm R_0 \sin(\psi)}{\sqrt{R_0 \cos(\psi) - r_0}} \tag{6.4}$$

The circumference at any distance along the radial axis r for each of the guided vanes may be defined as

$$\overline{C}_{r_i} = \frac{\pi}{2}(r_0 + x) - 2\left[\left(Z_i^2 + (r_0 + x)^2\right)^{1/2} \tan^{-1}\left(\frac{Z_i}{r_0 + x}\right)\right] \tag{6.5}$$

where i is the corresponding vane i.e. $i = 1, 2, 3$.

The local velocity over the surface of the wing with the vanes attached is calculated by applying the continuity as

$$v_i = \frac{1}{2} U_C \left[\frac{\pi r_0 t_C}{\overline{C}_r (t_C - t_x)}\right] \tag{6.6}$$

where t_C is the centrifugal fan outlet thickness.

Figure 94 highlights the change in circumference and the cross-sectional area facing the flow, CSFF, along the radial axis for the guided vanes considered. The vanes substantially reduce the effective circumference and the CSFF; the circumference increases linearly along the radial axis of the annulus without the vanes, the inclusion of vanes keep a rather constant circumference along the radius. Figure 95 shows the plots of local pressure distribution over the surface of the wing with and without the vanes. From the figure it is visible that the local pressure is proportional to the circumference and the CSFF. Vane 2 compensates the dynamic pressure loss due to the annulus configuration and simulates a rectangular wingform. Vane 1 achieves moderate rise in the dynamic pressure whereas vane 3 obtains the highest overall dynamic pressure. All three vanes give rise to the maximum local velocity at the maximum aerofoil thickness and this is because the aerofoil profile and the vanes together create a venturi around the wing; of which the narrowest point occurs at the maximum aerofoil thickness i.e. at the quarter chord length.

The analysis above demonstrates that the loss of dynamic pressure for the annular wing is recoverable by attaching guided vanes to the wing; vane 3 seems to offer the best pressure distribution.

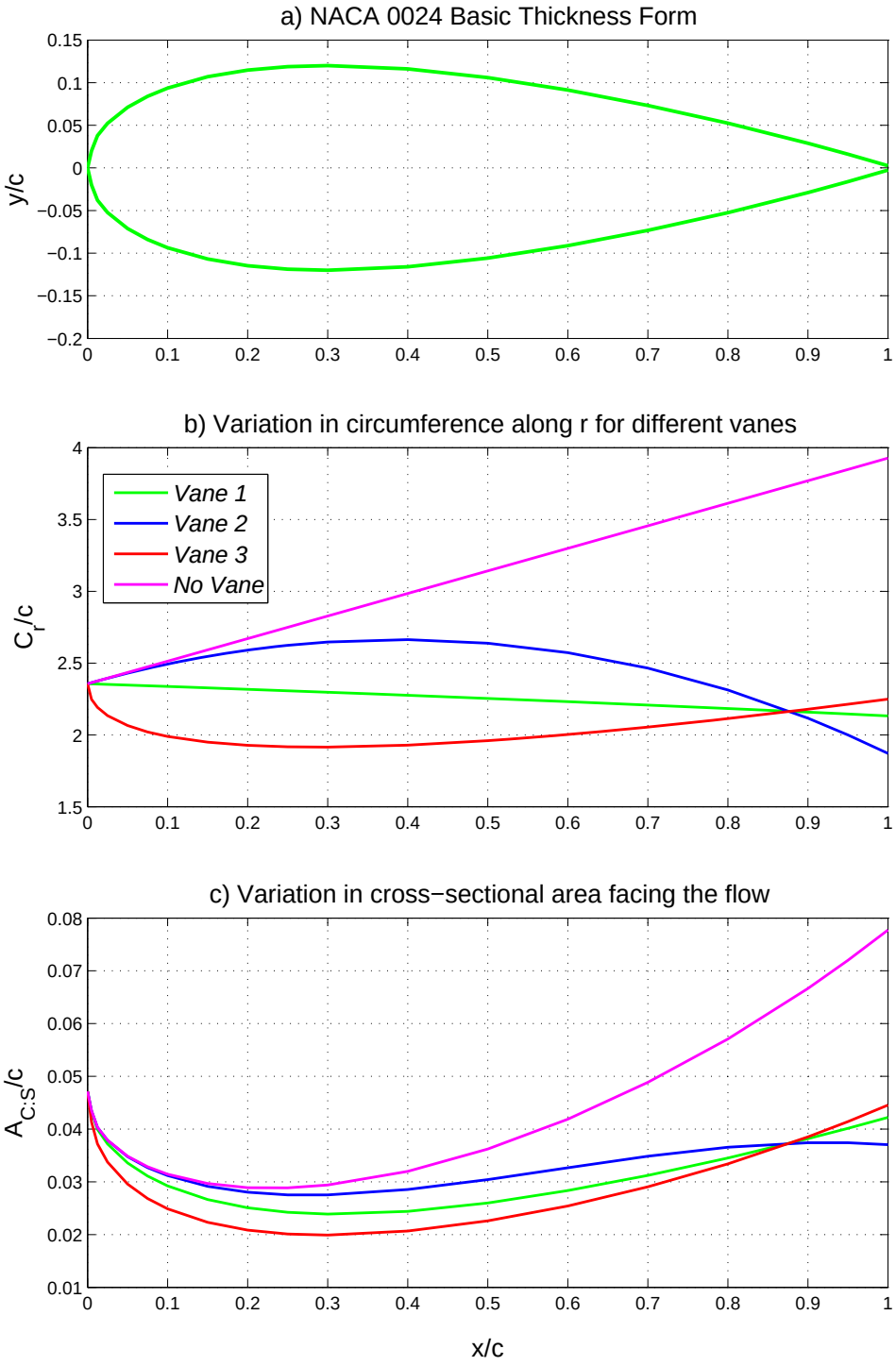

Figure 94: Theoretical comparison of variation in cross-sectional area facing the flow and variation in circumference for different guided vanes attached.

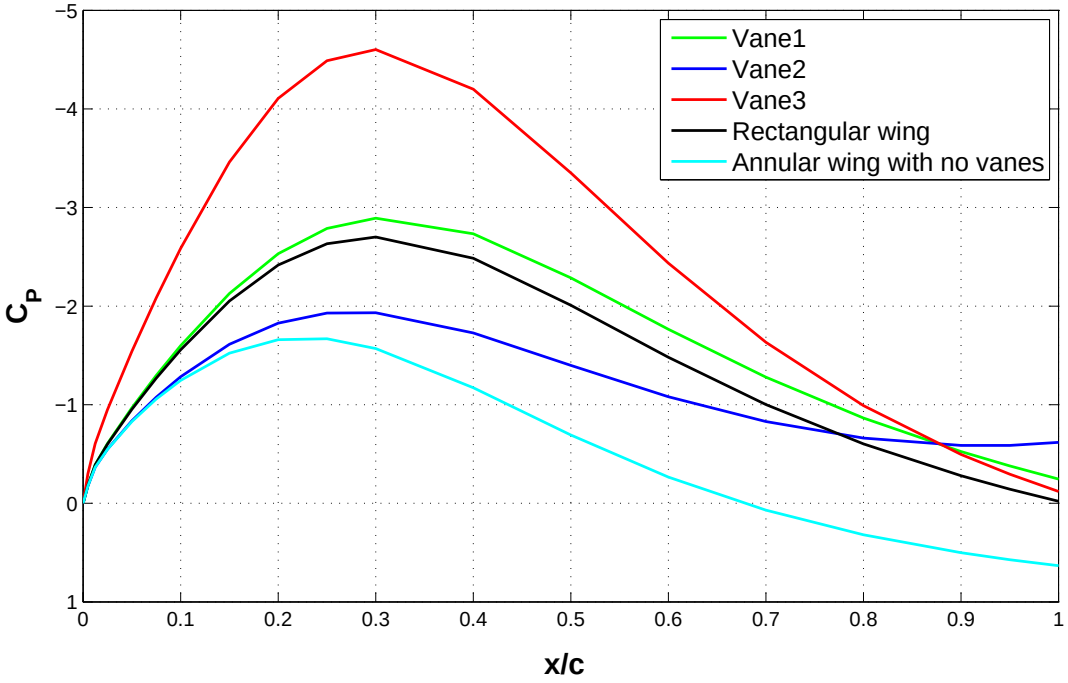

Figure 95: Theoretical comparison of local velocity distribution over the surface of annulus for different guided vanes.

6.4 Summary

- It has been shown, theoretically and experimentally, that the Gurney flap or the proposed guided vanes on an annular wing are capable of enhancing the baseline lift.
- Experimentation has shown that a Gurney flap of size, ~ 4% chord length, can enhance the baseline lift coefficient by 34% at zero angle of attack and to 9% at 22 degree.
- An increase in lift at lower angles of attack, $0 \leq \alpha \leq 14$, does not cause a significant rise in drag and the nose down pitching moment has been increased by 25% on average which may be beneficial in translational flight mode.
- A mathematical model for three guided vanes with different geometries has been developed.
- All the vanes have shown, theoretically, the capability of enhancing the baseline lift and hence overcome the loss of dynamic pressure due to annular flow expansion.

Chapter 7. An Evaluation of Existing Non-Helicopter V/STOL Capability

7.1 Introduction

V/STOL refers to Vertical or Short Take-Off and Landing capability, an aircraft that can perform either vertical or short take-off or landing is said to inherit V/STOL capability e.g. BAE Harrier. The term V/STOL is composed of two other VTOL, vertical take-off and landing, and STOL, short take-off and landing. An aircraft with insufficient vertical thrust may attempt a short take-off and vertical landing upon reducing weight from fuel consumption, this class of aircraft is specifically designated by STOVL.

V/STOL capability cuts the need for long runways and reduces the time to achieve horizontal flight: conventional jet aircraft land and take-off with speeds of, around, 80 to 120m/s and may require runways up to 3,500m in length in some cases – this is an expensive infrastructure problem that V/STOL has potential to solve.

Interest in V/STOL flight probably arose when early attempts at powered flight tried emulate the behaviour of birds; however, no early man made machine, based heavily on birds ever achieved controlled flight. It was not then recognised that the short and vertical take-off capability of birds is in large measure made possible by their low wing-loading, which is a natural result of their small size. Figure 96 depicts a chart of wing loading and flight speed for a variety of birds and it can be seen that the birds with relatively low wing-loading and forward velocity are actually VTOL capable, such as the hummingbird, blackbird and owl, other birds being either V/STOL or conventional take-off and landing (CTOL) capable. Sir George Cayley, who was the first to recognise the importance of distinguishing lift from thrust and in particular to recognise the fact that for level flight, the required thrust is one or two orders of magnitude less than the required lift[88].

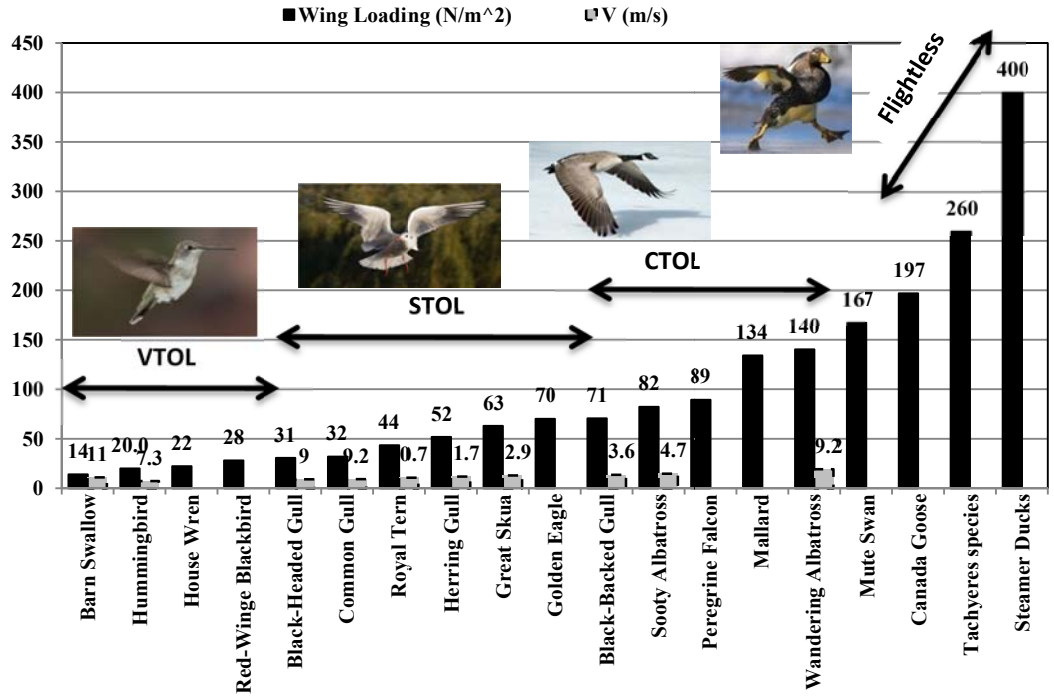

Figure 96: Take-off and landing characteristics of birds [data adapted from89,90,91,92].

In order to understand this phenomenon further, consider lift and drag curves for a typical wing section as shown in Figure 97.The lift is always larger in magnitude than the drag at typical flight conditions, which typically correspond to $10 < C_L / C_D < 15$, and hence the thrust required to overcome the drag is less than the

lift generated. Early vertical flight – as in the helicopters - was achieved by a rotary wing rather than a pure propulsive solution. The following equation best describes the relationship of the forces acting on an aeroplane in level flight.

$$\Rightarrow Thrust = Drag << L = Weight$$

Jet propulsion achieves Vertical Take Off, or VTO by working against an aircraft's weight due to gravity directly, whereas the rotary wing solution does work initially against drag (profile and induced) and hence benefits from the phenomenon of lift being much larger than drag.

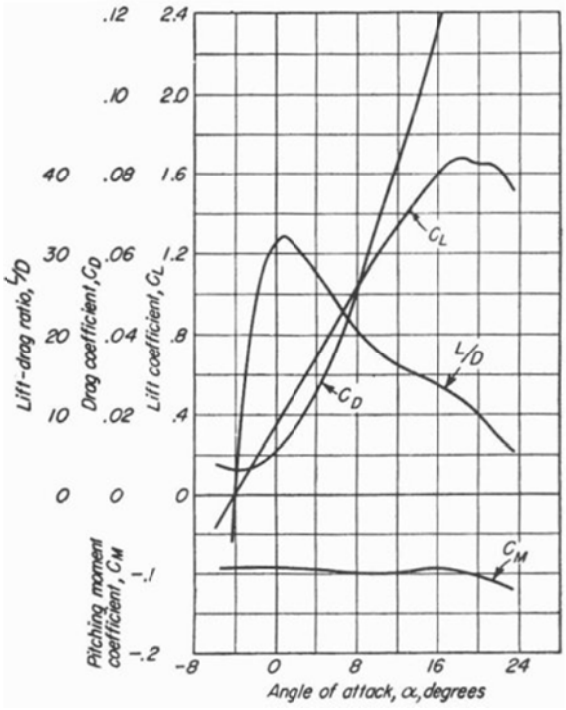

Figure 97: Typical NACA wing-section characteristics {taken from [93]}.

Regardless of mechanism, the development of V/STOL capability has also inevitably been reliant upon the availability of suitable power plants. In particular, the gas turbine engine, with its high thrust to weight ratio, made possible the eventual development of aircraft with static thrust to gross weight ratios greater than one – a prerequisite for VTOL capability. As the speeds of aircraft continue to increase, the power plant requirements for V/STOL operation and forward flight performance

become compatible. Furthermore, at speed above Mach 1 the thrust required is nearly equal to or exceeds the gross weight of the aircraft in level flight – coinciding some aspects of the design solutions for V/STOL and supersonic aeroplanes.

The most prolific V/STOL capable aircraft, so far, is clearly the helicopter; however, in level flight the helicopter is inefficient compared to a typical fixed-wing aeroplane, with speed and range only between a half or one third (approximately) that of the aeroplane. Also, due at-least in part to their greater complexity, helicopters demonstrate poorer safety than conventional aeroplanes [94]: with for example light conventional aeroplanes suffering a fatal accident rate of 11.7/million flying hours, versus 33.5/million flying hours for small helicopter. The same complexity also contributes to a greater cost: for example at time of writing the typical hire cost of a Robinson R44 helicopter in the UK is £400/hr or to purchase such an aircraft would cost £100-£200,000, whilst a Cessna C172 aeroplane, which has similar payload and cruise performance capability, can be rented for about £150/hr or purchased for about £30-£100,000 – costs around 30-40% of the cost of the helicopter.

The search for V/STOL capability has provoked research into embedding VTOL capability of a helicopter into a conventional fixed-wing aeroplane. However, this has rarely been achieved. The author has identified 45 fixed-wing aircraft which have attempted to combine V/STOL capability of the helicopter with high forward flight speed of a conventional aircraft. Of these 45, only four: the BAe Harrier, Yak-38, Bell-Boeing V-22 and Joint F-35 Strike Fighter have ventured much beyond the prototype stage. Table 6 below presents these 45 aircraft arranged according to their propulsion systems.

VTO Propulsion Strategy	Aircraft Model		
Same Propulsion System for Hover and Forward Flight	Tilt Shaft/Rotor	Trascendental Model 1G	1
		Bell XV-3	2
	Tilt Prop	Curtiss-Wright X-100	3
		Curtiss-Wright X-19	4
	Tilt Duct	Doak 16 VZ-4	5
		Bell-X22A	6
		Nord 500 Cadet	7
	Tilt Wing	Vertol 76 VZ-2	8
		Hiller X-18	9
		LTV-Hiller Ryan XC-142	10
		Canadair CL-84 Dynavert	11
	Tilt Rotor	Bell XV-15	12
		Bell Boeing V-22 Osprey	13
	Tilt Jet	Bell 65	14
	Deflected Slipstream	Robertson VTOL	15
		`Ryan 92 VZ-3 Vertiplane	16
		Fairchild 224 VZ-5	17
	Vectored Thrust	Bell X-14	18
		Hawker P.1127 Kestrel	19
		Yakovlev Yak-36	20
		BAe Harrier	21
		Boeing X-32	22
	Tail Sitters	Lockheed XFV-1	23
		Convair XFV-1 Pogo	24
		Ryan X-13 Verijet	25
		SNECMA C450	26
Separate Power Plant for Hover	Lift + Cruise	Short SC.1	27
		Dassault Balzac V	28
		Dassault Mirage III-V	29
Combined Power Plant for Hover	Lift + Lift/Cruise	EWR VJ101C	30
		Dornier Do 31	31
		Lockheed XV-4B	32
		VFW VAK 191B	33
		Yakovlev Yak-38	34
		Yakovlev Yak-141	35
	Tip Jets	McDonnel XV-1	36
		Fairey Rotodyne	37
Augmented Power Plant for Hover	Ejector	Lockheed XV-4A	38
		Rockwell XFV-12A	39
	Fan	Vangaurd Omniplane	40
		GE-Ryan XV-5A	41
		Lockheed Martin X-35	42
	Rotor	Kamov Ka-22	43
		Piasecki 16H-1	44
		Lockheed AH-56	45

Table 6: V/STOL aircraft arranged according to their propulsion systems.

This table is dominated by aircraft whose designs attempt to use the same power system for both VTOL-mode lift and propulsion: including the BAe Harrier and the Bell Boeing V-22. The Yak-38 and JSF X-35, which have both, also successfully, entered service, utilised combined power plant for hover and augmented power plant for hover respectively.

7.2 Distinct Aerodynamic Features of Aircraft

The main distinct feature of V/STOL capability is the high thrust to weight ratio which requires expanding the propulsion performance envelopes and makes the powerplant the most significant component of a V/STOL aircraft in terms of weight and body volume.

Most jet fighter aeroplanes developed since about 1960 have (at-least in lightweight configurations) the potential to generate a thrust to weight ratio T/W exceeding 1. However, conventionally the engine exhaust is located at the rear of aircraft and diverting the exhaust downward will not be the solution – this is useful for horizontal flight, but not hovering flight where a balance problem exists. To solve this, either the thrust must be co-incided with the centre of gravity, or an additional and controllable thrust device must be located away from the main thrustline, creating a balance – such as in the case of the BAe Harrier (Figure 98). Both of these approaches will tend to comprise the aircraft away from the traditional and usually optimal layout.

Figure 98: Hawker-Siddeley / BAe Harrier GR Mk.3 [photo courtesy of Guy Gratton].

For cruise-dominated VTOL aircraft – such as may be designed for transport purposes, a more severe problem involves thrust matching. If the thrust required for vertical flight is provided by the same engines used for cruise, the engines are likely to be far too large for efficient cruise. The thrust mismatch will produce great fuel consumption and range penalty for a cruise dominated design that uses only the vectored thrust of its cruise engines for vertical flight. For this reason many conceptual VTOL transport design have incorporated separate "lift engines" used during vertical flight. Figure 99 highlights the mismatch between thrust required for vertical flight and thrust for horizontal flight for a typical jet V/STOL aircraft. Also, the thrust mismatch may further increase with altitude as the thrust required to maintain a steady flight at higher altitudes, (~15,000 metres), decreases significantly.

These are known to be the fundamental problems which must be overcome in a VTOL aircraft.

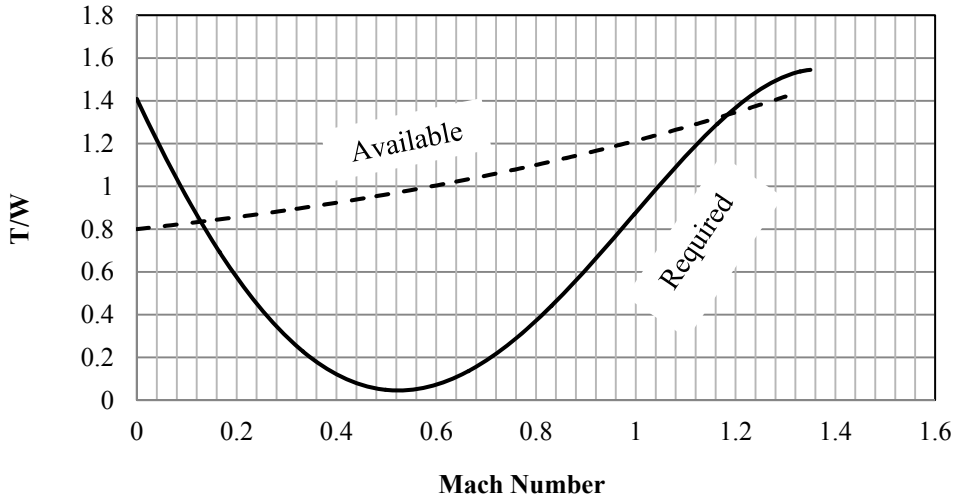

Figure 99: Thrust mismatch for jet V/STOL aircraft at sea level {derived from [95]}.

In a V/STOL aircraft it becomes necessary to also consider the factors influencing the performance for the CTOL and level flight cases. The factors can be evaluated by simplified analysis of the ground-roll distance of a landing aircraft and the relationship between them is defined by [95]:-

$$S_0 \approx \frac{(W/S)V_{ref}{}^2}{\rho g C_{L_{\max}} (T_R/W + \mu)} \tag{7.1}$$

$$\Rightarrow \begin{cases} S_0 \propto W/S \\ S_0 \propto {V_{ref}}^2 \\ S_0 \propto 1/C_{L_{\max}} \\ S_0 \propto 1/(T_R/W) \end{cases} \tag{7.2}$$

where S_0 is the ground-roll distance, V_{ref} the approach speed and the other symbols are designated to their usual meanings. The relationship clearly indicates that the thrust to weight ratio is the most significant parameter to achieve minimum ground roll distance and it could be further minimised by maximising C_{Lmax} and lowering the wing loading *W/S*. Figure 100 presents the landing performance of typical STOL aircraft unsurprisingly shows that the approach speed should be reduced to minimise the landing distance. To do so, C_{Lmax} and T_R (which is a function of forward thrust to weight ratio) need to be increased.

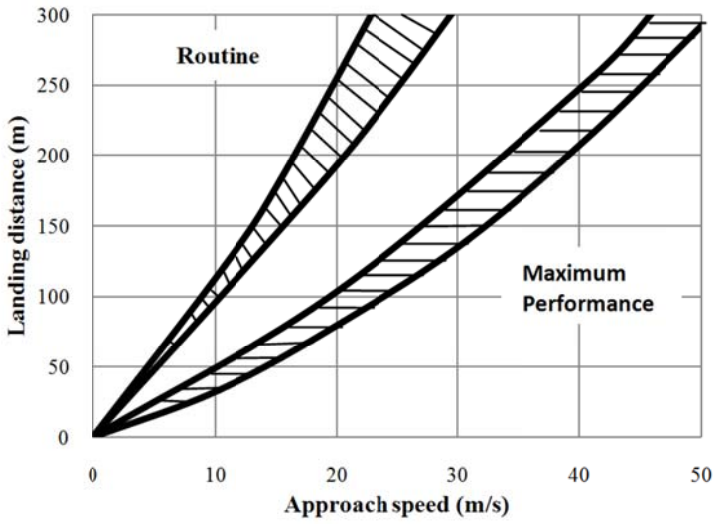

Figure 100**:** STOL landing performance {derived from [96, 97]}.

Of course, aircraft configuration is also very relevant to achieving STOL performance. In particular at the design stage, the inlet and exhaust of the lift-generator system should be considered. Proper exhaust location, such as that achieved on the Harrier, can enhance even conventionally augmented wing lift considerably [98] during a conventional runway take-off.

Figure 101also shows that wing loading must be reduced to achieve a better weight to power performance. Helicopters possess the highest weight to power ratio and the

rest, tilt rotor, lifting propellers and lifting jet, are significantly less efficient. However, this Chapter is concerned with fixed-wing V/STOL aircraft primarily and this makes the tilt rotor the best candidate within this class of aircraft.

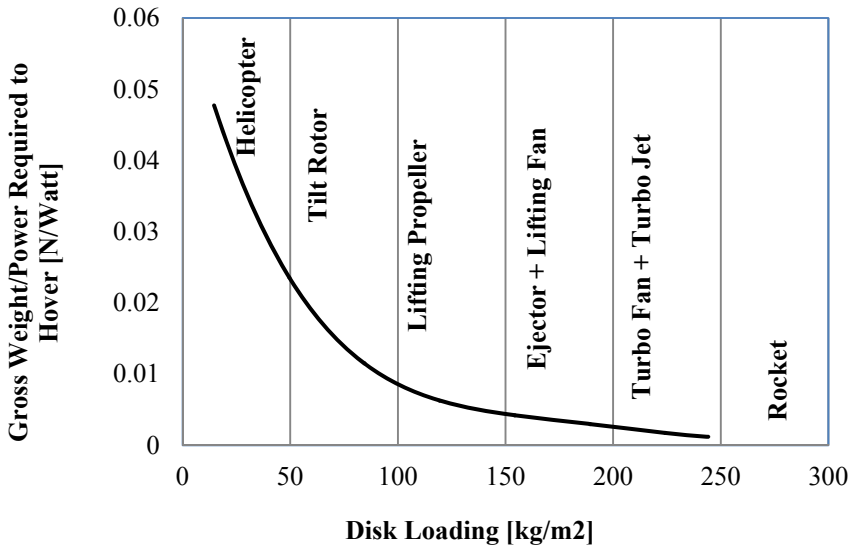

Figure 101**:** Weight to power ratio versus disk or wing loading for V/STOL aircraft with different propulsion systems {derived from [99]}.

7.3 Primary Causes of the Aerodynamic Losses

It is useful to review the main design penalties introduced into the well understood conventional aeroplane by the addition of a VTOL capability. During hovering or vertical flight the aircraft experiences several aerodynamic losses including suckdown, recirculation, hot-gas ingestion, thrust vectoring and reaction control system.

7.3.1 Suckdown and Fountain Lift

The downwash that keeps the aircraft in a steady state also accelerates the air flow around it which pushes downward on the aircraft with a vertical drag depending on the whole surface area of the aircraft facing the flow. The critical factors influencing the vertical drag are the relative location of the propeller or jet exhaust and the fixed wing. If the propeller is directly above the main wing, such as in the Lockheed AH-56, or the exhaust nozzles are directly under the wing, such as in the Bell 65 ATV, then a much larger downward force is exerted by the entrained airflow.

For a jet aircraft suckdown is a rather severe aerodynamic loss. The jet lift is a product of mass flow rate $\dot{m}$ and jet speed U_J, $T = \dot{m}U_J$. Significantly large amounts of air need to be drawn in from the surrounding which subsequently causes a complex flow field around the aircraft as shown in Figure 102. This complex flow field causes variation in total lift arising mainly from suckdown caused by low pressure at lower surface of the aircraft. This loss is often balanced by deploying vertical fins to divert the engine exhaust inwards and generate favourable fountain effect. The variation in lift may be summed up as

$$\frac{\Delta L}{T} = \frac{\Delta L_{OGE}}{T} + \frac{\Delta L_f}{T} + \frac{\Delta L_s}{T} \tag{7.3}$$

where L_{OGE} is the loss of lift due to profile drag acting at the plan-form surface of the aircraft depending on the climb rate.

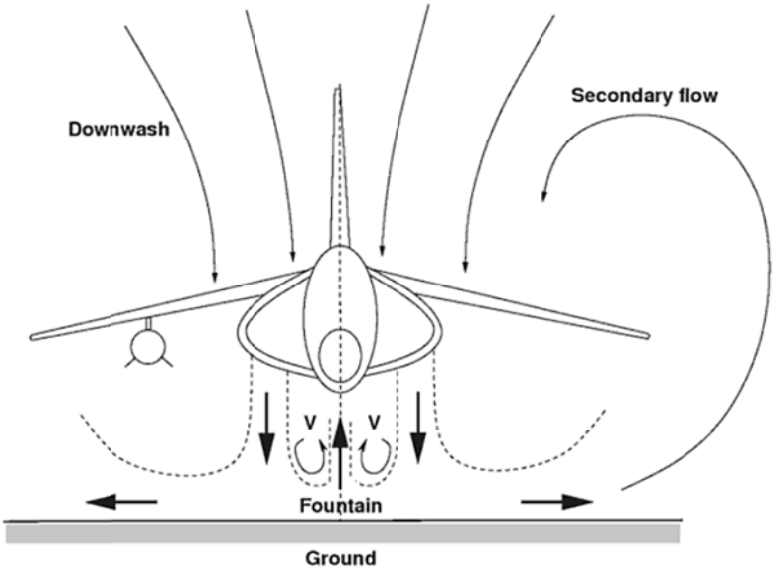

Figure 102: Twin- jet V/STOL aircraft in ground effect showing potential flow field {from [100]}.

7.3.2 Recirculation

A V/STOL aircraft near the ground experiences a potential flow field around it that injects its own downwash/exhaust gases into the inlet which results in a significant loss of lift/thrust. This recirculation also often injects dirt and erosion particles that can damage the engine.

7.3.3 Hot-Gas Ingestion

Hot-gas ingestion is only applicable to jet VTOL aircraft where hot exhaust gases are injected back into the engine which increases the inlet temperature and causes a significant reduction in thrust. The hot-gas ingestion is very configuration dependent, the nozzle arrangement, inlet position, and wing location being important variables. Relative head winds could also have a large effect on the magnitude of the inlet-air temperatures.

7.3.4 Thrust Vectoring

Thrust-vectoring is generally achieved by nozzle-vectoring and the nozzle arrangement has a significant effect on the thrust loss. Rectangular nozzle arrangements and the side-inlet single nozzle have the highest inlet-air temperature rises (up to 111º C) [101].

7.3.5 Reaction Control System (RCS) losses

In hovering flight, an RCS is necessary to aircraft control; this may for example be achieved through use of compressed air bleed at the wing tips, nose or tail (e.g. the Harrier and Yak-38). Such a system is both heavy in itself, and makes significant power demands upon the aircraft. For a rotary-wing aircraft balanced VTOL is achieved by a combination of pendular stability and dynamic control via disc angle.

The net T/W for VTO must obviously exceed 1 in the normal axis, however thrust losses must be considered in light of the above.

Heave Control	$T/W=0.05$
Suckdown	$T/W=0.03$
RCS	$T/W=0.1$
HGI	$T/W=0.08$
Landing Weight	$T/W=1.0$

from Ref [102].

Thus, to achieve hover for a jet aircraft, normally $1.3 \le T/W \le 1.5$.

7.4 V/STOL Performance Analysis

Conventionally, an aircraft's performance, as whole, is specified by power and thrust loading, P/W and T/W. The shorter the take-off distance, the higher the altitude and hotter the climate, the bigger the engine to provide enough power, or thrust. Specifically, for a V/STOL aircraft the most emphasised parameters, from conceptual design to performance analysis, are static thrust-to-weight ratio and wing loading[103]. For a CTOL aircraft the general performance equation [104] defining the relationship between power, thrust and weight is given by

$$\eta_p P = DV_t + Wv_c \tag{7.4}$$

where η_p is the propulsive efficiency, V_t the forward target velocity, v_c the rate of climb and a the acceleration of aircraft. This equation, in general, will hold for V/STOL aircraft as well by incorporating the different flight modes. Thus the analysis below will be based on the parameters given in the equation above.

Design and performance data has been collected for the aircraft, presented in Table 6, and tabulated in Table 7 and Table 8, categorised by propulsive class.

Figure 103 and Figure 104 present thrust and VTO weight chart for jet and the non-jet V/STOL aircraft respectively in order to highlight the scale of each aircraft. Using available technology, jet aircraft tend to be heaviest with weights respectively of 80 kN compared to 30 kN for other classes. The aircraft are arranged with time scale and there seems to be no strong evidence of improvement in terms of thrust to weight ratios through the history of V/STOL – presumably because most aircraft are designed to a weight which makes full use of the power available.

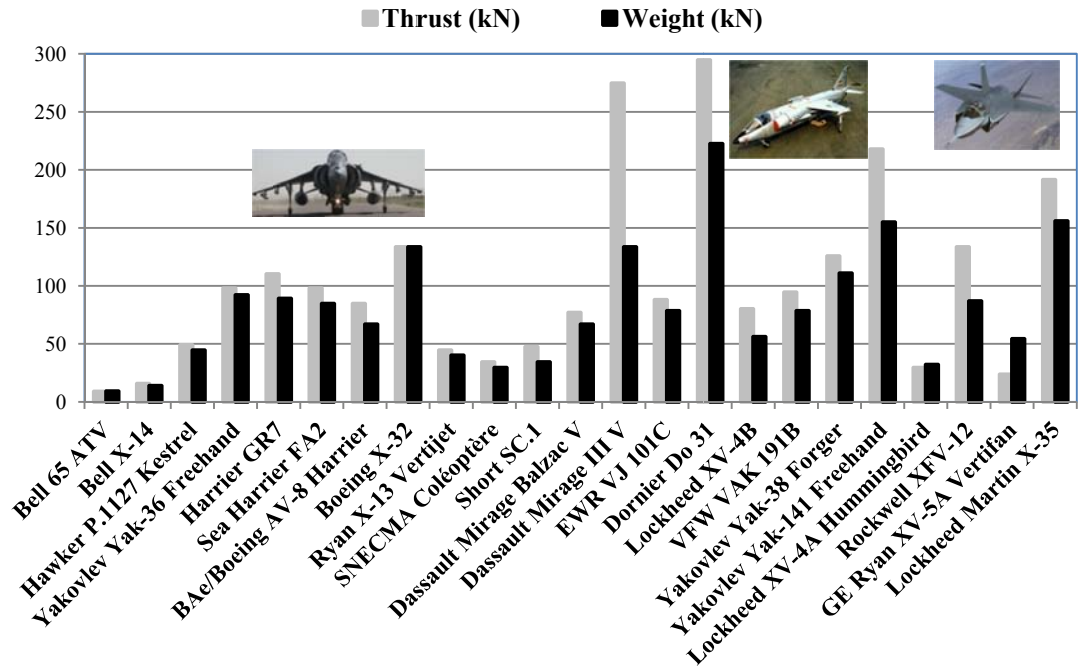

Figure 103**:**Available Jet-Thrust and Weight chart for jet V/STOL aircraft.

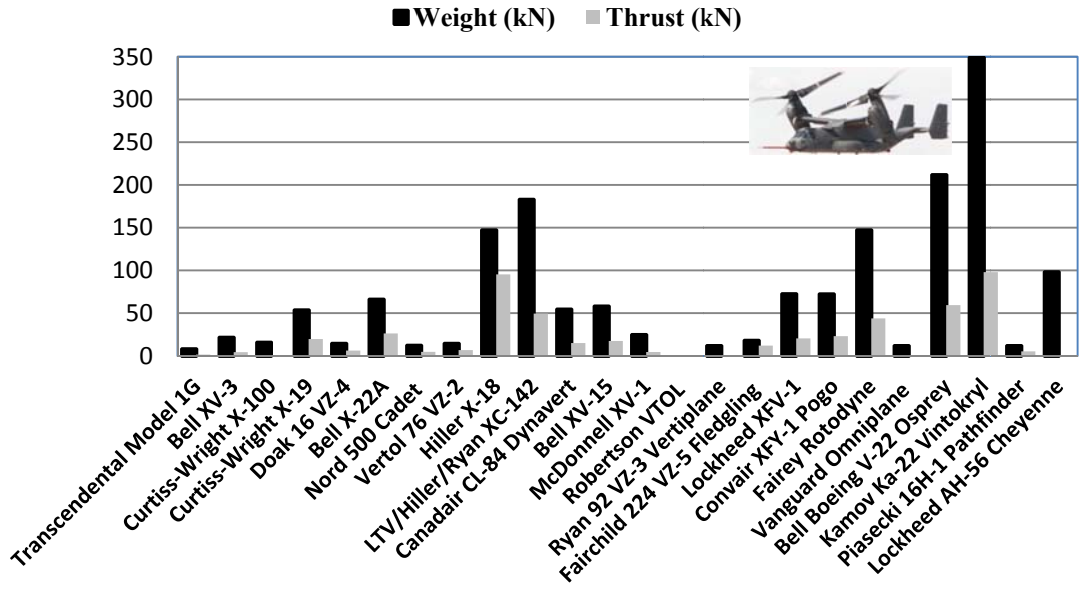

Figure 104, Thrust and Weight chart for non-jet V/STOL aircraft.

Once V/STOL capability is achieved, for many aircraft, the most significant performance parameter would then be the range. Figure 105 shows that the non-jet driven aircraft acquire much longer range for a given weight compared to the jet driven aircraft. The lighter non-jet aircraft, upto 50 kN weight, give around double the range available to a jet-powered equivalent aircraft.

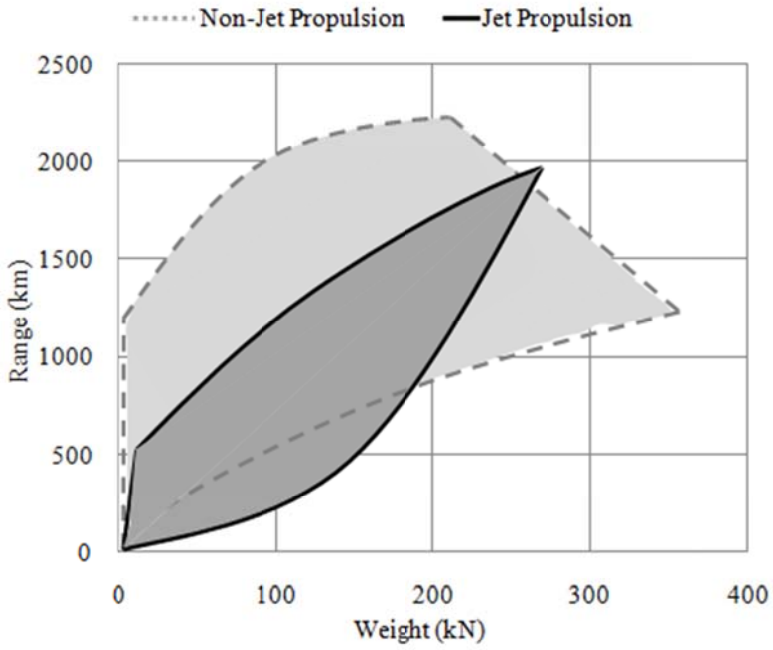

Figure 105, Range comparison for jet and non-jet propulsion driven V/STOL aircraft.

Another important parameter for some aircraft, particularly those with military applications, is maximum operating altitude (often called the aircraft *ceiling).* In contrast to range, jet propelled aircraft attain much higher maximum cruise velocities compared to the non-jet, see Figure 106.

The average cruising speed of heavier jet aircraft is around 300 m/s, which is in the transonic region, and around 100 m/s for the non-jet aircraft. However, for the smaller/lighter class of aircraft, up to 50 kN, the difference is insignificant. Rotary winged aircraft are excluded from the high speed flight regime by well-known limiting factors, particularly tip compressibility and retreating blade stall.

The high profile drag met at transonic speeds, inevitably, leads to a requirement for a higher T/W for higher speed (normally jet) aircraft, as may be seen in Figure 107. The average T/W for the jet aircraft is around 1.2 which is a function of Mach number as shown in Figure 99 above. The average T/W value for the non-jet is 0.35 which again highlights the fact that rotary wing benefits from aerodynamic fact that lift generated is much larger than the drag. Rotary wing and jet propulsion efficiencies are given below respectively.

$$\eta_P = \frac{1}{1+a} \tag{7.5}$$

$$\eta_j = \frac{2}{1+a} \tag{7.6}$$

where a is the ratio of vehicle velocity to the exhaust (for jet) or the induced (for propeller) velocity.

For jet engines, propulsive efficiency is therefore highest when the engine emits an exhaust jet at a speed that is nearly the same as the vehicle velocity. While for the rotary wing the smaller the induced velocity the more efficient the system.

The relationship between performance parameters even for successful aircraft such as X-35 is nonlinear – this aircraft weighing approximately twice the weights of the Harrier and Yak-38 but displaying triple the range and double the top speed. However, given the small sample and that the X-35 is a much more recent aircraft, this is probably due to improved strength to volume ratio of composite materials used on the X-35 which has direct impact on lift to drag ratio.

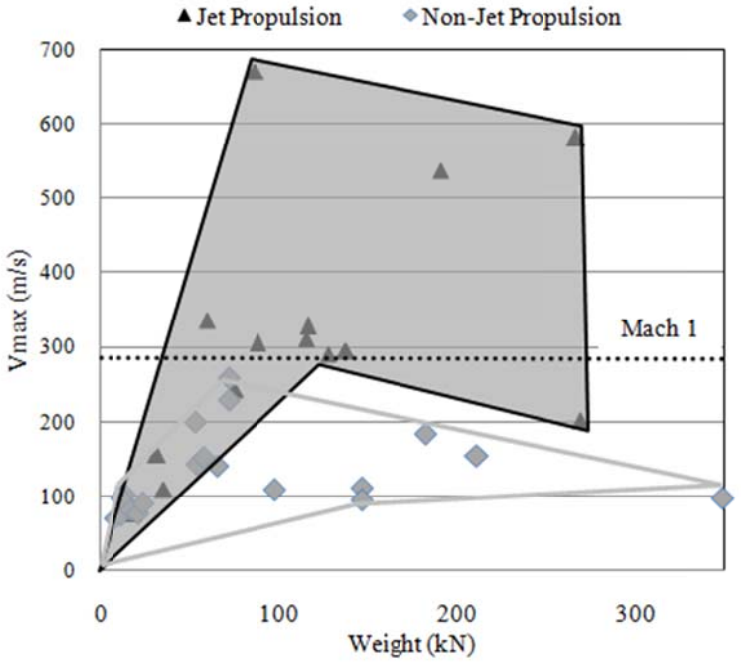

Figure 106: V_{max} -weight envelope comparison for jet and non jet propulsion driven aircraft.

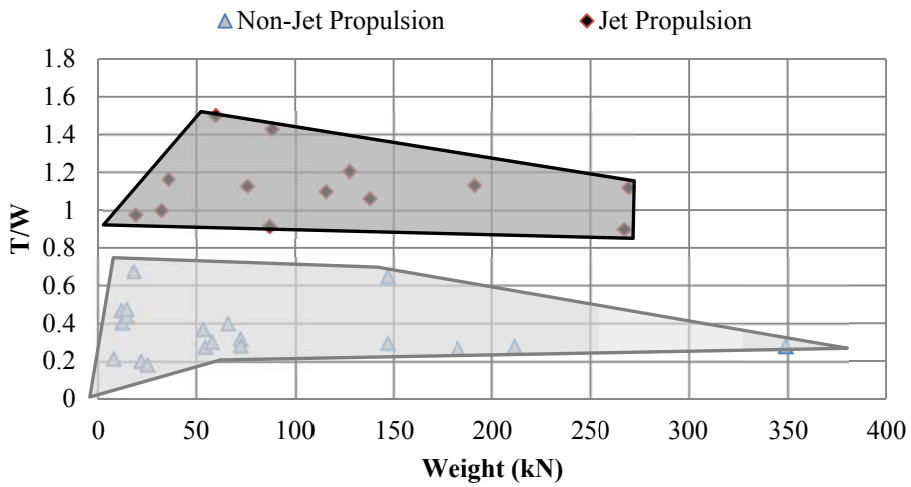

Figure 107: T/W comparison for jet and non-jet propulsion aircraft.

Figure 108 highlights the difference in power required to hover for the jet and non-jet aircraft and the non-jet proves to be way more efficient in this regard, it consumes around 4 times less power, in average, to lift a corresponding weight.

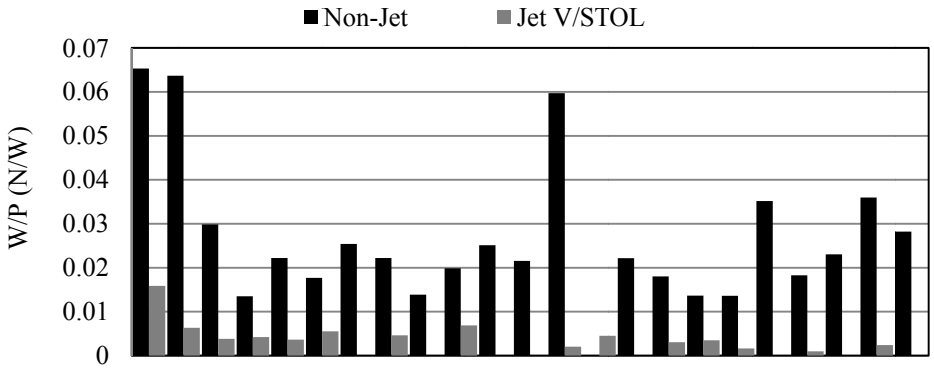

Figure 108: Power loading comparison for jet and non-jet V/STOL aircraft.

7.5 Flying Cars: The Future V/STOL Vehicles

The flying car is a category of V/STOL aircraft which has been projected for many years, but is only now approaching possible utility. These are low speed, light weight and short-range vehicles for non-traditional roles such as close area surveillance or personal transport. There are several projects currently receiving publicity, but which have so far failed to demonstrate commercial success – or in some cases, the ability to sustain flight. The projected V/STOL capable cars that might be in service in the near future are described below and their specifications are given in Table 9.

7.5.1 Mule UAV

The flying car displayed in Figure 109 is a UAV developed by Urban Aeronautics, an Israeli company, for a proposed market with the emergency services. It is also related to a projected manned aircraft, the X-Hawk, see Figure 110. The distinct feature of the vehicle is the vane control system: actuating guided vanes are installed around the main lift fan. Forward flight is achieved by ducted fans powered by the main powerplant. A scale prototype of the vehicle is reported to have been tested in August 2008 in hover and low-speed forward flight, and flight of the first Mule prototype is projected for mid-2009.

The vehicle is predicted to be capable of obtaining 51 m/s of maximum forward velocity, 2 to 4 hours of flight endurance and can lift a payload of up to 2.5kN with 480 kW of power.

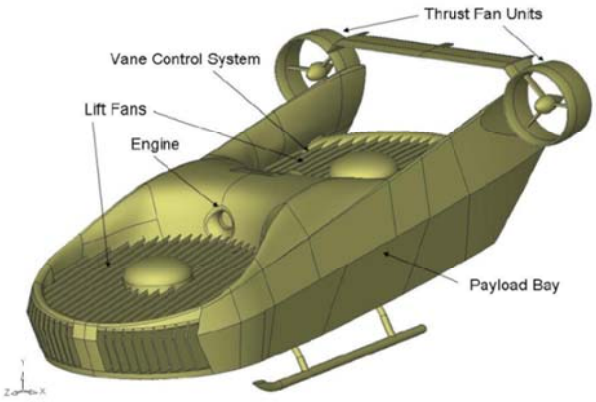

Figure 109: Mule UAV by Urban Aeronautics {photo courtesy of Urban Aeronautics [105]}.

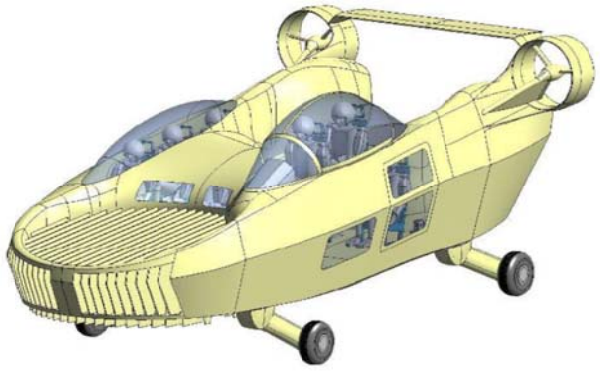

Figure 110: X-Hawk by Urban Aeronautics {photo courtesy of Urban Aeronautics [106]}

7.5.2 Moller Skycar

The Moller M400, displayed in Figure 111, claims a better performance compared to the Mule, claiming to be capable of 161 m/s top speed, carriage of up to 3.9kN of payload, 1,200 km range, despite a stated maximum weight of 1.7kN (identical to that of the Mule). The vehicle hopes to achieve stable cruise flight but has shown poor stability in hover during the test carried out by the design team [106]. Nevertheless, the vehicle seems to be the most advanced in course to a certified operational V/STOL flying car.

Figure 111: Moller Skycar M400 {photo courtesy of Moller International [107]}.

7.5.3 Skyrider

The Skyrider, depicted in Figure 112, is also based on the ducted fan technology and achieves control by the same means. It is similar to the Moller M400 to a great extent; however, promises better performance with 172m/s top speed, 1,482km range and power consumption of 522kW. The stability is of great concern as the vehicle significantly lacks static-wing area. However, the design is also implemented as a UAV, the Skyrider Scout, which comprises of a much slimmer fuselage, see Figure 113, and tends to generate lift. Nevertheless, the design is at its prototyping stage and may well be modified to tackle its weaknesses [107].

Figure 112: Skyrider {photo courtesy of Macro Industries [108]}.

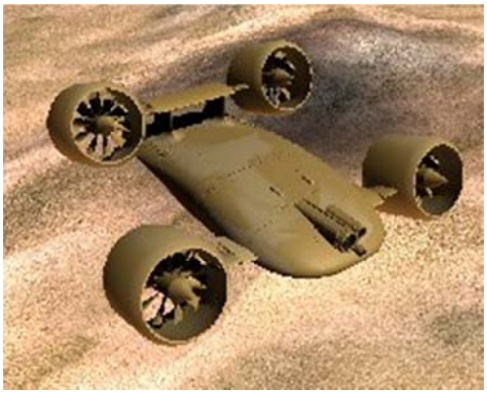

Figure 113: Skyrider Scout {photo courtesy of Macro Industries [107]}.

7.5.4 Dragonfly

The dragonfly UAV, displayed in Figure 114, is designed to serve communication purposes in the battlefield. Based around articulated ducted fan technology to achieve VTOL and also has sufficient tail area to enhance stability. Dragonfly's unique feature is the ability to quickly change its flight options from remote, to unmanned or manned result in a well-rounded vehicle with unlimited potential.

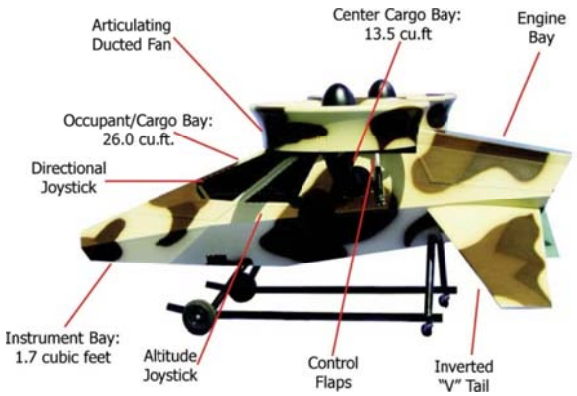

Figure 114: Dragonfly {photo courtesy of Trek Aerospace [109]}.

7.5.5 Flying Cars Performance Analysis

It is visible in the vehicles described above that the most common feature in them is the ducted/shrouded fan/propeller. The concept of ducted propellers as a suitable propulsive device for many V/STOL applications has been explored for more than half a century; the Doak 16 VZ-4 and Bell X-22A are good examples of successful application. Ducted fans, or shrouded propellers, hold promise as devices for high static thrust propulsion systems. When compared to an isolated propeller of the same diameter and power loading, ducted propellers typically produce significantly greater static thrust [110]. However, a better efficiency compared to an un-ducted propeller is only achieved at relatively lower airspeeds. Ducted fans also offer lower noise, uniform loading along the blade span and elimination of the propeller induced tip vortices subsequently eliminating induced drag. In addition, the ducted fan system offers a supplementary safety feature attributed to enclosing the rotating fan in the duct, therefore making it an attractive option for various advanced unmanned air vehicle configurations or for small/personal air vehicles as described above.

The flying cars claim to be V/STOL capable and recalling that V/STOL is composed of two separate characteristics: VTOL and STOL. Thus the feasibility study may begin by investigating whether these vehicles comply the main condition of VTOL capability that is $T/W > 1$. The thrust required for this flight mode may be evaluated by assuming that the aircraft behaves like a flat plate perpendicular to the flow as shown in Figure 115. Applying Newton's second law of motion and assuming sum of the forces act through the geometrical centre of the plate/aircraft the following relationship is derived.

$$\sum F = ma \tag{7.7}$$

$$T_{req} - D_p - W = \frac{W}{g}a \tag{7.8}$$

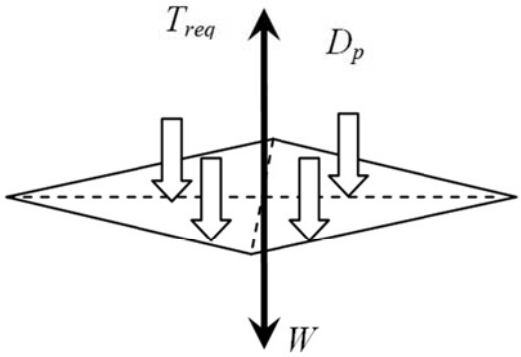

Figure 115: Flat plate theory to estimate VTOL performance.

It is known that for a VTOL aircraft the minimum vertical acceleration requirement is 0.1g so the thrust required for vertical take-off is given by

$$\Rightarrow T_{req} = 1.1W + k_s \frac{1}{2}\rho v_c^2 S_p C_{D_P} \tag{7.9}$$

where k_s is a factor to incorporate loss in lift from suck down (as described above) and C_{D_P} is the profile drag coefficient for a flat plate, a typical value taken to be 1.28 [111]. Also, the typical range of distance from ground to out of ground effect is $5m < H_{OGE} < 10m$ [112, 113]. Taking $H_{OGE} = 8m$ as mean OGE height; the climb rate v_c may be evaluated by using the equation of uniformly accelerated motion (strictly for point mass object) as

$$v_c^2 = u_i^2 + 2aH_{OGE} \tag{7.10}$$

and taking the initial velocity u_i near the ground to be zero.

$$\Rightarrow v_c = \sqrt{2aH_{OGE}} \tag{7.11}$$

Hence $v_c \geq 4$ m/s.

The thrust available for a given engine power, applying the simple momentum theory, for a ducted propeller is defined [114] as

$$\frac{P_{0.8}}{T_{ava}} = \frac{1}{4}\left[3v_c + \sqrt{{v_c}^2 + 4\phi\frac{T_{ava}}{\rho A}}\right] \tag{7.12}$$

where ϕ is the area ratio between the fan and the exhaust and $P_{0.8}$ is 80% of the engine power transmitted to the fan since ducted propellers are typically 80% efficient(104). Assuming the climb rate of the range $4 \le v_c \le 10$ has negligible effect the relationship for thrust available may be further simplified as

$$\Rightarrow T_{ava} = \left[\frac{\rho\pi}{\phi}\right]^{\frac{1}{3}}\left[P_{0.8}d\right]^{\frac{2}{3}}. \tag{7.13}$$

From the equation above it can clearly be seen that the thrust available from a ducted propeller depends on the fan diameter *d* and the ratio between the fan disc area and the duct exhaust area.

Figure 116 compares the thrust available to the thrust required to achieve VTOL for the flying cars. From the figure it is visible that the Moller M400 and the Mule are just capable of providing enough thrust for VTOL. The Dragonfly and the Skyrider lack sufficient thrust to overcome the weight and the vertical drag. However, Moller and Mule projects are comparably much advanced in reaching their prospective goals. Also, nevertheless, the publishers/designers have clearly mentioned that the performance estimates are preliminary and subject to change. So the analysis above suggests that a higher degree of precision is required for better estimation.

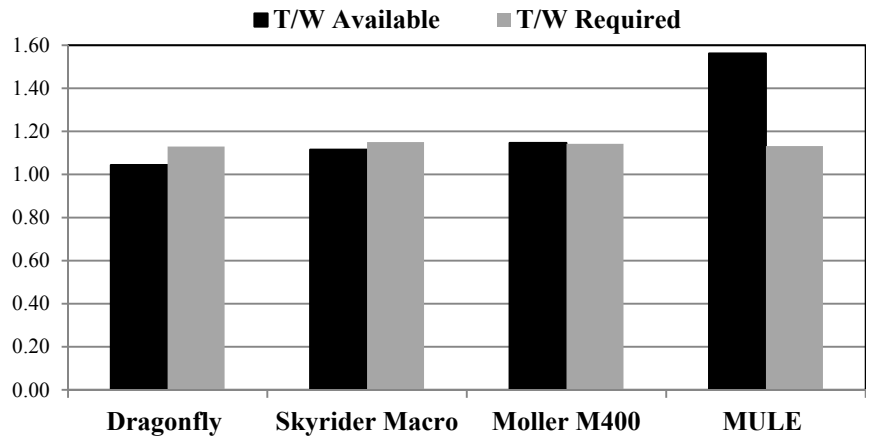

Figure 116: Chart comparing thrust available to thrust required for flying cars.

The specifications and flight performance data for the flying cars depicted above are presented in **Error! Not a valid bookmark self-reference.** and plotted in Figure 117 to Figure 120. These figures compare the flying cars performance to the past, relatively, lighter/smaller non-jet V/STOL aircraft. It is perhaps curious that, despite a lack of any real track record for any of these projects, they consistently propose significantly better performance: as defined by speed, range and payload, per power and weight, than previous aircraft. It will be interesting, should any of these projects reach fruition, so see the extent to which this claimed performance is ever achieved – the author ventures that they may not, although certainly the extensive use of ducted fan technology may carry some benefits [115].

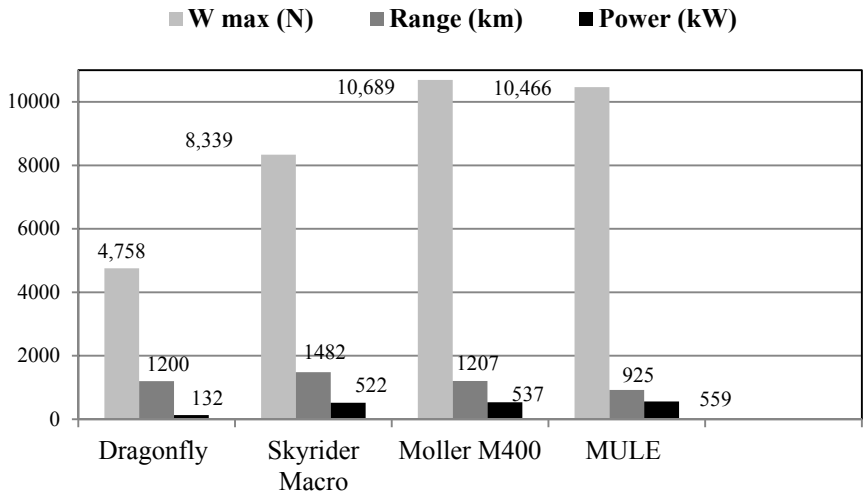

Figure 117: Flying cars specifications.

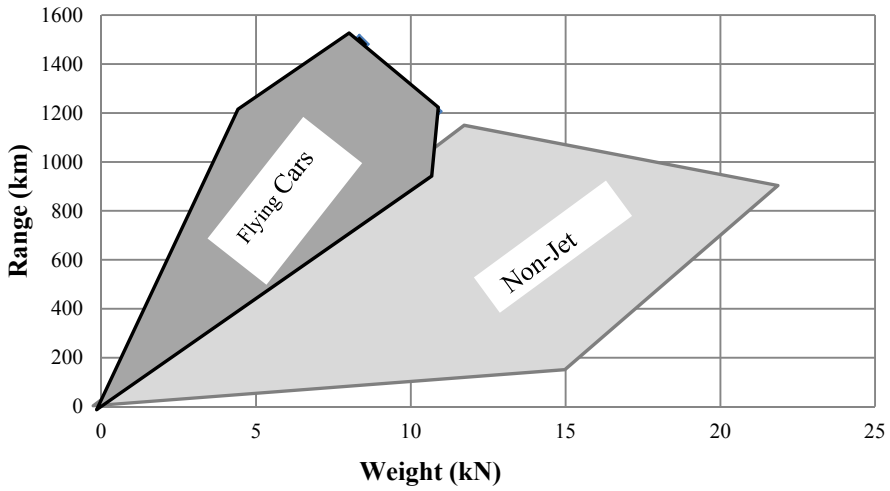

Figure 118: Range-weight envelope of future flying cars and non-jet V/STOL aircraft.

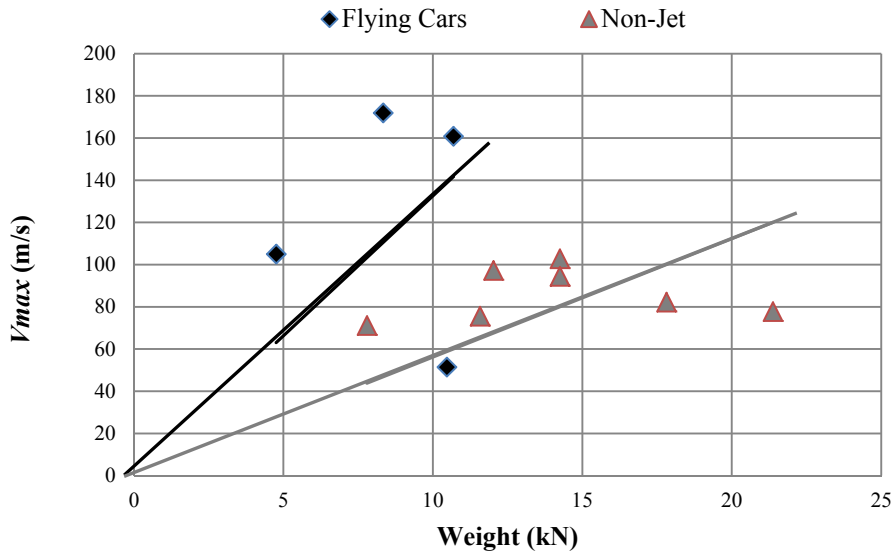

Figure 119: Maximum cruise velocity comparison of future flying cars and non-jet V/STOL aircraft.

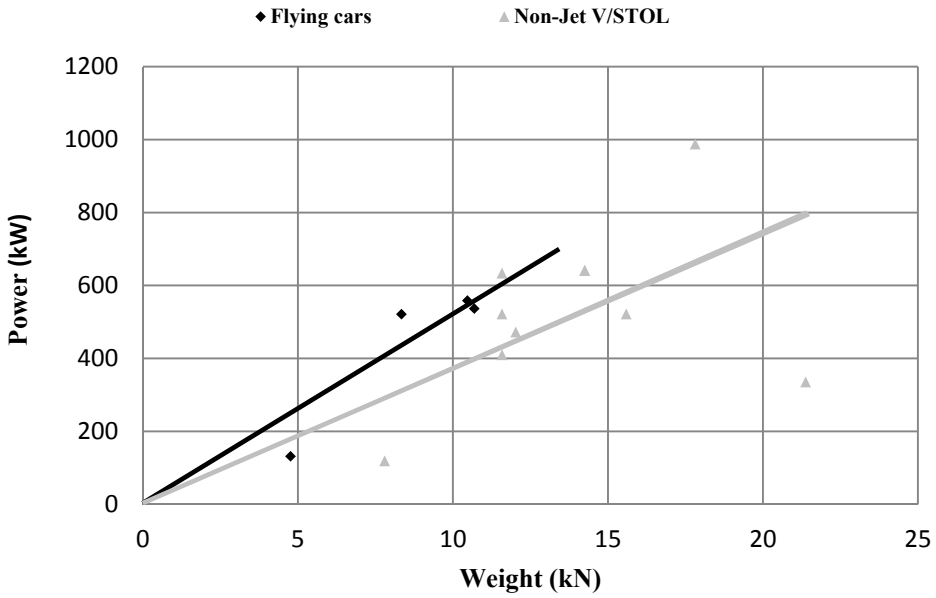

Figure 120: Power consumption comparison of flying cars and non-jet V/STOL aircraft.

7.6 Summary

The above analytical review of the past V/STOL aircraft based on their performance parameters has resulted in useful findings.

- V/STOL optimisation is best achieved with light-weight vehicles, with low wing loading.
- The V/STOL aircraft may usefully be divided into two categories, i.e. jet and non-jet, as there exists a significant performance difference between the two.
- Non-jet driven V/STOL aircraft acquire better range and consume significant less power.
- Several different propulsive arrangements have been tried on past V/STOL aircraft; however, for jet propelled aircraft a clear best solution has yet to emerge.
- An attempt has been made to define relationship between several parameters by plotting the data presented in the database and most of it depicted a nonlinear relationship.
- Performance is not linearly related to aircraft weight.
- Aerodynamic based propulsion systems best serve low speed V/STOL aircraft – most of the future V/STOL aircraft are being developed based on this fact. The dominant branch of V/STOL "the helicopter" works with an aerodynamic solution, that is, Rotary wing.
- The thrust to weight requirements of a modern fighter aircraft tend towards also satisfying the same requirement for V/STOL.
- Whilst proposed future V/STOL vehicles validate the findings above by adopting non-jet propulsion system and keeping the overall size to the minimum, most current projects claim performance unlikely to be met by comparison with historical data.

Aircraft	VTOW (kN)	Length (m)	b (m)	Vmax (m/s)	Range (km)	Thrust (kN)	Power Plant	T/W
Bell 65 ATV	-	-	-	-	-	9	(2) Fairchild J-44 (1,000 lb)	0.98
Bell X-14	19	8	10	77	483	16	(2) AS V8 Viper (1,750 lb)	1.13
Hawker P.1127 Kestrel	76	13	7	244	563	49	BS Pegasus (11,000 lb)	1.10
Yakovlev Yak-36	116	17	7	311	409	98	(2) Soyuz R-27 (11,000 lb)	1.06
Harrier GR7	138	14	9	296	483	110	Pegasus 11 Mk.103	1.24
Sea Harrier FA2	117	14	8	328	370	98	Pegasus 11-21 Mk.106	1.16
BAe/Boeing AV-8 Harrier	138	15	9	296	483	85	GR.1: RR Pegasus 6 (19,000 lb)	1.27
Boeing X-32	-	-	-	536	1573	133	PW F119-SE614 (approx 30,000 lb vertical)	1.00
Ryan X-13 Vertijet	32	7	6	156	309	44	RR Avon (10,000 lb)	1.11
SNECMA Coléoptère	-	-	-	313	700	34	SNECMA Atar 101E (7,700 lb)	1.16
Short SC.1	36	8	7	110	241	47	(5) RB.108 (2,130 lb)	1.38
Dassault Mirage V	-	-	-	-	-	77	(8) RB.108 (2,160 lb) + BS Orpheus (5,000 lb)	1.15
Dassault Mirage III V	-	16	9	626	463	275	(8) RB.162-31 (5,400 lb) + PW TF30 (18,520 lb)	1.50
EWR VJ 101C	60	16	7	335	-	88	(2) RB.145 (2750 lb) + (4) RB.145R (3560 lb a/b)	1.12
Dornier Do 31	269	21	18	202	1802	295	(2) BS Pegasus 5-2 (15,500 lb) + (8) RR RB.162-4D (4,400 lb)	1.32
Lockheed XV-4B	-	10	8	150	-	80	(6) J85-GE-19 (3,000 lb)	1.43
VFW VAK 191B	88	16	6	306	396	94	RB.193 (10,000lb) + (2) RR/MTU RB.162-81 (5,600 lb)	1.20
Yak-38 Forger	128	15	7	291	1299	126	Soyuz R-27V-300 (14,770 lb) + (2) Rybinsk RD-35-36FVR (6,725 lb)	1.13
Yakovlev Yak-141	191	18	14	536	1400	218	Soyuz R-79V-300 (30,864 a/b) + (2) Rybinsk RD-41 (9,040 lb)	1.41
Lockheed XV-4A	-	-	-	-	-	29	(2) PW JT12A-PW-3 (3,300 lb)	0.92
Rockwell XFV-12	87	13	9	671	-	133	P&W F401-PW-400 (30,000 lb a/b)	1.54
GE Ryan XV-5A	-	13	9	179	-	24	(2) GE J85-GE-5 (2,650 lb)	0.43
Lockheed Martin X-35	267	15	11	581	1931	191	P&W F119-SE611 (approx 20,000 lb vertical)	1.23

Table 7: Jet V/STOL Aircraft Data {source [116, 117, 118, 119]}.

Aircraft	VTOW (kN)	Length (m)	b (m)	Vmax (m/s)	Range (km)	Thrust (kN)	Power Plant	T/W
Transcendental Model 1G	8	7.93	11.58	71	384	2	Lycoming O-290-A (160 hp)	0.22
Bell XV-3	21	14.00	9.15	78	890	4	P&W R-985 radial (450 hp)	0.20
Curtiss-Wright X-100	16	7.90	8.64	0	-		Lycoming T53-L-1 (1,000 shp)	
Curtiss-Wright X-19	53	12.83	6.55	200	536	20	(2) Lycoming T55-L-7 (2,650 shp)	0.37
Doak 16 VZ-4	14	9.75	7.77	103	370	6	Lycoming YT53 (860 bhp)	0.44
Bell X-22A	66	12.07	11.96	141	716	26	(4) GE YT58-GE-8D (1,250 shp)	0.40
Nord 500 Cadet	12	6.69	6.08	97	-	5	(2) Allison T63-A-5A (317 shp)	0.40
Vertol 76 VZ-2	14	-	-	94	210	7	Lycoming YT53-L-1 (860 hp)	0.48
Hiller X-18	147	19.20	14.60	111	736	95	(2) Allison T40-A-14 (7,100 eshp) + West J34 (3,400 lb)	0.65
LTV/Hiller/Ryan XC-142	183	17.70	20.60	185	756	50	(4) GE T64-GE-1 (3,080 shp)	0.27
Canadair CL-84 Dynavert	54	16.34	10.16	144	547	15	(2) Lycoming T53-LTC K-4A (1,450 shp)	0.28
Bell XV-15	58	12.83	17.42	153	800	18	(2) Avco Lycoming LTC1K-4K (1,800 shp)	0.30
Bell Boeing V-22 Osprey	212	17.50	14.00	154	2200	60	(2) Allison T406-AAD-400 (6,150 shp)	0.28
Robertson VTOL	-	-	-	-	-	-	Lycoming GSO-480 (340 hp)	
Ryan 92 VZ-3 Vertiplane	12	-	-	-	-	-	Lycoming T53-L-1 (1,000 shp)	
Fairchild 224 VZ-5 Fledgling	18	10.26	9.98	82	-	12	GE YT58-GE-2 (1,024 shp)	0.67
Lockheed XFV-1	72	11.23	8.36	258	-	21	Allison YT-40-A-14 (7,100 eshp)	0.28
Convair XFY-1 Pogo	72	10.66	8.43	229	-	23	Allison YT-40-A-14 (7,100 eshp)	0.32
McDonnell XV-1	24	15.37	7.92	91	400	5	Continental R-975-19 radial (550 hp)	0.18
Fairey Rotodyne	147	17.90	27.40	95	830	44	(2) Napier Eland 7 (2,800 shp)	0.30
Vanguard Omniplane	12	-	-	-	-	-	Lycoming O-540-A1A (850 hp)	
Kamov Ka-22 Vintokryl	349	27.00	22.50	99	1200	98	(2) Soloviev D-25VK (6,500 shp)	0.28
Piasecki 16H-1 Pathfinder	12	-	-	76	1152	5	P&W Canada PT6B-2 (550 shp)	0.47
Lockheed AH-56 Cheyenne	98	16.66	15.62	109	1971	-	GE T64-GE-16 (3,435 lb)	

Table 8: Non-Jet V/STOL Aircraft Data {source [120, 121, 122, 123]}.

Flying Car	Vmax (m/s)	Range (km)	Length (m)	Wmax (kg)	Payload (kg)	Power (kW)	T/W available	T/W required
Dragonfly	105	1200	4.0	485	204	132	1.04	1.13
Skyrider Macro	172	1482	4.3	850	318	522	1.12	1.15
Moller M400	161	1207	5.9	1090	340	537	1.15	1.14
MULE	51	925	5.3	1067	227	559	1.56	1.13

Table 9: Flying cars specifications and performance data.

Chapter 8. Integrating the Annular Wing into a Useable Aircraft - A Feasibility Study

These airplanes we have today are no more than a perfection of a toy made for children to play with. My opinion is we should search for a completely different flying machine, based on other flying principles. I consider the aircraft of the future, which should have no parts in movement.

Henri Coanda, 1967

8.1 Introduction

In fact, V/STOL is the quest here and this section aims to present with conceptual design studies for appropriate classes of aircraft to demonstrate the developed wing's usability. The primary goal of the preceding chapters is to develop an understanding of controlled powered flight at different physical scales. From this, the obvious next stage is to show how flight vehicles with an annular wing could be designed, and to investigate their feasibility, focussing on the major components of the wing, compressor, powerplant and structures.

Chapter 4 has shown that the compressor (or the radial flow generator) is the component against which everything else must be scaled. Selecting the radial fan will start estimation of annular size, power requirement, and thus powerplant size and mass. This will subsequently allow initial estimation of the primary vehicle mass from which it will be inferred whether the vehicle can vertically take-off. The next task will be to quantify the achievable performance of the vehicle. The road map to vehicle integration is summarised in Figure 121.

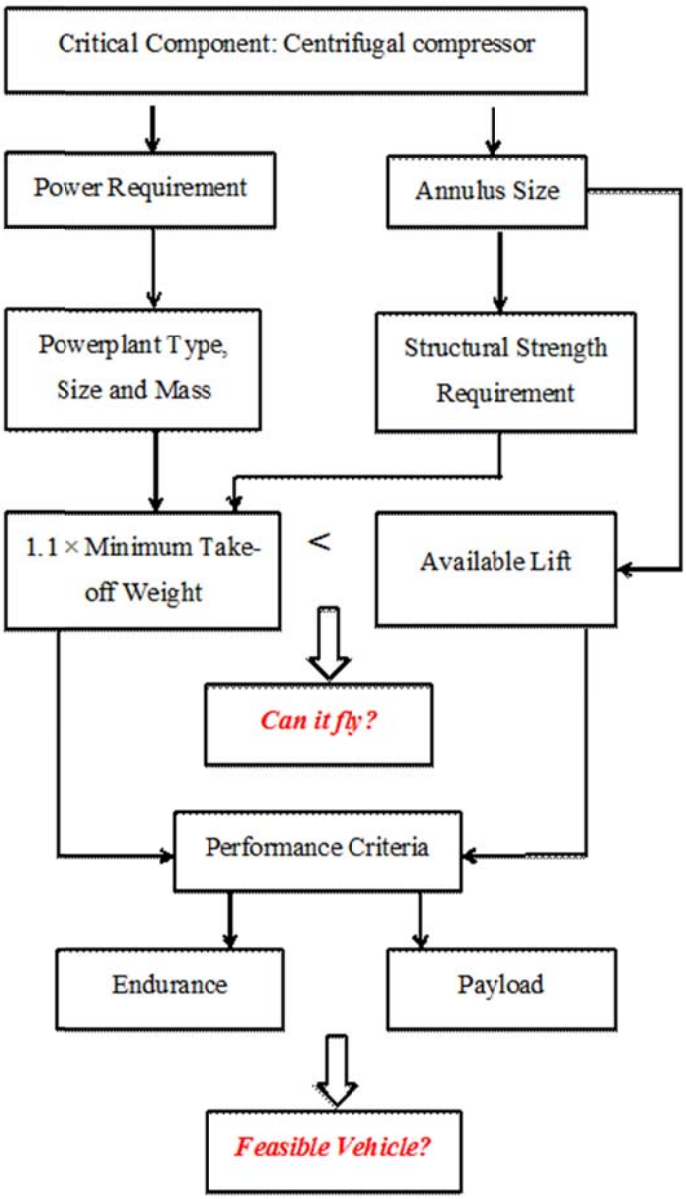

Figure 121: Conceptual design process to integrate the annular wing into a vehicle.

8.2 Structural Weight Estimation and Material Selection

To initially estimate structural mass we will assume that the largest dimension of the vehicle will be the outer diameter of annular wing. The major components are located within the wing, mounted, or (more likely) hung from it, at or close to the point of maximum lift, which will be around the 25% mean chord. The resultant forces and moments are transmitted to the wing with uniform distribution around the annulus as shown in Figure 122.

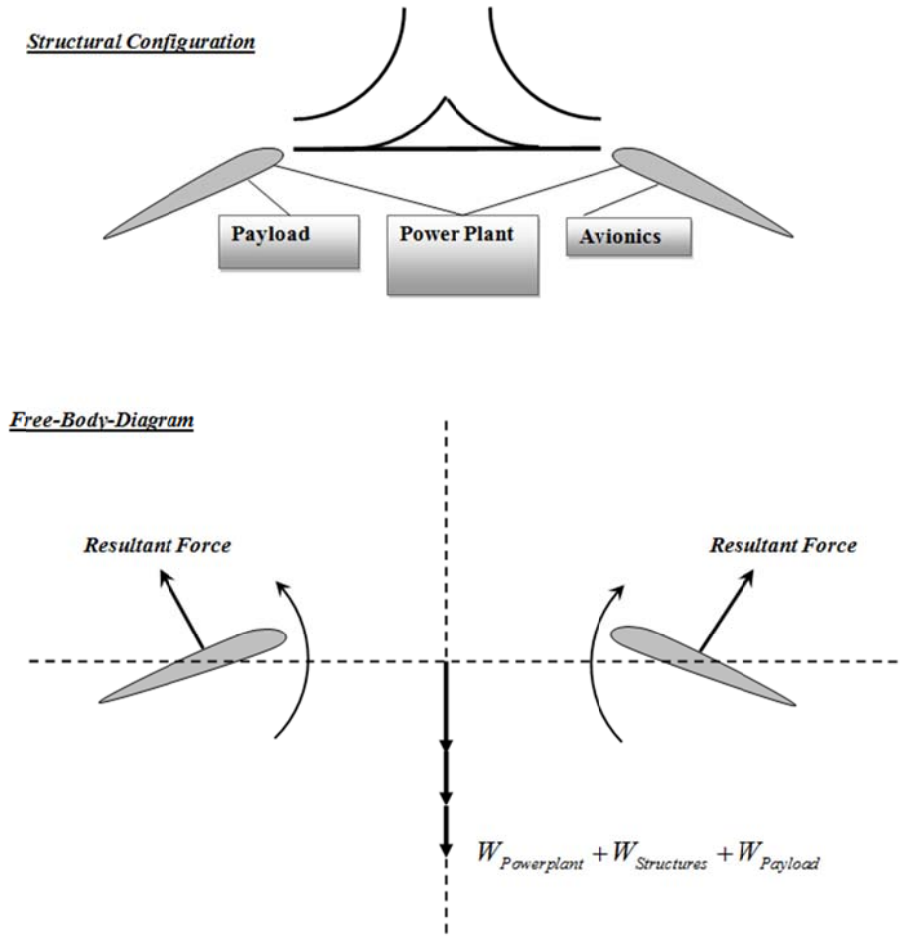

Figure 122: Simplified structural configuration and free-body-diagram (strictly schematic).

The structural mass of annular wing was deduced in Section 4.4 and evaluated by the following geometrical relationship.

$$\Rightarrow m_a \propto t_{\max} 2\pi \left(r_0 + \frac{R_0 - r_0}{4} \right) \bar{c}$$

This is most valid for micro-scale vehicles where low density materials such as foams, are feasible. For larger vehicles, typically, most of the volume covered by wing surface area is left hollow and the structural weight will be dominated by a spar and ribs. However, the shape and lift distribution, combined with an assumption of payload primarily being distributed around the main spar, mean that the peak structural loads on both the main spar and ribs, will be low: of the order of skin loads – in effect we have near 100% structural alleviation, such as typically permits ~2/3 of wing mass to be disregarded in conventional aeroplane structural approvals [124]. So, with a lightweight spar and ribs, the latter being evenly distributed around the annulus, the wing may for conceptual design purposes continue to be treated as if it is manufactured from a foam-like material of constant density; values for this density will be discussed later, but can initially be based upon wing structural density of lightweight existing aircraft of a similar scale.

8.3 Example Vehicle 1: Miniature/Micro UAV

It appears so far that the annular-wing will be most mass efficient with smallest possible overall size. The smallest current class of aircraft are micro aerial vehicles (MAV): typically with a maximum dimension of about 150 mm and maximum operating speeds of 11m/s [125]. Current MAV development is concentrating upon surveillance roles, where larger vehicles are inappropriate (for example inside buildings).

Most MAVs will operate in the Reynolds number range between 10^3 and 10^5 (Figure 124), within this range viscous forces dominate, this can cause sudden increases in drag and hence loss of efficiency. However, it is observed in Section 7.1 that VTOL capable birds with such low Reynolds numbers fly stably due to their exceptional low wing-loadings. This is similarly the case for many current MAVs, such as those shown in Figure 123 below, with large wing area and ultra-low body masses (~50g).

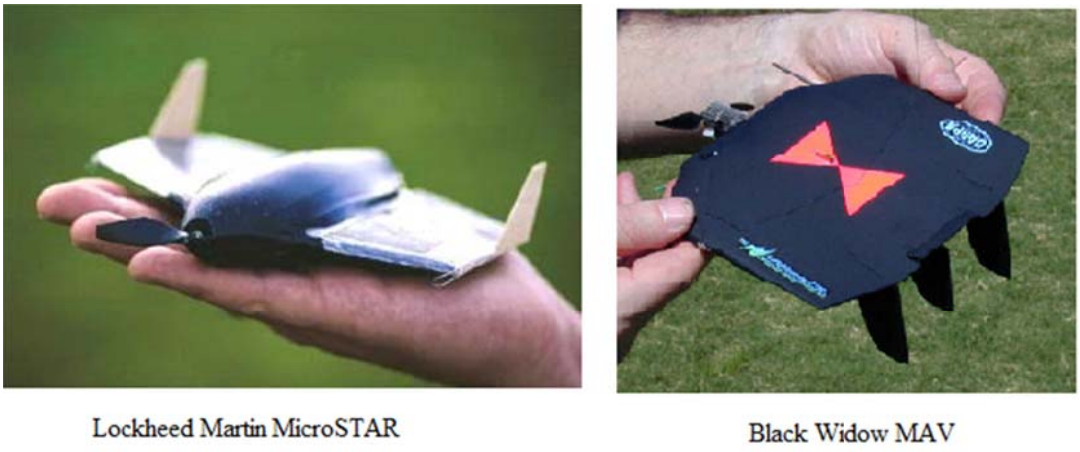

Lockheed Martin MicroSTAR

Black Widow MAV

Figure 123: Current micro-aerial vehicles [126].

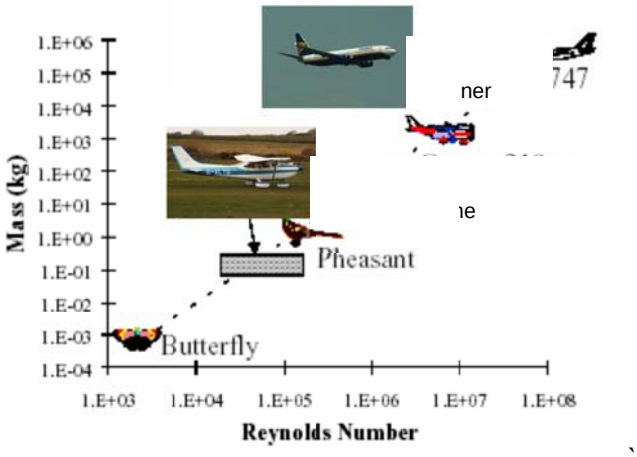

Figure 124: The Micro Air Vehicle Flight Regime Compared to birds and flight vehicles [127].

For existing MAVs, the propulsion system typically constitutes 50-80% of the vehicle mass. Sensitivity analysis of CTOL MAVs has shown that an additional 0.01 N of drag will typically decrease the endurance by 180 seconds and additional 1 gram of mass can typically decrease the endurance by 20 seconds [128]. These numbers have a significant impact on the overall performance of MAVs as the typical endurance values lie in the range of 15 to 30 minutes. This indicates that the propulsion system's thrust to weight ratio is a key parameter in maximizing endurance of an MAV. MAV propulsion system will typically have the following characteristics: [129]

- A direct drive propulsion system (which appears to be more efficient than a geared propulsion system at the MAV scale).
- Propeller efficiencies of 80% or greater (possible due to low Reynolds numbers).
- Electrical propulsion (avoiding the mass penalties of fuel storage and transmission systems).
- Motor efficiencies of 70% or greater (possible on very small electric motors).

Figure 125 displays some of the common motors used in the miniature aircraft, with one small 2-stroke internal combustion engine shown for comparison. The smallest available electric motor, the Firefly coreless planetary motor will be chosen for this conceptual design. Figure 126 shows a compatible battery and a signal receiver. Table 10 provides with specifications of some commercially available propellers for small micro-scale aircraft, with an indication of the efficiency following in Figure 128. In propeller selection at any scale, the relationship between thrust, power and size is nonlinear **[**130**]** and available design data is limited, so at this stage propeller selection will be nominal: this will be the GWS4540 with 114mm diameter giving annular size of 187mm.

The motor will require a compatible power source for which a lithium-ion battery with lowest possible mass is selected (as indicated in Figure 127). The battery life, and thus vehicle endurance, will subsequently be estimated as:

$$Battery\_life(\text{sec}onds) \approx \frac{Battery\_Capacity(Joules)}{Power\_Consumption(Watts)}$$

Noting that the motor may well be operating below capacity to match the propeller or performance requirements, thus the power consumption should be factored accordingly (e.g. if a 10W motor is running at 7W to match a 7W propeller, then the power consumption is 7W, not the 10W motor capacity).

Figure 125: Common torque generator systems for micro/miniature vehicles {data source Ref [131]}.

Figure 126: 250mah / 900J Lithium Battery (Mass: 24 grammes, Volume: 16 x 21 x 40mm) and Ch Receiver MICROSTAMP 4 [132].

	Diameter (mm)	Current (Amps)	Power (Watts)	Speed (rpm)	Thrust (grams)	Lift/Thrust by Coanda Effect
GWS4350	109	0.26	2.5	6300	26	18.2
GWS4540	114	0.47	3.3	6100	30	21
GWS4530	114	0.69	7.1	9000	56	39.2
GWS4540	114	0.85	9	8600	64	44.8
GWS5030	127	0.42	3	6200	36	25.2
GWS5030	127	0.79	8.3	8800	74	51.8
GWS6030	152	0.64	3.7	6000	44	30.8
GWS7035	178	0.82	5.8	5400	60	42

Table 10: Data collected for different propellers used with coreless planetary motor [133].

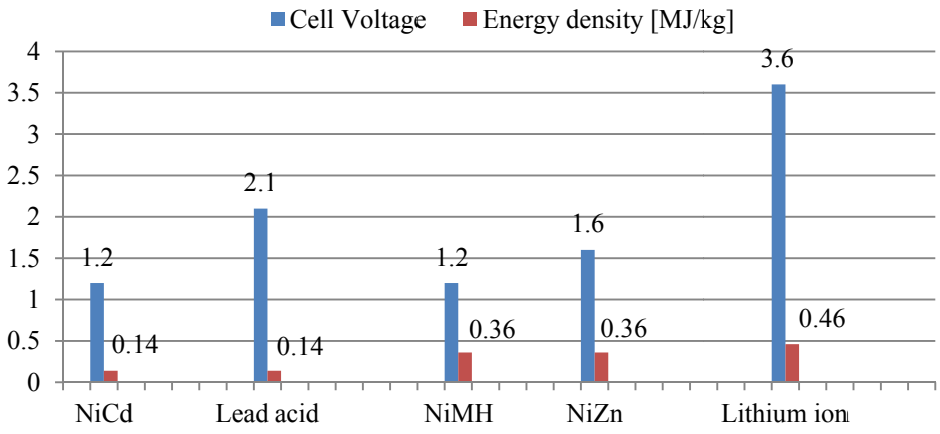

Figure 127: Energy density and voltage for different closed batteries {data source Ref [134]}

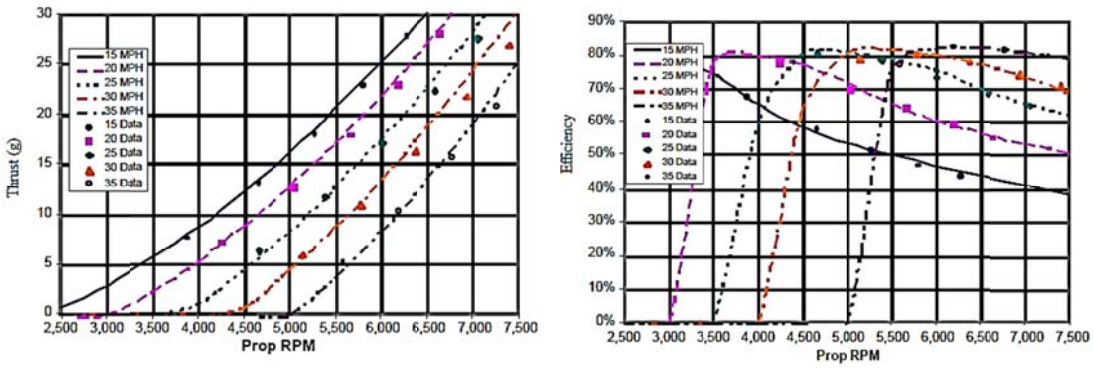

Figure 128: Performance characteristics of a 97mm diameter propeller {from Ref [129]}.

Table 11 indicates now the mass of each of the major components. The minimum take-off mass (excluding any payload) is approximately 37.2 grammes, indicating that for VTOL, at-least 0.40 N thrust (=37.2g x 1.1 = 40.9g at 1g) will be required. Now, referring to Table 10 for thrust available the previously selected GWS4540 is unsuitable, but the slightly larger GWS4530, generating 0.55 N of thrust (=56g at 1g) and with a mass of 1.25g [135] appears more suitable.

Payload and endurance calculations below show that larger power setting achieves better payloads and a lower will achieve better endurance – which is intuitively correct and consistent with all other scales of aircraft. Therefore, a trade-off may occur depending on the exact function of this vehicle.

Component	Specification	Mass (grammes)
Propeller	GWS4530 (114mm)	1.2
Batteries	250mah Lithium Battery	24
Electric Motor	Firefly Coreless Planetary Motor	14
Structure	Foam (1500g/m^3)	8
Avionics	4 Ch Receiver MICROSTAMP 4	4
Minimum Take-off Mass		37.2

Table 11: Mass allocation for the primary flight system of MAV.

So, let us consider briefly the performance and potential mission of this vehicle, then the form of it. Let us assume a mass of 37.2g (from Table 11) for the empty vehicle, and a 10g payload, giving a gross mass of 47.2g, or weight of 0.463N. Available thrust at the propeller's optimised condition of 7.1W is 0.549N (56g) – an excess of 18.6% thrust over weight; this is satisfactory for both VTOL and for sustained flight. Constructing a power budget for a flight, Table 13 indicates that a mission endurance of around 149s: 2½ minutes is potentially achievable; this is short but may fit the vehicle for a short term emergency services surveillance mission inside a building carrying a micro scale camera/transmitter package. Nevertheless, its hover capability will provide a further benefit with clearer image capturing compared to a forward moving vehicle.

For comparison Table 12 below shows a selection of current MAVs in use; it will be seen that at a similar size to this study, the Black Widow, which is a successful 150mm span electric MAV capable of downlinking live colour video from a range of 1.8 km, and provides a good benchmark, is of a similar size and mass, but has a substantially (order of magnitude) better endurance and thus range. This clearly

shows that the annular-Coanda wingform MAV must find advantages over conventional forward flight forms to hold any advantage – it is likely that this advantage, if it exists, will depend upon the ability to hover.

It is then interesting to conject the form of this vehicle. Figure 129 conjects as to the form of such an MAV – with the propeller mounted over the annulus driven by a thin shaft and bevel gear from a small electrical motor protruding from the wing surface, whilst the battery, any control circuitry and mission payload are contained within the wing annulus. If required, fine structural wires, similar to external bracing and undercarriage on a conventional microlight or vintage aeroplane, may be used to support the structure. A circular tapered fuselage is chosen to have a minimum possible profile drag which for preliminary calculation purpose is taken to be equal to of a semi sphere ($C_{D_P} \sim 0.42$).

		Black Widow	WASP	HoverFly C	Carolo 40	Carolo 50	Dragon Slayer
Wingspan	*b [mm]*	152	330	~200	400	490	330
Length	*l [mm]*	152	-	-	-	-	-
Wing area	*S [m²]*	0.0195	-	-	-	-	-
Weight	*W [g]*	80	170	180	350	550	300
Endurance	*t [min]*	30	107	13.2	45	-	35
Airspeed	*V [m/s]*	13.4	-	15-20	20	15-20	18-40
configuration		flying wing	flying wing	flying wing	canard	classical	flying wing
planform		modified rectangular	tapered	rectangular	semi-elliptical	rectangular , T-tail	delta

Table 12: Trend study of MAVs {from [126]}.

Phase	*Thrust (N)*	*Time (s)*	*Power (W)*	**Energy Usage (J)**
Take-off and initial climb, full power	0.549	20	7.1	142
Cruise, power set to give thrust = weight, power scaling with thrust (first approximation only)	0.463	119	6.0	713
Descent and landing, assuming thrust = 75% weight (likely all that is available at end of battery life)	0.347	10	4.5	45
	Total:	149	-	900

Table 13: power and time budget for sample annular MAV on surveillance mission.

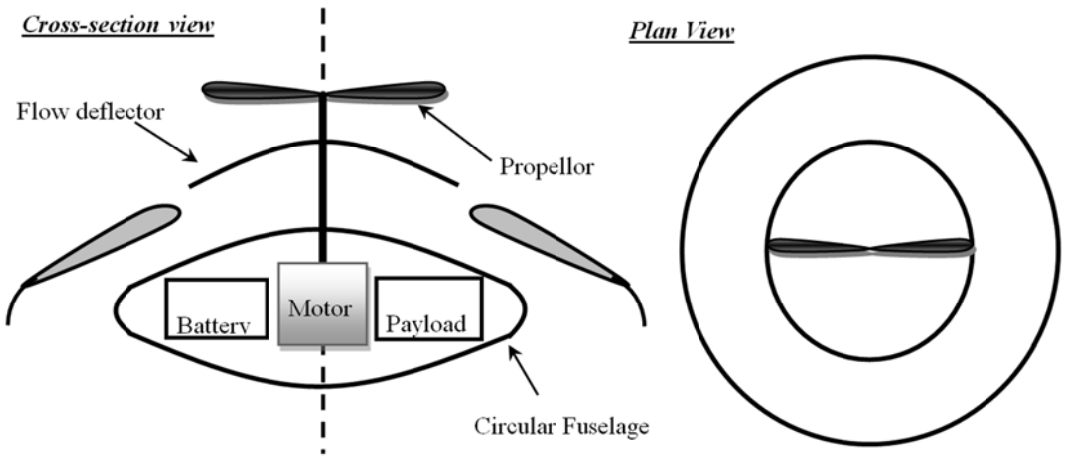

Figure 129: Conjected form of Annular UAV with electric propulsion.

8.4 Example Vehicle 2: Mid-Scale Unmanned Aerial Vehicle

Currently UAVs are used primarily for military purposes; however, there has been considerable discussion about other potential roles including urban area surveillance or 3-D imaging for everyday improving mapping. This variety of roles precludes easy classification in terms of weight, size or endurance, as illustrated by Figure 130, Figure 131 and Figure 132 below. Typically smaller vehicles will achieve better endurance and payload fraction values.

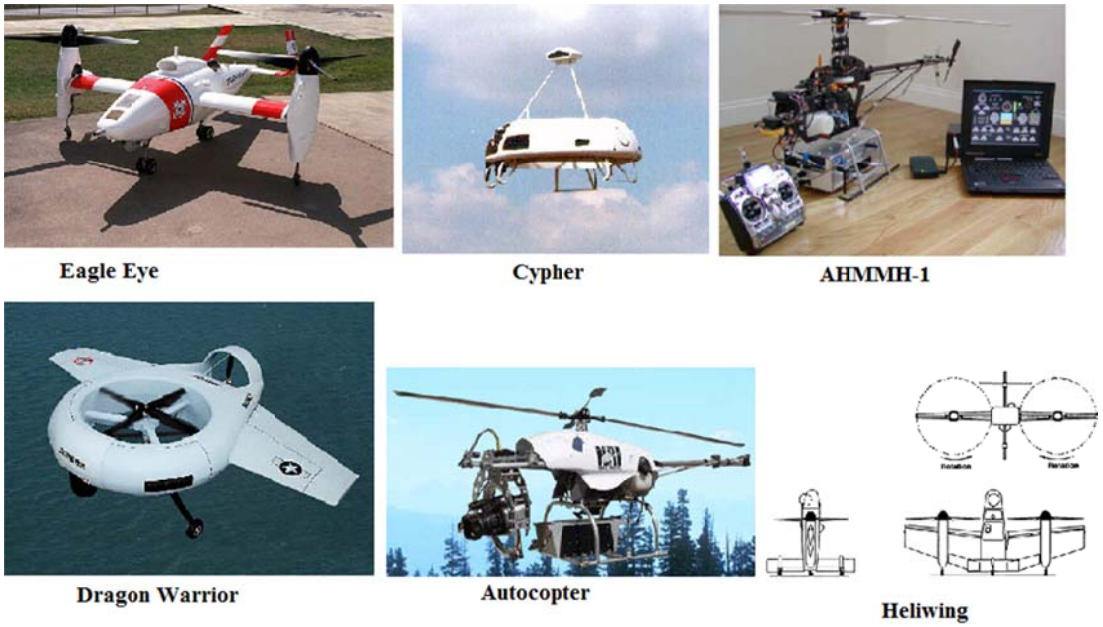

Figure 130: Illustrations of small VTOL UAVs.

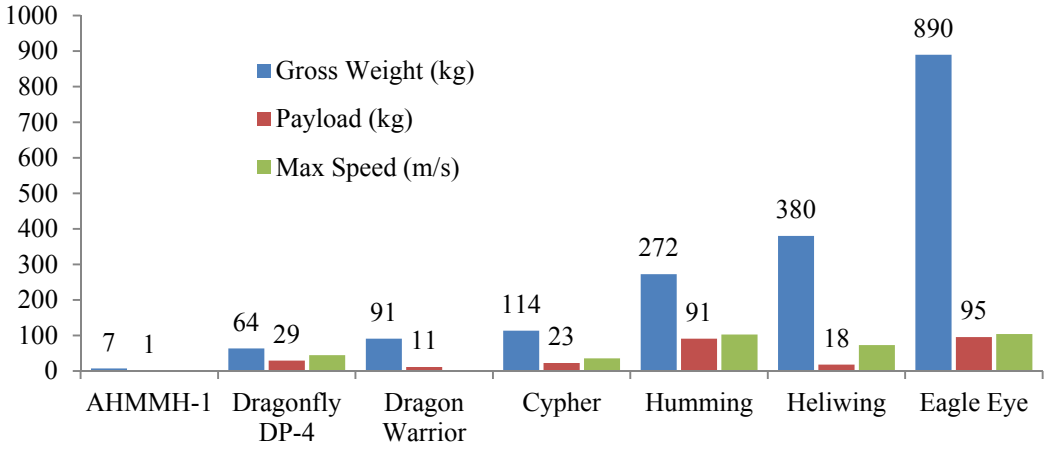

Figure 131: VTOL UAV Data {data source Ref [136]}

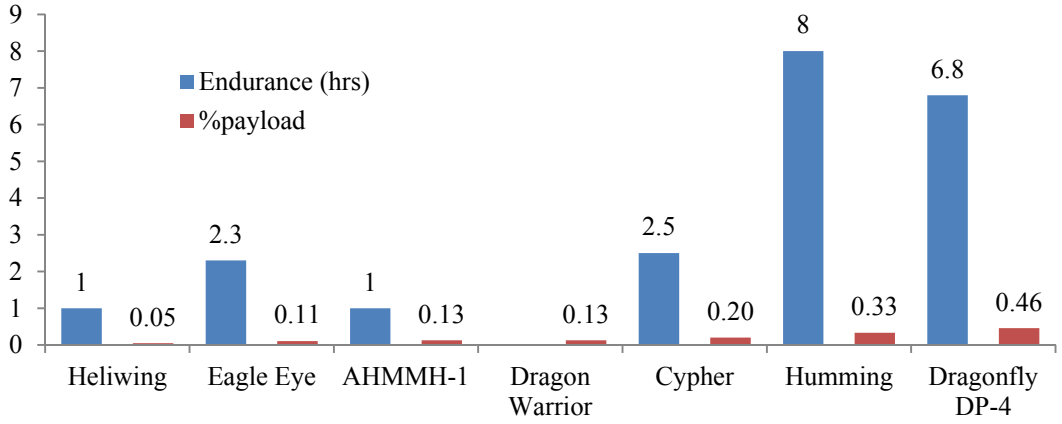

Figure 132: VTOL UAV performance Chart.

So, for the time being, this scale will not be considered further since it offers no new lessons not found above for the MAV or in the following sections for larger vehicles.

8.5 Example Vehicle 3: Flying Car Scale with internal combustion engine

In the light aircraft design community, it has become common practice to design aircraft around common and preferred powerplant combinations; this approach will also be taken here in selecting the Rotax 914 liquid cooled 4-stroke light aircraft engine, and an Airmaster AP332 propeller, shown in Figure 133, this is a constant speed propeller specifically developed for Rotax 900 series engines (note: constant

speed propellers are more commonly used with these engines, but a variable pitch / constant speed propeller offers certain efficiency advantages). Selecting this propulsion system enables us to again estimate primary vehicle components; this is shown in Table 14 below, which also assumes a standard pilot of 86kg (as in accordance with [124]).

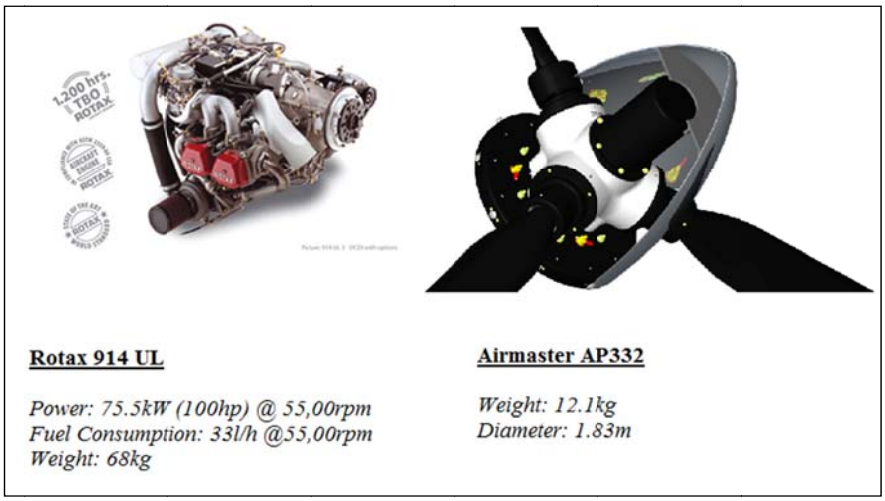

Figure 133: Engine and Propeller specifications [137].

Component	Specification	Mass (kg)
Propeller	Airmaster AP332 (1.83m)	12
Fuel	50 litres (90mins) + 5kg lightweight tank and hosing	40
Engine	Rotax 914 UL (100hp)	68
Structure including wing	Represented by mass of the Alatus AL12 Ultralight Sailplane [138]	90
Avionics	AC200 SmartPitch	2
Pilot	Standard pilot as per CS.VLA	86
Minimum Take-off Mass		298

Table 14: Mass allocation for the primary flight system (flying car with Rotax 914 engine).

Figure 134 shows thrust characteristics of the fixed pitch propeller, indicating the static / fine pitch condition which has been estimated as equivalent to an air velocity through the propeller of about 33 m/s. This indicates that the static thrust generated by the fan is only 1.8KN (175kgf) which is approximately half of the 298kg minimum take-off mass. So, with currently available technology, an internal combustion engine powered "flying car" at the single seat scale would not be feasible.

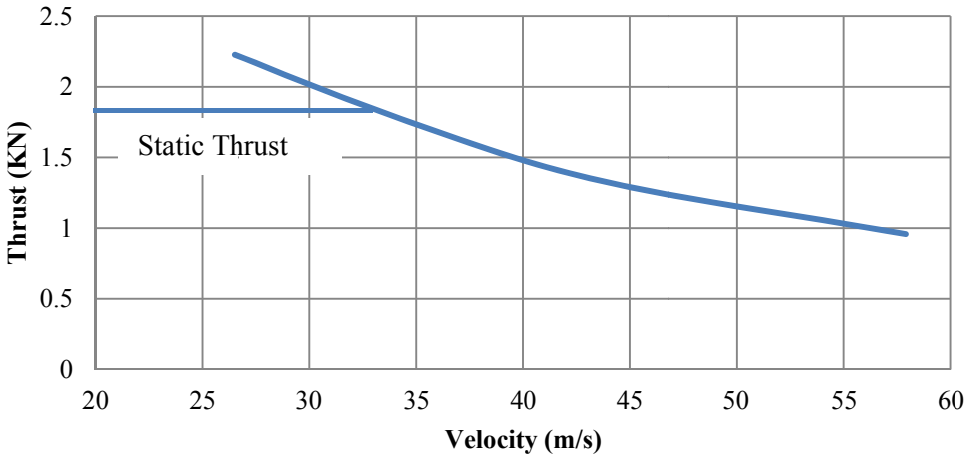

Figure 134: Thrust generated by propellers at different flow velocities {derived from [139]}.

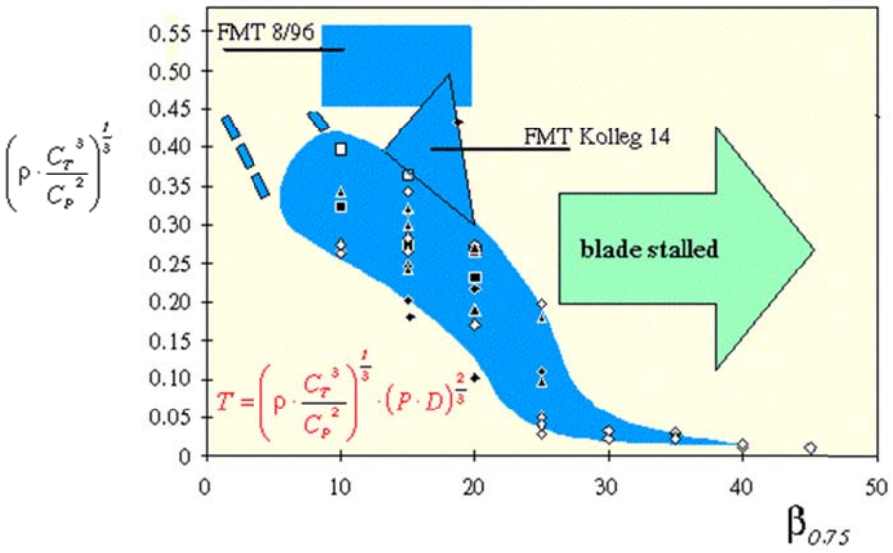

Figure 135: Static thrust parameter (units: $kg^{1/3}$ / m) versus blade angle for different propellers [140].

Component	*Specification*	*Mass (kg)*
Propeller	Estimated propeller mass	20
Fuel	200 litres (90mins at 60% available power) + 15kg lightweight tank and hosing	195
Engine	P&WC PT6a-6	129
Structure including wing	50% greater than that for 914 engined vehicle at Table 14	135
Avionics	AC200 Smart Pitch	2
Pilot	Standard pilot as per CS.VLA	86
Minimum Take-off Mass		567

Table 15: Mass allocation for the primary flight system (flying car with P&WC PT6a-6 engine).

However, lightweight turbo-shaft engines are readily available, for example the Pratt and Whitney Canada PT6 family. Taking for example the P&W PT6a-6 at its most basic low power free turbine model, this has a minimum available power output of 550hp which will generate a thrust of ~9kN whilst only requiring a slightly larger installed mass of 129kg [141]. This apparently permits a feasible "flying car" scale vehicle, along the lines given in Table 15.

This offers the potential of a turboshaft operated flying car, which may be feasible although will clearly be an expensive way of generating low performance single seat flight compared to most currently available options – an aircraft role would have to be found which justified this cost compared to the well-established helicopter option, given the low payload and low endurance. Nonetheless, such a role may potentially be found – most likely a reconnaissance or low-payload role in an environment where FOD (Foreign Object Damage) is a major concern – such as for example into confined spaced in jungle or urban areas. A conceptual design for such vehicle is generated as shown in Figure 136. The proposal is to integrate the annular wing onto a radial flow generator driven by a turboshaft engine, also, driving a propeller to generate thrust in translational flight mode. The fuselage may be split into two compartments; one housing the powerplant, fuel/engine, and the other payload. Canards may be integrated to encounter pitching moment resulting from reverse flow, as discussed in Section 4.7, and hence may also offer better pitch stability.

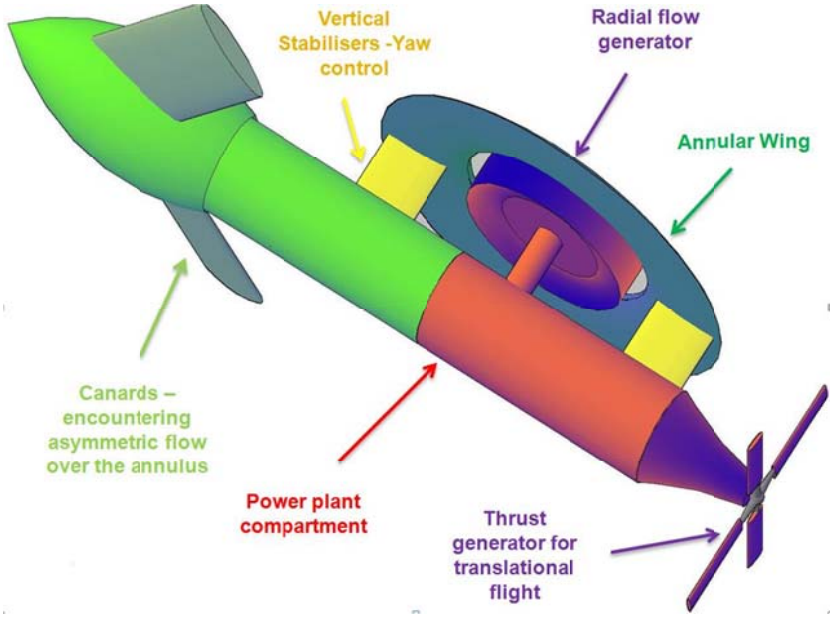

Figure 136: A conceptual sketch of single seat turboshaft powered flying car.

8.6 Example Vehicle 4: Large Vehicle with Gas Turbine Engine

The next and obvious scale here would be a larger vehicle making fuller use of the capabilities of gas turbine engine technology. There are three major kinds of gas turbine engines: turbojet, turbofan and turboshaft/turbopropeller. This section proposes the integration of a high-bypass turbofan engine into an annular wing vehicle, a possible configuration for which is shown in Figure 137. The arrangement is such that the by-pass flow, or the cold air from the fan, is extracted and blown over the annular wing which further deflects the flow vertically downwards. Typically, for a turbofan engine around 70% of the thrust is generated by the fan and 30% from the hot exhaust gases [142]. This derives a new relationship of net lift/thrust generated by the annular-turbofan configuration.

$$Lift_{net} = \underbrace{0.3Thrust_{engine}}_{\text{Thrust from hot-gas impulse}} + \underbrace{0.65}_{\text{Annular Reduction Factor}} \times \underbrace{\left(0.7 \times Thrust_{engine}\right)}_{\text{Thrust from by-pass flow}} \tag{8.1}$$

$$\Rightarrow L_{net} \approx 0.76T_{engine} \tag{8.2}$$

The above expression shows that this arrangement, with partial axial flow, achieves significantly higher net lift/thrust compared to pure Coanda lift, although from operating experience there will be substantial operational concerns – particularly those associated with damage to the surface below the aircraft during take-off [143]. As shown in Chapter 7 and [144] the thrust to weight ratio for a typical combat aircraft is in excess of one, hence, making their propulsion system a suitable design starting point for V/STOL applications, although some such aeroplanes with low bypass ratios will not suit this application whilst large commercial engines may well do. Figure 138 displays specifications of a range of engines used on combat aircraft; these engines have a range of bypass ratio from 0.4 to 6.42. The thrust to weight ratio of these engines is plotted versus the fan diameter in Figure 139; there exists no pattern/relationship, the installed thrust to weight values for these engines range from 4 to 10 with a mean of 6.

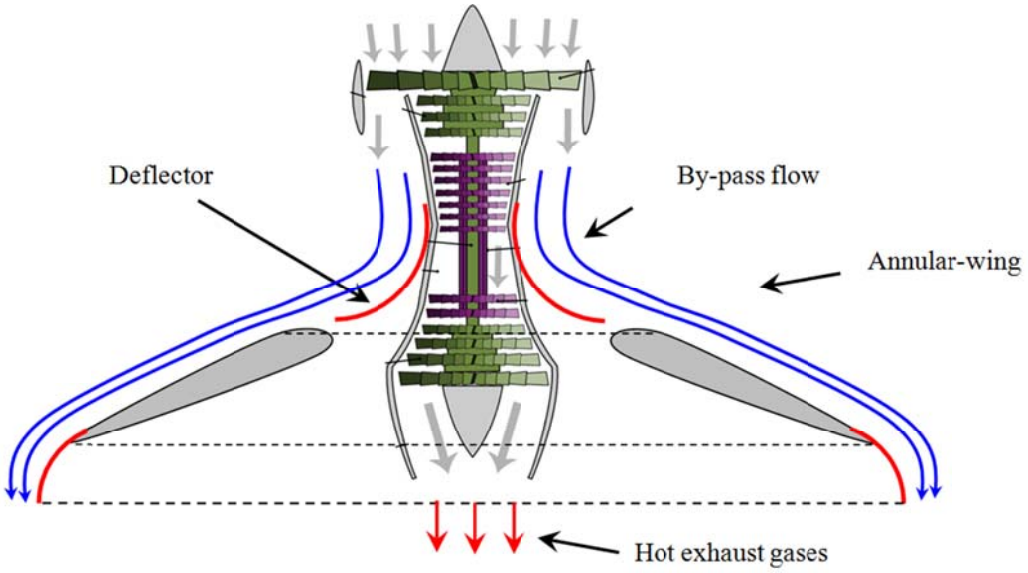

Figure 137: Possible configuration to integrate the annular-wing around a turbofan engine.

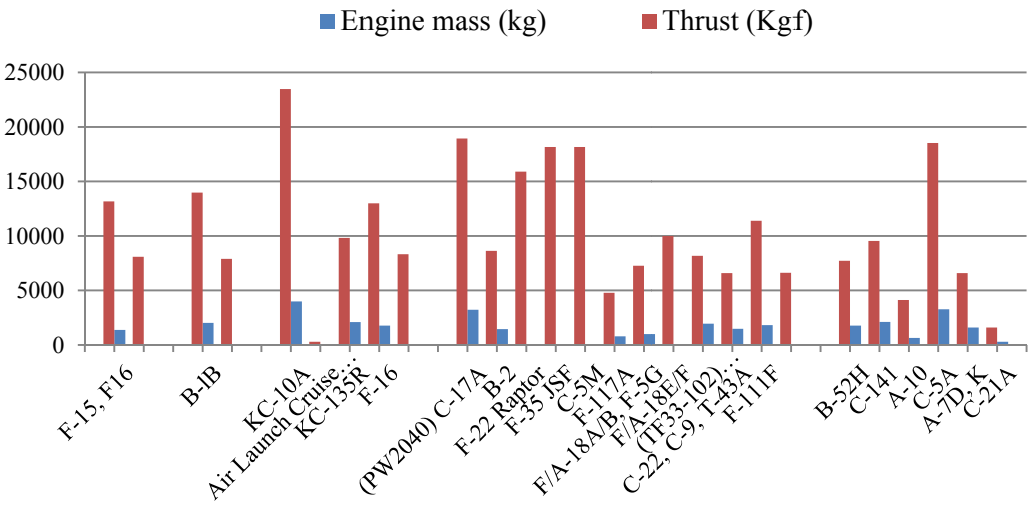

Figure 138: Military aircraft engine data {data source [145]}.

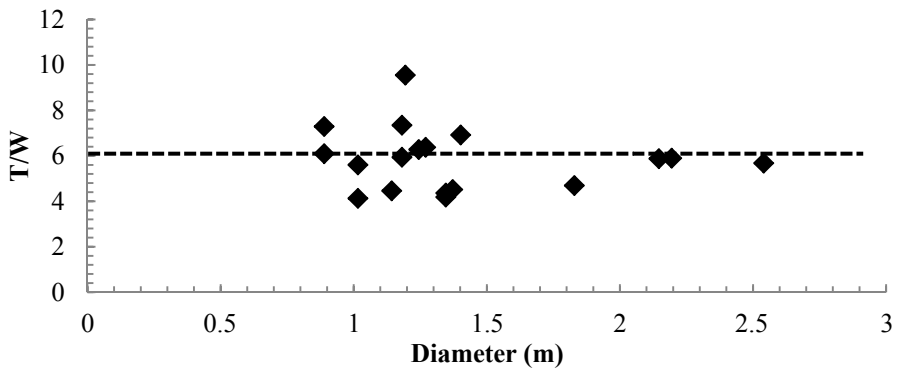

Figure 139: Thrust to weight ratio versus outer diameter of military aircraft engines.

Generally, an engine's performance is evaluated from its thrust to weight ratio and thrust specific fuel consumption TSFC. However, for this particular configuration another crucial parameter, the diameter of the fan, needs to be considered. The specific performance parameter may be defined as $\left(\frac{T}{W}\right)\left(\frac{1}{TSFC \times diameter}\right)$, which must then be maximised to ensure maximum endurance and payload, whilst keeping the diameter minimum to reduce the overall vehicle size and thus mass. The derived performance parameter is plotted in Figure 140 for the range of turbofan engines presented in Figure 138. The relationship between engine mass and the performance parameter is nonlinear forming two curves with lower and upper limits. There exists clear maxima and hence maximum performance may be achieved by the engine "General Electric T34" used on military aircraft A-10 Thunderbolt II and S-3 Viking. An interesting point to be noted here is that the winning engine has the highest bypass ratio (6.42) from the range considered; this suggests that engines with higher bypass ratio may offer better performance.

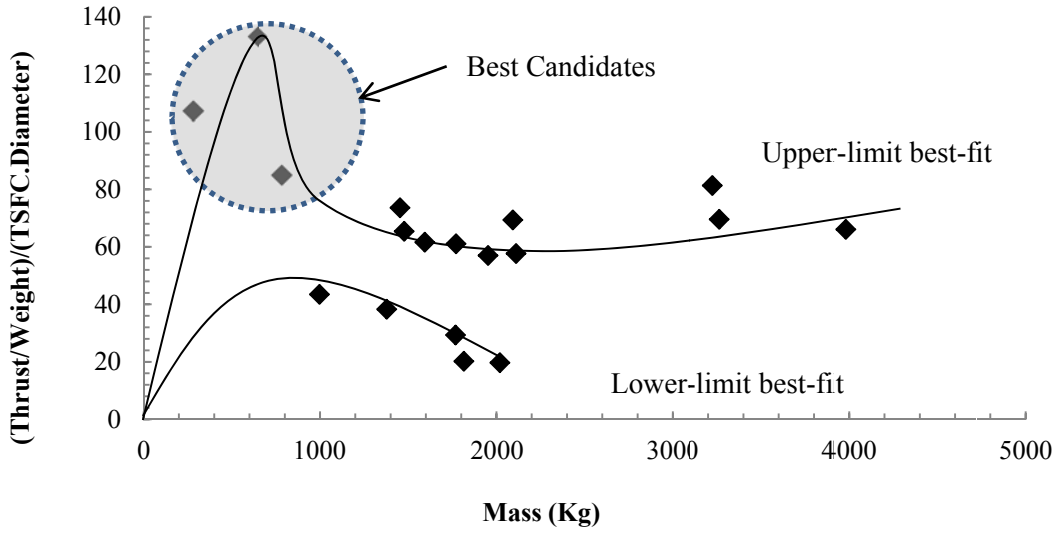

Figure 140: Performance parameter versus mass of engine.

Selecting the best engine allows mass of the whole vehicle to be deduced in the table below.

The flight endurance is given by

$$Endurance = \frac{Mass_{fuel}}{Thrust_{req.} \times TSFC} \tag{8.3}$$

where the required thrust is defined as

$$T_{req} = \underbrace{1.1 \times 1.32}_{\text{Reduction Factor}} \times \left(W_e + W_f \right) \tag{8.4}$$

This might potentially now be extended to a conceptual vehicle in the class of the Hawker Harrier, such as shown in Figure 141. In this configuration the exhaust flow momentum would need to be deflected to generate forward thrust in cruise flight: in effect the core flow provides forward propulsion whilst the bypass flow provides lift, unlike a Harrier in semi-jetborne flight.

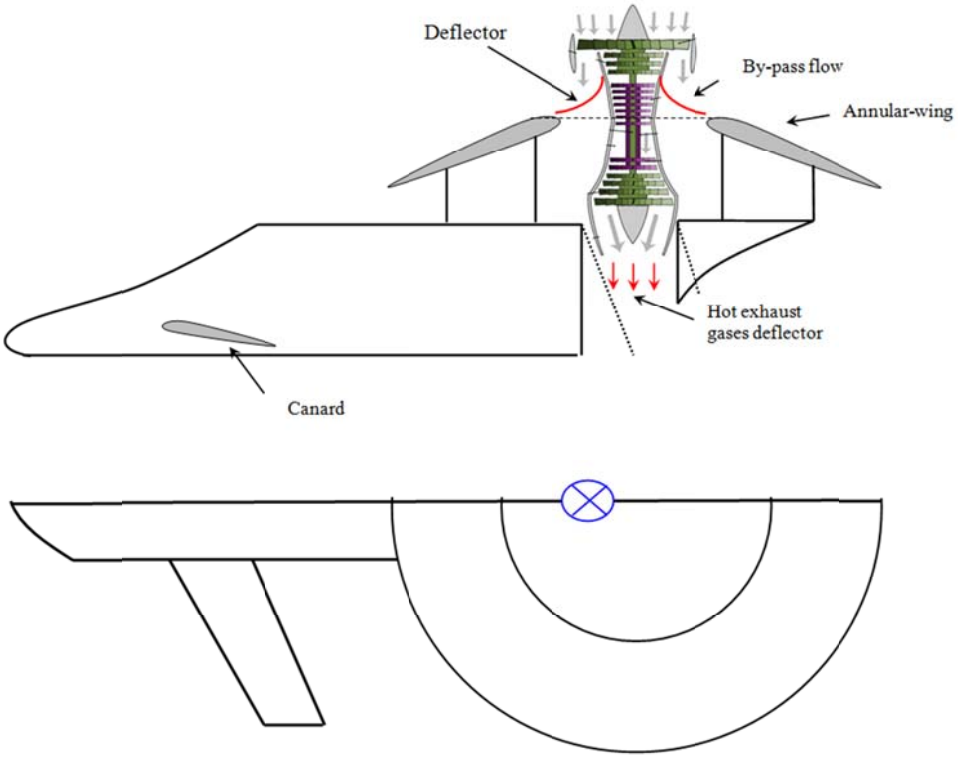

Figure 141: Sketch and basic configuration.

For comparison the specifications of the Harrier are presented in Table 16.

Length:	14.12 m
Wingspan:	9.25 m
Height:	3.55 m
Empty weight:	6,340 kg
Loaded weight:	10,410 kg
Maximum speed:	297m/s at sea level
Range:	2,200 km
Combat radius:	556 km
Ferry range:	3,300 km
Rate of climb:	75 m/s

Table 16: Specification of an AV-8B Harrier {from [146]}

The predicted mass budget for this aircraft is given in Table 17 below.

Component	Specification	Mass (kg)
Engine	F108-CF-100 (1.83m diameter)	2093
Fuel	1000 litres	3000
Payload		-
Structure	CFRP (1600kg/m^3)	1200
Avionics		250
Minimum Take-off Mass		6543

	Payload Fraction %	Endurance (mins)
@T=1.1W	7	56
@Tmax	36	50

Table 17, Component mass breakdown for proposed Harrier-like annular-Coanda vehicle

Whilst this aircraft may have an equivalent weapons carriage role to that of the Harrier, it appears unlikely that it will at the current state of technology compare to it in terms of manoeuvrability or high speed flight.

8.7 Performance Summary

This section has shown that an annular-Coanda wing vehicle is feasible at MAV scale, at a single-seat flying car scale if a turboshaft/turboprop (but not internal combustion) engine is used, and at a large Harrier-like scale by integrating a large high bypass turbofan engine into the annular wing into a new type of combined lift/propulsion system. In none of these cases the annular-Coanda wing offers performance advantages over existing technology, as defined by range, endurance or payload fraction. The advantage then, if it exists, will concern the specific characteristics of this wing – that is the combination of VTOL capability, and lack of external moving parts of lower/forward surface air intakes.

The achievable Endurance and Payload performance is evaluated in Figure 142 and Figure 143 respectively for a range of take-off mass; each mass corresponds to a minimum and an absolute performance value. The maximum values on Endurance chart correspond to minimum values on Payload chart. The performance charts display two regions, with regard to powerplant, split by an asymptote where the flight is not possible at that scale “flying car with internal combustion”. Hence,

indicating that internal combustion engines are not feasible for medium scale annular wing configuration.

Figure 144 summarises the achievable performance range of different sized vehicles that may fall into certain class of aircraft. The net performance is taken as a product of endurance and payload fraction for two different thrust settings: 1) thrust required for minimum take-off weight and 2) maximum engine thrust available. Several crucial finding are derived from the above feasibility study and these are highlighted below.

- For a given class of propulsion, the performance must be evaluated with regard to the size/diameter of fan/compressor, particularly because this influences vehicle size and thus empty mass.
- A turbofan engine with high bypass ratio achieves relatively better performance range for the Coanda-annular wing configuration
- Maximum performance is achieved by selecting the engine with maximum specified performance parameter, defined above, that includes the fan diameter
- A larger vehicle (>600kg) with turbofan engine achieves significantly higher net performance compared to electric powered aircraft.

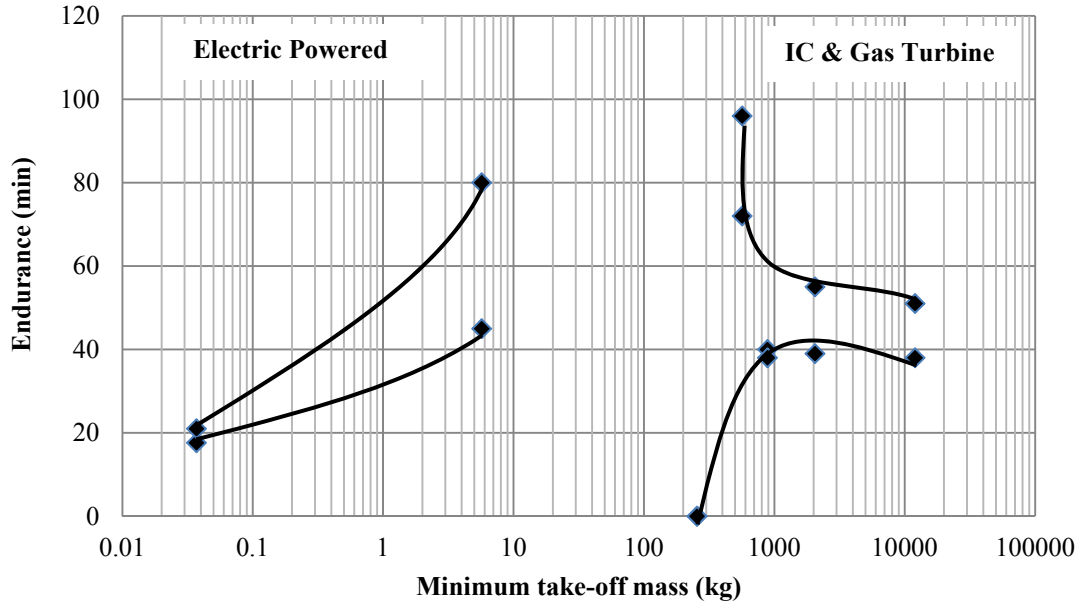

Figure 142: Endurance profile for different sized aircraft.

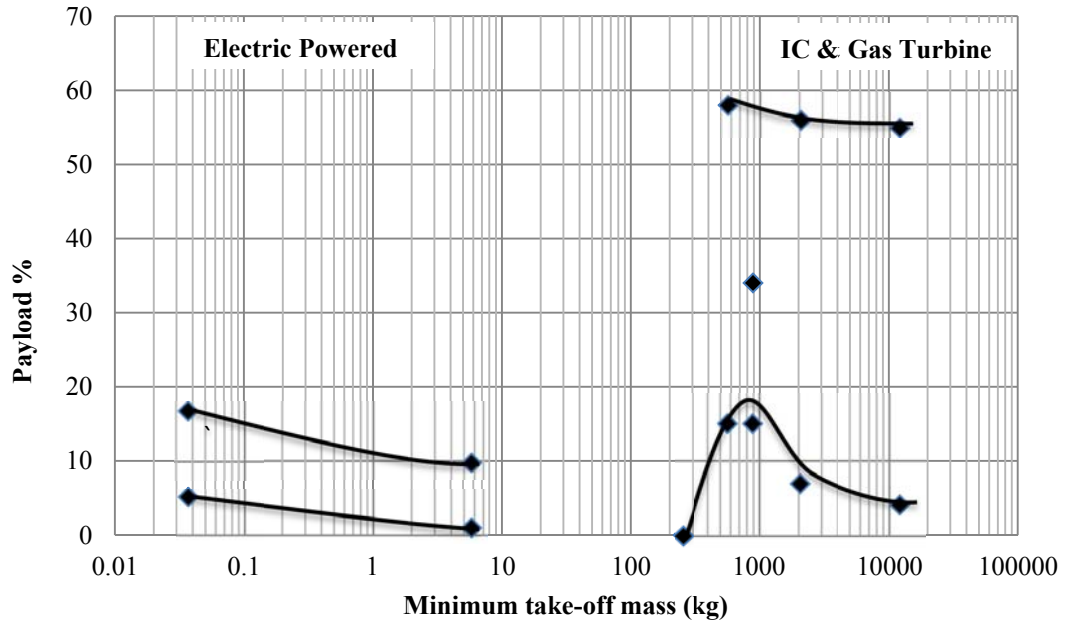

Figure 143: Payload performance for different sized aircraft.

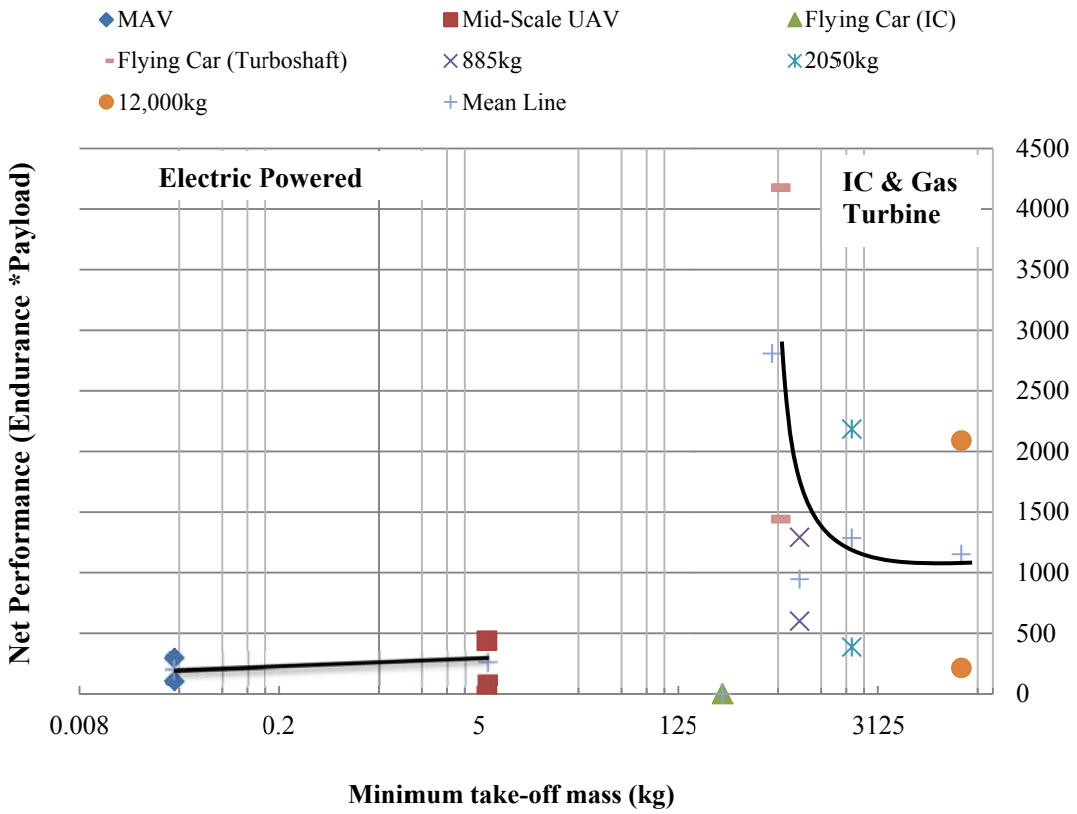

Figure 144: Performance summary.

Chapter 9. Conclusions & Future Work

9.1 Conclusions

This report has examined the aerodynamic characteristics of the proposed blown annular wing. Basic characteristics, including C_L, C_D and C_M have been established by experimentation for hover and translational flight modes. This has resulted in several crucial findings, as listed below.

- The annular wing experiences two major losses in lift: 1) due to annular flow expansion 2) relatively smaller blower-slot-height.
- The annular-wing in this arrangement experiences upper surface flow attachment and Coanda effect which is anticipated to increase the stalling angle of attack by a factor of about 2.8 compared to a conventional rectangular wingform.
- A further loss of 16% in C_{Lmax} value has been observed, suggesting a need for further work to modify and expand the theoretical analysis: most likely this will need to include the effect of finite blower-slot height but possibly also the shear effects.
- A thicker aerofoil, such as the NACA-0024, achieves greater lift for given flow velocity and leading edge angle of attack.

There has been found an incompatibility between slot height and wing size for symmetrical blowing across the longitudinal axis of the aerofoil as initially hypothesised. Symmetrical blowing for optimal wing size is nearly impossible with current centrifugal compressors available. This suggested a shift/modification in the blowing layout for realistic size and compatibility: that is to have pure upper surface blowing and relying upon the Coanda effect to create adhered flow and thus lift.

Upper surface blowing over annular wing showed that the wing with such blowing is capable of generating lift/thrust. The analysis showed that for maximum lift efficiency the flow needs further turning that may be achieved by deploying flaps around the trailing edge. Experimental investigation showed that 90 degree flow deflection can be achieved by addition of a flap. The annular-Coanda-wing with flap achieves a lifting efficiency of approximately 61% which may be further enhanced by reducing the outer diameter of the blower.

Two passive lift enhancement devices, the Gurney flap and guided vanes, have been explored theoretically and experimentally and have shown certain benefits. The Gurney flap on annular wing enhanced the baseline lift by 30% and, actually, reduced drag for moderate angles of attack. It also enhances nose down pitching moment which is beneficial in translational flight mode. The guided vanes proposal has been investigated theoretically; a mathematical model to predict local pressures for three different geometries has been developed. All three vanes have shown the capability of enhancing the baseline lift by overcoming the loss of dynamic pressure due to annular flow expansion.

Upon establishing that the proposed “annular-blown-wing” configuration is viable, the past V/STOL aircraft have been reviewed and analysed with regard to their performance parameters. The analytical review found two embedded categories in this class of aircraft based on their propulsion systems, i.e. jet and non-jet propulsion, and highlighted the significant performance differences between them. The performance of a relatively new class of aircraft, the flying cars, was evaluated. Among the most crucial findings are:

- Non-jet driven V/STOL aircraft acquire better range and consume significantly less power.

- Several different propulsive arrangements have been tried on past V/STOL aircraft; however, for jet propelled aircraft a clear best solution has yet to emerge.
- The aerodynamic based propulsion systems best serve low speed V/STOL aircraft – most of the future V/STOL aircraft are being developed based on this fact. The dominant branch of V/STOL "the helicopter" works with aerodynamic solution i.e. rotary wing.
- The thrust to weight requirements of a modern fighter aircraft tend towards also satisfying the same requirement for V/STOL.
- Whilst proposed future V/STOL vehicles validate the findings above by adopting non-jet propulsion system and keeping the overall size to the minimum, most current projects claim performance unlikely to be met by comparison with historical data.

In light of the historical experience of V/STOL aircraft a feasibility study has been conducted where it is shown that the developed annular-blown-wing can be integrated into a flyable vehicle. The centrifugal fan/compressor has been the component against which everything else is scaled. Different sizes (MAV to a Harrier equivalent) and propulsion have been explored. The best performance in terms of range and endurance is achieved by importing a turbofan engine into the annular-wing. A larger vehicle, i.e. a Harrier equivalent, with turbofan engine achieves significantly higher net performance compared to electric powered aircraft.

9.2 Future Work

Whilst an initial investigation of the annular wing is presented here, moving forward the following areas are proposed as developments of this work:

- Test the upper surface blowing with higher turning angles and evaluate the optimum turning angle with optimum lifting efficiency
- From a larger range of experimental data for upper surface blowing over the annular wing, improve the theoretical model by including non-ideal flow conditions, i.e. viscosity, shear stress and boundary layer profile

- Import the annular-wing geometry into a CFD package (i.e. Fluent) to generate the fine the fine aerodynamic characteristics and compare with the existing experimental results. This may also aid in designing the further experiments
- Design an experiment to test compressibility effects on the upper surface of the annular wing.
- Further explore the turbulence with more specifics, flow velocity direction and magnitude; this may be achieved by using a multi-wire probe.
- Develop theoretical and empirical models to enhance lifting efficiency, e.g. circulation control
- A broader range of Reynolds number needs to be brought into the analysis and investigate its effect on the lifting efficiency and the overall vehicle performance. This may initially be addressed with the aid of a CFD package
- Investigate and develop optimal aerofoil sections for use on the annular-wing
- It has been assumed that uniform or at-least symmetric velocity profiles for the flow generator are preferable – this may not be true and could be explored further
- The guided vane proposal presented in Section 6.3 needs to be validated by experimental results. Also, the theoretical model should be developed further to include different aerofoils sections at a range of angle of attack.
- It has been established that the annular-wing is most efficient with smallest possible overall size with regard to lift/mass design factor. However this does not reflect scale effects in available powerplant systems. Further work should also explore conceptual or eventually actual vehicle designs at a range of scales
- Finally, design, make and test a radio controlled model to demonstrate the developed technology

APPENDIX

	x = 2 mm		x = 5 mm		x = 9 mm		x = 20 mm		x = 50 mm	
Ypos	U Mean	U RMS	U Mean	U RMS	U Mean	U RMS	U Mean	U RMS	U Mean	U RMS
0	42.37	7.63	39.49	7.73	37.57	7.90	32.17	8.04	22.75	6.52
1	44.62	6.23	41.36	6.89	39.39	7.35	33.31	7.81	23.98	6.22
2	42.94	6.88	40.02	7.80	37.14	8.13	30.71	8.33	23.53	6.24
3	40.43	8.26	37.49	8.76	33.53	9.12	29.76	8.21	22.92	6.32
4	38.15	9.34	33.51	9.69	29.93	9.59	26.53	8.14	20.30	6.34
5	33.30	10.35	29.75	10.52	28.25	9.55	22.85	7.87	21.33	6.32
6	29.15	11.04	27.25	10.47	25.09	9.74	23.18	8.01	18.59	6.30
7	28.35	11.65	24.85	10.49	22.83	9.68	18.97	7.34	18.16	6.27
8	22.17	10.95	22.91	10.41	21.36	9.45	19.22	7.33	16.38	6.00
9	23.58	10.98	21.95	10.21	19.55	8.87	17.48	7.30	13.89	5.79
10	21.03	10.56	20.95	9.92	18.45	8.27	13.84	6.65	11.25	5.16
11	21.43	10.28	19.64	9.35	18.32	8.32	12.83	6.45	10.82	5.00
12	20.37	9.83	19.14	8.77	18.02	7.99	12.26	6.16	10.06	4.60
13	17.88	9.08	18.38	8.23	17.54	7.66	11.54	5.84	8.78	4.37
14	19.77	8.95	17.57	7.77	15.81	7.39	10.90	5.42	7.79	3.80
15	18.65	8.30	17.27	7.64	13.62	6.95	8.53	4.42	7.11	3.22
16	18.41	7.51	14.84	7.25	13.20	6.51	7.60	3.84	6.88	3.15
17	15.15	6.30	12.97	6.21	10.28	5.36	6.29	2.59	5.95	2.35
18	15.30	6.53	11.88	5.77	8.48	4.23	6.05	2.49	5.62	1.75
19	9.64	4.19	8.47	4.11	7.43	3.47	5.64	1.92	5.47	1.78
Average	26.14	8.74	23.98	8.40	21.79	7.78	17.48	6.21	14.08	4.87

Table 18: Velocity values recorded by hot-wire anemometer at different locations away from blower outlet.

NACA-0012		NACA-0024		NACA-0012 at 6 deg	
Chord (mm)	$v / \overline{U}_{L.E}$	Chord (mm)	$v / \overline{U}_{L.E}$	Chord (mm)	$v / \overline{U}_{L.E}$
0	0.9926	0	1.1095	0	1.3387
1.78	1.0410	1	1.1669	1	1.4290
2.78	1.0747	2	1.2052	2	1.5151
3.78	1.0850	3	1.2147	5	1.6043
4.78	1.0952	5	1.2912	7	1.6226
7.78	1.1289	6	1.3104	8	1.5806
9.78	1.1246	7	1.3266	9	1.5484
11.78	1.1026	9	1.3343	11	1.5161
13.78	1.0674	10	1.3327	12	1.4366
15.78	1.0681	11	1.3066	13	1.3796
7.78	1.0520	15	1.2482	17	1.4484
18.78	1.0556	17	1.1688	20.4	1.4409
19.78	1.0622	18	1.1946	23	1.3624
20.78	1.0615	20	1.0713	27	1.2925
22.78	1.0087	23	0.9871	31	1.2538
24.78	0.9889	25	0.9507	33	1.2452
27.78	0.9706	27	0.9163	35	1.2258
31.78	0.9537	29	0.9087	37	1.2000
35.78	0.9647	31	0.8924	39	1.1333
39.78	0.8885	39	0.8168	49	0.9785
43.78	0.8577	43	0.7174	52	0.9570
47.78	0.7917	47	0.7652	56	0.9140
52.78	0.7712	52	0.7642	60	0.9570
57.78	0.7316	57	0.7269	64	0.9032
62.78	0.5454	62	0.7154	68	0.8925
67.78	0.7038	68	0.6313	72	0.8634
72.78	0.6305	72	0.6370	76	0.8570
77.78	0.6451	77	0.6121	80	0.8925
80.13	0.6715	81	0.5930	82	0.9032

Table 19: Local flow distribution for different wing sections [Experiment Date: 18/11/2008, $P_{atm} = 100.1$ kPa , $T_{atm} = 20^{o}c$, $\rho_{air} = 1.1604\ kg/m^3$]

	Experimental		Theoretical	
$\overline{U}_{L.E}$ (m/s)	Lift (kgf)	Lift (N)	Lift(rect)	Lift (annular)
12	0.03	0.294	1.127	0.789
15	0.04	0.392	1.761	1.233
17	0.079	0.775	2.262	1.583
19	0.1	0.981	2.825	1.978
21	0.2	1.962	3.451	2.416

Table 20: Data for NACA-2214 { $P_{atm} = 99Kpa$, $T_{atm} = 21.5^{o}c$, $\rho_{air} = 1.1705\ kg/m^3$ }.

	Experimental		Theoretical	
$\overline{U}_{L.E}$ (m/s)	Lift (kgf)	Lift (N)	Lift(rect)	Lift (annular)
13	0.055	0.53955	1.356287	0.949
15	0.075	0.73575	1.805708	1.264
18	0.115	1.12815	2.600219	1.8202
19	0.16	1.5696	2.897157	2.0280
21	0.208	2.04048	3.539187	2.477

Table 21: NACA-0024 [$P_{atm} = 101 Kpa$, $T_{atm} = 20^{o} c$, $\rho_{air} = 1.2\ kg/m^3$].

	Reading 1				Reading 2			
	Fan Off		Fan On		Fan Off		Fan On	
Alpha	Maxima	Minima	Maxima	Minima	Maxima	Minima	Maxima	Minima
6	0.040	-0.130	-0.419	-1.323	0.120	-0.036	-0.396	-1.225
9	-0.013	-0.116	-0.820	-1.759	0.018	-0.138	-0.641	-1.635
12	0.000	-0.116	-1.060	-1.986	-0.013	-0.138	-0.913	-1.839
15	0.062	-0.125	-0.748	-2.317	-0.031	-0.174	-1.122	-2.369

Table 22: Maxima and minima values recorded by load cell for NACA-0012@12deg.

Alpha	Lift Minima-1 (N)	Lift Maxima 1 (N)	Lift mean 1 (N)	Lift Minima-2	Lift Maxima-2	Lift Mean-2 (N)	Lift Mean (N)
6	0.289	1.363	0.826	0.360	1.345	0.853	0.8394
9	0.704	1.746	1.225	0.503	1.653	1.078	1.1513
12	0.944	1.986	1.465	0.775	1.826	1.300	1.3826
15	0.999	2.379	1.689	0.948	2.338	1.643	1.6661

Table 23: Interpolated lift values for NACA-0012@12deg.

Alpha	CL Minima-1	CL Maxima-1	CL Mean-1	CL Minima-2	CL Maxima-2	CL Mean-2	CL Mean
6	0.176	0.187	0.181	0.220	0.184	0.202	0.192
9	0.429	0.239	0.334	0.307	0.226	0.267	0.300
12	0.576	0.272	0.424	0.472	0.250	0.361	0.392
15	0.609	0.326	0.467	0.578	0.320	0.449	0.458

Table 24: Interpolated CL values for NACA-0012@12deg.

XFOIL Version 6.94
xtrf = 1.000 (top) 1.000 (bottom)
Mach = 0.050 Re = 0.042 e 6 Ncrit = 7.000

alpha	CL	CD	CDp	CM	Top_Xtr	Bot_Xtr
3.000	0.4334	0.02381	0.01396	-0.0271	0.7733	1.0000
4.000	0.5241	0.02387	0.01394	-0.0171	0.6296	1.0000
6.000	0.6732	0.02844	0.01735	0.0020	0.3137	1.0000
7.000	0.7501	0.03353	0.02205	0.0082	0.2131	1.0000
8.000	0.8251	0.04079	0.02974	0.0134	0.1611	1.0000
9.000	0.8677	0.05185	0.04203	0.0195	0.1354	1.0000
10.000	0.8681	0.06632	0.05739	0.0250	0.1240	1.0000
11.000	0.7608	0.09072	0.08233	0.0202	0.1259	1.0000

Table 25: Data for NACA-0012 wing section [$P_{atm} = 102.7 Kpa$, $T_{atm} = 19.5^{o} c$, $\rho_{air} = 1.227\ kg/m^3$].

XFOIL Version 6.94

Calculated polar for: NACA 0024

Mach = 0.050 Re = 0.042 e 6 Ncrit = 7.000

alpha	CL	CD	CDp	CM	Top_Xtr	Bot_Xtr
1.000	0.0823	0.05388	0.04365	0.0040	0.6808	0.7789
2.000	0.3296	0.05218	0.04187	-0.0142	0.6391	0.8224
3.000	0.4330	0.05332	0.04309	-0.0149	0.5899	0.8715
4.000	0.5367	0.05528	0.04516	-0.0176	0.5422	0.9219
5.000	0.6639	0.05711	0.04710	-0.0251	0.4973	0.9713
6.000	0.8182	0.05603	0.04598	-0.0346	0.4574	1.0000
8.000	0.3885	0.08981	0.07962	0.0132	0.3923	1.0000
9.000	0.3539	0.09888	0.08848	0.0212	0.3670	1.0000
10.000	0.3371	0.10938	0.09882	0.0254	0.3441	1.0000
11.000	0.3266	0.12136	0.11072	0.0265	0.3252	1.0000
13.000	0.3242	0.14850	0.13785	0.0216	0.3218	1.0000

Table 26: Data for NACA-0024 wing section [$P_{atm} = 102.7 Kpa$, $T_{atm} = 19.5^{o} c$, $\rho_{air} = 1.227\ kg/m^3$].

		NACA-0012@6deg		NACA-0012@9deg		NACA-0012@12deg		NACA-0012@15deg		NACA-0024@12deg	
Xpos	Ypos	U Mean	U RMS	U Mean	U RMS	U Mean	U RMS	U Mean	U RMS	U Mean	U RMS
50	0	16.76	7.21	13.91	6.56	12.44	6.33	10.29	5.78	12.31	6.31
50	1	18.33	7.20	15.24	7.21	14.05	6.33	11.55	5.88	13.47	6.51
50	2	19.78	7.44	16.63	7.00	15.31	6.85	12.88	6.13	14.64	6.97
50	3	21.37	7.28	18.10	7.26	16.89	7.12	14.44	6.43	16.53	7.23
50	4	22.95	7.21	19.25	7.45	18.46	7.05	15.79	6.84	18.03	7.20
50	5	23.48	7.09	21.26	7.34	20.58	7.44	16.64	6.85	19.15	7.31
50	6	24.40	6.84	21.87	7.20	21.05	7.20	18.30	7.46	20.81	7.53
50	7	24.71	6.23	23.03	7.15	21.91	7.13	20.10	6.58	21.54	7.20
50	8	24.66	6.39	24.17	6.87	22.90	6.64	20.96	7.02	22.06	7.14
50	9	24.25	6.16	24.00	6.52	23.27	6.35	21.84	7.04	23.14	6.88
50	10	22.86	6.58	23.75	6.47	23.41	6.06	22.15	6.61	23.32	6.71
50	11	20.24	6.54	23.81	6.15	23.20	6.23	22.60	6.42	23.12	6.45
50	12	11.39	3.75	22.39	6.30	22.37	6.55	22.60	6.22	22.40	6.09
50	13	10.92	4.10	20.36	6.12	20.20	6.41	22.02	6.47	21.67	6.29
50	14	11.67	4.21	14.92	4.40	14.31	4.27	20.45	6.47	19.75	6.26
50	15	11.43	4.25	12.56	4.13	13.90	4.47	17.52	5.80	15.86	6.10
50	16	10.28	4.19	12.15	4.24	14.10	4.93	14.69	4.01	8.94	3.15
50	17	9.18	3.75	11.52	4.27	13.42	4.60	16.08	4.89	10.61	3.85
50	18	8.08	3.45	10.49	4.05	11.81	4.50	15.23	4.97	11.04	3.92
50	19	7.26	2.98	9.27	3.89	10.67	4.17	14.23	4.83	10.91	3.96
Average		17.20	5.64	17.93	6.03	17.71	6.03	17.52	6.13	17.47	6.15

Table 27: Data recorded at 50 mm away from blower outlet , approximately 2 mm in the wake of corresponding wing.

X = 2mm		X = 14mm		X = 20mm		X = 30mm		X = 40mm		X = 45mm		X = 50mm	
Ypos	U Mean	Ypos	U Mean	Ypos	U Mean	Ypos	U Mean	Ypos	U Mean	Ypos	U Mean	Ypos	U Mean
0	41	0	37	0	35	0	32	0	22	0	14	0	11
1	43	1	36	1	35	1	33	1	23	1	15	1	12
2	41	1	36	1	35	1	34	1	24	1	16	1	13
3	38	2	35	2	35	2	34	2	25	2	17	2	14
4	35	2	33	2	35	2	34	2	26	2	17	2	15
5	32	2	31	2	35	3	32	3	27	3	18	3	16
6	28							3	27	3	19	3	16
7	25							4	27	4	20	4	16
8	23							4	28	4	21	4	18
9	20							5	28	5	21	5	18
10	19							5	27	5	22	5	19
11	17							6	24	6	23	6	20
12	17									6	23	6	20
13	16									7	24	7	20
14	15									7	24	7	21
15	15									7	23	8	21
16	15									8	23	8	22
17	15									8	23	9	22
18	13									9	23	9	22
19	9									9	22	10	22
										9	21	10	22
												11	22
												11	21
												12	21
												12	19
Average	24		35		35		33		26		20		19

Table 28: Flow profile across upper surface of NACA-0024@12deg

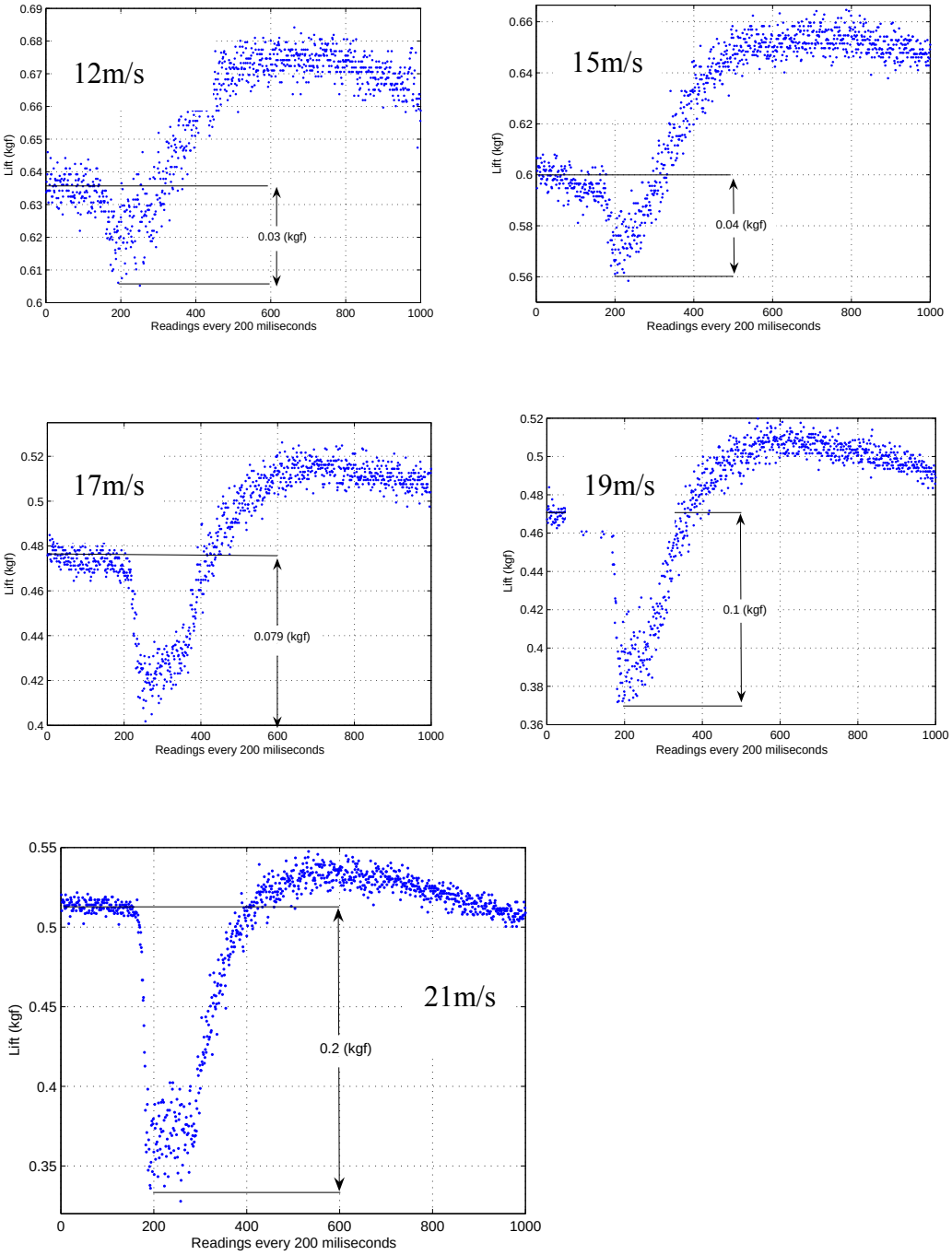

Figure 145: Lift force measured with load cell at different blower-outlet flow velocities {Parameters: NACA-4412, $\alpha = 12^{o}$, $T_{atm} = 23.4^{o}C$, $P_{atm} = 102.9$ kPa }..

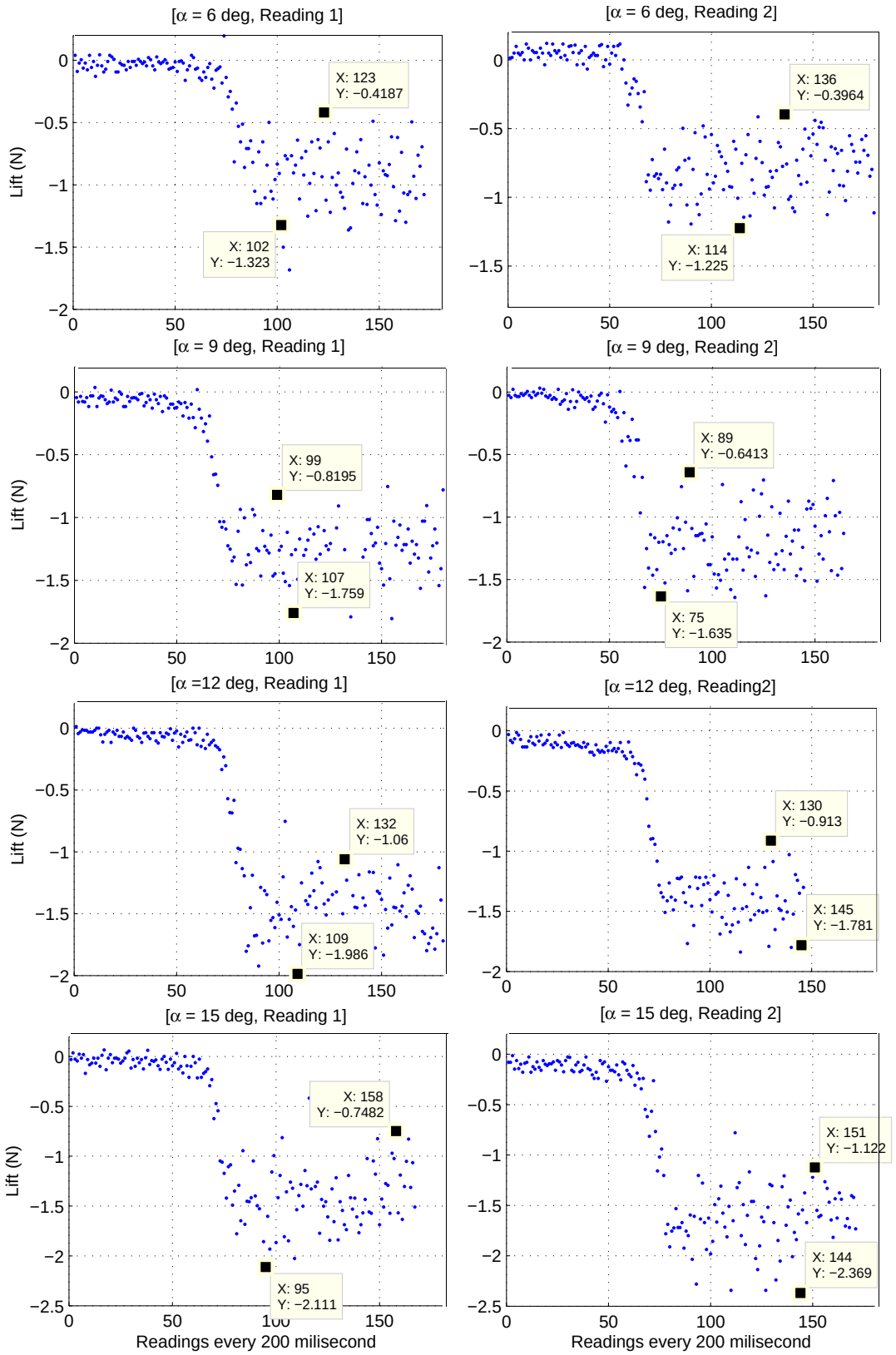

Figure 146: Lift force measured with load cell for different angles of attack{Parameters: NACA-0012, U_{eff} = 20 m/s, $T_{atm} = 20.3^{o}C$, $P_{atm} = 102.7$ kPa }..

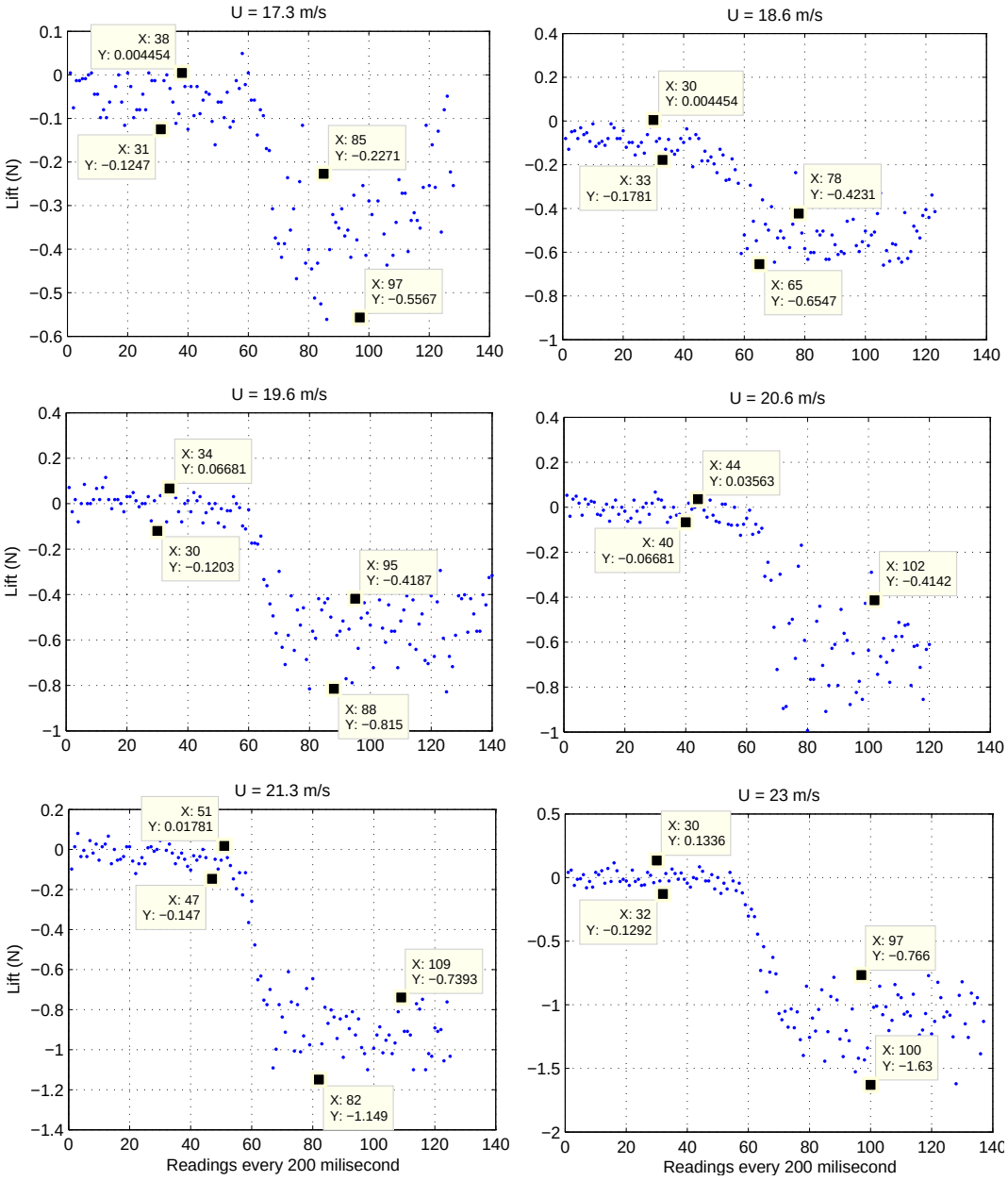

Figure 147: Lift force measured with load cell at different blower-outlet flow velocities {Parameters: NACA-0012, $\alpha = 12^{o}$, $T_{atm} = 22.3^{o}C$, $P_{atm} = 102.3$ kPa }..

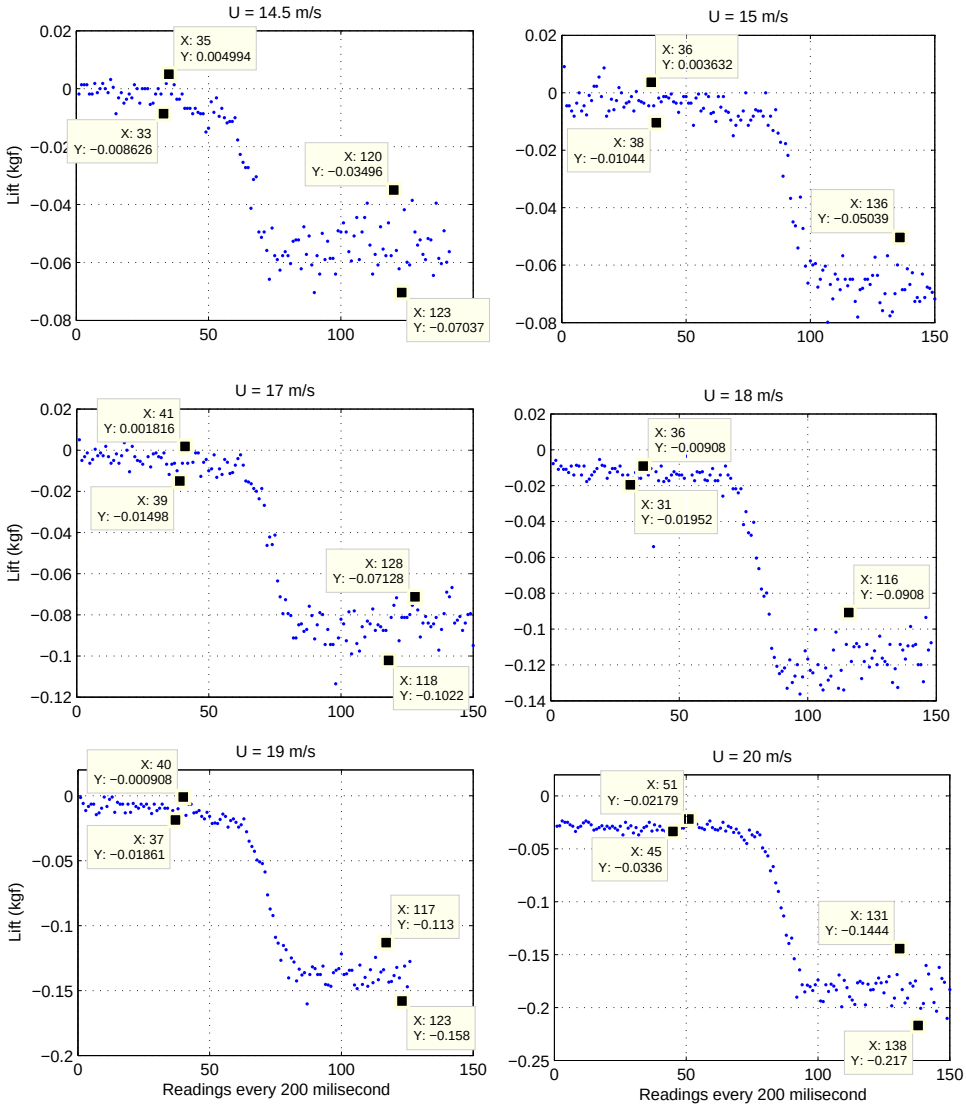

Figure 148: Lift force measured with load cell for different blower-outlet flow velocities {Parameters: NACA-0024, α=12^{o}, T$_{atm}$=22.3^{o}C, P_{atm}=102.3 kPa }..

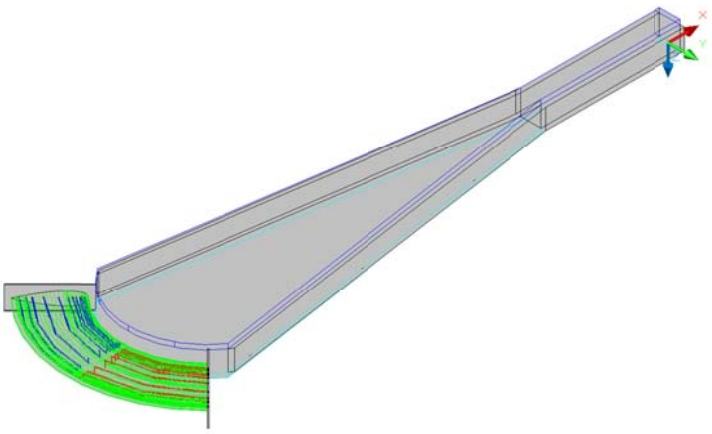

Figure 149: 3-D drawing of blown-annular-wing rig

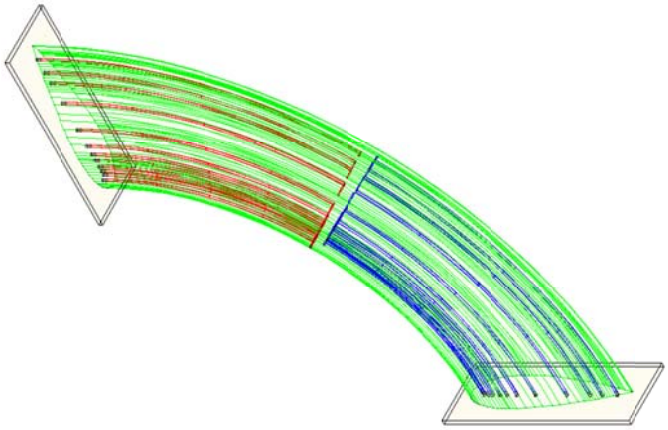

Figure 150: 3-D image of arc-wing

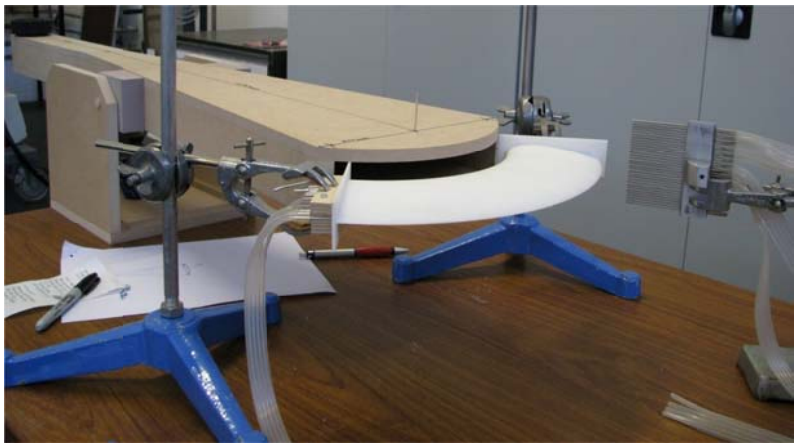

Figure 151: Close up of blown wing and wake-rake

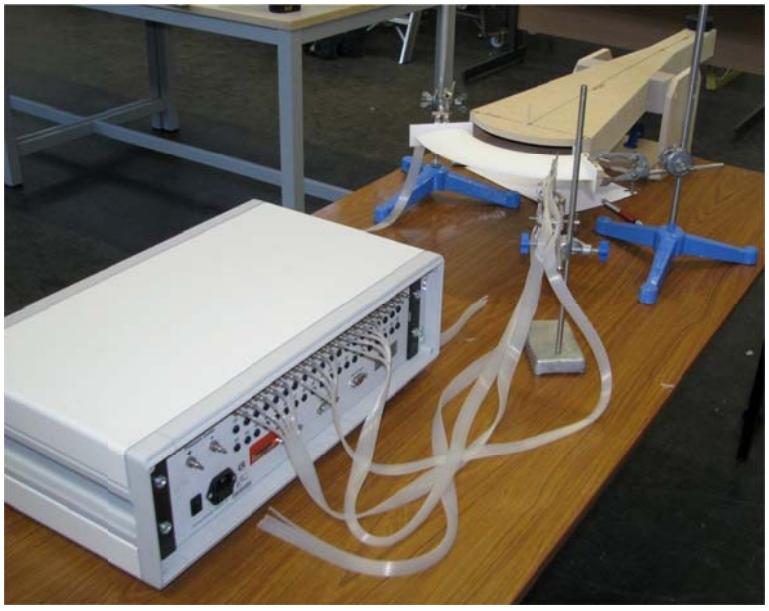

Figure 152: Depiction of pressure taps and pressure scanner

References

[1] Frost-Gaskin, P. *Static Wing for an Aircraft*. UK Patent Application, No 2438848A, 2007.

[2] Raymer, D.P. *Aircraft Design: A Conceptual Approach, 4th Ed*. AIAA Education Series, 2006.

[3] Coanda, H. *Device for Deflecting a Stream of Elastic Fluid Projected into an Elastic Fluid*. US Patent No: 2,052,869, 1936.

[4] Yen, K. T. *An Analysis of the Flow Turning Characteristics of Upper Surface Blowing Devices for STOL Aircraft*. Naval Air Development Centre, Report No. NADC-82007-60, 1982.

[5] Nicolai, L. *Fundamentals of Aircraft Design*. Mets; Revised edtion, 1984.

[6] William, J., Buttler, S. F. J and Wood, M. N. *The Aerodynamics of Jet Flaps*. Aeronautical Research Council Reports and Memoranda, R. & M. No. 3304, 1963.

[7] Spence, D. A. *The lift coefficient of a thin, jet-flapped wing*. Proceedings of the Royal Society of London. Series A, Mathematical and Physical Sciences, Vol. 238, No. 1212, pp. 46-68, December 1956.

[8] Green, P.N., and Carpenter, P.W. *The Aeroacoustics and Aerodynamics of High-Speed Coanda Devices, Part I: Conventional Arrangement of Exit Nozzle and Surface*. Journal of Sound and Vibration 208, 777-801, 2005.

[9] Voedisch, A. Jr. *Analytical Investigation of the Coanda Efffect (Project No. FP-188)*. Air Material Command, Wright Field, Dayton, OH, Report F TR-2155-ND, April 1947.

[10] Rodman, L. C., Wood, N. J., and Roberts, L. *An Experimental Investigation of Straight and Curved Annular Wall Jets*. JIAA TR-79, 1987.

[11] Fekete, G. I. *Coanda Flow in a Two-Dimensional Wall Jet on the Outside of a Cylinder*. Mech. Eng. Dept. Rep. 63-11, McGill University, 1963.

[12] Coanda, H. Device for Deflecting a Stream of Elastic Fluid Projected into an Elastic Fluid. US Patent 2,052,869, 1936.

[13] Coanda, H. Silencer for Engines. US Patent 2, 173, 549 , 1936.

[14] Von-Glahn, V.H. *Use of the Coanda Effect for Jet Deflection and Vertical Lift With Multiple-Flat-Plate and Curved-Plate Deflection Surfaces*. NACA Technical Note No, 4377, Washington: National Advisory Committee for Aeronautics, 1958.

[15] Nijhuis, G. *Secret Flying Discs of the Third Reich* (1922-1945). http://www.thebirdman.org/Index/Others/Others-Doc-History/+Doc-History-WW2Period/NaziFlyingDiscs-ASurprisingHistory.htm [retrieved 7/6/09].

[16] http://vortex-dynamics.com.au/r-d.html [retrieved 07/05/09]

[17] http://www.timesonline.co.uk/tol/news/uk/science/article4534995.ece [retrieved 05/07/09]

[18] Englar, R. J. *Overview of Circulation Control Pneumatic Aerodynamics: Blown Force and Moment Augmentation and Modification as Applied Primarily to Fixed-Wing Aircraft*. Proceedings of the NASA/ONR Circulation Control Workshop, 2004..

[19] Loth, J. L. *Why Have Only Two Circulation-Controlled STOL Aircraft Been Built and Flown In Years 1974 - 2004*. Proceedings of the 2004 NASA/ONR Circulation Control Workshop, 2004.

[20] Loth, J. L. Advantages of Combining BLC Suction with Circulation Control High-Lift Generation.

[21] Jones, G. S. Lin, J. C. Allan, B. G. Milholen, W. E. Rumsey, C. L. Swanson, R. C. Overview of CFD Validation Experiments for Circulation Control Applications at NASA. NASA Langley Research Center, Hampton, Virginia, 23681.

[22] Joslin, R. D., and Jones, G. S. *Applications of Circulation Control Theory*. AIAA, 2005.

[23] Sussman, M.B., Reed, J.B., O'Keefe, J.V., and Eldridge, W.M. *USB Environment Assessment Based on YC-14 Flight Test Measurements*. AIAA Paper 77-0593, 1977.

[24] Lindenbaum, B., and William, B. The VZ-9 Avrocar. www.vtol.org. [retrieved 25/08/2010]

[25] Imber, R., and Rogers, E. *Investigation of a Circular Planform Wing with Tangential Fluid Ejection*. 34th Aerospace and Sciences Meeting and Exhibition, AIAA 96-0558, Jan 1996.

[26] Imber, R., Rogers, E., and Abramson, J. *Investigation of CC Technology at NSWCCD*. Proceedings of the 2004 NASA/ONR Circulation Control Workshop, March 2005.

[27] VZ-9A Avro Car Development, sponsored by the US Air force and The US Army. http://www.virtuallystrange.net [Retrieved 15/06/2009].

[28] Phelps, A. E. III, and Smith, C. C. *Wind-Tunnel Investigation of an Upper Surface Blown Jet-Flap Powered-Lift Configuration*. NASA TND-7399, December, 1973.

[29] Phelps, A. E. III, Johnson, J. L, Jr. and Margason, R. J. *Summary of Low-Speed Aerodynamic Characteristics of Upper-Surface-Blown Jet-Flap Configurations*. NASA 406, pp. 63-87, May, 1976.

[30] Sleenman, W. C., Jr. and Hohlweg, W. *Low-Speed Wind-Tunnel Investigation of a Four-Engine Upper Surface Blown Model Having a Swept Wing and Rectangular and D-Shaped Exhaust Nozzles*. NASA TND-8061, December, 1975.

[31] Henderson, C., and Walters, M. *High-Lift STOL Aerodynamics /Stability and Control Techniques Assessment*. Naval Air Development Centre Report No. 81261-60, March, 1983.

[32] Newman, B. G. *The Deflexion of Plane Jets by Adjacent Boundaries– Coanda Effect*. Boundary Layer and Flow Control , edited by G. V. Lachmann, Vol.1, Pergamon Press, Oxford, pp. 232–264, 1961.

[33] Fekete, G. I. *Coanda Flow of a Two-Dimensional Wall Jet on the Outside of a Circular Cylinder.* Tech. Rept. 63-11, Mechanical Engineering Research Laboratories, McGill University, 1963.

[34] Juvet, P. J. D. *Control of High Reynolds Number Round Jets.* Ph.D. thesis, Department of Mechanical Engineering, Stanford University, 1993.

[35] Roberts, D.W. *A Zonal Method for Modeling Powered-Lift Aircraft Flow Fields.* NASA CR-177521, March, 1989.

[36] Theodorsen, T. Theory of Wing Sections of Arbitrary Shape. NACA Report No. 411, 1933.

[37] Kroo, I. Applied Aerodynamics: A Digital Textbook. www.desktopaero.com [retrieved 3 November 2007].

[38] Abbott, I. H. and Doenhoff, A. E. Summary of Airfoil Data. NACA Report No. 824, 1945.

[39] McCroskey, W. J. *A Critical Assessment of Wind Tunnel Results for the NACA-0012 Aerofoil*. NASA TM-100019, October, 1987.

[40] XFoil data validation. http://www.aerofoilengineering.com [retrieved 13/11/2010]

[41] Atmospheric Flight Mechanics. Clarkson Education. http://people.clarkson.edu/~pmarzocc/AE429/AE-429-2.pdf [Retrieved 07/03/08].

[42] iLoad Digital USB Integrated Load Sensor, Spec Sheet. Load Star Sensor, Inc. www.loadstarsensors.com [retrieved 28/12/2008].

[43] Hot-wire anemometry spec sheet. www.dantecdynamics.com [retrieved 20/10/2008].

[44] *Introduction to design and performance data for diffusers*. ESDU 76027, 2007.

[45] Asberg, B., Blanco, G., Bose, P., Garcia-Lopez, J., Overmars, M., Wilfong, G., and Zhu, B. *Feasibility of design in stereolithography*. Algorithmica, Special Issue on Computational Geometry in Manufacturing, Vol. 19, No. 1/2, pp. 61-83, Sept/Oct, 1997,.

[46] Stern, F., Muste, M., Beninati, L-M., and Eichinger, B. *Summary of Experimental Uncertainty Assessment Methodology with Examples.* IIHR Technical Report No. 406, 1999.

[47] Girdhar, P., and Moniz, O. *Practical Centrifugal Pumps*. Elsevier, 2004.

[48] Ferguson, T. B. *The Centrifugal Compressor Stage*. London Butterworths, 1963.

[49] Chanin Tongchitpakdee. *PhD Thesis: Computational Studies of the Effects of Active and Passive Circulation Enhancement Concepts on Wind Turbine Performance*. School of Aerospace Engineering, Georgia Institute of Technology, 2007.

[50] Freankie Ka Chun NG. *Project Report: Compare the effect of varying slot width to chord ratio (h/c) on the 2-D wing performance*. Division of Mechanical and Aeronautical Engineering, University of Hertfordshire, 1993/94.

[51] Pope, A., Barlow, J. B., and Rae, W. H. *Low-Speed Wind Tunnel Testing (3rd Edition)*. A Wiley-Interscience Publication, 1999.

[52] Seyfang, G. (Retired BAE officer) Work done in his private labs [waiting for George's paper to be published on this work for complete reference]

[53]. Abbott, I. H. and Von Doenhoff, A. E. *Theory of Wing Sections*.Newyork: Dover Publication, Inc., 1959.

[54]. Abbott, I. H. and Von Doenhoff, A. E. *Summary of Airfoil Data.* NACA Report No. 824, 1945.

[55] Anderson, D. F. and Eberhardt, S. *Understanding Flight, Second Edition*. McGraw Hill, 2010.

[56] Sun, H. Shin, H. Lee, S. *Analysis and optimization of aerodynamic noise*. Journal of Sound and Vibration, 999–1018, 2006.

[57] Mckain, T. F., and Holbrook, G. J. *Coordinates for a High Performance 4:1 Pressure ratio Centrifugal Compressor.* NASA Contractor Report 204134, 1997.

[58] Mizuki, S., and Hirano, T. *Design and Prototyping of Micro Centrifugal Compressor for Ultra Micro Gas Turbine*. Journal of Thermal Science. pringerLink, 2007.

[59] Coanda, H. *Device for Deflecting a Stream of Elastic Fluid Projected into an Elastic Fluid*. US Patent No: 2,052,869, 1936.

[60] Glauert, M. B. *The Wall Jet*.J1, of F1.Mech. Vol. 1, Pt. 6, pp 625-643, 1956.

[61] Roberts, L. *A Theory of Turbulent Curved Wall Jets*.Circulation Control Workshop, 1986.

[62] Bradshaw, P., and Gee, M. T. *Turbulent Wall Jets With and Without an External Stream*. ARC R&M 3252, 1962.

[63] Harting, A. *Experimental investigation of two dimensional incompressible curved wall jets in still air, flowing along circular cylinders because of the Coanda effect*. NLR, Report No. A1585, 1964.

[64] Henderson, C., and Walters, M. *High-Lift STOL Aerodynamics /Stability and Control Techniques Assessment*. Naval Air Development Centre Report No. 81261-60, March, 1983.

[65] Newman, B. C. *Deflection of Plane Jets by Adjacent Boundaries – Coanda Effect*. Boundary Layer and Flow Control , Vol. 1, Oxford Pergamon Press, 1961.

[66] Hall, J. W., and Ewing, D. *A Combined Spatial and Temporal Decomposition of the Coherent Structures in the Three-Dimensional Wall Jet*.AIAA 2006-308, 18pp, 2006.

[67] Yen, K. T. *An Analysis of the Flow Turning Characteristics of Upper Surface Blowing Devices for STOL Aircraft*.Naval Air Development Centre, Report No NADC-82007-60, 1982.

[68] Proceedings of the Circulation-Control Workshop 1986. NASA Ames Research Centre, California, 1986.

[69] Lieback, R. H. *Design of Subsonic Aerofoils for High Lift*. Journal of Aircraft, Vol. 15, No. 9, pp. 547-561, Sep. 1978.

[70] Giguère, P., Lemay, J., and Dumas, G. *Gurney Flap Effects and Scaling for Low-Speed Aerofoils*. AIAA Paper 95-1881, 1995.

[71] Myose, R., Papadakis, M., and Heron, I. *Gurney flap experiments on aerofoils, wings, and reflection plane model*. Journal of Aircraft 1998, 35 (2): 206–211.

[72] http://www.allamericanracers.com/gurney_flap.html [retrieved 04/08/09]

[73] Giguère, P., Lemay, J., and Dumas, G. *Gurney Flap Effects and Scaling for Low-Speed Aerofoils*. AIAA Paper 95-1881, 1995.

[74] Storms, B. L., and Jang, C. S. *Lift Enhancement of an Aerofoil Using a Gurney Flap and Vortex Generators*. Journal of Aircraft, Vol. 31, No. 3, pp.542-547, May 1994.

[75] Jeffrey, D. R. M., and Hurst, D. W. *Aerodynamics of the Gurney Flap*. AIAA Paper 96-2418, 1996.

[76] Van Dam, C. P., Yen, D. T., and Vijgen, P. M. H. W. *Gurney Flap Experiments on Aerofoil and Wings*. Journal of Aircraft, Vol. 36, No. 2, Mar. 1999, pp.484-486.

[77] Chandrasekhara, M. S., Martin, P. B., and Tung, C. *Compressible Dynamic Stall Performance of Variable Droop Leading Edge Aerofoil with a Gurney Flap*. AIAA Paper 2004-0041, 2004.

[78] Rhee, M. A. *Computational Study of an Oscillating VR-12 Aerofoil with a Gurney Flap*. AIAA 2004-5202, 2004.

[79] Guzel, G., Sankar, L. N., and Rhee, M. *Computational Investigation of the Effects of Gurney Flap on the Aerodynamic Performance of VR-12 Aerofoil*. AIAA Paper 2005-4960, 2005.

[80] Bieniawski, S., and Kroo, I. *M. Flutter Suppression Using Micro-Trailing Edge Effectors.* AIAA Paper 2003-1941, 2003.

[81] Lee, H., Kroo, I. M., and Bieniawski, S. *Flutter Suppression for High Aspect Ratio Flexible Wings Using Microflaps*. AIAA 2002-1717, 2002.143.

[82] Yen, D. T., van Dam, C. P., Bräeuchle, F., Smith, R. L., and Collins, S. D. *Active Load Control and Lift Enhancement Using MEM Translational Tabs*. AIAA Paper 2000-2422, 2000.

[83] Neuhart, D. H. and Pendergraft Jr, O. C. A *Water Tunnel Study of Gurney Flaps*. NASA TM 4071, 1988.

[84] Jang, C. S., Ross, J. C, and Cummings, R. M. *Computational Evaluation of an Aerofoil with a Gurney Flap*. AIAA Paper 92-2708, pp. 801-809.142, 1992.

[85] Lieback, R. H. *Design of Subsonic Aerofoils for High Lift*. Journal of Aircraft, Vol. 15, No. 9, pp. 547-561, Sep. 1978.

[86] Neuhart, D. H., and Pendergraft, O. C. *A water Tunnel Study of Gurney Flaps*. NASA Technical Memorandum 4071, 1988.

[87] Giguere, P., Dumas, G. and Lemay, J. *Gurney Flap Scaling for Otimum Lift-to-Drag Ratio*. AIAA Journal, Vol. 35, No. 12, 1997.

[88] Roberts, L., and Deckert, W. R. *Recent Progress in V/STOL Technology*. NASA Technical Memorandum 84238, 1982.

[89] Tennekes, H. *The Simple Science of Flight*. Cambridge, MA: MIT Press, 1997.

[90] Wanless, R. M. *Can the Aldabra White-Throated Rail Dryolimnas Cuvieriald Abranus Fly?* National Museum Of Natural History, Smithsonian Institution Washington D.C, U.S.A. August 2003.

[91] Alexander, D. E. *Nature's Flyers: Birds, Iinsects, and the Biomechanics of flight.* The Johns Hopkins University Press, Baltimore, 2002.

[92] Marden, J. H. *Maximum Lift Production During Take-off In Animal Flying.*Department of Zoology, University of Vermont, Burlington, VT 05405, USA, 1987.

[93] Abbot, I. H., and Von Doenhoff, A. V. *Theory of Wing Sections*. Dover Publications, INC. New York, 1959.

[94] UK Civil Aviation Authority, *Aviation Safety Review 2008,* CAP 780 issued 11 November 2008

[95] Lindenbaum, B. *V/STOL Concepts and Developed Aircraft Vol I - A Historical Report (1940 – 1986).* Air Force Wright Aeronautical Laborataries, ADA175379.

[96] McCormick, B. W. *Aerodynamics of V/STOL Flight*. Academic Press, 1967.

[97] Kuhn, R. E. *Take-Off and Landing Distance and Power Requirements of Propeller-Driven Airplanes*. IAS preprint 690, presented at Twenty-fifth Annual meeting, New York, January 28-31, 1957.

[98] Anderson, S. B. *Historical Overview of V/STOL Aircraft Technology*. NASA Technical Memorandum 81280.

[99] Proceedings of V/STOL Aircraft Aerodynamics, Volume II. Naval Air Development Center, California, 1979.

[100] Filippone, A. *Flight Performance of Fixed and Rotary Wing Aircraft*. Butterworth-Hienemann, 2006.

[101] McLemore, H. C., and Smith, C. C. *Generalised Hot-Gas Ingestion Investigation of Large-Scale Jet VTOL Fighter-Type Models*. NASA Langley Research Center, NASA TN D-5581.

[102] Raymer, D. P. *Aircraft Design: A Conceptual Approach, 4th Edition*. AIAA Education Series, 2006.

[103] Gologan, C., Broichhausen, K. and Seifert, J. *A Calculation Method for Parametric Design Studies of V/STOL Aircraft.*The Aeronautical Journal, Vol. 113 No 1143, 2009.

[104] Stinton, D. *The Design of the Aeroplane, 2nd Edition*.Blackwell Sciences, 2001.

[105] MULE Stat Sheet, Urban Aeronautics. www.urbanaero.com [Retrieved 02/08/08].

[106] X-Hawk Stat Sheet, Urban Aeronautics. www.urbanaero.com [Retrieved 01/02/09]

[107] The New M400 Design, Moller International. www.moller.com [Retrieved 02/08/08].

[108] Skyrider Specifications, Macro Industries Inc. www.macroindustries.com [Retrieved 22/07/08].

[109] Dragonfly UMR1 Preliminary Specifications and Performance, Trek Aerospace.www.trekaero.com [Retrieved 01/08/08].

[110] Moshier, M., and Bulaga, R. *Wind Tunnel Performance Investigation of the SoloTrekTM XFVTM Ducted Fan System*. DARPA/DSO, Arlington,VA, 2001.

[111] Clancy, L. J. *Aerodynamics*. Pitman Publishing Limited, London, 1975.

[112] Greco, C., and Paulo, S. J. *Effect of wing sweep direction on suckdown for a hovering STOVL model*. AIAA-1997-2315, 1997.

[113] Turner, H. L., and Drinkwater, F. J. *Some Flight Characteristics of a Deflected Slipstream V/STOL Aircraft*. NASA TN D-1891, 1963

[114] Newman, S. *The foundations of Helicopter Flight*. Butterworth Heinemann, 2003.

*[*115*]* *Proceedings of Special Course on V/STOL Aerodynamics*. Advisory Group For Aerospace Reseach &Development, AGARD Report No.710, 1984.

[116] All The World's Rotorcraft.www.aviastar.org [Retrieved 01/08/08].

[117] Skyaid Organisation.www.skyaid.org [Retrieved 02/08/08].

[118] Jet Engine Specification Database.www.jet-engine.net [Retrieved 01/07/08].

[119] International V/STOL Historical Society.www.vstol.org [Retrieved 05/04/08].

[120] All The World's Rotorcraft.www.aviastar.org [Retrieved 01/08/08].

[121] Skyaid Organisation.www.skyaid.org [Retrieved 02/08/08].

[122] Jet Engine Specification Database.www.jet-engine.net [Retrieved 01/07/08].

[123] International V/STOL Historical Society.www.vstol.org [Retrieved 05/04/08].

[124] European Aviation Safety Agency, *Certification Specification for Very Light Aeroplanes,* CS.22 to Al1.

[125] Wei Shyy, Y. L., Jian, T., Dragos, V. and Hao, L. *Aerodynamics of Low Reynolds Number Flyers*. Cambridge University Press, 2008.

[126] Marek, P. *Design, Optimization and Flight Testing of a Micro Air Vehicle*. A thesis submitted to the Faculty of Engineering, University of Glasgow, 2007.

[127] Michael, j. M., and Francis, M. S. *Micro Air Vehicles - Toward a New Dimension in Flight*. DARPA Report, 1997.

[128] Stanciu, V., Causa, H. A., and Boscoianu, M. *Alternative Propulsion Systems for Micro Aerial Vehicles*. European Micro Air Vehicle Conference and Flight Competition EMAV, Conference Proceedings, 2006.

[129] Grasmeyer, J. M., and Keennon, M. T. *Development of the Black Widow Micro Air Vehicle*. American Institution of Aeronautics and Astronautics, AIAA-2001-0127, 2001.

[130] British Microlight Aircraft Association, *Propellers,* Technical Information Leaflet No.11 issue 2

[131] www.astroflight.com [retrieved 05/03/2010]

[132] http://www.rctoys.com/ [retrieved 01/03/2010]

[133] http://www.gwsprops.com/ {retrieved 21-07-2010}.

[134] Energy Density of Aviation Fuel. Hypertextbook.com. {retrieved 10-06-2010}.

[135] http://www.microflight.com/Prop-EP-4530 {retrieved 21-07-2010}.

[136] http://www.uavforum.com/vehicles/overview.htm [retrieved 01/03/2010]

[137] www.rotax-aircraft-engines.com [retrieved 28/02/2010]

[138] http://www.flylight.co.uk/gliding/index.htm {retrieved 21-07-2010}

[139] Conceptual Design Report for the Agricultural Unmanned Aircraft System. courses.ae.illinois.edu [retrieved 01/03/2010]

[140] Propulsion by Propellers, *http://www.mh-aerotools.de/airfoils/prpstati.htm* [retrieved 03/03/2010]

[141] http://www.iascanada.com/engmodels.html accessed 21/7/10

[142] http://www.grc.nasa.gov/WWW/K-12/airplane/aturbf.html [retrieved 21-07-2010]

[143] J A Johnston, *Kestrel P-1127 Evaluation Trials*, Proceedings of the 9th annual symposium of the Society of Experimental Test Pilots (1965)

[144] Saeed, B., and Gratton, GB. *An evaluaton of the historical issues associated with achieving non-helicopter V/STOL capability and the search for the flying car*, AeroJ Vol 114, No.1152, pp91-101, Feb 2010.

[145] Turbofan Engine Data Table 2, www.aircraftenginedesign.com [retrieved 06/04/2010]

[146] McDonnell Douglas/British Aerospace AV-8B Harrier II Attack Fighter. Aircraft Museum. Aerospaceweb.org. [Retrieved 15/05/2010]